

Abstract

A Practical Quantum-Limited Parametric Amplifier Based on the Josephson Ring Modulator

Flavius Dietrich Octavian Schackert

2013

This dissertation has addressed the problem of developing the Josephson Parametric Converter (JPC) as a practical phase-preserving microwave parametric amplifier operating at the quantum limit of added noise. The device consists of two superconducting resonators coupled through the Josephson Ring Modulator (JRM), which in essence consists of a loop of four identical Josephson tunnel junctions, threaded by an applied magnetic flux. The nonlinearity of the JRM is of the tri-linear form XYZ without spurious nonlinear terms and involving only the minimal number of modes, thus placing the JPC close to the ideal non-degenerate parametric amplifier. This pure form of the nonlinearity is confirmed here by the observation of coherent attenuation (CA), the time-reversed process of three-wave parametric amplification, with signal, idler, and pump modes in the fully nonlinear regime. The design developed in this dissertation allows fabrication of the amplifier in a single lithography step, greatly simplifying parameter adjustments from one device to the next. Measured device characteristics and amplifier performances are presented, and limitations linked to the junction energy E_J and the circuit parameters discussed. The use of these JPCs in the readout of superconducting qubits is shown to lead to almost ideal quantum measurements, as the measurement efficiency can approach the ideal value of 1.

A Practical Quantum-Limited Parametric Amplifier

Based on the Josephson Ring Modulator

A Dissertation
Presented to the Faculty of the Graduate School
of
Yale University
in Candidacy for the Degree of
Doctor of Philosophy

by
Flavius Dietrich Octavian Schackert

Dissertation Director: Professor Michel H. Devoret

December 2013

Copyright © 2013 by Flavius Dietrich Octavian Schackert
All rights reserved.

To my parents Marina and Dietrich, to my sister Lili, and to Paloma.

Contents

1	Introduction	1
1.1	Parametric Amplifiers - A Brief Overview	3
1.1.1	Previous Work on Parametric Amplification	3
1.1.2	Parametric Amplification and Nonlinear Media	5
1.1.3	Phase-Sensitive and Phase-Preserving Amplification	10
1.1.4	XYZ Nonlinearity and JPC Scattering Matrix	12
1.2	A Practical Parametric Amplifier Based on the Josephson Ring Modulator	16
1.2.1	Paramp Requirements	17
1.2.2	The Josephson Ring Modulator	18
1.2.3	Microstrip JPC Design	20
1.3	Main Measurement Results	24
1.3.1	Tuning Bandwidth	24
1.3.2	Gain and Dynamical Bandwidth	26
1.3.3	Gain and Power Limitations	27
1.3.4	SNR Improvement	31
1.3.5	Qubit Measurements	33
1.3.6	Coherent Attenuation	35
2	Josephson Ring Modulator	38
2.1	Ring Modulator with Four Junctions	38
2.1.1	Definitions and Sign Conventions	38
2.1.2	JRM Energy	41
2.1.3	Current Induced by Magnetic Flux	42

2.1.4	Adding External Microwaves	43
2.1.5	Lowest Ring Energy	44
2.1.6	Current-Flux Relation	44
2.1.7	Experiment	46
2.1.7.1	Flux Modulation	46
2.1.7.2	Degeneracy and Phase Shift	49
2.2	Shunted Ring Modulator	49
2.2.1	Circuit Equations	52
2.2.2	Shunted JRM Energy	53
2.2.3	Solutions (m, m, m, m)	55
2.2.3.1	Circulating Currents	55
2.2.3.2	Energy	57
2.2.3.3	Equivalent Inductance	57
2.2.4	Solutions $(m, -m, m, -m)$	58
2.2.4.1	Circulating Currents	58
2.2.4.2	Energy	59
2.2.4.3	Inductance	60
2.2.5	Crossover	61
2.2.6	Experiment	62
2.2.6.1	Shunting the JRM with Large Junctions	64
3	Scattering Matrix Description of Gain and Noise of Parametric Amplifiers	68
3.1	JPC Scattering Matrix	68
3.2	Phase-Sensitive and Phase-Preserving Amplification	72
3.2.1	Commutation Relations	74
3.2.1.1	Field Operators	74
3.2.1.2	Flying Oscillators	75
3.2.2	Two-Mode Squeezing Operator and JPC Scattering Matrix	77
3.2.3	One-Mode Squeezing Operator and JBA-paramp Scattering Matrix	79
3.2.3.1	Implementations of phase-sensitive amplifiers	80
3.2.3.2	Phase-preserving operation of a degenerate amplifier	81

3.2.4	Common and Differential Mode Representation: Link Between JPC and JBA-Paramp	83
3.2.5	Signal and Noise Properties: Averages and Standard Deviations	86
3.2.5.1	JPC	88
3.2.5.2	JBA-Paramp	89
3.2.6	Evolution of Coherent States	90
3.2.6.1	Coherent Attenuation	94
4	Operation of Amplifier, Experimental Results	96
4.1	Measured Devices	96
4.2	Circuit Characterization	97
4.2.1	Quality Factor	97
4.2.1.1	Coupling Capacitor	98
4.2.2	Participation Ratio	100
4.2.2.1	Four Junction JRM	100
4.2.2.2	Eight Junction JRM	102
4.3	Gain Scaling with Pump Power	104
4.4	Tunability with Pump Frequency	105
4.5	Saturation Powers for Tunable JPC	106
5	Coherent Attenuation and Reverse Operation of the JPC	108
5.1	Theory	109
5.1.1	Coherent Attenuation	109
5.1.2	Gain Modulation	110
5.2	Some Experimental Details and JPC Characteristics	111
5.3	Coherent Attenuation	114
5.4	Gain Enhancement	118
6	Experimental Methods	123
6.1	Sample Fabrication	123
6.1.1	E-beam Lithography with Converted SEM	124
6.1.1.1	Transmission Line Resonator with Holes	125
6.1.1.2	Resist Mask	125

6.1.1.3	Transmission Line Resonators without Holes	126
6.1.2	E-beam Lithography with EBPG	126
6.1.2.1	JRM with Four Dolan Junctions	128
6.1.2.2	Shunted JRM with Eight Dolan Junctions	128
6.1.2.3	Shunted JRM with Eight BFT Junctions	128
6.1.3	Junction Aging	130
6.2	Sample Holder	130
6.3	Setup	132
6.3.1	Heliox Refrigerator	132
6.3.2	Triton Refrigerator	132
7	Conclusion & Outlook	135
Bibliography		136
A	Transmission Line Resonators	146
A.1	Parallel RLC Resonator	146
A.2	Transmission Line Resonator	148
A.3	Mapping of an (unloaded) TL Resonator to a RLC Resonator	150
A.4	Loaded TL Resonator	151
A.4.1	Admittance of Load	151
A.4.2	External Q: Input Coupling Only	153
A.4.3	External Q: Input and Output Coupling	154
B	Recipes Used for JPC Fabrication	156
B.1	Spinning Resist	156
B.1.1	Wafer Cleaning	156
B.1.2	Spinning	156
B.2	Development	158
B.2.1	Dolan Bridge Technique	158
B.2.2	Bridge Free Technique	158
B.3	Aluminum Deposition	158
B.3.1	Dolan Bridge Technique	158

B.3.2 Bridge-Free Technique	159
---------------------------------------	-----

List of Figures

1.1	Degenerate and non-degenerate paramaps in frequency space.	8
1.2	Fresnel vector representation of the operation of quantum-limited amplifiers.	11
1.3	Schematic of the Josephson Ring Modulator (JRM).	18
1.4	SEM images of different implementations of the Josephson Ring Modulator (JRM). . .	21
1.5	Schematic of a frequency tunable Josephson Parametric Converter (JPC).	23
1.6	Measured JPC signal frequency as a function of the externally applied magnetic flux threading a shunted JRM.	25
1.7	Measured Lorentzian gain response functions of a JPC with inductively shunted JRM.	26
1.8	Measured gain and dynamical bandwidth of a JPC.	27
1.9	Measured JPC gain and output power dependence as a function of signal input powers.	30
1.10	Signal-to-noise ratio improvement with JPC in measurement chain.	32
1.11	Transmon qubit state measured with and without a JPC.	34
1.12	Quantum jumps of a transmon qubit measured with a JPC.	34
1.13	JPC gain enhancement at the Coherent Attenuation (CA) point $\phi = 2\pi$	37
2.1	Schematic of the Josephson Ring Modulator (JRM).	39
2.2	Schematic of branch element with arrows indicating sign convention used.	39
2.3	JRM energy dependence on external magnetic flux.	45
2.4	Schematic of transmission line resonators with JRM.	47
2.5	SEM picture of four junction JRM.	47
2.6	Phase response of JPC with four junction JRM for modulated magnetic flux.	48
2.7	Circulating current in JRM induced by magnetic flux.	50
2.8	JRM state jump as observed with coherent attenuation experiment at degenerate flux point $\Phi_{\text{ext}} = \Phi_0/2$	50

2.9	Schematic of shunted Josephson ring modulator.	51
2.10	Schematic of JRM with magnetic flux quanta and external magnetic flux.	52
2.11	Current pattern for the state (m, m, m, m) around $\varphi_{\text{ext}} = 0$ for shunted JRM.	56
2.12	Current pattern for the state $(m, -m, m, -m)$ around $\varphi_{\text{ext}} = 4\pi$ for shunted JRM.	59
2.13	Shunted JRM energy as a function of x , for different values of $-4\beta_L \cos(\varphi_{\text{ext}}/4)$.	61
2.14	Calculated frequency of JPC with shunted JRM as a function of the applied magnetic flux.	63
2.15	Schematic of JRM with eight Josephson junctions.	64
2.16	SEM image of two implementations of the JRM with eight junctions.	65
2.17	Phase response of JPC with shunted JRM for modulated magnetic flux. Sample fabricated with Dolan bridge technique.	66
2.18	Phase response of JPC with shunted JRM for modulated magnetic flux. Sample fabricated with bridge-free technique.	67
3.1	Schematic of JPC operation in frequency space.	73
3.2	Different implementations of degenerate paramaps in frequency space.	81
3.3	Operation of degenerate paramaps in frequency space.	82
3.4	Equivalent circuit of a phase-preserving amplifier, consisting of two phase-sensitive amplifiers.	84
3.5	Equivalent circuit of a phase-sensitive amplifier, consisting of one phase-preserving amplifier.	85
3.6	Fresnel vector representation of quasi-coherent signals and their transformation through quantum-limited paramaps.	91
4.1	Measurement of JPC signal mode center frequency and quality factor.	98
4.2	Coupling capacitance as function of microstrip gap size.	99
4.3	Participation ratio inferred from frequency tunability of a JPC with a four junction JRM.	101
4.4	Participation ratio inferred from frequency tunability of a JPC with shunted JRM.	103
4.5	JPC gain vs. applied pump power.	104
4.6	Measured JPC gain curves for varying pump frequencies.	105
4.7	Measured $P_{-1 \text{ dB}}$ input signal saturation powers.	107

5.1	Schematic of coherent attenuation measurement setup.	112
5.2	Schematic of frequencies involved in the coherent attenuation experiment.	113
5.3	JPC amplification bandwidths in the coherent attenuation experiment.	114
5.4	Applied power in small amplitude coherent attenuation experiment..	115
5.5	Schematic of frequency window measured by the spectrum analyzer in the small amplitude coherent attenuation experiment.	116
5.6	Measured phase dependent coherent attenuation at gain point $G_0 \approx 11$ dB.	117
5.7	Measured phase dependent coherent attenuation for varying gain.	117
5.8	Measured maximum coherent attenuation for varying gain.	118
5.9	Signal input powers in the gain enhancement experiment.	119
5.10	Schematic of frequency window measured by the spectrum analyzer in the gain enhancement measurement.	119
5.11	Single gain modulation trace and phase stability measurement.	120
5.12	Measured gain modulation for $G_0 = 11$ dB and $G_0 = 15$ dB.	121
5.13	Maximum gain enhancement at $G_0 = 11$ dB and $G_0 = 15$ dB.	122
6.1	Image of typical JPC sample.	125
6.2	SEM images of typical JRM resist masks.	126
6.3	Optical images of a JPC with solid microstrip lines.	127
6.4	Images of gap capacitor resist mask and gap capacitor.	127
6.5	SEM images of junction resist mask and actual junction.	128
6.6	SEM image of a shunted JRM with eight Dolan type Josephson junctions.	129
6.7	Mask design and junction fabricated with bridge-free technique.	129
6.8	Shunted JRM mask design and device fabricated using the bridge-free technique.	130
6.9	Change in measured Josephson junction resistance over time, measured after lift-off.	131
6.10	Photos of sample holder.	131
6.11	Insertion loss of sample box.	132
6.12	Wiring diagram of microwave lines in the Heliox refrigerator.	133
6.13	Wiring diagram of microwave lines in the Triton refrigerator.	134
6.14	JPC sample mounted on dilution refrigerator base stage.	134
A.1	RLC resonant circuit.	147

A.2	Open-ended TL.	148
A.3	Parallel RLC resonant circuit.	150
A.4	Open-ended TL resonator with input capacitor.	151
A.5	Parallel RLC resonator loaded with an input capacitor and a load resistor.	152
A.6	Parallel RLC resonator with parallel load.	152
A.7	TL resonator with input and output capacitor.	154
B.1	Co-polymer spinning curves, provided by manufacturer.	157
B.2	PMMA spinning curve, provided by manufacturer.	157

List of Tables

1.1	Classification of Josephson amplifiers developed in various research groups.	13
1.2	Desirable preamplifier characteristics and values typically achieved with the JPC in this work.	18
1.3	List of notable JPC samples with relevant measured parameters.	24
2.1	Symbols used in circuit element of Fig. 2.2.	40
4.1	List of notable JPC samples with relevant measured parameters. Meaning of symbols is given in Sec. 4.2.	97
4.2	List of notable resonator samples with relevant fabrication parameters.	100
6.1	List of notable JPC samples with relevant fabrication parameters.	124

List of Symbols

a, a^\dagger	cavity photon annihilation/creation operator
a_{in}	signal flying oscillator annihilation operator
$a^{\text{in/out}}(t)$	signal input/output field operator at time t
$a^{\text{in/out}}[\omega]$	Fourier transform of signal input/output field operator at frequency ω
\vec{A}	electromagnetic vector potential
b, b^\dagger	photon annihilation/creation operator
b_{in}	idler flying oscillator annihilation operator
$b^{\text{in/out}}(t)$	idler input/output field operator at time t
$b^{\text{in/out}}[\omega]$	Fourier transform of idler input/output field operator at frequency ω
B	angular 3dB amplification bandwidth
B_0	effective linear angular bandwidth
c, c^\dagger	photon annihilation/creation operator
$C_{a,b,c}$	capacitance corresponding to harmonic oscillator X, Y, Z
C_{in}	coupling capacitance
$C_{\text{in}}^{\text{S/I}}$	signal/idler coupling capacitance
Cov	covariance
$D_a(\alpha)$	harmonic oscillator displacement operator
\mathbb{D}^2	variance
e	elementary charge
\vec{E}	electric field
\mathbb{E}	expectation value
E_J	Josephson energy
E_J^{eff}	Josephson energy effectively available

E_J^{shunt}	Josephson energy of shunt junction
$E_{\text{JRM}}^{\text{shunted}}$	energy of shunted JRM
$E_{\text{JRM}}^{\text{4JJ}}$	energy of JRM (without shunt inductors/junctions)
$E_{\text{JRM}}^{\text{8JJ}}$	energy of JRM, shunted with Josephson junctions
$E_{X,Y,Z}$	electric field of mode X, Y, Z
$f_0^{\text{S/I}}$	signal/idler resonator center frequency
f_{I}	idler frequency
f_{p}	pump frequency
f_{s}	signal frequency
g_3	three-wave mixing coupling energy divided by \hbar
G	power gain
G_0	power gain in stiff pump regime
G_{JPC}	effective JPC power gain
G_{\max}	maximum power gain
G_{ZPF}^{\max}	maximum power gain limited by zero-point fluctuations
h	Planck constant
\hbar	reduced Planck constant, $\hbar = h/2\pi$
H_0	three-wave mixing Hamiltonian
H_0^{RWA}	three-wave mixing Hamiltonian under rotating wave approx.
i_k	current through branch k
I_a	in-phase quadrature operator corresponding to operator a
I_0	Josephson junction critical current
I_m	measured in-phase component of microwave field
k_{B}	Boltzmann constant
\vec{k}_{I}	idler wave vector
\vec{k}_{p}	pump wave vector
\vec{k}_{S}	signal wave vector
K	three-wave mixing coupling coefficient

$L_{a,b,c}$	inductance of corresponding to harmonic oscillator X, Y, Z
L_g	equivalent inductance of linear resonator
L_{J_0}	Josephson inductance, $L_{J_0} = \varphi_0/I_0$
L_J	flux dependent Josephson inductance, $L_J = L_{J_0}/\cos\varphi$
L_{JRM}	JRM inductance of signal or idler mode
$L_{X,Y,Z}$	JRM inductance of mode X, Y, Z
$\dot{n}_{a,b,c}$	signal, idler, pump photon flux
$\dot{n}_{S,I,p}$	signal, idler, pump photon flux
\dot{n}_c^{po}	threshold pump photon flux
$\mathcal{N}_{a,b}^{\text{in}}(\omega)$	photon spectral density of incoming signal/idler field
$p_{a,b,c}$	signal, idler, pump inductive participation ratio
$p_g^{\text{S/I}}$	signal/idler shunted JRM outer junction participation ratio, $p_g^{\text{S/I}} = L_{J_0}/L_g$
$P_{\text{in/out}}$	applied input/output power
$p_L^{\text{S/I}}$	signal/idler JRM inductive participation ratio
\vec{P}	electric polarization
P_{cav}^{\max}	maximum cavity circulating power
P_{Sig}^{\max}	maximum signal port input power
Q	resonator quality factor
Q_a	quadrature operator corresponding to operator a
$Q_{a,b}$	signal/idler resonant mode quality factor
$Q^{\text{S/I}}$	signal/idler resonator quality factor
Q_{ext}	resonator coupling quality factor
$Q_{X,Y,Z}$	conjugate charge variable of flux $\Phi_{X,Y,Z}$
R_L	load impedance
S_a	one-mode squeezing operator
S_{ab}	two-mode squeezing operator
t	time
T	temperature
T_1	qubit lifetime
T_m	measurement time

T_N^{sys}	total system noise temperature
$T_N^{\text{HEMT sys}}$	system noise temperature with HEMT only
$T_N^{\text{JPC sys}}$	system noise temperature with JPC and HEMT
T_Q	quantum limit of noise temperature, $T_Q = \hbar\omega/2k_B$
u_k	voltage across branch k
U_{JPC}	flying oscillator state evolution operator
v_i	electric potential at node i
W_e^{int}	electric interaction energy density
x	ratio between signal and pump photon flux
X, Y, Z	resonant modes
$Z_0^{a,b,c}$	characteristic impedance of harmonic oscillator X, Y, Z
Z_0	transmission line characteristic impedance
α	coherent state parameter, $\alpha \in \mathbb{C}$
β	coherent state parameter, $\beta \in \mathbb{C}$
$ \alpha, \beta\rangle_{\text{in}}$	incoming signal and idler flying oscillator states
β_L	ratio between shunt inductance and Josephson inductance
$\gamma_{a,b,c}$	angular bandwidth at resonant frequency $\omega_{a,b,c}$
$\gamma^{\text{S/I}}$	signal/idler angular bandwidth
$\delta\omega$	angular frequency offset
$\Delta\vec{k}$	phase-matching mismatch, $\Delta\vec{k} = \vec{k}_{\text{p}} - \vec{k}_{\text{S}} - \vec{k}_{\text{I}}$
$\Delta\omega$	angular frequency offset
ε	number small compared to 1
ε_0	vacuum permittivity
η	measurement efficiency
κ	bandwidth defining Shannon wavelet
λ	wavelength
λ_{C}	common mode wavelength
λ_{I}	idler mode wavelength
λ_{S}	signal mode wavelength
Λ	two-mode squeezing parameter, $\Lambda = \lambda e^{i\varphi} \in \mathbb{C}$

φ_0	reduced magnetic flux quantum, $\varphi_0 = \Phi_0/2\pi$
φ_{ext}	reduced external applied flux, $\varphi_{\text{ext}} = \Phi_{\text{ext}}/\varphi_0$
φ_{I}	idler phase
φ_k	reduced generalized flux across branch k , $\varphi_k = \Phi_k/\varphi_0$
φ_{n}	three-wave nonlinear phase, $\varphi_{\text{n}} = \varphi_{\text{S}} + \varphi_{\text{I}} - \varphi_{\text{P}}$
φ_{P}	pump phase
φ_{S}	signal phase
$\varphi_{X,Y,Z,M}$	reduced generalized flux variable, $\varphi_{X,Y,Z,M} = \Phi_{X,Y,Z,M}/\varphi_0$
ϕ	relative phase between signal and conjugate idler
ϕ_i	generalized flux at node i
Φ_0	magnetic flux quantum, $\Phi_0 = h/2e$
Φ_k	generalized branch flux
Φ_{ext}	external magnetic flux
Φ_k^{DC}	magnetic field induced flux across branch k
Φ_k^{RF}	flux across branch k induced by microwave current
Φ_{L_i}	generalized flux across shunt inductor i
$\Phi_{X,Y,Z,M}$	generalized flux variable of mode X, Y, Z, M
$\Phi_{X,Y,Z}^0$	zero-point fluctuation of flux variable $\Phi_{X,Y,Z}$
ξ	one-mode squeezing parameter, $\xi \in \mathbb{C}$
Ξ	number of order unity
ρ	dimensionless pump amplitude
ρ_0	dimensionless pump amplitude in stiff pump approx.
σ	standard deviation
$\sigma_{I,Q}$	standard deviation of field in-phase/quadrature component
$\chi^{(n)}$	n-th order susceptibility of nonlinear medium
ω	angular frequency
ω_{I}	idler angular frequency
ω_{P}	pump angular frequency
ω_{S}	signal angular frequency

ω_0	resonant mode angular frequency
$\omega_{1,2}$	applied tone angular frequency
$\omega_{a,b,c}$	resonant modes angular frequencies
$\omega_{X,Y,Z}$	angular frequency of mode X, Y, Z

List of Acronyms

JP_C Josephson Parametric Converter

JBA Josephson Bifurcation Amplifier

CW continuous wave

CPW coplanar waveguide

SQUID superconducting quantum interference device

paramp parametric amplifier

SNR signal-to-noise ratio

CA Coherent Attenuation

JRM Josephson Ring Modulator

SA spectrum analyzer

HEMT high electron mobility transistor

AM amplitude modulation

RBW resolution bandwidth

qubit quantum bit

FOPA fiber optic parametric amplifier

SHG second harmonic generation

DC direct current

RF radio frequency

RWA rotating wave approximation

e-beam electron beam

PMMA poly methyl methacrylate

MMA methyl methacrylate

SEM scanning electron microscope

EBPG electron beam pattern generator

cQED circuit quantum electrodynamics

QND quantum non-demolition

VNA vector network analyzer

Acknowledgments

This work would not have been possible without the help of many who have contributed to the success of this project during my time at Yale. First, I would like to thank my advisor Michel Devoret for giving me the opportunity to work in his group and for always taking the time to discuss physics concepts - no matter how simple or complex. I would further like to thank my committee members Dan Prober, Doug Stone, and Rob Schoelkopf for their invaluable comments and suggestions over the years, and in particular for taking the time to read through my thesis.

I am grateful to have had the opportunity to work with and learn from so many experienced researchers and post-docs: Luigi Frunzio, who has taught me sample fabrication and who always had a word of encouragement when the junction bridge collapsed for the n-th time, Nicolas Bergeal, who introduced me to low-temperature physics, the JPC, and to taking an efficient approach to research, and Michael Hatridge, who has always been more than willing to share his knowledge and ideas. There are many more who have been directly involved in the JPC project and who have been a great pleasure to work with: Benjamin Huard (both at Yale and in Paris), Baleegh Abdo, Chad Rigetti, Archana Kamal, Katrina Sliwa, Ananda Roy, and Anirudh Narla.

I had the pleasure to share the office and most of my graduate school experience with Nick Masluk. I would also like to thank the many current and former members and visitors of the labs on the fourth floor of Becton: Kurtis Geerlings, Ioan Pop, Shyam Shankar, Zaki Leghtas, Markus Brink, Hanhee Paik, Luyan Sun, Gerhard Kirchmair, Hannes Majer, Leo DiCarlo, Mazyar Mirrahimi, Bertrand Reulet, Steve Girvin, Emily Chan, R. Vijay, Vlad Manucharyan, Mike Metcalfe, Dan Santavicca, Joel Chudow, Anthony Annunziata, Yehan Liu, Zlatko Minev, and Uri Vool.

Finally a special thanks to the administrative staff on the fourth floor, who had a big part in making it such an agreeable work environment: Maria Rao, Giselle DeVito, Devon Cimini, and Terri Evangeliste.

Chapter 1

Introduction

In this thesis I will present the results of my effort to build and operate a practical, noise quantum-limited, phase-preserving Josephson parametric amplifier, called the Josephson Parametric Converter (JPC). The main goals of this thesis work were first, to develop a new JPC microwave circuit, making the amplifier design and fabrication simple, predictable, and reproducible. And second, to fabricate JPCs with properties making them immediately useful for the readout of superconducting quantum bits (qubits), while confirming that the JPC comes close to the ideal quantum-limited phase-preserving amplifier.

A practical amplifier needs to first and foremost bring some real improvement to an experimental setup when inserted into the measurement chain, and not merely be a proof-of-concept device. Superconducting microwave parametric amplifiers (paramps) are attractive due to their ability to reach the quantum limit of noise and it is desirable to exploit this to effectively reduce the overall measurement system noise. Several more requirements have to be met to make paramps like the JPC useful. In the case of qubit measurements relevant to this work, these requirements are: they must operate in the frequency range of 5 to 10 GHz, the typical qubit readout resonator frequency range. They need to have sufficiently large gain to overcome the noise of the following stage high electron mobility transistor (HEMT) amplifiers, i.e. about 20 dB, bandwidths larger than those of the readout cavities, i.e. 1-10 MHz, and be able to handle powers corresponding to a few photons in the readout cavities. And given the fact that paramps have rather narrow bandwidths, one of the most important practical requirements is for the amplifiers to be frequency tunable, to assure that the amplifier frequency can be easily tuned to the readout resonator frequency.

Apart from the operational aspects, the amplifier characteristics should ideally be calculable, making it possible to reliably design and predict its properties. The sample design needs to be flexible enough to allow for changes in relevant amplifier parameters, such as center frequency and amplification bandwidth, from one device to the next. It is desirable for the sample fabrication to be simple but at the same time robust enough to make the device parameters predictable and reproducible.

As will be shown in this chapter, the JPC amplifiers developed in this dissertation work fulfill all these requirements, and are currently used in several qubit experiments. In the following sections a brief overview of the field of paramps is given and examples of a few different implementations of paramps developed in the past 60 or so years are presented. The difference between degenerate and non-degenerate type paramps is explained, as well as the difference between phase-sensitive and phase-preserving amplification. The Hamiltonian of an ideal phase-preserving amplifier and its resulting scattering is described. The nonlinear element allowing to realize this Hamiltonian, the Josephson Ring Modulator (JRM), is presented next, and the implementation of the JPC with microstrip transmission lines explained. Lastly, the main experimental results of this thesis work are presented, describing typical properties of devices measured throughout this work. In particular, it is shown how the presence of the JPC significantly improves the measurement efficiency in a qubit measurement, and further, by operating the JPC in the fully nonlinear regime, the tri-linear form of the JPC Hamiltonian is confirmed.

Subsequent chapters present in more detail the theoretical basis of the JPC and experimental results obtained: Chapter 2 explains in detail how the JRM leads to a pure form of the three-wave mixing nonlinearity required for non-degenerate phase-preserving amplification. In particular it is shown how, by adding additional shunt inductors, the device frequency becomes tunable over more than 100 MHz. Chapter 3 explains how the JPC, under the stiff pump approximation, can be described by a two-port scattering matrix. The link between the scattering matrices of (quantum-limited) phase-sensitive and phase-preserving amplifiers is established and their relationship to the squeezing operator explained. Chapter 4 gives an overview of devices measured and describes important JPC characteristics. Chapter 5 presents the operation with three coherent tones beyond the stiff pump approximation and scattering matrix formalism, confirming the predicted interaction form of the full three-wave mixing Hamiltonian. Chapter 6 describes the sample fabrication and the setup used. Finally, Chapter 7 gives concluding remarks and discusses possible future directions.

1.1 Parametric Amplifiers - A Brief Overview

1.1.1 Previous Work on Parametric Amplification

Nowadays the context in which physics students are most likely to encounter the concepts of parametric amplification is in courses on quantum and nonlinear optics, in particular when studying the generation of squeezed coherent states of light [1]. These minimum-uncertainty states of electromagnetic radiation obey the Heisenberg uncertainty relation $\sigma_I\sigma_Q = 1/4$ for the standard deviations of the field's in-phase component I and quadrature component Q , as formally defined later in Sec. 3.2.5, while at the same time one of the quadratures' standard deviation will be below $1/2$ (the other one necessarily above). Parametric processes can generate these states with intriguing purely quantum aspects, and one can easily overlook the fact that parametric amplification has been extensively studied for decades before the birth of quantum or even nonlinear optics (one of the first nonlinear optics experiments, second harmonic generation, has been performed by Franken et al. in 1961 [2]). In particular there has been extensive research on parametric amplifiers in the microwave domain in the 1950's and 60's. Parametric amplifiers had at that time already been successfully operated decades earlier, but were then replaced with vacuum tubes. The realization that they have much better noise properties than vacuum tubes then revived interest in the field¹. The noise properties of parametric amplifiers, intricately related to their ability to generate squeezed electromagnetic radiation, later lead to increasing research interest in optics as well as in superconducting microwave circuits. In fact, a quantum limit exists for the amount of noise added by a linear phase-preserving amplifier [4, 5, 6], while a linear phase-sensitive amplifier can no noise at all. The interest in paramps in both optics and superconducting microwave circuits is very much owed to the fact that they can be operated close to (in case of a phase-preserving paramp) or below (in case of a phase-sensitive paramp) this quantum limit.

In optics, many different types of parametric amplifiers have been developed over time. Some examples include pulsed operation using the nonlinear properties of crystals (e.g. KTP crystals [7, 8]), or continuous wave (CW) operation in fiber optic parametric amplifiers (FOPAs) [9] or (optical) ridge waveguides [10, 11]. The first experimental realization of vacuum noise squeezing in optics, using the nonlinearity of a Na atomic beam, was reported by Slusher et al. in 1985 [12]. It was only three years later that squeezing of vacuum noise of microwave radiation using the

¹See [3] for a brief history on parametric amplifiers before 1960.

nonlinearity of Josephson junctions was reported by Yurke² and co-workers [13, 14, 15]. Parametric amplifiers based on Josephson junctions had already been developed for quite some time before that [16, 17, 18, 14], but were difficult to operate and far from being practical. Further, even though the paramps eventually approached the quantum limit of noise [14], the total system noise temperature remained well above the quantum limit. After these first pioneering experiments on superconducting Josephson parametric amplifiers, the field had gone into hibernation for about a decade, until the push for low-noise amplifiers for the readout of superconducting qubits³ has created renewed interest.

Degenerate superconducting Josephson paramps have now been realized with arrays of junctions [20, 21], junctions in a superconducting quantum interference device (SQUID) configuration for flux-pumping at two times the signal frequency [22] or pumped through the signal port at the signal frequency [23]. The JPC, which is the subject of this thesis work, has been developed first at Yale [24, 25, 26, 27] and later at ENS Paris [28], and is a non-degenerate Josephson paramp. Superconducting paramps with nonlinearities provided by the kinetic inductance of a transmission line have also been developed [29, 30]. The device presented in [30] is a traveling wave paramp, which has a distributed nonlinearity and does not require resonators as the other superconducting devices mentioned before. This has the advantage of leading to much larger amplification bandwidths (GHz rather than MHz) and to an increased dynamic range. It has yet to be seen though if these type of amplifiers are practical enough to be used as first amplifier stage in actual measurements. They for instance require pump powers several orders of magnitude larger than used for standing wave paramps, which could be a real concern for qubit measurements, as avoiding pump leakage would become increasingly difficult.

Another type of superconducting amplifier are microwave SQUID amplifiers, which typically are operated below 1 GHz [31], but ones operating in the 5-10 GHz range have also been recently developed [32, 33, 34]. Although the energy for the amplification process in those amplifiers is provided by a DC current, it has been suggested that they can be described by parametric processes, where the pump is provided by Josephson harmonics [35].

The research has matured to the point where superconducting microwave paramps can be used as first amplification stage in the measurement chain of actual experiments, as was first done in the detection of the state of mechanical oscillators [36]. Also by now, several experiments with

²Notably, B. Yurke was also one of the authors of [12].

³For a recent overview and outlook on the field of superconducting qubits, see [19].

superconducting qubits read out dispersively and using Josephson paramps as first amplification stage have been performed, observing quantum jumps, back-action of variable strength (quantum) measurements, and performing feedback [37, 38, 39, 40, 41, 42].

1.1.2 Parametric Amplification and Nonlinear Media

Parametric amplification is a multiple-wave mixing effect, which depends on the presence of a nonlinear medium. Typically, a strong tone, called the pump, is converted in frequency to amplify an incident small amplitude signal tone. For instance in three-wave mixing, this happens through the coherent conversion of one pump photon at frequency ω_p into one signal photon at ω_s and one idler photon at ω_i , with $\omega_p = \omega_s + \omega_i$. In the case of four-wave mixing, two pump photons are converted into one signal and one idler photon, with $2\omega_p = \omega_s + \omega_i$.

For the mixing process to be efficient and useful for near quantum-limited parametric amplification, the nonlinearity has to be lossless and provide a sufficiently strong wave coupling. In optics, nonlinear media have to be physically long compared to the wavelengths λ involved, as the frequency mixing is otherwise too weak. This however adds the additional complication of phase-matching of the signal, idler, and pump waves, which in the case of three-wave mixing requires fulfilling the momentum relationship

$$\vec{k}_p = \vec{k}_S + \vec{k}_I + \Delta \vec{k} \quad (1.1)$$

$$\text{with } |\Delta \vec{k}| \ll |\vec{k}_p|, \quad (1.2)$$

where $\vec{k}_{p,S,I}$ are the wave vectors of pump, signal, and idler waves. This further leads to limitations of the amplification bandwidth, as explained below. In superconducting microwave circuits on the other hand, the Josephson junction provides a dispersive nonlinearity which allows to achieve strong wave-mixing over distances short compared to the wavelengths involved. Strong nonlinearities can be engineered with desired coupling properties while at the same time being point-like compared to the wavelengths, eliminating the need for phase-matching.

Nonlinearities in Optics

In optics, parametric processes are typically described by nonlinear terms in the electric susceptibility, which links the electric field \vec{E} and the electric polarization \vec{P} :

$$P_i = \varepsilon_0 \left(\sum_j \chi_{ij}^{(1)} E_k + \sum_{jk} \chi_{ijk}^{(2)} E_j E_k + \sum_{jkl} \chi_{ijkl}^{(3)} E_j E_k E_l + \dots \right), \quad (1.3)$$

where i, j, k etc. correspond to the different relevant polarizations of the field.

Consider the case of a $\chi^{(2)}$ -type nonlinearity where the nonlinear electrical polarization term is of the form $P = \varepsilon_0 \chi^{(2)} E^2$, and \vec{E} and \vec{P} are collinear. Then three electric field modes $E = E_X + E_Y + E_Z$, each mode defined by a frequency (and bandwidth in case it describes a standing wave), wave vector, polarization etc. lead to an interaction energy density

$$W_e^{\text{int}} = \int_{-\infty}^t E \frac{\partial P}{\partial t'} dt' \quad (1.4)$$

$$\propto \varepsilon_0 \chi^{(2)} (E_X + E_Y + E_Z)^3 \quad (1.5)$$

$$\begin{aligned} &= \varepsilon_0 \chi^{(2)} (E_X^3 + E_Y^3 + E_Z^3 + 6E_X E_Y E_Z \\ &\quad + 3E_X E_Y^2 + 3E_X E_Z^2 + 3E_X^2 E_Y \\ &\quad + 3E_X^2 E_Z + 3E_Y E_Z^2 + 3E_Y^2 E_Z). \end{aligned}$$

The terms of the form XYZ and X^2Z represent three-wave-mixing interactions: photons at ω_Z are converted into two photons, one at ω_X and one at ω_Y , or into two photons at ω_X . Which of these parametric processes actually takes place in an optical $\chi^{(2)}$ medium depends very much on the experimental details, e.g. whether the medium is embedded into a resonator, which phase-matching conditions are met, what polarizations the incoming fields have etc., and the above considerations are only meant to sketch the basic principle.

To give two concrete examples of $\chi^{(2)}$ media used for parametric amplification: In a KTP crystal [8], three (non-resonant) waves X, Y, Z couple to each other, and the polarization of the incident waves becomes important in achieving the phase-matching condition of Eq. 1.1. The s polarized (perpendicular polarization w.r.t. the plane of incidence) wave X represents the small amplitude signal at frequency $\omega_S = \omega_0$, the p polarized (parallel polarization w.r.t. the plane of incidence) small amplitude wave Y represents the idler, also at frequency $\omega_I = \omega_0$, and finally the large s polarized Z wave is the pump at frequency $\omega_P = \omega_S + \omega_I = 2\omega_0$. So signal and idler beams are frequency degenerate and distinguishable only through their polarizations (polarization non-degenerate). The absence of a resonant cavity and magnitude of the nonlinearity require pulsed operation (e.g a Q-switched laser) to obtain sufficiently large powers for the amplification process.

Further, signal, idler, and pump pulses are all obtained from the same laser through a first nonlinear process that provides frequency doubling. This stands in contrast to experiments in the microwave domain, where phase-locked generators can provide tones that are octaves apart with phase stability over several minutes. Parametric amplification in this system occurs over a finite bandwidth. Not all signal and idler frequencies $\omega_S = \omega_0 + \delta\omega$ and $\omega_I = \omega_0 - \delta\omega$ will mix with the pump frequency, even though $\omega_P = \omega_S + \omega_I = 2\omega_0$ is satisfied, as the process is limited by phase-matching (here type II phase matching, which determines the polarization scheme).

A second example of an optical paramp using a $\chi^{(2)}$ nonlinear element is a PPLN (periodically poled LiNbO₃) ridge waveguide [11]. Again, a first nonlinear process creates the pump wave through second harmonic generation (SHG), so that the pump is at twice the signal frequency $\omega_P = 2\omega_S$, this time both waves are CW. Signal and idler fall within the same bandwidth centered around $\omega_P/2$ and have the same polarization as the pump. Phase-matching determines the possible bandwidth of the process (about 60nm at center wavelength of about 1.5μm) also in this case.

While both examples make use of three-wave mixing processes, $\chi^{(3)}$ media exhibit four-wave mixing, with nonlinear electric polarization of the form $P = \varepsilon_0\chi^{(3)}E^3$. Similarly to Eq. 1.4 this leads to interaction terms of the form X^4 , X^2Z^2 , and XYZ^2 . An example of such a paramp based on this type of interaction is the FOPA as used in [9]. In those experiments, signal and pump stem from different sources, but the idler is created through a first nonlinear process (a first FOPA). All waves are CW and have the same polarization. In contrast to the previous examples, all three waves coexist in the same bandwidth, given again by phase-matching (tens of nm centered around 1.5μm) and their frequencies are related by $\omega_S + \omega_I = 2\omega_P$.

All three examples above have in common that no resonating mode exists and the amplification bandwidths are determined by phase-matching condition. Since signal and idler coexist in this bandwidth they can be considered degenerate paramps, independent from the fact that one of them is described by four-wave mixing and the other two by three-wave mixing. Further, signal, idler, and pump waves are usually derived from the same source.

Nonlinearities in Superconducting Circuits

The relevant modes in (standing wave) paramps based on superconducting circuits correspond to (distributed or lumped) resonators defining a mode frequency and bandwidth.⁴ In Josephson

⁴Traveling wave type microwave paramps using the kinetic inductance of superconducting transmission lines have also been developed recently [30].

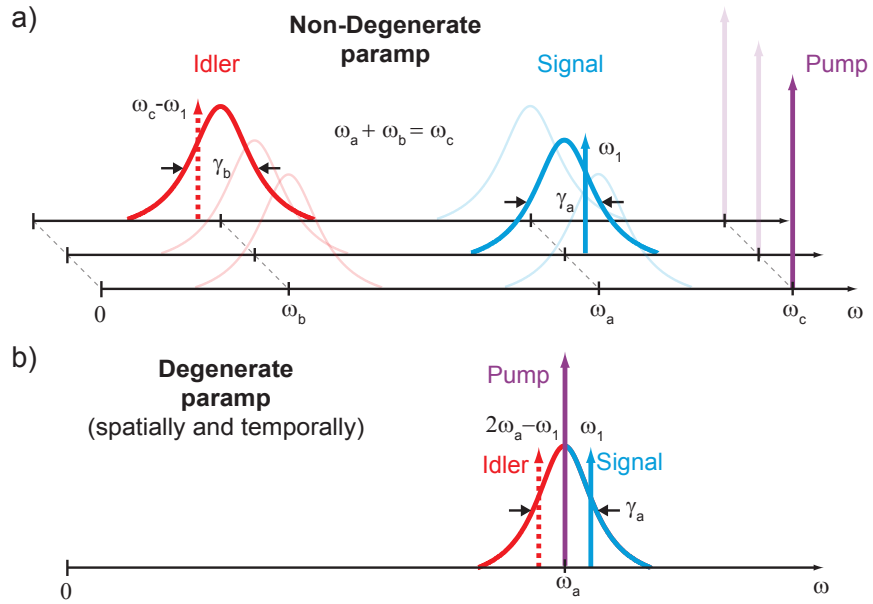


Figure 1.1: Parametric amplifiers in frequency space. a) Spatially and temporally non-degenerate parametric amplifier (three wave mixing). This paramp has two resonant modes (signal and idler) represented by their Lorentzian gain response functions. A strong pump tone at the sum frequency of signal and idler (purple arrow) provides the energy for the amplification process and determines the device gain. An injected signal tone (blue arrow) at ω_1 will be amplified at that frequency and also amplified and converted into the idler band at $\omega_c - \omega_1$ (dashed red arrow). The three different axes represent different spatial ports. b) A spatially and temporally degenerate parametric amplifier (four wave mixing). Signal, idler and pump tones co-exist in the same resonant mode and are injected in the same spatial port.

circuits the nonlinearities are point-like (small compared to the wavelengths involved), so that phase matching is not an issue. Whether the device is considered frequency degenerate or non-degenerate depends on whether signal and idler modes coincide (or at least have overlapping bandwidths). A further distinguishing attribute is spatial degeneracy vs. non-degeneracy, i.e. whether or not signal and idler modes are excited through the same spatial port and travel on the same transmission line. These properties are schematically shown in Fig. 1.1, where the clear distinction between the signal *mode* at frequency ω_a and bandwidth γ_a and the *applied tone* at frequency ω_1 is made. It should be noted that in optics the term “non-degenerate” is often used to describe an experimental situation where *applied* signal and idler waves are not at the same frequency, even though signal and idler *modes* do have overlapping bandwidths, and thus the term does not refer to a property of the paramp itself as in microwave circuits.

Josephson devices allow for the nonlinearities to be engineered to have the desired energy mixing terms, without complications arising from spurious nonlinearities as in the case of $\chi^{(2)}$ and $\chi^{(3)}$ media. Higher order nonlinear terms exist, but are usually negligible. Josephson paramps can be grouped into three-wave mixing and four-wave mixing devices.

a) Four-Wave Mixing

Degenerate paramps based on Duffing type oscillators have been successfully built and operated using Josephson junction arrays as nonlinear metamaterial in a coplanar waveguide (CPW) resonator [43, 20], or using two Josephson junctions in a direct current (DC)-SQUID configuration (for magnetic flux tunability) as nonlinear inductance in a quasi-lumped LC-circuit [44, 45, 46, 23]. These devices have nonlinear energy mixing terms of the form X^4 , where X denotes the generalized flux across the nonlinear inductance term of the resonant mode at ω_a and bandwidth γ_a . Assuming a signal tone is applied at $\omega_a + \delta\omega$, $\delta\omega \ll \gamma_a$, then in this four-wave mixing interaction, two pump photons at ω_a are coherently converted into one signal photon at $\omega_a + \delta\omega$ and one idler photon at $\omega_a - \delta\omega$, as schematically shown in Fig. 1.1 b). These devices can be considered to be doubly-degenerate in frequency, since signal, idler, and pump modes coincide. More recently, doubly pumped operation has been achieved at Yale, with pump tones symmetrically detuned in frequency above and below ω_a [47], making the four-wave mixing nature of these devices more obvious.

b) Three-Wave Mixing

An example of a singly frequency degenerate Josephson paramp is given in [22], where two Josephson junctions in a DC-SQUID configuration are embedded at the voltage node of a $\lambda/4$ CPW transmission line resonator, with resonance frequency ω_a . The pump is provided by the modulation at $2\omega_a$ of the flux through the SQUID loop. This degenerate three-wave mixing interaction is described by the nonlinear mixing term X^2Z , where X again is proportional to the generalized flux across the nonlinear inductance, and Z describes the pump mode. In frequency space this amplifier is similar to Fig. 1.1 b), with the difference that the pump is now at $2\omega_a$.

The three above examples cover both three-wave mixing and four-wave mixing interactions, but are all degenerate in both frequency and space, as signal and idler tones are injected through the same ports and travel on the same transmission lines.

The JPC, on the other hand, is non-degenerate in frequency and space. It is described by a pure three-wave mixing energy interaction term of the form XYZ , where X , Y , and Z stand for the signal, idler, and pump modes respectively. Signal, idler, and pump modes are described by frequencies ω_a , ω_b , ω_c and bandwidths γ_a , γ_b , γ_c , with the three-wave mixing frequency relation $\omega_c = \omega_a + \omega_b$. As schematically depicted in Fig. 1.1 a), signal tones injected within the signal mode bandwidth at frequency ω_1 are amplified at that frequency and also converted and amplified into idler photons at $\omega_c - \omega_1$, so that the three-wave mixing frequency relation still holds. In practice, the pump is applied non-resonantly and ω_c represents the pump tone frequency. This assures that the pump is stiff, i.e. that its amplitude is much larger than signal and idler amplitudes and its dynamics thus not affected by the signal and idler dynamics. The gain of the JPC then remains constant over a large range of signal input powers.

1.1.3 Phase-Sensitive and Phase-Preserving Amplification

For experiments in dilution refrigerators at frequencies of several GHz, $k_B T \ll \hbar\omega$ and consequently, all Johnson noise of matched loads is replaced by zero-point fluctuations. Superconducting circuits as well as Josephson junctions are dissipation-free and full control of all modes can be achieved while avoiding unwanted dissipation. This makes it possible for superconducting paramps to achieve quantum-limited operation [5] and is the reason for the increasing interest the field has seen in the past few years.

Parametric amplifiers are usually not only classified into degenerate and non-degenerate types,

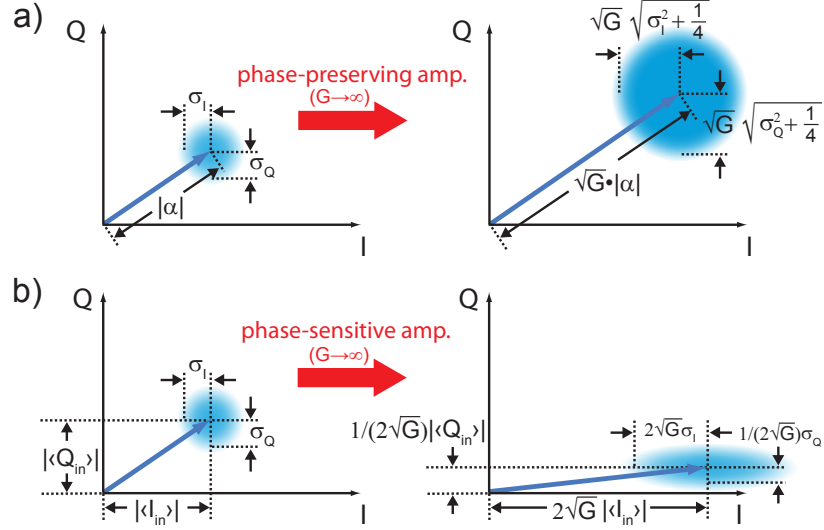


Figure 1.2: Fresnel vector representation of quantum-limited amplifiers. a) Phase-preserving operation of a paramp such as the JPC. A coherent tone of $|\alpha|^2$ photons is amplified by an amplitude gain \sqrt{G} and its phase is unaltered in the process. Half a photon of noise is added to the original noise (referring the noise back to the input). b) Phase-sensitive operation, e.g. of a JBA-paramp. One quadrature (here I) is amplified by an amplitude gain $2\sqrt{G}$, while the other (Q) is deamplified by the inverse $(2\sqrt{G})^{-1}$. The noise in the two quadratures is amplified by the same factor, so that the signal-to-noise ratio (SNR) in each quadratures stays constant. For coherent states, $\sigma_{I,Q}^2 = 1/4$.

which depends on their physical implementation, but also by whether they are operated in phase-preserving or phase-sensitive mode. All paramps, whether optical or made of superconducting microwave circuits, can be operated in both modes, phase-preserving *and* phase-sensitive. This essentially depends on whether or not the signal to be processed is distributed over both signal and idler. Consider for instance the case of a doubly-degenerate paramp as schematically shown in Fig. 1.1 b): applying a signal tone exactly at the center of the resonant mode at frequency ω_a (or more generally a pulse with carrier frequency ω_a and frequency components symmetric about the carrier frequency) will lead to phase sensitive amplification. In that case one can not distinguish between signal and idler, as the signal information is distributed over and mixed into both. In case the signal to be processed is contained on one side of ω_a , the amplification process is phase-preserving and a copy of the amplified signal will appear on the opposite side of ω_a as idler.

The non-degenerate JPC is usually operated in the phase-preserving mode, as the signal to be amplified is injected on the signal port. However it can also be operated in the phase-sensitive mode, which is discussed detail in Chapter 5.

Figure 1.2 a) shows the operation of a phase-preserving amplifier, such as the JPC at large

power gains G . A signal with amplitude α is amplified with amplitude gain \sqrt{G} , and its phase is the same before and after the amplification. The noise (standard deviation), represented as a disc, grows by slightly more than \sqrt{G} : an energy corresponding to half a photon is added so that the power signal-to-noise ratio (SNR) deteriorates by a factor $1 + 1/(2\sigma^2)$, where for quantum-limited signals (coherent states) $\sigma^2 = \sigma_I^2 + \sigma_Q^2 = 1/2$, so that the SNR is lowered by a factor of 2 in the amplification process. Figure 1.2 b) shows the operation of a phase-sensitive amplifier, such as the Josephson Bifurcation Amplifier (JBA)-paramp at large gains. One quadrature is amplified by an amplitude gain $2\sqrt{G}$, where G is the power gain in the phase-preserving operation of the same device at the same working point, while the other quadrature is deamplified by the inverse factor $1/(2\sqrt{G})$. Since the noise in each quadrature is amplified/deamplified by the same respective factors, schematically represented by the conversion of the noise disc into a noise ellipse, the overall SNRs in each quadrature stays constant for any gain. This feature is very attractive in experiments where the signal phase is known *a priori*, or where two digital outcomes, differing in phase, are of interest, and where an offset phase is known/adjustable *a priori* (see e.g. [37]).

Table 1.1 classifies Josephson amplifiers developed in various research groups. Paramps are powered by external microwave tones, while microwave SQUID amplifiers are powered with a DC bias. The circuit properties of paramps determine whether they are of the degenerate or non-degenerate type. Even though either can be operated in phase-sensitive or phase-preserving mode, degenerate paramps are more easily operated in the phase-sensitive mode, while non-degenerate paramps such as the JPC are more easily operated in the phase-preserving mode. Microwave SQUID amplifiers on the other hand are always phase-preserving.

1.1.4 XYZ Nonlinearity and JPC Scattering Matrix

What makes the JPC stand apart from other paramps is that its Hamiltonian contains the pure tri-linear mixing term XYZ . No other nonlinear mixing term of this order exists. When neglecting drive and dissipation, its Hamiltonian consists of three harmonic oscillators coupled by this pure three-wave mixing term:

		Amplifier Type	
		RF Powered	
		Degenerate	Non-Degenerate
Operation of Amplifier	Phase-Sensitive	Boulder ("JPA"), Yale ("JBA"), Berkeley ("JBA"), NEC, etc.	
	Phase-Preserving		Yale ("JPC"), ENS-Paris ("JPC")
			Berkeley, LLNL, NIST, etc.

Table 1.1: Classification of Josephson amplifiers developed in various research groups. Microwave SQUID amplifiers are DC powered and always phase-preserving. Paramps are either of the degenerate or non-degenerate type, depending on the specific circuit, and can be operated in both the phase-sensitive and phase-preserving mode. Non-degenerate paramps such as the JPC are usually operated in the phase-preserving mode, while degenerate paramps are usually operated in the phase-sensitive mode.

$$\begin{aligned}
H_0 = & \frac{\Phi_X^2}{2L_a} + \frac{\Phi_Y^2}{2L_b} + \frac{\Phi_Z^2}{2L_c} \\
& + \frac{Q_X^2}{2C_a} + \frac{Q_Y^2}{2C_b} + \frac{Q_Z^2}{2C_c} \\
& + K\Phi_X\Phi_Y\Phi_Z,
\end{aligned} \tag{1.6}$$

where $\Phi_{X,Y,Z}$ are the generalized flux variables and $Q_{X,Y,Z}$ their conjugate charge variables. The three harmonic oscillators have frequencies $\omega_{a,b,c} = 1/\sqrt{L_{a,b,c}C_{a,b,c}}$ and characteristic impedances $Z_0^{a,b,c} = \sqrt{L_{a,b,c}/C_{a,b,c}}$ and are coupled to each other through the three-wave mixing coefficient K . As explained in Chapter 3, under the rotating wave approximation (RWA) and for $\boxed{\omega_c = \omega_a + \omega_b}$ the Hamiltonian becomes

$$H_0^{\text{RWA}} = \hbar\omega_a a^\dagger a + \hbar\omega_b b^\dagger b + \hbar\omega_c c^\dagger c + \hbar g_3 (a^\dagger b^\dagger c + abc^\dagger), \tag{1.7}$$

where the three-wave mixing interaction is now described by the coupling energy $\hbar g_3 = K\Phi_X^0\Phi_Y^0\Phi_Z^0$, where $\Phi_{X,Y,Z}^0 := \sqrt{\langle 0 | \Phi_{X,Y,Z}^2 | 0 \rangle}$ are the zero-point fluctuation of the flux variables. The first three terms are simply those of three harmonic oscillators with annihilation operators a, b, c , whereas the coupling term of the form $a^\dagger b^\dagger c + abc^\dagger$ can be interpreted in the following way: $a^\dagger b^\dagger c$ describes the annihilation of one pump photon at ω_c and the creation of a pair of signal and idler photons at ω_a and ω_b , respectively. This is predicted by the Manley-Rowe relations [48], which state that the change in photon flux of signal and idler modes are equal to each other and opposite to the change in pump photon flux: $\dot{n}_a^{\text{out}} - \dot{n}_a^{\text{in}} = \dot{n}_b^{\text{out}} - \dot{n}_b^{\text{in}} = \dot{n}_c^{\text{in}} - \dot{n}_c^{\text{out}}$. It is the term $a^\dagger b^\dagger c$ in the Hamiltonian which gives rise to parametric amplification. The hermitian conjugate term abc^\dagger describes the reverse process: a pair of signal and idler photons are annihilated to create one pump photon. For balanced signal and idler inputs and with the correct phase relation between signal, idler, and pump, this other process leads to Coherent Attenuation (CA), which is discussed in Chapter 5.

As explained in Ch. 3, under the stiff pump approximation and for incoming and outgoing signal and idler tones at zero detuning, i.e. at $\omega_1 = \omega_a$ and $\omega_2 = \omega_b$, Eq. 1.7 leads to the two-port

scattering matrix

$$\begin{pmatrix} a^{\text{out}}[\omega_1] \\ b^{\text{out}\dagger}[\omega_2] \end{pmatrix}_{\omega_1=\omega_a; \omega_2=\omega_b} \begin{pmatrix} \sqrt{G_0} & -ie^{-i\varphi_p}\sqrt{G_0-1} \\ ie^{i\varphi_p}\sqrt{G_0-1} & \sqrt{G_0} \end{pmatrix} \begin{pmatrix} a^{\text{in}}[\omega_1] \\ b^{\text{in}\dagger}[\omega_2] \end{pmatrix}, \quad (1.8)$$

which links incoming and outgoing signal and idler fields $a^{\text{in/out}}[\omega]$ and $b^{\text{in/out}}[\omega]$, and where φ_p is the phase of the applied pump tone. The power gain G_0 is given by

$$\boxed{\sqrt{G_0} = \frac{1 + |\rho_0|^2}{1 - |\rho_0|^2}}, \quad (1.9)$$

and goes to infinity as the dimensionless pump amplitude $|\rho_0| \rightarrow 1^-$. As shown in Chapter 3, it is exactly the scattering matrix of Eq. 1.8, linking input and output operators, which describes quantum-limited phase-preserving amplification, as schematically shown in Fig. 1.2. In particular, for large gains $\sqrt{G_0-1} \approx \sqrt{G_0}$ and Eq. 1.8 simply describes the addition (up to a phase) and subsequent amplification with amplitude gain $\sqrt{G_0}$ of signal and idler field amplitudes⁵. And it allows to explicitly identify the origin of the added amplifier noise on the signal output: zero-point fluctuations of the incoming idler field. It also shows that an injected signal tone will be not only amplified, but its conjugate will also be converted to the idler frequency and amplified by the amplitude gain $\sqrt{G_0-1}$.

The gain as a function of frequency around and close to the signal and idler band centers is described by the Lorentzian:

$$\boxed{G_0(\Delta\omega) = G_0 \frac{1}{1 + \left(\frac{\Delta\omega}{B(G_0)/2}\right)^2}}, \quad (1.10)$$

where $\Delta\omega = \omega_1 - \omega_a = \omega_b - \omega_2$ and

$$\boxed{B(G_0) = B_0 G_0^{-1/2}} \quad (1.11)$$

is the JPC amplification bandwidth at gain G_0 . The constant bandwidth B_0 is given by a sort of

⁵Note that it is the phase conjugated idler amplitude which is added to the signal amplitude.

average of the signal and idler mode bandwidths γ_a , γ_b through

$$B_0 = \frac{2\gamma_a\gamma_b}{\gamma_a + \gamma_b}. \quad (1.12)$$

Figure 1.1 a) schematically shows the two Lorentzian gain response functions centered around the signal and idler mode frequencies ω_a , ω_b . An applied and amplified signal tone at ω_1 is shown as solid arrow, and the resulting idler tone at $\omega_2 = \omega_c - \omega_1$ as dashed arrow.

1.2 A Practical Parametric Amplifier Based on the Josephson Ring Modulator

The goal of this thesis work was to build and operate a *practical* quantum-limited, non-degenerate and phase-preserving parametric amplifier at microwave frequencies based on the *XYZ* nonlinearity described above. This means that the amplifier needs to be useful when inserted into the measurement chain of an experiment, and not simply be a proof-of-concept device. In particular, the amplifier needs to noticeably reduce the system noise temperature by not only having a lower noise temperature than the following stage amplifier, but also by having sufficient gain. At the same time the device needs to have sufficient bandwidth and the capability to operate at large enough input powers. A practical amplifier should further either have a very large bandwidth, or be frequency tunable over a sufficiently large range. Paramps are rather high Q devices, making frequency tunability crucial to match the amplifier center frequency to the measurement frequency. As explained in this section, the JPC amplifier developed in this work fulfills those requirements and can be used in the readout of the state of superconducting qubits. The qubit architecture of choice in our group at Yale is circuit quantum electrodynamics (cQED), where a microwave resonator is used to manipulate and measure the state of a qubit [49, 50, 51]. Similar to the case of an atom in a cavity [52, 53], superconducting qubit and resonator exchange energy so that the qubit state encoded in the resonator microwave field can be dispersively measured by monitoring this field, leading to a quantum non-demolition (QND) measurement. For a preamplifier such as the JPC to be useful in such a measurement scheme, several requirements have to be met.

1.2.1 Paramp Requirements

Commercially available cryogenic HEMT amplifiers [54] have noise temperatures typically corresponding to 10-20 added photons at frequencies of 1-12 GHz. The most obvious requirement for a paramp preamplifier sitting between qubit readout resonator and HEMT amplifier is for it to have a significantly lower noise temperature and enough gain at the readout frequency, in order to reduce the combined system noise temperature. This noise temperature should ideally approach the standard quantum limit of half a photon of added noise, and allows for instance monitor the qubit state in real-time through partial (non-projective) measurements [37, 42] and to implement feedback loops [40, 38, 41].

With a JPC in the measurement chain, the system noise temperature is given by

$$T_N^{\text{sys}} = \frac{1}{G_{\text{JPC}}} T_N^{\text{HEMT}} + T_N^{\text{JPC}}, \quad (1.13)$$

where the gain G_{JPC} is the JPC gain including possible losses between qubit and JPC, T_N^{HEMT} is the HEMT noise temperature including possible losses before the HEMT, and T_N^{JPC} is the JPC noise temperature, including possible losses between qubit and JPC. This expression shows that it is not sufficient for the JPC to operate at the quantum limit of $T_Q = \hbar\omega/2k_B$ corresponding to half a photon of added noise, but that it also needs to exhibit sufficient gain to lead to a significant improvement of the SNR of the system.

A further requirement is that the JPC has a sufficiently large dynamical 3dB amplification bandwidth B , in the range $B/2\pi = 1 - 10 \text{ MHz}$, and which corresponds to a signal processing time (or more exactly: cavity rise time) of $160 - 16 \text{ ns}$. The transmon [55, 56, 57] and fluxonium [58] qubits pioneered at Yale nowadays routinely achieve lifetimes of the order of one hundred microseconds [59] and have readout cavities with bandwidths in the $1 - 10 \text{ MHz}$ range [60]. But even for qubit lifetimes T_1 of a few microseconds, a JPC dynamical bandwidth of order $1 - 10 \text{ MHz}$ allows to extract many bits of information per T_1 even when measuring with few photons. The JPC also needs to be able to handle the powers with which qubits are measured. In QND schemes this power typically corresponds to a few photons per readout cavity lifetime at the readout frequency.

In terms of ease of operation, the JPC center frequency needs to be tunable over at least 100 MHz, to make it easy to match JPC and qubit readout frequencies. Lastly, a flexible and simple sample fabrication process is desirable.

Characteristic	Desired	Achieved
$\omega_{a,b}/2\pi$	5 – 12 GHz	5 – 8.5 GHz
dynamical BW $B/2\pi$	1 – 10 MHz	3 – 10 MHz
G_{\max}	≥ 20 dB	≥ 20 dB
frequency tunability	100 MHz	≥ 400 MHz
$k_B T_N/\hbar\omega_a$	$\frac{1}{2}$	$\lesssim 2 - 3$
$P_{\text{Sig}}^{\max}/\hbar\omega_a B$	≥ 1 @ 20 dB	1 – 10 @ 20 dB
out-of-band backaction	negligible	none observed

Table 1.2: Desirable preamplifier characteristics and values typically achieved with the JPC in this work.

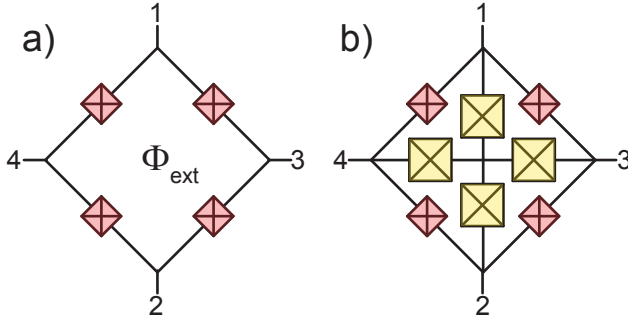


Figure 1.3: Schematic of the Josephson Ring Modulator (JRM). a) Unshunted JRM with four Josephson junctions (red). b) Shunted JRM with four additional shunt junctions (yellow).

Table 1.2 summarizes requirements to a preamplifier for qubit readout and shows typical values achieved with the JPC in this work. Devices were designed to typically have signal and idler frequencies around 8 GHz and 5 – 6 GHz, with linear bandwidths $\gamma_{a,b}/2\pi$ of up to 100 MHz. Gains of above 20 dB were routinely achieved (see Table 4.1 in Ch. 4).

1.2.2 The Josephson Ring Modulator

The circuit element used to achieve a pure three-wave mixing nonlinearity of the tri-linear form XYZ is the JRM, which consists, in its simplest form, of a ring of four nominally identical Josephson junctions, as shown in Fig. 1.3 a). The JRM is inspired by the diode ring modulator as used in double balanced microwave mixers [61] and which perform a similar (but lossy) frequency conversion scheme to that of the JPC.

As explained in Chapter 2, this (unshunted) JRM is well described by the approximate energy expression

$$E_{\text{JRM}}^{\text{4JJ}} \stackrel{\varphi_{X,Y,Z} \ll 1}{=} -E_J \sin\left(\frac{\varphi_{\text{ext}}}{4} + n\frac{\pi}{2}\right) \varphi_X \varphi_Y \varphi_Z + E_J \cos\left(\frac{\varphi_{\text{ext}}}{4} + n\frac{\pi}{2}\right) \left(\frac{\varphi_X^2}{2} + \frac{\varphi_Y^2}{2} + 2\varphi_Z^2 - 4\right), \quad (1.14)$$

where E_J is the Josephson energy, φ_{ext} is the reduced applied magnetic flux through the ring, $n = 0, 1, 2, 3$, and $\varphi_{X,Y,Z}$ are reduced generalized fluxes of modes X, Y, Z . In terms of generalized node fluxes $\phi_i \equiv \int_{-\infty}^t v_i(t') dt'$ at nodes $i = 1, 2, 3, 4$, where v_i is the electric potential at node i , these modes can be expressed as

$$\varphi_X \stackrel{\text{JRM}}{=} \varphi_0^{-1} (\phi_3 - \phi_4) \quad (1.15)$$

$$\varphi_Y \stackrel{\text{JRM}}{=} \varphi_0^{-1} (\phi_1 - \phi_2) \quad (1.16)$$

$$\varphi_Z \stackrel{\text{JRM}}{=} \varphi_0^{-1} \left(\frac{\phi_1 + \phi_2 - \phi_3 - \phi_4}{2} \right), \quad (1.17)$$

where $\varphi_0 \equiv \hbar/2e$ is the reduced magnetic flux quantum. Thus X represents a differential excitation across nodes 3 and 4, Y represents a differential excitation across nodes 1 and 2, and Z corresponds to a differential excitation with a gradient in flux between nodes 1, 2 and 3, 4.

The first term in Eq. 1.14 is the desired XYZ coupling term, maximized at $\varphi_{\text{ext}} = 2\pi$. The system has four solutions $n = 0, 1, 2, 3$ for a given applied magnetic flux, leading to different values of the coupling strength $-E_J \sin\left(\frac{\varphi_{\text{ext}}}{4} + n\frac{\pi}{2}\right)$. The state n of the system depends on the history of the magnetic flux φ_{ext} and jumps between these states can occur, so that in practice the device is operated at $\varphi_{\text{ext}} = \pi$ (i.e. $\Phi_{\text{ext}} = \Phi_0/2$), as explained in more detail in Ch. 2. The second term in Eq. 1.14 is quadratic in $\varphi_{X,Y,Z}$, only renormalizing the mode frequencies. The prefactor $E_J \cos\left(\frac{\varphi_{\text{ext}}}{4} + n\frac{\pi}{2}\right)$ suggests that the mode frequencies can be tuned with the external magnetic flux φ_{ext} , but in practice this tunability is severely limited by the fact that jumps can occur between the different states n .

By quartering the ring with four additional larger junctions (Fig. 1.3 b)), which behave like linear inductors, tunability over a large frequency range can be achieved. In this case, the device becomes frequency tunable over the range $\varphi_{\text{ext}} \in [0, \varphi_{\text{ext}}^{\text{crossover}}]$, where $\varphi_{\text{ext}}^{\text{crossover}}$ is given by the solution of $-4\beta_L \cos(\varphi_{\text{ext}}^{\text{crossover}}/4) = 1$, or by 2π if no solution exists. Here, β_L is the ratio between the Josephson energy E_J of the smaller outer Josephson junction and the Josephson energy E_J^{shunt}

of the larger shunt junction, and φ_{ext} is the reduced magnetic flux threading the area defined by the four outer junctions. In this regime, the energy of the shunted JRM is given by

$$E_{\text{JRM}}^{\text{8JJ}} \stackrel{\varphi_{X,Y,Z} \ll 1}{=} -E_J \sin\left(\frac{\varphi_{\text{ext}}}{4}\right) \varphi_X \varphi_Y \varphi_Z + \left(E_J \cos\left(\frac{\varphi_{\text{ext}}}{4}\right) + \frac{E_J^{\text{shunt}}}{2} \right) \left(\frac{\varphi_X^2}{2} + \frac{\varphi_Y^2}{2} \right) + 2 \left(E_J \cos\left(\frac{\varphi_{\text{ext}}}{4}\right) + \frac{E_J^{\text{shunt}}}{4} \right) \varphi_Z^2 - 4E_J \cos\left(\frac{\varphi_{\text{ext}}}{4}\right). \quad (1.18)$$

The first term has again the desired mixing properties, and the subsequent terms simply renormalize the mode frequencies. This time however only one solution exists, so that the tunability with externally applied magnetic field can be exploited.

Figure 1.4 shows three implementations of the JRM, a) one unshunted version with four Josephson junctions fabricated using the Dolan bridge technique [62], b) one shunted version with eight Josephson junctions using the Dolan bridge technique, and c) one shunted version using the bridge-free technique [63]. The red areas show the outer JRM junctions providing the nonlinearity for the amplification process, while the yellow areas show the shunt junctions. The bridge-free technique allows one to fabricate large junctions without having to worry about the collapse of resist bridges during the fabrication process (which sometimes happens during the plasma cleaning step), and also to increase the junction size without having to modify the resist stack height and evaporation angles.

1.2.3 Microstrip JPC Design

In order to realize the Hamiltonian of Eq. 1.7 with the JRM, it needs to be embedded in a resonant circuit. The first generation of JPC consisted of two edge coupled microstrip resonators [24], connected to two nodes each to excite the X and Y modes. The design is inconvenient for several reasons: to achieve Q 's of about 100, large coupling capacitors are required and finger capacitors, which are a convenient planar solution, turn out to be difficult to predict in this case. Plate capacitors are a good alternative, but come with the drawback of requiring an additional lithography step. A more problematic issue is the fact that signal and idler coupled microstrip lines necessarily have to cross to connect to JRM nodes on opposite sides, and so a multilayer fabrication

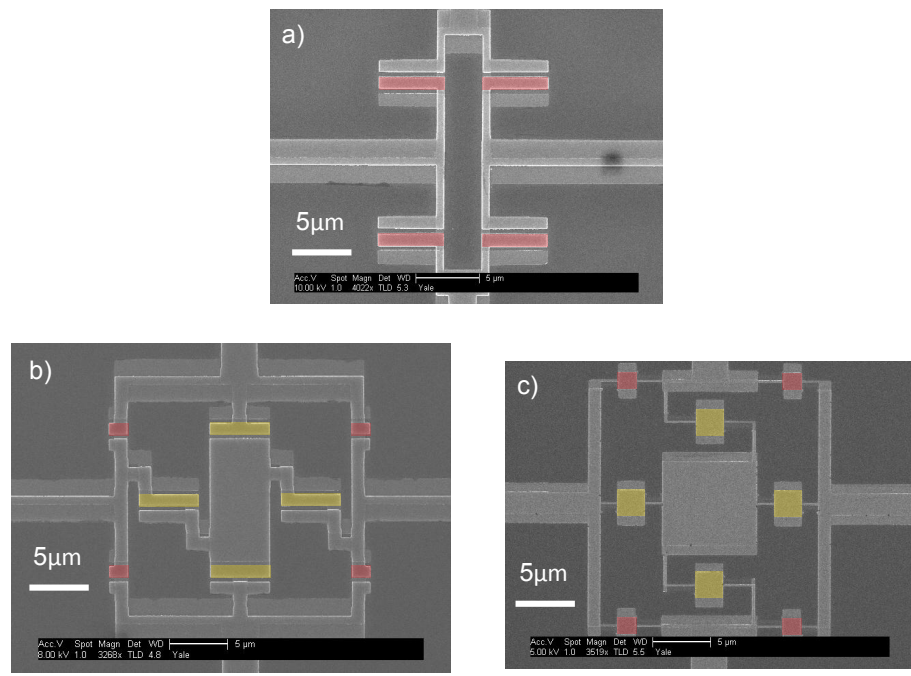


Figure 1.4: SEM images of different implementations of the Josephson Ring Modulator (JRM). The devices are fabricated with aluminum evaporated on high resistivity silicon substrates. a) A JRM with four Josephson junctions and no shunts, fabricated using the Dolan bridge technique. b) A shunted JRM with 8 Josephson junctions fabricated using the Dolan bridge technique. The four large Josephson junctions are dividing the ring into four parts, adding frequency tunability to the device. c) A shunted JRM fabricated using the bridge-free technique. The red areas show the JRM junctions, and the yellow areas the shunt junctions.

process is required.

One of the goals of this thesis work was to come up with a resonator design solution which allows for a single layer fabrication process. This is achieved by realizing the signal and idler resonant modes with two microstrip $\lambda/2$ resonators, crossing at their voltage nodes, where the JRM is inserted. The full JPC circuit with a shunted JRM is shown in Fig. 1.5, where the blue resonator corresponds to the higher frequency signal mode, and the red resonator corresponds to the lower frequency idler mode. A picture of a full device is shown in Fig. 6.1 of Chapter 6.

The transmission line resonators are connected to the 50Ω environment through coupling capacitors. In most devices, one of the signal feedlines is shorted to ground, so that the signal mode can be excited through the remaining port, as seen in Fig. 1.5 a). The idler resonator is always connected to a hybrid. The disadvantage of this asymmetry is that the signal mode voltage node is shifted away from the center, opening up the possibility of power leaking out of the idler port. In newer generation devices, signal resonators are also connected to hybrids, as seen in Fig. 1.5 b), assuring that the JRM is at a voltage node and thus reducing cross-talk to the idler ports. The pump at the sum frequency of signal and idler is coupled in through the Σ port of the idler hybrid, and is non-resonant in the system.

The reason coupling capacitors are necessary is that the impedance of the $300\mu\text{m}$ wide microstrip transmission lines fabricated on $250\mu\text{m}$ thick silicon wafers lead to characteristic impedances of the resonances of close to 50Ω , close to the impedance of the environment. Coupling capacitors then act as impedance transformers at frequencies around the resonance frequency (here $\omega_0/2\pi \sim 5 - 8\text{ GHz}$), and from the point of view of the close to 50Ω transmission line resonators, they transform the environment to impedances of order $\sim Q_{\text{ext}} \times 50\Omega$, where the coupling quality factor for a symmetrically coupled transmission line resonator is given by (see Appendix A, [64]):

$$Q_{\text{ext}} = \boxed{\frac{\pi}{4} \frac{1}{Z_0} \cdot \frac{R_L}{(\omega_0 C_{\text{in}} R_L)^2}}, \quad (1.19)$$

with Z_0 the characteristic impedance of the transmission line (typically 40 to 50Ω), R_L the impedance of the environment (50Ω), ω_0 the resonance frequency, and C_{in} the coupling capacitance. In the case of the shorted signal feedline as in a), the factor $\pi/4$ in the expression is replaced by $\pi/2$.

Another feature of this JPC design that has to be kept in mind is the fact that the circuit actually has three fundamental resonances: one for which the two red transmission line arms combined have

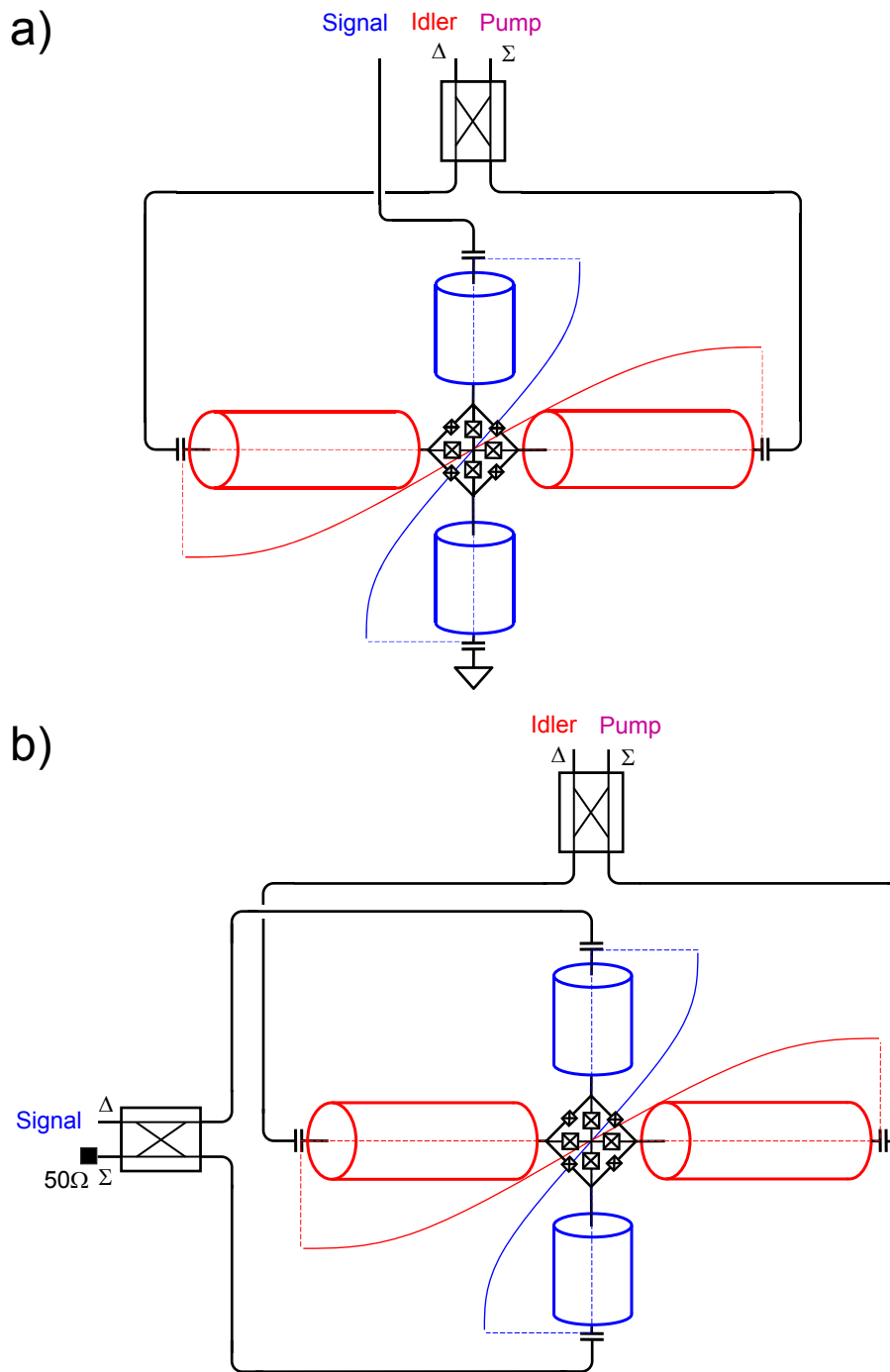


Figure 1.5: Schematic of a frequency tunable Josephson Parametric Converter (JPC). Two transmission line $\lambda/2$ resonators define the signal (blue) and idler (red) modes. The two resonators cross each other at their voltage nodes, where a Josephson Ring Modulator (JRM) is inserted, providing the mode-coupling nonlinearity for the amplification process. The JRM is threaded by an external magnetic flux, allowing for frequency tunability. a) One of the signal feedlines is shorted to ground, while a hybrid on the two idler feedlines allows to also couple in the non-resonant pump tone. b) Both signal and idler are coupled in through hybrids.

device	JPX09	JPX14	JPX16	JPX22	JPX26	JPX30	JPXs01	JPXs04
$\frac{\omega_{a,b}}{2\pi}$ (GHz)	8.32/6.63	8.12/6.45	8.18/6.22	7.63/5.4	7.90/5.37	7.26/5.3	7.4-7.8/5.2-5.3	7.7-7.8/5.7
$Q_{a,b}$	67/63	73/66	140/100	290/280	350/256	200/150	240/220	140/100
$\frac{\gamma_{a,b}}{2\pi}$ (MHz)	124/105	111/98	58/62	26/19	22/21	36/35	$\sim 38/\sim 24$	$\sim 55/\sim 57$
$p_{a,b}$	5%/4%	4%/3%	2%/3%	4%/3%	6%/4%	7%/6%	7 - 15%/5 - 12%	4 - 5%/3%
$p_a p_b Q_a Q_b$	8	6	8	97	215	126	185-950	17-21
meas. G_0^{\max} (dB)	19	21	25	> 40	> 40	> 30	~ 30	> 30

Table 1.3: List of notable JPC samples with relevant measured parameters.

the length $\lambda_I/2$ (the idler mode), one for which the two blue arms correspond to $\lambda_S/2$ (the signal mode), and a third common mode for which one red arm and one blue arm have the combined length $\lambda_C/2$, so that $\lambda_C = (\lambda_S + \lambda_I)/2$. The second harmonic of this mode can actually be close to the pump frequency, potentially leading to a softening of the pump, and care was taken to avoid this situation.

The big advantage of the microstrip design is that the fabrication is relatively easy. Devices were fabricated by depositing aluminum on silicon substrates, requiring only one electron beam (e-beam) lithography and evaporation step. This allows for flexible sample design, as Josephson junction parameters, resonator lengths (i.e. JPC frequencies), and coupling capacitors (i.e. dynamical bandwidths) can all easily be changed from one device to the next.

1.3 Main Measurement Results

In this section, important measured JPC characteristics are presented. Many devices were fabricated and measured over the course of this thesis work, and an overview of notable devices can be found in Table 1.3. For more details on device characteristics and parameters, in particular on how the participation ratios $p_{a,b}$ are determined, see Chs. 4 and 6.

1.3.1 Tuning Bandwidth

The dynamical bandwidth of the JPC is of the order of the bandwidths of typical qubit readout cavities, so that center frequency matching becomes an important practical concern when using the JPC as preamplifier in the readout of qubits. As explained in Sec. 1.2.2, the inductively shunted JRM allows for significant frequency tuning. This is most easily understood by considering the effective inductance of the shunted JRM of the signal and idler modes X, Y in the relevant applied magnetic flux region:

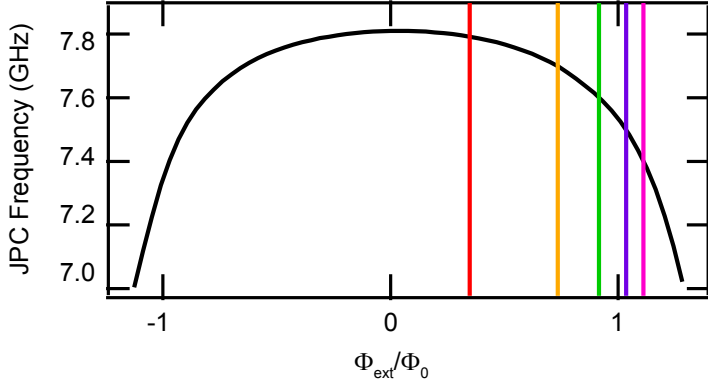


Figure 1.6: Measured JPC signal frequency as a function of the externally applied magnetic flux threading a shunted JRM (sample JPXs01). The flux is expressed in number of flux quanta $\Phi_0 = h/2e$ and refers to the area enclosed by the outer loop. The colored lines correspond to the data shown in Fig. 1.7. Similar results have been obtained in [28].

$$L_{X,Y}^{-1} \stackrel{\varphi_{X,Y,Z} \ll 1}{=} \frac{(L_J^{\text{shunt}})^{-1}}{2} \left(2\beta_L \cos\left(\frac{\varphi_{\text{ext}}}{4}\right) + 1 \right), \quad (1.20)$$

where $\beta_L = E_J/L_J^{\text{shunt}}$, and L_J^{shunt} is the Josephson inductance of the shunt junctions. For β_L large enough, there exist external magnetic fluxes such that the term $2\beta_L \cos\left(\frac{\varphi_{\text{ext}}}{4}\right) + 1$ becomes small and thus the effective JRM inductance large, pulling the frequency down. This behavior is shown in Fig. 1.6, where the measured JPC signal center frequency as a function of applied magnetic flux around zero is shown. The linear signal frequency can be tuned by close to 1 GHz, compared to only tens of MHz typically achieved by detuning the pump frequency with a four junction JRM.

The colored lines in the figure indicate the flux bias points at which gain was measured, when applying a pump tone at the sum of signal and idler frequencies (13.1 to 12.5 GHz) with the appropriate powers. The measured Lorentzian-like power gain response functions are shown in Fig. 1.7. The gains of 20 dB were chosen only as reference; maximum gains achieved for this device were ~ 30 dB. The photon flux at which the JPC saturates at this gain depends on the biasing point. The numbers next to the gain curves correspond to the measured saturation photon flux per dynamical bandwidth at those points ($B \approx 2\pi \cdot 3$ MHz). The data of the saturation photon numbers presented here are to be understood as a proof of principle only. Those numbers can be maximized by carefully choosing the flux bias and pump frequency, and differences of up to 10 dB in the saturation powers for the same gain and center frequency have been observed. Newer devices

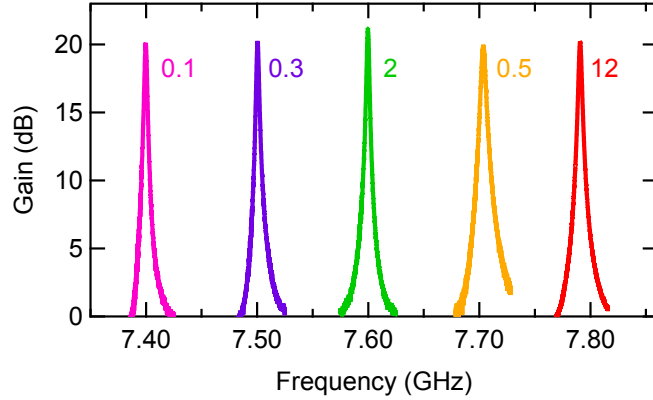


Figure 1.7: Measured Lorentzian gain response functions of a JPC with inductively shunted JRM (sample JPXs01) for different magnetic flux bias points. Bias points are shown in Fig.1.6. Similar results have been obtained in [28]. Numbers represent saturation photon numbers at those gain points. Note that the operating points shown here were not optimized to give the largest possible saturation photon numbers, but rather chosen as a proof of principle, as explained in the text. More recent devices fabricated in our group are able to routinely process 10 photons or more [65].

measured while this thesis was written appear to have better saturation powers for similar gains and bandwidths, and saturation powers generally about 10 dB larger than those shown here have been reported in [28].

1.3.2 Gain and Dynamical Bandwidth

The gain of the JPC depends on the pump power applied. As the normalized pump amplitude $|\rho_0| \rightarrow 1^-$, the gain G_0 at the JPC center increases, as explained in Sec. 1.1.4. At the same time, the dynamical bandwidth reduces as $G_0^{-1/2}$, so that the amplitude-gain-bandwidth product $B \times G_0^{1/2}$ is constant and equal to $B_0 = 2\gamma_a\gamma_b/(\gamma_a + \gamma_b)$, where $\gamma_{a,b}$ is the linear signal/idler bandwidth.

Figure 1.8 a) shows the measured gain response function of a JPC with a four junction JRM. The gain curves all lie on top of each other, but the 3 dB bandwidth reduces with increasing gain, from about 28 MHz at a gain of 9 dB to about 9 MHz a gain of 19 dB. The white trace on top of the red trace is a Lorentzian fit to the 0 dB pump power trace. Figure 1.8 shows the bandwidth of the same data as a function of the inverse amplitude gain together with a line fit. The fit gives an amplitude-gain-bandwidth product of 80 MHz, which is close to the expected value of 100 MHz from the measured signal and idler linear bandwidths.

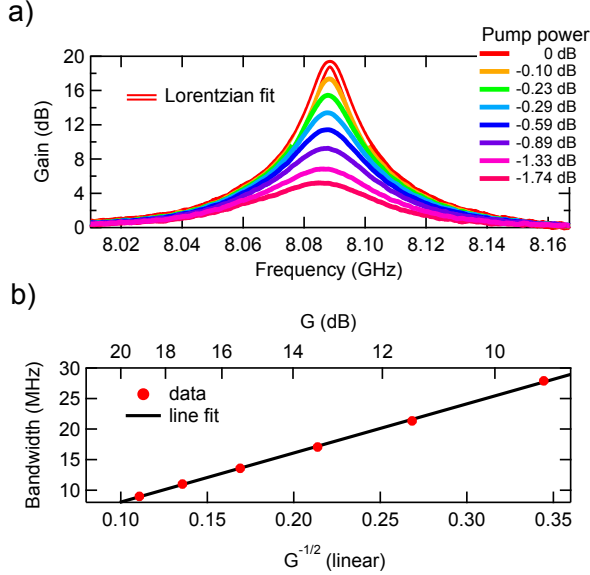


Figure 1.8: Gain and dynamical bandwidth of a JPC (sample JPX14). a) Measured power gain response function as a function of frequency. The maximum gain increases from 5 dB to 19 dB with increasing applied pump power (purple to red). Note that the applied pump power is changed by less than 60% (2 dB). A Lorentzian fit to the 0 dB pump data is shown as white trace. b) 3 dB bandwidth as a function of maximum gain. The bandwidth increases linearly with the inverse of the amplitude gain.

1.3.3 Gain and Power Limitations

The previous discussion about dynamical JPC bandwidth seems to suggest that the linear resonator bandwidths need to simply be increased in order to achieve more amplifier bandwidth, and so the question arises why the coupling capacitors are necessary at all in the presented microstrip design. In fact, there are several more limitations on the power and gain of the JPC, which require the linear resonator quality factors $Q_{a,b} = \omega_{a,b}/\gamma_{a,b}$ to be sufficiently large. The limitations on the gain, power, and bandwidth are ultimately determined by the Josephson energy E_J made available by the junctions, the frequency $\omega_{a,b}$ at which the device is operated, and the participation ratios $p_{a,b}$ of the JRM inductance compared to resonant circuit inductance, as defined later in Sec. 3.1.

The following mechanisms restrict the maximum gains and powers the JPC can handle [25, 27]:

1. The signal power is too large and excites higher order nonlinearities.

In the derivation of the JRM energy (Eqs. 1.14, 1.18), it is assumed that the generalized fluxes $\Phi_{X,Y}$ remain small compared to Φ_0 , so that the expansion to only third order remains valid. Or, using the particle analogy commonly used in the description of Josephson junctions, it means that the position $\Phi_{X,Y}$ needs be small enough so that the particle remains close to

the bottom of the potential well. This requires the maximum power in the signal (and idler) resonator to remain finite, and the limit is given by

$$P_{\text{cav}}^{\max} = \frac{\gamma_{a,b}}{p_{a,b}} E_J^{\text{eff}}, \quad (1.21)$$

where E_J^{eff} is an effective Josephson energy available for the amplification process. This maximum power is to be understood as the maximum power the JPC can provide at the output of signal and idler ports. This suggests that large junctions, small participation ratios, and large bandwidths are desirable.

2. The pump power is too large and excites higher order nonlinearities.

In this case, the pump power can never reach the limit $|\rho_0| \rightarrow 1^-$, required to achieve appreciable gains (Eq. 1.9), without excitation of higher order nonlinear terms. To assure that high gains are possible, the circuit needs to be designed such that the $Q \cdot p$ -product is large enough,

$$Q_a Q_b p_a p_b > \Xi, \quad (1.22)$$

where Ξ is a number of order unity [27]. In practice (see Table 4.1) it was observed that a $Q \cdot p$ -product smaller than 10 leads to maximum gains of 20 dB and below, whereas a $Q \cdot p$ -product larger than 10, gains of above 30 dB were routinely achieved. A second effect observed with samples of small $Q \cdot p$ -product is that the gain abruptly drops once the signal input power becomes too large [26]. Thus, for large bandwidth (small Q 's), large participation ratios are required.

3. The signal photon flux becomes comparable to the pump photon flux.

The two requirements above are still met, i.e. $\Phi_{X,Y,Z} \ll \Phi_0$ is still true, large gains can be achieved, and the power circulating in the signal resonator is easily handled by the junctions, and the three-wave mixing term in the Hamiltonian fully describes the system. However, the stiff pump approximation, which says the dynamics of the pump can be neglected, is not true anymore. In this case, the fully nonlinear regime is reached and signal, idler, and pump modes are to be treated on the same footing, as described by the three coupled nonlinear equations of motion presented in Chapter 3 (Eq. 3.5). The consequence is that when the signal input photon flux is increased, the gain G will eventually drop to $1 - \varepsilon$ of its original value G_0 . For

this drop not to exceed $1 - \varepsilon$, the following condition has to be met:

$$x < 2\varepsilon G_0^{-3/2}, \quad (1.23)$$

where $x \equiv \dot{n}_a/\dot{n}_c$ is the ratio between signal and pump photon fluxes (the signal and pump power is given by $P_{a,c} = \hbar\omega_{a,c}\dot{n}_{a,c}$). This expression predicts for instance that at the operating point $G_0 = 20$ dB, the gain will drop by 1 dB ($\varepsilon \approx 0.2$) when the signal photon flux \dot{n}_a is about 34 dB lower than the pump photon flux, but says nothing about the absolute photon fluxes. These absolute photon fluxes are determined by noting that, at high gains, the pump photon flux is close to the threshold photon flux equivalent to $|\rho_0| \approx 1^-$, $\dot{n}_c \approx \dot{n}_c^{\text{po}} = \gamma_a\gamma_b\gamma_c/4g_3^2$, and $g_3^2/\hbar = p_a p_b p_c \omega_a \omega_b \omega_c / E_J^{\text{eff}*}$, where $E_J^{\text{eff}*} \propto E_J$ with a numerical prefactor. So one finally arrives at the condition for the incoming signal photon flux not to lead to the softening of the pump with associated drop in gain (by $1 - \varepsilon$):

$$\dot{n}_a < 2\varepsilon G_0^{-3/2} \times \dot{n}_c^{\text{po}} = 2\varepsilon G_0^{-3/2} \times \frac{1}{Q_a Q_b p_a p_b} \cdot \frac{\gamma_c}{4p_c \omega_c} \cdot E_J^{\text{eff}*} / \hbar \quad (1.24)$$

4. Amplified zero-point fluctuations become too large for junctions.

The JPC signal and idler resonator always have to amplify zero-point fluctuations, and this circulating power in the resonators, can overwhelm the junctions for too large gains. This sets the limit of the maximum gain achievable to

$$G_{\text{ZPF}}^{\max} = E_J^{\text{eff}} \frac{2}{\hbar\omega_{a,b} p_{a,b}}, \quad (1.25)$$

where again E_J^{eff} is the effectively available junction energy. Large junctions and small participation ratios are favorable in this case.

Equations 1.11, 1.12, 1.21, 1.22, 1.24, and 1.25 thus show that it is not possible to simultaneously optimize for gain, bandwidth, and input power handled by the JPC, and compromises need to be made. The bandwidths typically achieved here of 3 – 10 MHz at gains of 20 dB with participation ratios of a few percent allow to achieve saturation input powers of a few photons. It should be possible to even further increase the JPC dynamical bandwidth and saturation powers in future generation devices, by increasing the linear bandwidths and Josephson junction size while at the same time increasing the participation ratio.

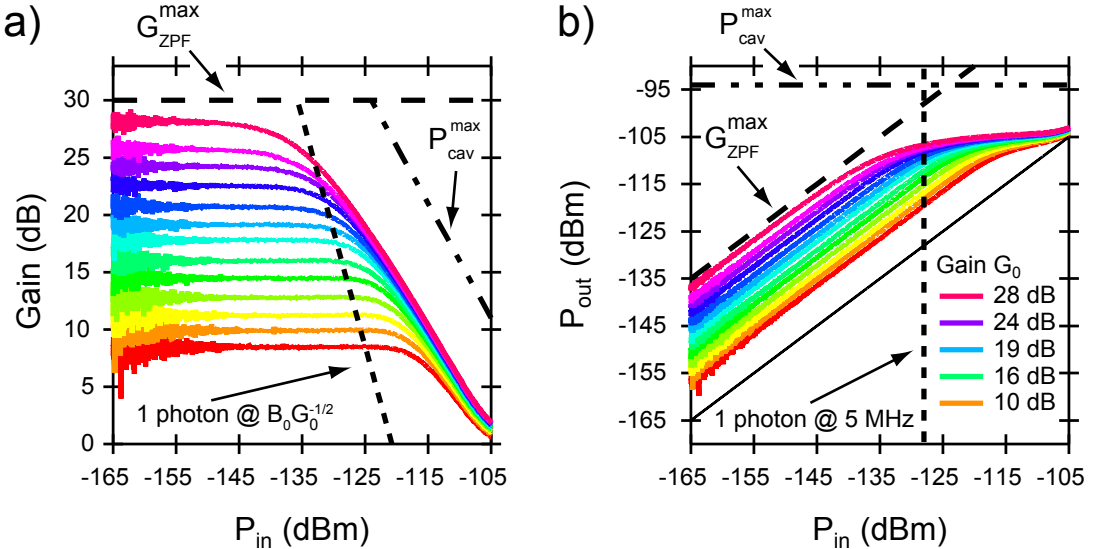


Figure 1.9: Measured JPC gain and output power dependence as a function of signal input powers (sample JPXs01). a) The gain is constant for small input powers and drops at larger powers. The dashed lines represent the expected maximum gain, maximum power (see text), and the power representing one photon at the bandwidth $B = B_0 G^{-1/2}$. b) Same data as a), plotted as output power $G_0 P_{\text{in}}$. The dashed line referring to the one photon input power is with respect to a constant bandwidth of 5 MHz. Device parameters: $p_a = 0.1$, $I_0 = 1 \mu\text{A}$ ($E_J/h = 496 \text{ GHz.}$), $\gamma_a \approx B_0 = 2\pi \times 31 \text{ MHz}$, $\omega_a = 2\pi \times 7.6 \text{ GHz}$, $p_a p_b Q_a Q_b \sim 10^2$ ($E_J^{\text{eff}} = E_J/\sqrt{2}$ chosen [27]).

Figure 1.9 a) shows how the measured gain of a JPC depends on the signal input power, and the discussed expected limitations are drawn as dashed lines for the parameters of this device (see caption text and Table 4.1). This device has a $Q \cdot p$ -product of several hundred, so that large gains (~ 30 dB) can be easily achieved. This device can handle about 1 photon at gains of 20 dB, as indicated by a dashed line, and shows constant gains G_0 for input powers below the saturation powers. Note that the calculated G_{ZPF}^{\max} is also around 30 dB, where it was assumed that $E_J^{\text{eff}} = E_J/\sqrt{2}$ [26]. It is likely that the estimations of E_J^{eff} and p_a for this particular device were not accurate, as one should not expect to be able to operate too close to G_{ZPF}^{\max} . Figure 1.9 b) shows the same data as in a), but plotted as output power vs. input power. Even though the calculated maximum output power $P_{\text{cav}}^{\max} = -94$ dB is clearly above the maximum power achieved by this device, the device appears to be limited by an effective maximum output power about 10 dB lower when saturating. This suggests that the relevant saturation mechanism here is either that a maximum circulating power in the signal resonator has been reached, or that the signal photon flux starts to become large compared to the idler photon flux.

1.3.4 SNR Improvement

Adding a JPC in a measurement chain as preamplifier to a HEMT amplifier leads to a decrease of the measurement system noise temperature. In principle, the JPC adds only half a photon of noise if operated in the low temperature regime $k_B T \ll \hbar\omega$. To date, reported measurements of the JPC noise temperature set an upper bound at about 1.5 to 2 added photons [66, 28]. What is more important to the experimenter than the measured or inferred noise temperature however, is to verify that the JPC in the measurement chain actually improves the overall system noise performance compared to the case where the JPC is absent. This change in the system properties then also reflects possible losses from cryogenic circulators, transmission lines connecting the various components, connectors, etc..

The ratio between the *system* noise temperature with and without JPC in the measurement chain is the noise rise, given by

$$\text{noise rise} = \frac{G_{\text{JPC}} \cdot T_N^{\text{JPC sys}} + T_N^{\text{HEMT sys}}}{T_N^{\text{HEMT sys}}} \quad (1.26)$$

and the improvement of the SNR due to the JPC can then be expressed as the ratio of the JPC

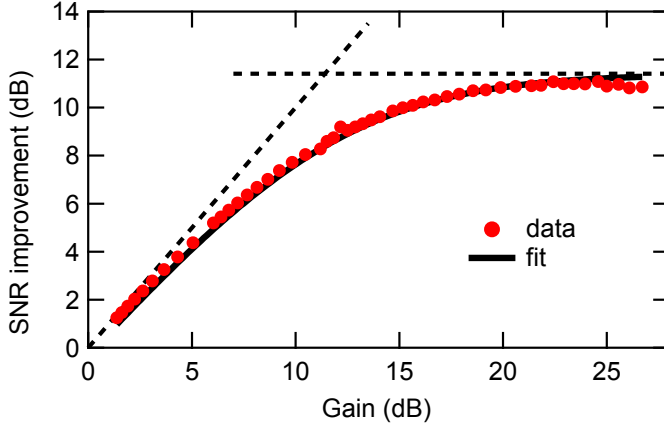


Figure 1.10: Signal-to-noise ratio improvement with JPC in measurement chain (JPXs01). At low JPC gain, the system noise is dominated by the HEMT amplifier noise, while at large JPC gain it is dominated by the JPC noise.

gain to the noise rise:

$$\text{SNR impr.} = \frac{G_{\text{JPC}}}{\text{noise rise}} \quad (1.27)$$

$$= \frac{G_{\text{JPC}}}{(G_{\text{JPC}} \cdot T_N^{\text{JPC sys}} + T_N^{\text{HEMT sys}}) / T_N^{\text{HEMT sys}}} \quad (1.28)$$

$$= \frac{1}{T_N^{\text{JPC sys}} / T_N^{\text{HEMT sys}} + 1/G_{\text{JPC}}}, \quad (1.29)$$

where $T_N^{\text{JPC sys}}$ and $T_N^{\text{HEMT sys}}$ refer to the effective noise temperatures of the JPC and HEMT, taking into account the imperfections of the setup. As expected, this expression predicts that for small JPC gain the SNR improvement increases linearly as G_{JPC} , since the noise at the JPC output $G_{\text{JPC}} \cdot T_N^{\text{JPC sys}}$ is small compared to $T_N^{\text{HEMT sys}}$. Note that commercially available HEMT amplifiers nowadays have noise temperatures of 4 K at 8 GHz, but taking into account the setup, system noise temperatures of 10 K are more realistically achieved. At the same time, the noise temperature of half a photon, T_Q , at 8 GHz is about 190 mK. On the other hand, at large JPC gains, Eq. 1.29 shows that the SNR improvement saturates at the ratio of the HEMT noise temperature to the JPC noise temperature.

Figure 1.10 shows the measured SNR improvement on the signal port as a function of JPC gain for a sample with shunted JRM. The gain was measured with a small amplitude probe tone at

the amplification center frequency of 7.64 GHz and in a 10 Hz bandwidth. The probe power was reduced with increasing gain, to ensure not to saturate the device. The noise rise was measured at the center frequency in a 1 kHz bandwidth, which is much smaller than the dynamical bandwidth of this device of 3 MHz at 20 dB of gain. The SNR improvement shown must thus be understood as an ideal value, which is reduced when the signal to be processed is making use of the entire dynamical bandwidth available. The dashed lines show the behavior in the limiting cases of low and high gains. The fit function (black line) has only one free fit parameter, the ratio $T_N^{\text{JPC sys}}/T_N^{\text{HEMT sys}}$, which is found to be -11.4 dB (equal to the negative of the dashed constant line). Assuming a system noise temperature of 10 K with only the HEMT, this implies an added noise of 2 photons (720 mK) of the system consisting of the JPC sample at the given bias point and embedded in the measurement chain, consistent with previous results.

1.3.5 Qubit Measurements

The frequency tunable JPCs developed in the course of this thesis work are now routinely used in the readout of superconducting transmon [57, 59] and fluxonium [58] qubits. The dispersive readout scheme consists of monitoring coherent states injected at the readout cavity frequency for the measurement time T_m . The qubits interact with the field in the cavity, so that its state is ultimately mapped onto the state of the itinerant microwave field [50].

Figure 1.11 shows measured microwave field quadrature histograms obtained in the dispersive readout of a transmon qubit⁶[42]. The quantum state of the qubit is mapped onto the phase of the coherent states injected at the cavity frequency of 7.541 GHz. By rotating the $I - Q$ plane appropriately, all qubit state information is contained in the I_m quadrature, where I_m is the in-phase quadrature of the measured field (here in uncalibrated units). As is clearly visible, using a JPC amplifier considerably improves the ability to discriminate between the qubit population being in the ground vs. the excited state, leading to a separation of the two Gaussian histograms of almost 5σ . In particular, it reveals that even without an excitation pulse, the qubit has 8% of its population in the excited state (small blue hump), corresponding to a qubit temperature of ~ 100 mK.

This increased discrimination capability for instance makes it possible for the qubit state to be monitored in real time, revealing quantum jumps between the ground and the excited state [37, 42].

⁶Qubit measurements presented here were performed by S. Shankar and M. Hatridge.

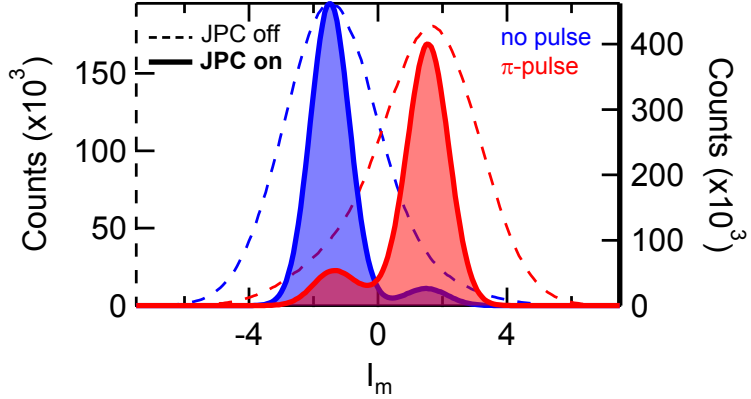


Figure 1.11: Transmon qubit measured with (solid lines) and without (dashed lines) a JPC (JPXs01), tuned to the qubit readout frequency of 7.541 GHz. The dynamical bandwidth at the gain of 13 dB is 6 MHz, greater than the readout cavity bandwidth of 5.5 MHz. The readout power corresponds to 5 photons in the readout cavity. A measurement of $I_m = \pm 2$ corresponds to the qubit most likely being in the excited/ground state. Gaussian histograms are separated by almost 5σ when measured with JPC. (Data courtesy of S. Shankar and M. Hatridge.)

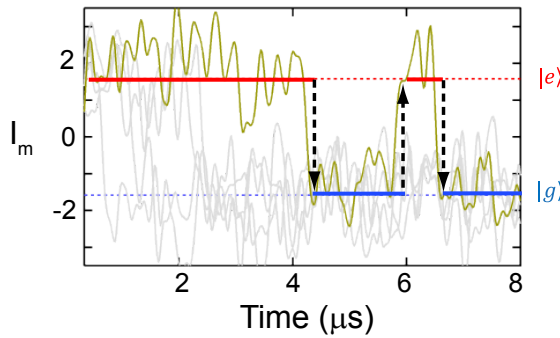


Figure 1.12: Quantum jumps of a transmon qubit measured with a JPC (JPXs01). (Data courtesy of S. Shankar and M. Hatridge.)

Figure 1.12 shows quantum jumps measured in the same device of Fig. 1.11, where the measurement time $T_m = 240$ ns is short compared to the qubit lifetime $T_1 = 2.8 \mu\text{s}$, but long compared to the cavity lifetime (30 ns).

The figure of merit in such measurements is the measurement efficiency, defined as

$$\eta := \frac{\sigma_{\text{ideal}}^2}{\sigma_{\text{meas.}}^2}, \quad (1.30)$$

where $\sigma_{\text{ideal}}^2 = (1/4 + 1/4)$ is the resulting quadrature variance of a coherent state *after* the measurement with an *ideal* phase-preserving amplifier and *referred to the amplifier input*, as explained in Fig. 1.2 a), and $\sigma_{\text{meas.}}^2$ is the quadrature variance of a coherent state *after* the measurement with the JPC and *referred to the amplifier input* (see supplemental material of [42]). The added noise of the measurement setup can be expressed in terms of the noise rise defined in Sec. 1.3.4 as

$$T_N^{\text{sys}} = T_N^{\text{JPC sys}} \times \left(\frac{\text{noise rise}}{\text{noise rise-1}} \right), \quad (1.31)$$

so that the bound on the JPC noise temperature can usefully be expressed as

$$\boxed{\frac{k_B T_N^{\text{JPC sys}}}{\hbar \omega_a} = \left(\frac{\text{noise rise-1}}{\text{noise rise}} \right) \times \left(\frac{1}{\eta} - \frac{1}{2} \right)}. \quad (1.32)$$

In this experiment the efficiency was found to be $\eta = 0.2$, which, taking into account the noise rise of about 3.5 dB at a JPC gain of 13 dB, puts the bound on the added amplifier noise at $k_B T_N^{\text{JPC sys}} / \hbar \omega_a = 2.5$ photons. Note that the noise rise prefactor in Eq. 1.32 disappears at large enough gain, as the noise rise increases proportionally to the gain (see Fig. 1.10), so that η becomes a direct measure of the noise temperature. In more recent experiments, $\eta \approx 0.4$ is achieved with tunable JPC devices similar to the one presented here.

1.3.6 Coherent Attenuation

What makes the JPC an attractive system is of course its use as paramp, working close to the quantum limit of added noise. Then only one of its ports is used (up to now typically the higher frequency “signal” port) while the second port is terminated with a matched load. Further, the JPC is operated in the stiff pump regime, which, as explained later in Chapter 3, requires the device to be designed and fabricated such that the pump is either resonant with a very broad bandwidth ($\gamma_c \gg$

$\gamma_{a,b}$) or non-resonant and significantly detuned from any close by resonant mode ($|\omega_p - \omega_c| \gg \gamma_c$). The second requirement for the stiff pump regime, which depends on the operation, is that injected signal (and/or idler) tones are sufficiently small. More precisely, the incoming signal photon flux has to be small compared to the pump photon flux: $x := \dot{n}_S / \dot{n}_p \ll 1$ (see Eq. 1.23).

When all of these conditions are met, the operation of the JPC can be described by the two-port scattering matrix of Eq. 1.8, which is non-unitary as it completely neglects any dependence on the pump. Interestingly, the full tri-linear term $\Phi_X \Phi_Y \Phi_X$ of Eq. 1.6, which under the rotating wave approximation leads to the terms $a^\dagger b^\dagger c + abc^\dagger$ in the Hamiltonian (Eq. 1.7), is not needed to derive the scattering matrix in the stiff pump approximation (see Ch. 3). The term $a^\dagger b^\dagger c$, which in photon language predicts the (coherent) creation of a pair of signal and idler photons at the expense of the annihilation of one pump photon is completely sufficient. In fact, while $a^\dagger b^\dagger c$ describes the coherent amplification when balanced beams are injected at signal and idler ports ($\dot{n}_I = \dot{n}_S$), the term abc^\dagger describes the time-reversed process, CA. This process corresponds to the annihilation of a pair of signal and idler photons and the creation of a pump photon.

The scattering matrix can predict the effects of coherent amplification and CA on signal and idler ports for small signal and idler flux, $\dot{n}_{S/I} \ll \dot{n}_p$ (see Ch. 5, Eq. 5.9), which are closely related to the phase-sensitive operation of the JPC (Ch. 3). It does however not reveal anything about the pump dynamics for fluxes close to \dot{n}_p . To confirm that the JPC Hamiltonian indeed is of the form of Eq. 1.7, containing the term abc^\dagger , balanced signal and idler tones were injected and the relative phase ϕ between them slowly varied in time at a rate of 0.1 Hz⁷, while the pump phase was kept constant [67]. When the CA condition $\phi = 2\pi$ is met, signal and idler tones are absorbed and converted into additional pump photons. Since it is extremely difficult to observe the tiny change of the reflected pump power on top of the large pump tone background, an additional small signal probe tone was monitored, allowing one to detect changes in the JPC gain as a function of ϕ .

Figure 1.13 shows how at the CA condition the gain measurably increases when the device is operated with pump powers corresponding to stiff pump gains G_0 of 11 dB (blue dots) and 15 dB (red dots) and for increasing signal and idler photon fluxes ($\dot{n}_I = \dot{n}_S$ in the experiment). This gain increase is expected: signal and idler photons are converted to extra circulating pump photons, leading to an increase of the pump parameter $|\rho|$ closer to 1 and thus an increase in the gain (Eq. 1.9). At phases away from $\phi = 2\pi$ signal and idler tones do not exactly cancel each other out and

⁷More precisely, ϕ is the relative phase between signal and conjugated idler.

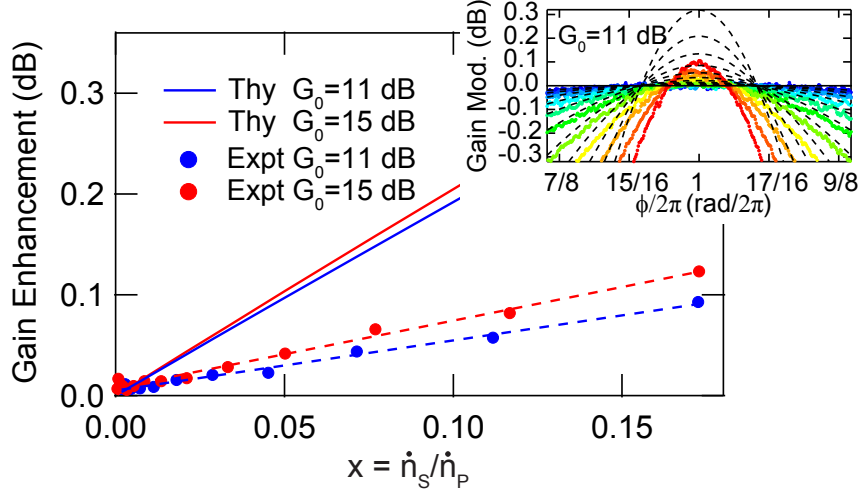


Figure 1.13: JPC gain enhancement at the Coherent Attenuation (CA) point $\phi = 2\pi$. Balanced photon fluxes $\dot{n}_S = \dot{n}_I$ are injected in signal and idler ports, and the pump photon flux \dot{n}_P is set such that the JPC gain is G_0 for low signal input powers ($\dot{n}_S \ll \dot{n}_P, \dot{n}_I = 0$). Inset: The JPC gain G (as system parameter and corresponding to the reflection coefficient of any additional small tone) is modulated with the nonlinear phase ϕ . The colored traces (blue to red; in 2 dB steps) correspond to increasing relative signal photon fluxes $x = \dot{n}_S / \dot{n}_P$ and $G_0 = 11$ dB.

thus demand a significant pump power to be converted to signal and idler photons. This leads to a diminishing circulating pump amplitude and thus a decrease of gain. This phase dependent effect is shown in the inset of Fig. 1.13, where the colored traces correspond to an increase of signal and idler photon flux in 2 dB steps (from blue to red). This CA effect on the gain is calculable (the theory is presented in Ch. 5) and as can be seen in the figure, the measured gain increase is about 1/3 of the expected value, believed to be largely due to experimental limitations. There is of course the possibility that there is some spurious dissipation in the conversion process, so that the above result can be regarded as a benchmark result of how close the JPC Hamiltonian comes to the form of Eq. 1.7.

Chapter 2

Josephson Ring Modulator

The four-port circuit element that provides the nonlinearity for the parametric amplification process in the Josephson Parametric Converter (JPC) is the Josephson Ring Modulator (JRM). Two variations are presented below, principally consisting of a ring of four identical Josephson junctions, threaded by an externally applied magnetic flux. As will be shown in the following, the JRM provides an energy mixing term of the form $K\Phi_X\Phi_Y\Phi_Z$, which, when embedded into a circuit with three resonant modes, leads to non-degenerate parametric amplification. In this chapter, first the four junction version of the JRM will be discussed. In particular, it will be shown that the energy has the required generalized flux dependence. As this device is degenerate with respect to the external magnetic flux, its frequency tunability is limited. In the second section, it will be shown how this degeneracy is lifted by quartering the original loop with four shunt inductors leading to frequency tunability over more than 100 MHz.

2.1 Ring Modulator with Four Junctions

In the following, the properties of the JRM with four identical Josephson junctions, as shown in Fig.2.1, will be discussed.

2.1.1 Definitions and Sign Conventions

Before analyzing the JRM, it is useful to define some variables (and the sign convention used) for an arbitrary circuit element. Figure 2.2 shows circuit branch k connected to nodes 1 and 2, together

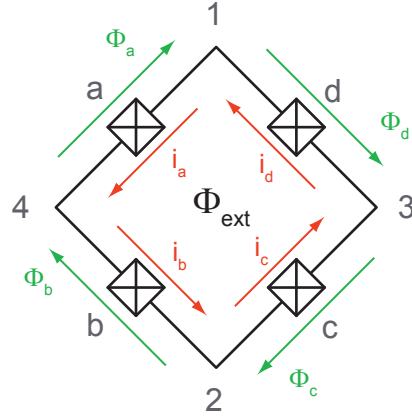


Figure 2.1: The Josephson Ring Modulator, consisting of a ring of four identical Josephson junctions, threaded by an external magnetic flux Φ_{ext} . Arrows indicate sign convention of currents and fluxes.

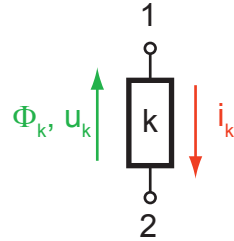


Figure 2.2: Schematic of branch element with arrows indicating sign convention used.

with the sign convention used. Two quantities are of interest in the following analysis: first the generalized flux across the element, $\Phi_k := \int_{-\infty}^t \int_1^2 \vec{E}(\vec{s}, t') d\vec{s} dt'$, where \vec{E} is the electric field and the integration path is inside the element, and second the current i_k flowing through the branch. When the integral of the vector potential \vec{A} is zero (e.g. no external applied magnetic field), then the generalized flux reduces to $\Phi_k = \phi_1 - \phi_2$, where the ϕ_i are the time integrated electric potentials at nodes i . Ultimately the goal is to express the JRM in terms of generalized fluxes which reduce to the time integrals of microwave voltages. Since various notations for the generalized flux, reduced flux, electric potential, etc. are used in the literature, a summary of the notation used here is given in Table 2.1 (the sign convention is illustrated in Fig. 2.2).

Variable	Symbol used
Electric potential at node i :	v_i
Voltage across branch k :	$u_k \equiv v_1 - v_2$
Current through branch:	i_k
Node flux:	$\phi_i \equiv \int_{-\infty}^t v_i(t') dt'$
Generalized branch flux:	$\Phi_k \equiv \int_{-\infty}^t u_k(t') dt' + \int_2^1 \vec{A}(t) d\vec{s} = \phi_1 - \phi_2 + \int_2^1 \vec{A}(t) d\vec{s}$
Reduced branch flux:	$\varphi_k \equiv \frac{\Phi_k}{\varphi_0}$
Magnetic flux quantum:	$\Phi_0 \equiv \frac{\hbar}{2e} \equiv 2\pi\varphi_0$
Reduced magnetic flux quantum:	$\varphi_0 \equiv \frac{\hbar}{2e} \equiv \frac{\Phi_0}{2\pi}$
External magnetic flux:	Φ_{ext}

Table 2.1: Symbols used in circuit element of Fig. 2.2.

Two circuit elements are of interest in this chapter, the inductor with current-phase relation

$$\Phi_k = L i_k \quad (2.1)$$

and energy

$$E = \frac{\Phi_k^2}{2L} = E_L \frac{\varphi_k^2}{2}, \quad (2.2)$$

where $E_L \equiv \varphi_0^2/L$ and $\varphi_k = \Phi_k/\varphi_0$, and the (large) Josephson junction, with current-phase relation

$$i_k = I_0 \sin(\varphi_k), \quad (2.3)$$

where I_0 is the critical current, and energy

$$E = -E_J \cos(\varphi_k), \quad (2.4)$$

with $E_J \equiv I_0 \varphi_0$. Typical junctions described in this work have critical currents of $3 - 5 \mu\text{A}$, with areas of $\sim 5 \mu\text{m}^2$, and capacitance per unit area $\sim 50 \text{fF}/\mu\text{m}^2$. The charging energy term of the junctions can thus safely be neglected, as all junctions in this work typically have $E_J \approx 10^4 E_C$, where $E_C \equiv \frac{e^2}{2C}$.

A flux dependent inductance of the Josephson junction can be defined through

$$\frac{1}{L_J} := \frac{1}{\varphi_0^2} \frac{\partial^2 E}{\partial \varphi_k^2} = \frac{\cos(\varphi_k)}{L_{J_0}}, \quad (2.5)$$

where $L_{J_0} := \varphi_0/I_0$.

2.1.2 JRM Energy

The total energy of the JRM is the sum over the junction energies:

$$E_{\text{JRM}}^{\text{4JJ}} = - \sum_k E_{J_k} \cos(\varphi_k) \quad (2.6)$$

$$= -E_J (\cos(\varphi_a) + \cos(\varphi_b) + \cos(\varphi_c) + \cos(\varphi_d)). \quad (2.7)$$

Introducing the fluxes

$$\begin{pmatrix} \varphi_X \\ \varphi_Y \\ \varphi_Z \\ \varphi_M \end{pmatrix} := \begin{pmatrix} \frac{1}{2} & -\frac{1}{2} & -\frac{1}{2} & \frac{1}{2} \\ \frac{1}{2} & \frac{1}{2} & -\frac{1}{2} & -\frac{1}{2} \\ \frac{1}{4} & -\frac{1}{4} & \frac{1}{4} & -\frac{1}{4} \\ 1 & 1 & 1 & 1 \end{pmatrix} \begin{pmatrix} \varphi_a \\ \varphi_b \\ \varphi_c \\ \varphi_d \end{pmatrix} \quad (2.8)$$

and its inverse relation

$$\begin{pmatrix} \varphi_a \\ \varphi_b \\ \varphi_c \\ \varphi_d \end{pmatrix} = \begin{pmatrix} \frac{1}{2} & \frac{1}{2} & 1 & \frac{1}{4} \\ -\frac{1}{2} & \frac{1}{2} & -1 & \frac{1}{4} \\ -\frac{1}{2} & -\frac{1}{2} & 1 & \frac{1}{4} \\ \frac{1}{2} & -\frac{1}{2} & -1 & \frac{1}{4} \end{pmatrix} \begin{pmatrix} \varphi_X \\ \varphi_Y \\ \varphi_Z \\ \varphi_M \end{pmatrix} \quad (2.9)$$

then allows one to re-express the JRM energy as

$$\boxed{E_{\text{JRM}}^{\text{4JJ}} = -4E_J \left[\cos\left(\frac{\varphi_X}{2}\right) \cos\left(\frac{\varphi_Y}{2}\right) \cos(\varphi_Z) \cos\left(\frac{\varphi_M}{4}\right) + \sin\left(\frac{\varphi_X}{2}\right) \sin\left(\frac{\varphi_Y}{2}\right) \sin(\varphi_Z) \sin\left(\frac{\varphi_M}{4}\right) \right]}, \quad (2.10)$$

with

$$\boxed{\varphi_M \stackrel{\text{4JJ JRM}}{\equiv} \varphi_{ext} + 2\pi n}, \quad (2.11)$$

according to Kirchhoff's law (Eq. 2.13). Note that this last equality remains true throughout all the cases discussed in this chapter (with or without microwave currents/voltages, with or without shunt inductors). At this point, the choice of the factors 1/2 and 1/4 in the definition of the fluxes

$\varphi_{X,Y,Z}$ is not obvious. It will become clear shortly (Eq. 2.24 ff.) that these factors make it possible to identify $\varphi_{X,Y,Z}$ to be exactly the relevant generalized branch fluxes of the system.

There are four distinct energy states, parametrized by $n = 0, 1, 2, 3$. For small fluxes, $\varphi_{X,Y,Z} \ll 1$, the energy term becomes

$$\boxed{E_{\text{JRM}}^{\text{4JJ}} \stackrel{\varphi_{X,Y,Z} \ll 1}{=} -E_J \sin\left(\frac{\varphi_{\text{ext}}}{4} + n\frac{\pi}{2}\right) \varphi_X \varphi_Y \varphi_Z + E_J \cos\left(\frac{\varphi_{\text{ext}}}{4} + n\frac{\pi}{2}\right) \left(\frac{\varphi_X^2}{2} + \frac{\varphi_Y^2}{2} + 2\varphi_Z^2 - 4\right)} \quad (2.12)$$

and thus has the desired mixing form $\sim \varphi_X \varphi_Y \varphi_Z$. The terms in $\varphi_{X,Y,Z}^2$ merely renormalized the mode frequencies and don't lead to any unwanted additional nonlinear mixing. The $\varphi_X \varphi_Y \varphi_Z$ form in itself is not sufficient, as the fluxes $\varphi_{X,Y,Z}$ defined above have to have the "correct" dependence of externally applied microwave voltages at the nodes in order to be *meaningful* variables. As will be shown below, this is the case and the $\varphi_{X,Y,Z}$ can be expressed as differences of the node fluxes ϕ_i , which justifies the choice of the modes X, Y, Z through Eq. 2.8. Note also that Eq. 2.12 has a coupling energy term $-E_J \sin\left(\frac{\varphi_{\text{ext}}}{4} + n\frac{\pi}{2}\right)$ whose sign depends on the external magnetic flux. This leads to a phase difference of π in the mixing term g_3 and thus ultimately to a π phase shift in the two-mode squeezing parameter phase φ (see Eq. 3.42).

2.1.3 Current Induced by Magnetic Flux

Before treating the general case of externally applied direct current (DC) magnetic field and radio frequency (RF) microwave currents and voltages, consider the case where just a (DC) external magnetic flux Φ_{ext} is applied, but without any applied microwave fields. Let Φ_k , $k \in \{a, b, c, d\}$ be the generalized flux across junction k (at branch k) as seen in the schematic of Fig. 2.1.

Applying Kirchhoff's laws for currents and fluxes together with flux quantization yields

$$\Phi_a + \Phi_b + \Phi_c + \Phi_d = \Phi_{\text{ext}} + n\Phi_0 \quad (2.13)$$

$$-i_a + i_d = 0 \quad (2.14)$$

$$-i_c + i_b = 0 \quad (2.15)$$

$$-i_d + i_c = 0 \quad (2.16)$$

$$-i_b + i_a = 0, \quad (2.17)$$

where $n \in \mathbb{Z}$. Together with the Josephson relation $i_k = I_0 \sin(\Phi_k/\varphi_0)$ this leads to the solution

$$\boxed{\Phi_a^{\text{DC}} = \Phi_b^{\text{DC}} = \Phi_c^{\text{DC}} = \Phi_d^{\text{DC}} \stackrel{4\text{JJ-JRM}}{=} \frac{\Phi_{\text{ext}}}{4} + n \frac{\Phi_0}{4}} \quad (2.18)$$

and

$$\boxed{i_a^{\text{DC}} = i_b^{\text{DC}} = i_c^{\text{DC}} = i_d^{\text{DC}} \stackrel{4\text{JJ-JRM}}{=} I_0 \sin\left(\frac{\varphi_{\text{ext}}}{4} + n \frac{\pi}{2}\right),} \quad (2.19)$$

where the notation Φ_k^{DC} and i_k^{DC} is used to indicate that these solutions correspond to currents and fluxes which are due only to the external applied magnetic field. Equation 2.19 shows that a DC magnetic flux threading the loop will lead to four different possible circulating current configurations in the ring: $\pm I_0 \sin(\varphi_{\text{ext}}/4)$ and $\pm I_0 \cos(\varphi_{\text{ext}}/4)$.

2.1.4 Adding External Microwaves

When connecting nodes 1, 2, 3, 4 to an outside circuit, the influence of possible additional microwave currents/voltages on the fluxes $\Phi_{a,b,c,d}$ and thus $\Phi_{X,Y,Z,M}$ has to be considered. As mentioned above, $\Phi_M \equiv \Phi_{\text{ext}} + n\Phi_0$, so it is decoupled from outside currents/voltages. These RF voltages will influence the node fluxes, while the vector potential \vec{A} (i.e. the applied magnetic field) remains unaffected. In general one can write

$$\phi_i = \phi_i^{\text{DC}} + \phi_i^{\text{RF}}, \quad (2.20)$$

where ϕ_i^{DC} is the node flux due to the magnetic field, and ϕ_i^{RF} the node flux due to the microwave field. It then follows that $\Phi_k = \Phi_k^{\text{DC}} + \Phi_k^{\text{RF}}$ and since Eqs. 2.8 are linear, also that

$$\Phi_X = \phi_3^{\text{RF}} - \phi_4^{\text{RF}} + \Phi_X^{\text{DC}} \quad (2.21)$$

$$\Phi_Y = \phi_1^{\text{RF}} - \phi_2^{\text{RF}} + \Phi_Y^{\text{DC}} \quad (2.22)$$

$$\Phi_Z = \frac{\phi_1^{\text{RF}} + \phi_2^{\text{RF}} - \phi_3^{\text{RF}} - \phi_4^{\text{RF}}}{2} + \Phi_Z^{\text{DC}}. \quad (2.23)$$

Since $\boxed{\Phi_{X,Y,Z}^{\text{DC}} \stackrel{4\text{JJ-JRM}}{=} 0}$ in the four junction JRM (Eqs. 2.8 and 2.18), one finally arrives at

$$\Phi_X \stackrel{4\text{JJ-JRM}}{=} \phi_3^{\text{RF}} - \phi_4^{\text{RF}} \quad (2.24)$$

$$\Phi_Y \stackrel{4\text{JJ-JRM}}{=} \phi_1^{\text{RF}} - \phi_2^{\text{RF}} \quad (2.25)$$

$$\Phi_Z \stackrel{4\text{JJ-JRM}}{=} \frac{\phi_1^{\text{RF}} + \phi_2^{\text{RF}} - \phi_3^{\text{RF}} - \phi_4^{\text{RF}}}{2}. \quad (2.26)$$

These expressions justify the choice of $\Phi_{X,Y,Z}$ as relevant generalized branch fluxes. For instance, when the JRM is inserted into a circuit as a two-node (black-box) element with nodes 3 and 4, then Φ_X is simply the generalized branch flux across this element.

2.1.5 Lowest Ring Energy

When no microwave currents/voltages are applied, $\varphi_{X,Y,Z} = 0$ and the energy expression reduces to

$$E_{\text{JRM}}^{4\text{JJ}} \stackrel{\varphi_{X,Y,Z}=0}{=} -4E_J \cos\left(\frac{\varphi_{\text{ext}}}{4} + n\frac{\pi}{2}\right), \quad (2.27)$$

with $n = 0, 1, 2, 3$. Figure 2.3 shows the four magnetic flux degenerate energy states together with the lowest energy envelopes. Since there is a potential barrier to switching from energy state n to $n' \neq n$, there will be hysteresis, i.e. the energy state depends on the sweep direction, as indicated in Fig. 2.3 b).

2.1.6 Current-Flux Relation

The current-flux relation for modes X, Y, Z can be found by noting that the JRM is a non-linear inductance, with

$$L_{X,Y,Z}^{-1} := \frac{1}{\varphi_0^2} \frac{\partial^2 E}{\partial \varphi_{X,Y,Z}^2}. \quad (2.28)$$

So in the case where $\Phi_k \neq 0$, while $\Phi_{k'} = 0$ for $k, k' \in \{X, Y, Z\}$, and using Eq. 2.10, one finds

$$L_X^{-1} \stackrel{\varphi_{Y,Z}=0}{=} L_J^{-1} \cos\left(\frac{\varphi_X}{2}\right) \cos\left(\frac{\varphi_{\text{ext}}}{4} + n\frac{\pi}{2}\right) \quad (2.29)$$

$$L_Y^{-1} \stackrel{\varphi_{X,Z}=0}{=} L_J^{-1} \cos\left(\frac{\varphi_Y}{2}\right) \cos\left(\frac{\varphi_{\text{ext}}}{4} + n\frac{\pi}{2}\right) \quad (2.30)$$

$$L_Z^{-1} \stackrel{\varphi_{X,Y}=0}{=} 4L_J^{-1} \cos\left(\frac{\varphi_Z}{2}\right) \cos\left(\frac{\varphi_{\text{ext}}}{4} + n\frac{\pi}{2}\right), \quad (2.31)$$

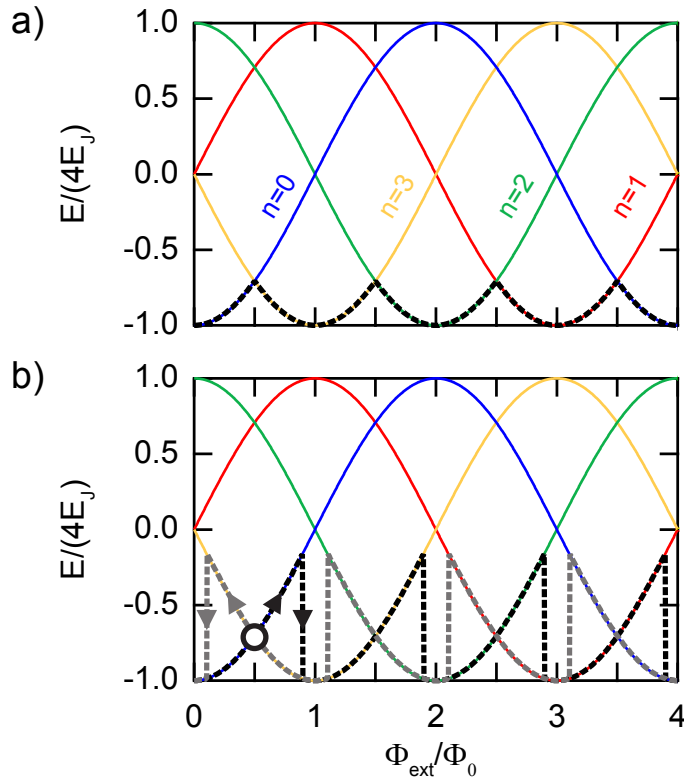


Figure 2.3: JRM energy for $\varphi_{X,Y,Z} = 0$. a) Schematic of magnetic flux degenerate energy states (colored) and lowest energy envelope (black). b) Same as a), but with hysteresis. Depending on the magnetic field sweep direction, different energy states are attained (black and gray). An energy barrier (not shown here) separates the different flux states and is associated with the cost of entrance of additional flux quanta into the loop [68]. The exact locations of jumps between flux states are determined by the barrier height and the amount of noise present in the system. JPC working points are typically at $\Phi_0/2 \pmod{\Phi_0}$, indicated by the white disk.

where $L_J \equiv I_0/\varphi_0$. Again, four different solutions are found, parametrized by $n = 0, 1, 2, 3$. The JRM thus has a current-flux relation very similar to a single junction, with a critical current reduced by the external field. To first order in $\varphi_{X,Y,Z} \ll 1$, one finds

$$4\text{JJ JRM: } L_{X,Y}^{-1} \stackrel{\varphi_{X,Y,Z} \ll 0}{=} L_J^{-1} \cos\left(\frac{\varphi_{\text{ext}}}{4} + n\frac{\pi}{2}\right) \quad (2.32)$$

$$L_Z^{-1} \stackrel{\varphi_{X,Y,Z} \ll 0}{=} 4L_J^{-1} \cos\left(\frac{\varphi_{\text{ext}}}{4} + n\frac{\pi}{2}\right). \quad (2.33)$$

2.1.7 Experiment

The JRM energy state as a function of Φ_{ext} can be monitored in the JPC by measuring the resonance frequency of e.g. the signal mode as a function of the applied magnetic flux. When no idler and pump tones are applied, no coupling between modes $\varphi_{X,Y,Z}$ exists, as $\varphi_{Y,Z} = 0$ and the ring modulator energy (Eq. 2.10) reduces to $E_{\text{JRM}}^{\text{4JJ}} \stackrel{\varphi_{Y,Z}=0}{=} -4E_J \cos\left(\frac{\varphi_X}{2}\right) \cos\left(\frac{\varphi_{\text{ext}}}{4} + n\frac{\pi}{2}\right)$. For small signal probe powers ($\varphi_X \ll 1$), the inductance of the JRM is given by Eq. 2.32, and the equivalent circuits are shown in Fig. 2.4. a) Shows the equivalent JPC circuit for balanced coupling through a 180-degree hybrid coupler, while b) shows the JPC circuit when one of the transmission line resonator ports is shorted to ground. Some of the devices fabricated were of the type shown in a) on the idler port, while being of type shown in b) on the signal port. In either case, around their respective resonance frequencies they can be represented by LC-circuits with a linear inductor in series with the nonlinear inductance given by the JRM (Eq. 2.32).

Figure 2.5 shows a picture of a typical JRM fabricated using the Dolan bridge technique [62]. The junctions are in the range of $I_0 = 3 - 5\mu\text{A}$ and have an area of $5 \times 1\mu\text{m}^2$.

2.1.7.1 Flux Modulation

When varying the magnetic flux through the JRM and measuring the phase response of the JPC signal or idler ports (without pump tone), the degeneracy of the energy state can be observed, as the system is hysteretic.

As seen in Fig. 2.6 a) and b), the resonance frequencies are changing with the magnetic field and jumps occur, which correspond to a change in energy states ($n = 0 \rightarrow n = 3 \rightarrow n = 2 \rightarrow n = 1 \rightarrow n = 0$ when increasing the flux). When reversing the sweep direction of the flux, the jump locations change and hysteresis can be observed. The yellow traces are the resonator center

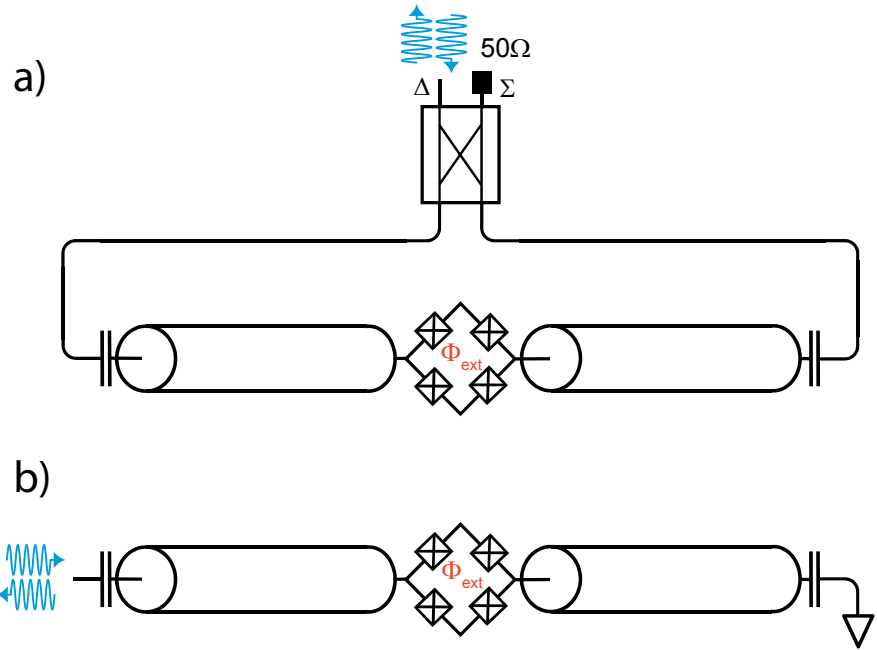


Figure 2.4: Schematic of transmission line resonators with 4JJ JRM. a) Symmetric coupling through 180-degree hybrid. b) Single ended resonator. This type of transmission line resonator has the advantage that no hybrid coupler is needed to excite its differential mode, but the disadvantage that the current anti-node is shifted from its geometric mid-point, where the JRM is usually located.

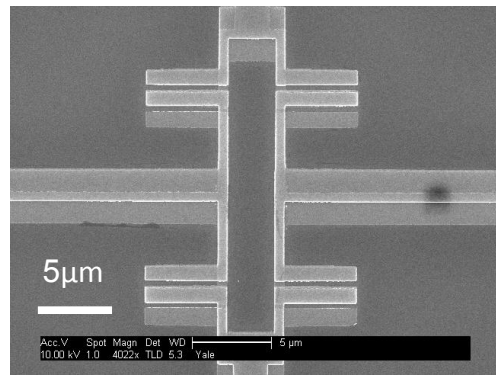


Figure 2.5: A four junction JRM fabricated with e-beam lithography and using the Dolan bridge technique.

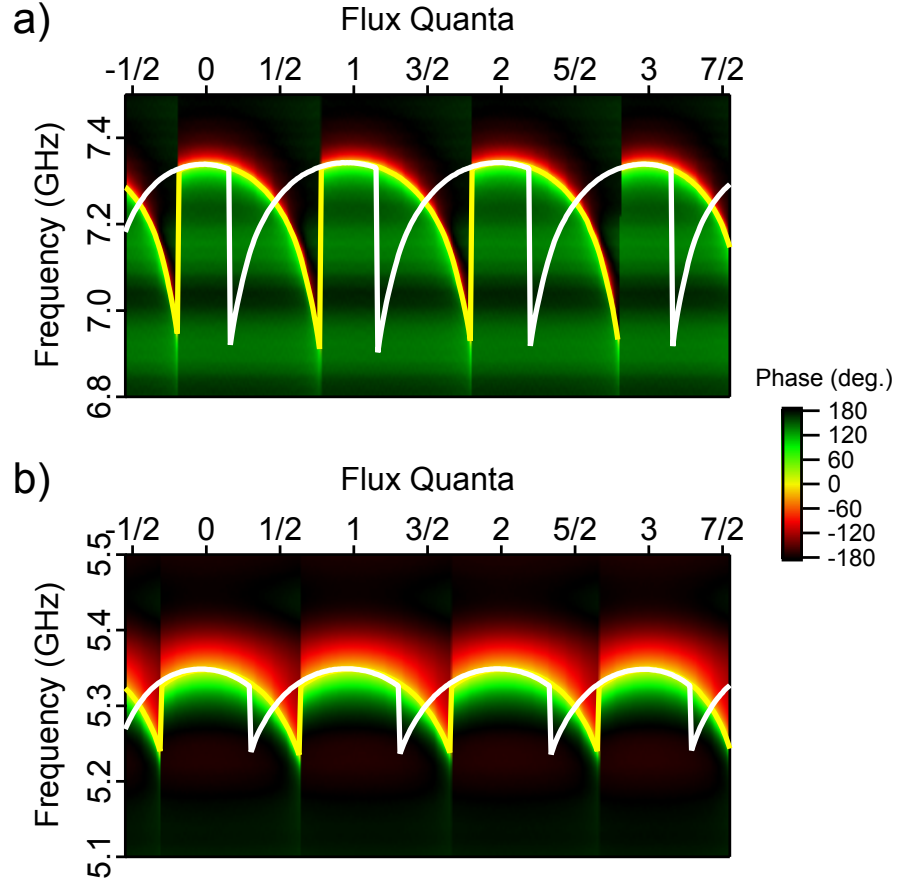


Figure 2.6: Phase response of JPC for modulated magnetic flux. No pump power is applied. a) Reflected phase of microwaves injected on signal port. 2D color plot: phase for increasing magnetic flux. Yellow trace: resonance frequency for increasing magnetic flux. White trace: resonance frequency for decreasing magnetic flux. b) Same as a), but for idler resonator. The signal resonator of this sample (JPX30; JRM similar to one shown in Fig. 2.5) is of the type shown in Fig. 2.4 b), while the idler resonator is of the type shown in Fig. 2.4 a).

frequencies as the flux is swept upward, while the white traces are the resonance frequencies as the flux is swept downward. The JPC is typically operated at flux points $\Phi_{\text{ext}} = \Phi_0/2 \pmod{\Phi_0}$, as this point is usually sufficiently far away from jump locations and also provides non-zero coupling (the coupling vanishes at $\Phi_{\text{ext}} = 0 \pmod{\Phi_0}$)¹. This working point is shown as white disk in Fig. 2.3.

2.1.7.2 Degeneracy and Phase Shift

The hysteresis is due to the energy cost associated with switching from e.g. state $n = 0$ to state $n = 3$ around $\Phi_{\text{ext}} = \Phi_0/2$. This energy degenerate state corresponds to two circulating currents with equal magnitude but opposite circulation direction, as shown in Fig. 2.7 (the two white disks). While increasing or decreasing the flux far away from $\Phi_0/2$ and then returning to that flux value will always return the JRM to the energy $-4E_J/\sqrt{2}$, the current will change direction. This change can be observed experimentally as it corresponds to a phase shift π in the (effective) pump phase φ , as mentioned in Sec. 2.1.2. As shown in Sections 5.1.1 and 3.2.6.1 (e.g. Eq. 3.127), when balanced ($\dot{n}_S = \dot{n}_I$) signal and idler tones are applied to the JPC, the signal (and also idler) reflection coefficient depends on the nonlinear phase $\varphi_n = \varphi_S + \varphi_I + \varphi$, where φ is related to the applied pump phase φ_p by $\varphi \equiv -\varphi_p \pm \pi/2$. The sign in front of the $\pi/2$ term depends on the direction of the circulating current. When fixing the values of φ_p and φ_S and changing the phase of the idler tone at a rate of 0.1Hz, the signal reflection coefficient changes from $4G_0$ to $(4G_0)^{-1}$, i.e. from amplification to attenuation. This is shown in Fig. 2.8, where the red trace is the measured reflected signal port power, normalized by G_0 .

When forcing the JRM to jump from state $n = 3$ to $n = 0$ by sweeping the magnetic flux sufficiently far below $\Phi_0/2$ and back, φ will change by π , and this change will appear in the idler phase dependence of the Coherent Attenuation (CA) experiment. The blue trace of Fig. 2.8 shows the same measured signal port power as a function of the nonlinear phase, just after a forced state jump.

2.2 Shunted Ring Modulator

As seen in Fig. 2.6, the four junctions JRM can have some modest range of frequency tunability with magnetic flux. In practice, however, it is always operated around $\Phi_0/2$ and its tunability thus

¹This is true, if, as it does, the system returns to the lowest energy state at multiples of Φ_0 .

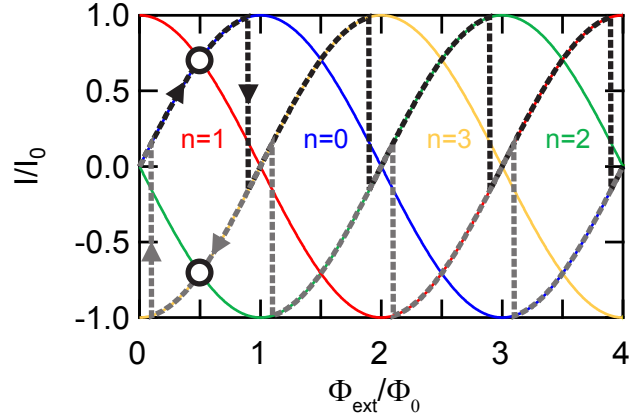


Figure 2.7: Circulating current in JRM induced by magnetic flux. Working points are typically at $\Phi_0/2$ (mod Φ_0) and indicated by the two white disks, representing clockwise and anti-clockwise circulating currents. These two states are degenerate in energy (see Fig. 2.3). Note that the current direction is defined in Fig. 2.2, so that a positive current is flowing in the opposite direction of the integration path defining Φ_{ext} .

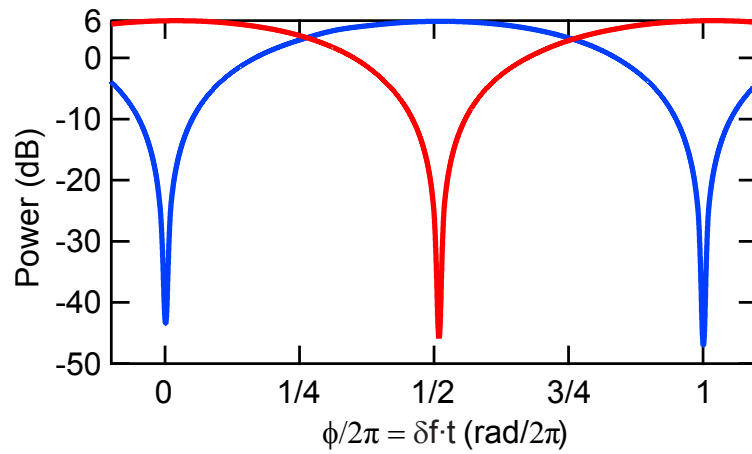


Figure 2.8: Coherent attenuation experiment at degenerate flux point $\Phi_{\text{ext}} = \Phi_0/2$ (sample JPX26). The reflected signal port power is measured as a function of the idler phase, which is changed at a rate of 0.1Hz. Red trace: flux is set to $\Phi_0/2$ (in decreasing field sweep direction). Blue trace: flux also set to $\Phi_0/2$, but only after sweeping it below $\Phi_{\text{ext}} = 0$ and back up, to induce jump in JRM state.

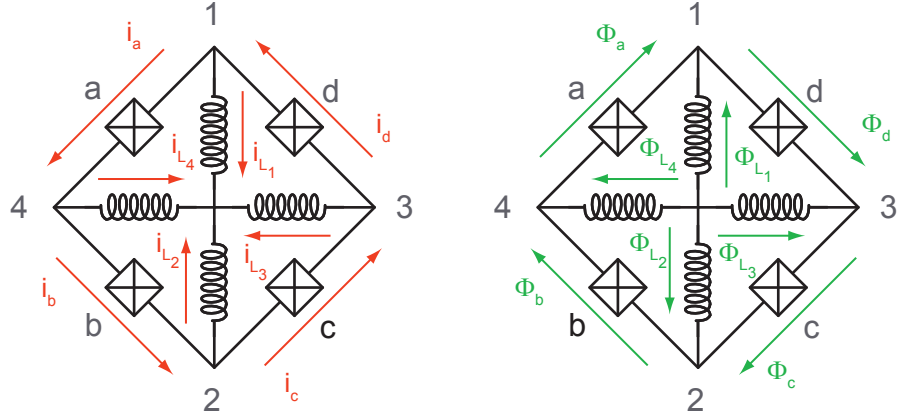


Figure 2.9: Schematic of shunted Josephson ring modulator. The sign of currents is defined with respect to the red arrows, while the sign of fluxes is defined with respect to the green arrows.

very limited. At fluxes Φ_{ext} between 0 and $\Phi_0/2$, there is not much change in the JPC frequency, as L_X (defined in Eq. 2.32) changes only by $\sim 30\%$, and makes up only $\sim 5\%$ of the total equivalent resonator inductance. Further, and more importantly, the coupling term between modes X, Y, Z goes as $\sin(\varphi_{\text{ext}}/4)$ (Eq. 2.12), so that it vanishes around $\Phi_{\text{ext}} = 0$. Beyond $\Phi_{\text{ext}} = \Phi_0/2$ however, the device becomes more sensitive to magnetic field noise and more likely to undergo flux state jumps.

The degeneracy can be lifted by quartering the ring with shunt inductors, which will create four loops with only one junction per loop, as seen in Fig. 2.9. As will be shown below, when using Kirchhoff's loop rule and evaluating the integral $\oint \vec{A} d\vec{s} = \Phi_{\text{loop}} + n_{\text{loop}} \Phi_0$, the term $n_{\text{loop}} \Phi_0$ is entirely absorbed by the junction flux, which is unique up to multiples of Φ_0 anyways, so that the degeneracy is lifted. Note that simply shunting each junction outside of the loop will not lift the degeneracy, but will simply create an uncoupled current through the inductors, while the junction current is still set by the flux through the large loop².

²One could think of it as two independent rings: an unshunted JRM and a ring with four linear inductors.

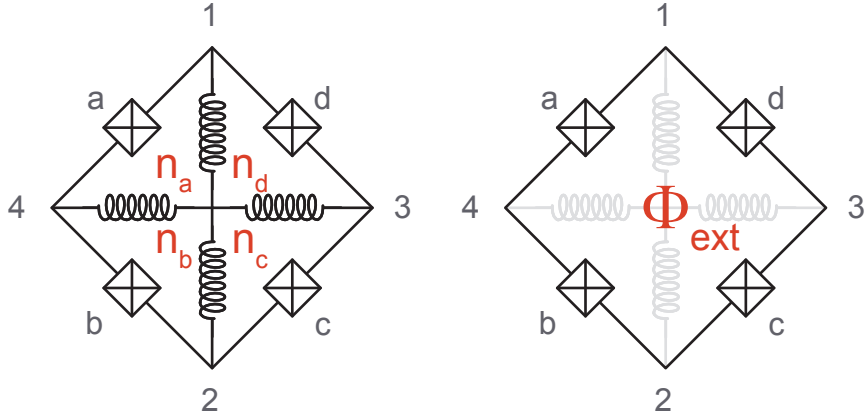


Figure 2.10: Schematic of JRM with magnetic flux quanta in each loop (left) and external magnetic flux (right). The flux Φ_{ext} is defined with respect to the area enclosed by the four outer junctions.

2.2.1 Circuit Equations

It is useful to write out the circuit equations for the JRM in the absence of external (microwave) currents and voltages, in order to understand how the energy states are parametrized. The loop rule gives (with or without external currents/voltages)

$$\Phi_a - \Phi_{L_1} + \Phi_{L_4} = \frac{\Phi_{\text{ext}}}{4} + n_a \Phi_0 \quad (2.34)$$

$$\Phi_b - \Phi_{L_4} + \Phi_{L_2} = \frac{\Phi_{\text{ext}}}{4} + n_b \Phi_0 \quad (2.35)$$

$$\Phi_c - \Phi_{L_2} + \Phi_{L_3} = \frac{\Phi_{\text{ext}}}{4} + n_c \Phi_0 \quad (2.36)$$

$$\Phi_d - \Phi_{L_3} + \Phi_{L_1} = \frac{\Phi_{\text{ext}}}{4} + n_d \Phi_0, \quad (2.37)$$

where Φ_{ext} is the external magnetic flux threading the area enclosed by the four junctions, and the $n_{a,b,c,d} \in \mathbb{Z}$ are the flux quanta per partial loop, as shown in Fig. 2.10. The Φ_k , $k \in \{a, b, c, d\}$ and Φ_{L_i} , $i \in \{1, 2, 3, 4\}$ are the generalized fluxes shown in Fig. 2.9.

The node rule (without external currents) gives

$$i_d - i_a - i_{L_1} = 0 \quad (2.38)$$

$$i_b - i_c - i_{L_2} = 0 \quad (2.39)$$

$$i_c - i_d - i_{L_3} = 0 \quad (2.40)$$

$$i_a - i_b - i_{L_4} = 0, \quad (2.41)$$

where the i are the currents again shown in Fig. 2.9. With identical junctions and inductors, the current-flux relations are

$$i_k = I_0 \sin(\varphi_k) \quad k \in \{a, b, c, d\} \quad (2.42)$$

$$i_{L_i} = \frac{1}{L} \Phi_{L_i} \quad i \in \{1, 2, 3, 4\}, \quad (2.43)$$

where $\varphi_k \equiv \Phi_k / \varphi_0$.

2.2.2 Shunted JRM Energy

The goal is again to show that the energy term of the shunted JRM provides a mixing of the modes of the form $\varphi_X \varphi_Y \varphi_Z$, for certain values of the external magnetic flux Φ_{ext} . The energy of the shunted ring modulator is given by

$$\begin{aligned} E_{\text{JRM}}^{\text{shunted}} &= -E_J [\cos(\varphi_a) + \cos(\varphi_b) + \cos(\varphi_c) + \cos(\varphi_d)] \\ &\quad + \frac{E_L}{2} [\varphi_{L_1}^2 + \varphi_{L_2}^2 + \varphi_{L_3}^2 + \varphi_{L_4}^2], \end{aligned} \quad (2.44)$$

where $E_L \equiv \varphi_0^2 / L$, $E_J \equiv \varphi_0^2 / L_{J_0}$, and $L_{J_0} \equiv \varphi_0 / I_0$. The modes X, Y, Z are again defined in Eq. 2.8, and again, the M mode is decoupled from the JRM, since

$$\varphi_M \stackrel{\text{shunted JRM}}{\equiv} \varphi_{\text{ext}} + 2\pi \sum_k n_k.$$

(2.45)

The difference to the four junction case (Eq. 2.11) is that $(\sum_k n_k / 4) \in \mathbb{Z}$, so that the Josephson term can be expressed as

$$E = -E_J [\cos(\varphi_a) + \cos(\varphi_b) + \cos(\varphi_c) + \cos(\varphi_d)] \quad (2.46)$$

$$\begin{aligned} &= -4E_J \left[\cos\left(\frac{\varphi_X}{2}\right) \cos\left(\frac{\varphi_Y}{2}\right) \cos(\varphi_Z) \cos\left(\frac{\varphi_{\text{ext}}}{4}\right) \right. \\ &\quad \left. + \sin\left(\frac{\varphi_X}{2}\right) \sin\left(\frac{\varphi_Y}{2}\right) \sin(\varphi_Z) \sin\left(\frac{\varphi_{\text{ext}}}{4}\right) \right]. \end{aligned} \quad (2.47)$$

The degeneracy of this term is now lifted (compare to Eq. 2.10), as the magnetic field enters with unique values as $\cos(\varphi_{\text{ext}}/4)$ and $\sin(\varphi_{\text{ext}}/4)$.

For any value of (n_a, n_b, n_c, n_d) , the inductive part can be expressed as

$$\begin{aligned} \varphi_{L_1}^2 + \varphi_{L_2}^2 + \varphi_{L_3}^2 + \varphi_{L_4}^2 &= \frac{\varphi_X^2}{2} + \frac{\varphi_Y^2}{2} + \varphi_Z^2 \\ &\quad + 2\pi^2 (n_X^2 + n_Y^2 + 2n_Z^2) \end{aligned} \quad (2.48)$$

$$\begin{aligned} &\quad - 2\pi (n_X \varphi_X + n_Y \varphi_Y + 2n_Z \varphi_Z) \\ &= \frac{(\varphi_X - 2\pi n_X)^2}{2} + \frac{(\varphi_Y - 2\pi n_Y)^2}{2} \\ &\quad + (\varphi_Z - 2\pi n_Z)^2, \end{aligned} \quad (2.49)$$

where the $n_{X,Y,Z}$ are defined analogous to the $\varphi_{X,Y,Z}$:

$$n_X := \frac{n_a - n_b - n_c + n_d}{2} \quad (2.50)$$

$$n_Y := \frac{n_a + n_b - n_c - n_d}{2} \quad (2.51)$$

$$n_Z := \frac{n_a - n_b + n_c - n_d}{4}. \quad (2.52)$$

Note that in general the $n_{X,Y,Z}$ need not be integers, but rather multiples of $\pm 1/2$ or $\pm 1/4$.

So finally the shunted JRM energy can be expressed as:

$$\begin{aligned}
E_{\text{JRM}}^{\text{shunted}} = & -4E_J \left[\cos\left(\frac{\varphi_X}{2}\right) \cos\left(\frac{\varphi_Y}{2}\right) \cos(\varphi_Z) \cos\left(\frac{\varphi_{\text{ext}}}{4}\right) \right. \\
& + \sin\left(\frac{\varphi_X}{2}\right) \sin\left(\frac{\varphi_Y}{2}\right) \sin(\varphi_Z) \sin\left(\frac{\varphi_{\text{ext}}}{4}\right) \left. \right] \\
& + \frac{E_L}{2} \left[\frac{(\varphi_X - 2\pi n_X)^2}{2} + \frac{(\varphi_Y - 2\pi n_Y)^2}{2} + (\varphi_Z - 2\pi n_Z)^2 \right].
\end{aligned} \tag{2.53}$$

Just as in the case of the unshunted JRM, this energy has the useful $\varphi_X \varphi_Y \varphi_Z$ nonlinear mixing term for small $\varphi_{X,Y,Z}$, but it still needs to be assured that the modes X, Y, Z are the *relevant* ones. Again, in general the branch fluxes can be expressed as superpositions between DC fluxes Φ^{DC} induced by the applied external magnetic field Φ_{ext} and the RF fluxes Φ^{RF} due to the externally applied microwave fields, $\Phi_k = \Phi_k^{\text{DC}} + \Phi_k^{\text{RF}}$. By noting that the vector potential terms $\int \vec{A} d\vec{s}$ remain the same with or without the Φ^{RF} terms, it is not difficult to show that for any state (n_a, n_b, n_c, n_d) the $\Phi_{X,Y,Z}$ can be expressed as functions of the (applied) node fluxes ϕ_i^{RF} , $i \in \{1, 2, 3, 4\}$:

$$\Phi_X = \phi_3^{\text{RF}} - \phi_4^{\text{RF}} + \Phi_X^{\text{DC}} \tag{2.54}$$

$$\Phi_Y = \phi_1^{\text{RF}} - \phi_2^{\text{RF}} + \Phi_Y^{\text{DC}} \tag{2.55}$$

$$\Phi_Z = \frac{\phi_1^{\text{RF}} + \phi_2^{\text{RF}} - \phi_3^{\text{RF}} - \phi_4^{\text{RF}}}{2} + \Phi_Z^{\text{DC}}. \tag{2.56}$$

To determine the energy mixing term, all that remains to do is to find the magnetic field induced fluxes $\Phi_{X,Y,Z}^{\text{DC}}$, or equivalently, the circulating DC currents in the ring.

The JRM energy state can be parametrized by the integers (n_a, n_b, n_c, n_d) and two cases with high symmetry are of interest and considered below: $(n_a, n_b, n_c, n_d) = (m, m, m, m)$ and $(n_a, n_b, n_c, n_d) = (m, -m, m, -m)$, where $m \in \mathbb{Z}$.

2.2.3 Solutions (m, m, m, m)

In this case, $\sum_k n_k = 4m$ and $n_{X,Y,Z} = 0$, $\forall m \in \mathbb{Z}$.

2.2.3.1 Circulating Currents

Solving Kirchhoff's Eqs. 2.34ff. and 2.38ff. one finds

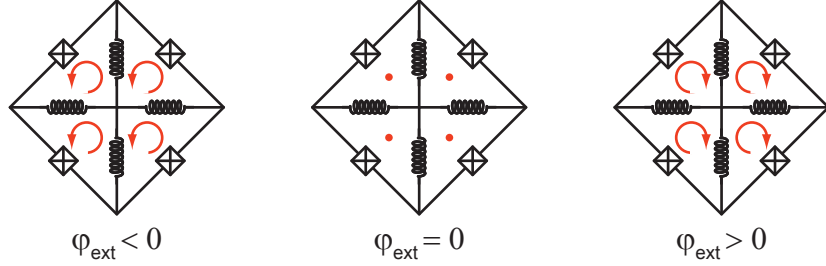


Figure 2.11: Current pattern for the state (m, m, m, m) around $\varphi_{\text{ext}} = 0$. The arrows indicate the direction of the current flow, while the dots indicate that the circulating currents are zero.

$$\Phi_{a,b,c,d}^{\text{DC}} \stackrel{(m,m,m,m)}{=} \frac{\Phi_{\text{ext}}}{4} + m\Phi_0 \quad (2.57)$$

$$\Rightarrow i_{a,b,c,d}^{\text{DC}} \stackrel{(m,m,m,m)}{=} I_0 \sin\left(\frac{\varphi_{\text{ext}}}{4}\right) \quad (2.58)$$

$$\Phi_{L_{1,2,3,4}}^{\text{DC}} \stackrel{(m,m,m,m)}{=} 0 \quad (2.59)$$

$$\Rightarrow i_{L_{1,2,3,4}}^{\text{DC}} \stackrel{(m,m,m,m)}{=} 0. \quad (2.60)$$

Figure 2.11 shows the current pattern for this state, centered around $\varphi_{\text{ext}} = 0$. No current flows through the central inductors, while a current is circulating in the loop defined by the four junctions, and whose direction and magnitude is uniquely determined by the magnetic flux φ_{ext} .

In particular, this means that

$$\boxed{\Phi_{X,Y,Z}^{\text{DC}} \stackrel{(m,m,m,m)}{=} 0} \quad (2.61)$$

and thus that

$$\Phi_X \stackrel{(m,m,m,m)}{=} \phi_3^{\text{RF}} - \phi_4^{\text{RF}} =: \Phi_X^{\text{RF}} \quad (2.62)$$

$$\Phi_Y \stackrel{(m,m,m,m)}{=} \phi_1^{\text{RF}} - \phi_2^{\text{RF}} =: \Phi_Y^{\text{RF}} \quad (2.63)$$

$$\Phi_Z \stackrel{(m,m,m,m)}{=} \frac{\phi_1^{\text{RF}} + \phi_2^{\text{RF}} - \phi_3^{\text{RF}} - \phi_4^{\text{RF}}}{2} =: \Phi_Z^{\text{RF}}, \quad (2.64)$$

which is the desired dependence on the ϕ^{RF} .

2.2.3.2 Energy

Thus Eq. 2.53 becomes

$$E_{\text{JRM}}^{\text{shunted}} \stackrel{(m,m,m,m)}{=} -4E_J \left[\cos\left(\frac{\varphi_X^{\text{RF}}}{2}\right) \cos\left(\frac{\varphi_Y^{\text{RF}}}{2}\right) \cos(\varphi_Z^{\text{RF}}) \cos\left(\frac{\varphi_{\text{ext}}}{4}\right) + \sin\left(\frac{\varphi_X^{\text{RF}}}{2}\right) \sin\left(\frac{\varphi_Y^{\text{RF}}}{2}\right) \sin(\varphi_Z^{\text{RF}}) \sin\left(\frac{\varphi_{\text{ext}}}{4}\right) \right] + \frac{E_L}{2} \left[\frac{(\varphi_X^{\text{RF}})^2}{2} + \frac{(\varphi_Y^{\text{RF}})^2}{2} + (\varphi_Z^{\text{RF}})^2 \right]. \quad (2.65)$$

The energy expression shows in particular that no dependence on the parameter $m \in \mathbb{Z}$ exists, which means that all solutions (m, m, m, m) are in fact physically identical.

For small $\varphi_{X,Y,Z}^{\text{RF}}$, one obtains the desired mixing term $\varphi_X^{\text{RF}} \varphi_Y^{\text{RF}} \varphi_Z^{\text{RF}}$, but this time *without degeneracy*:

$$E_{\text{JRM}}^{\text{shunted}} \stackrel{\varphi_{X,Y,Z}^{\text{RF}} \ll 1}{=} -E_J \sin\left(\frac{\varphi_{\text{ext}}}{4}\right) \varphi_X^{\text{RF}} \varphi_Y^{\text{RF}} \varphi_Z^{\text{RF}} + \left(E_J \cos\left(\frac{\varphi_{\text{ext}}}{4}\right) + \frac{E_L}{2} \right) \left(\frac{(\varphi_X^{\text{RF}})^2}{2} + \frac{(\varphi_Y^{\text{RF}})^2}{2} \right) + 2 \left(E_J \cos\left(\frac{\varphi_{\text{ext}}}{4}\right) + \frac{E_L}{4} \right) (\varphi_Z^{\text{RF}})^2 - 4E_J \cos\left(\frac{\varphi_{\text{ext}}}{4}\right). \quad (2.66)$$

It is this energy state that is of interest for the parametric amplification process, and care has to be taken to ensure the JRM is operated in this state. Below it will be shown for which magnetic fluxes this state is attained. For $\varphi_{X,Y,Z}^{\text{RF}} = 0$, the energy reduces to the non-degenerate value

$$E_{\text{JRM}}^{\text{shunted}} \stackrel{\varphi_{X,Y,Z}^{\text{RF}} = 0}{=} -4E_J \cos\left(\frac{\varphi_{\text{ext}}}{4}\right). \quad (2.67)$$

2.2.3.3 Equivalent Inductance

Using Eq. 2.28³ for $\varphi_{X,Y,Z}^{\text{RF}} \ll 1$ the magnetic field dependent equivalent inductances of the shunted JRM become

³The derivative is of course with respect to $\varphi_{X,Y,Z}^{\text{RF}}$.

$$\text{shunted JRM: } (m, m, m, m) \quad L_{X,Y}^{-1} \stackrel{\varphi_{X,Y,Z}^{\text{RF}} \ll 1}{=} \frac{L^{-1}}{2} \left(2\beta_L \cos\left(\frac{\varphi_{\text{ext}}}{4}\right) + 1 \right) \quad (2.68)$$

$$L_Z^{-1} \stackrel{\varphi_{X,Y,Z}^{\text{RF}} \ll 1}{=} L^{-1} \left(4\beta_L \cos\left(\frac{\varphi_{\text{ext}}}{4}\right) + 1 \right), \quad (2.69)$$

where $\beta_L \equiv L/L_{J_0} = E_J/E_L$. Note that Eq. 2.68 is the solution also found through simple circuit analysis, by assuming that the junctions are linear inductors with inductance $L_J/\cos(\varphi_{\text{ext}}/4)$.

2.2.4 Solutions $(m, -m, m, -m)$

The second set of solutions of interest are those for which $(n_a, n_b, n_c, n_d) = (m, -m, m, -m)$, $m \in \mathbb{Z}$, or equivalently $(n_X, n_Y, n_Z, n_W) = (0, 0, m, 0)$, where $n_W := \sum_{k \in \{a,b,c,d\}} n_k$.

2.2.4.1 Circulating Currents

Solving the loop and node equations, one finds

$$\Phi_{a,c}^{\text{DC}} \stackrel{(m, -m, m, -m)}{=} +(\textcolor{red}{x}\varphi_0 + m\Phi_0) + \frac{\Phi_{\text{ext}}}{4} \quad (2.70)$$

$$\Phi_{b,d}^{\text{DC}} \stackrel{(m, -m, m, -m)}{=} -(\textcolor{red}{x}\varphi_0 + m\Phi_0) + \frac{\Phi_{\text{ext}}}{4} \quad (2.71)$$

$$\Rightarrow i_{a,c}^{\text{DC}} \stackrel{(m, -m, m, -m)}{=} I_0 \sin\left(\textcolor{red}{x} + \frac{\varphi_{\text{ext}}}{4}\right) \quad (2.72)$$

$$\Rightarrow i_{b,d}^{\text{DC}} \stackrel{(m, -m, m, -m)}{=} I_0 \sin\left(-\textcolor{red}{x} + \frac{\varphi_{\text{ext}}}{4}\right) \quad (2.73)$$

$$\Phi_{L_{1,2}}^{\text{DC}} \stackrel{(m, -m, m, -m)}{=} -\Phi_{L_{3,4}}^{\text{DC}} = \frac{\textcolor{red}{x}}{2}\varphi_0 \quad (2.74)$$

$$\Rightarrow i_{L_{1,2}}^{\text{DC}} \stackrel{(m, -m, m, -m)}{=} -i_{L_{3,4}}^{\text{DC}} = \frac{\textcolor{red}{x}\varphi_0}{2L}, \quad (2.75)$$

where x is solution to the RF-superconducting quantum interference device (SQUID)-like equation

$$\boxed{\textcolor{red}{x} = -4\beta_L \cos\left(\frac{\varphi_{\text{ext}}}{4}\right) \sin(\textcolor{red}{x})}, \quad (2.76)$$

with $\beta_L := \frac{L}{L_{J_0}} \equiv \frac{E_J}{E_L}$.

Figure 2.12 shows the current pattern found above, centered around $\varphi_{\text{ext}} = 4\pi$. This time, a current flows through the central inductors, given by $x\varphi_0/(2L)$. At magnetic fluxes away from 4π , the current through the shunt inductors remains the same, but the junction currents are pairwise

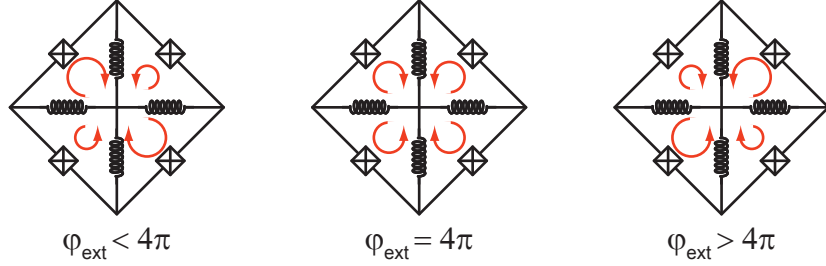


Figure 2.12: Current pattern for the state $(m, -m, m, -m)$ around $\varphi_{\text{ext}} = 4\pi$. One of the two degenerate solutions is shown (the second one corresponds to each ring modulator rotated by 90 degrees). The arrows indicate the direction of the current flow, while the size of the rings indicate the magnitude. Note that all three sub-figures shown here belong to the same solution, characterized by the net current flow through the shunt inductors (here: from top/bottom nodes into center and outward from center into left/right nodes). Passing through $\varphi_{\text{ext}} = 4\pi$ does not change this pattern, it only changes the relative current magnitudes in the outer ring junctions.

different in magnitude (the respective junction fluxes are frustrated by $\pm x\varphi_0$). Note that the state is degenerate, and Fig. 2.12 shows only one of the two solutions. The second solution is obtained by simply rotating each sub-figure by 90 degrees.

So finally one finds

$$\boxed{\Phi_{X,Y}^{\text{DC}} \stackrel{(m,-m,m,-m)}{=} 0} \quad \text{and} \quad \boxed{\Phi_Z^{\text{DC}} \stackrel{(m,-m,m,-m)}{=} x\varphi_0 + m\Phi_0}, \quad (2.77)$$

so that

$$\Phi_X \stackrel{(m,-m,m,-m)}{=} \phi_3^{\text{RF}} - \phi_4^{\text{RF}} \quad (2.78)$$

$$\Phi_Y \stackrel{(m,-m,m,-m)}{=} \phi_1^{\text{RF}} - \phi_2^{\text{RF}} \quad (2.79)$$

$$\Phi_Z \stackrel{(m,-m,m,-m)}{=} \frac{\phi_1^{\text{RF}} + \phi_2^{\text{RF}} - \phi_3^{\text{RF}} - \phi_4^{\text{RF}}}{2} + x\varphi_0 + m\Phi_0. \quad (2.80)$$

2.2.4.2 Energy

Using these expressions for $\Phi_{X,Y,Z}$ (Eq. 2.78ff.), the JRM energy (Eq. 2.53) can be expressed as

$$E_{\text{JRM}}^{\text{shunted}} \stackrel{(m,-m,m,-m)}{=} -4E_J \left[\cos\left(\frac{\varphi_X^{\text{RF}}}{2}\right) \cos\left(\frac{\varphi_Y^{\text{RF}}}{2}\right) \cos(\varphi_Z^{\text{RF}} + \textcolor{red}{x}) \cos\left(\frac{\varphi_{\text{ext}}}{4}\right) \right. \\ \left. + \sin\left(\frac{\varphi_X^{\text{RF}}}{2}\right) \sin\left(\frac{\varphi_Y^{\text{RF}}}{2}\right) \sin(\varphi_Z^{\text{RF}} + \textcolor{red}{x}) \sin\left(\frac{\varphi_{\text{ext}}}{4}\right) \right] \\ + \frac{E_L}{2} \left[\frac{(\varphi_X^{\text{RF}})^2}{2} + \frac{(\varphi_Y^{\text{RF}})^2}{2} + (\varphi_Z^{\text{RF}} + \textcolor{red}{x})^2 \right], \quad (2.81)$$

where x is the DC term determined by Eq. 2.76. Again, there is no explicit dependence on m , so that all solutions $(m, -m, m, -m)$ represent the same physical state. Note also that x is essentially the current flowing through the central inductors, induced by the magnetic flux. This energy expression in fact also exhibits the desired nonlinearity $\varphi_X^{\text{RF}} \varphi_Y^{\text{RF}} \varphi_Z^{\text{RF}}$, only that the prefactor now is $-E_J \cos(x) \sin(\varphi_{\text{ext}}/4)$. There are also other additional mixing terms compared to the case $x = 0$.

For no applied external microwave fields, one finds

$$E_{\text{JRM}}^{\text{shunted}} \stackrel{\varphi_{X,Y,Z}=0}{=} E_L \left(\frac{\textcolor{red}{x}^2}{2} - 4\beta_L \cos\left(\frac{\varphi_{\text{ext}}}{4}\right) \cos(\textcolor{red}{x}) \right), \quad (2.82)$$

and minimizing this expression in terms of x yields exactly Eq. 2.76. An important remark is that there is again no dependence on the parameter m in either the currents (Eqs. 2.72ff.) or the energy expressions (Eqs. 2.81 and 2.82). Nonetheless, this state is energy degenerate, as x and $-x$ yield the same energy (Eq. 2.82) but currents circulating in opposite directions.

2.2.4.3 Inductance

The inductances $L_{X,Y}$ now become (using Eq. 2.28 for small $\varphi_{X,Y,Z}^{\text{RF}}$):

$$\begin{aligned} \text{shunted JRM: } (m, -m, m, -m) \quad L_{X,Y}^{-1} &\stackrel{\varphi_{X,Y,Z}^{\text{RF}} \ll 1}{=} \frac{L^{-1}}{2} \left(2\beta_L \cos(\textcolor{red}{x}) \cos\left(\frac{\varphi_{\text{ext}}}{4}\right) + 1 \right) \quad (2.83) \\ L_Z^{-1} &\stackrel{\varphi_{X,Y,Z}^{\text{RF}} \ll 1}{=} L^{-1} \left(4\beta_L \cos(\textcolor{red}{x}) \cos\left(\frac{\varphi_{\text{ext}}}{4}\right) + 1 \right). \quad (2.84) \end{aligned}$$

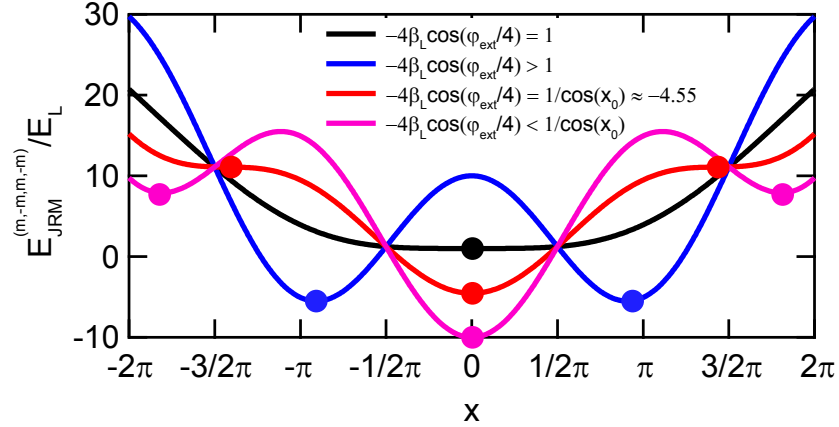


Figure 2.13: JRM energy as a function of x , for different values of $-4\beta_L \cos(\varphi_{\text{ext}}/4)$. The dots correspond to local and global energy minima. The blue trace corresponds to the case where $\exists x \neq 0$ which are the energetically most favorable solutions and the ring modulator is in state $(m, -m, m, -m)$. All other cases lead to $x = 0$ and the ring modulator is in state (m, m, m, m) .

2.2.5 Crossover

As stated above, it is desirable to operate the JRM in the regime corresponding to state (m, m, m, m) , so it is important to understand which energy expression (Eq. 2.65 or Eq. 2.81) describes the JRM for a given magnetic flux. This comes down to comparing the energy expressions in the two cases for $\varphi_{X,Y,Z}^{\text{RF}} = 0$, i.e. Eq. 2.67 and 2.82. It is clear that for $x = 0$, the two states are identical, so that one needs to find the condition for when $x \neq 0$, and one needs to distinguish between different cases.

$\varphi_{\text{ext}} \in [0, 2\pi] \cup [6\pi, 8\pi]$: **amplification always possible**

This is the flux region where $\cos(\frac{\varphi_{\text{ext}}}{4}) > 0$ and which is of interest for parametric amplification, as the state (m, m, m, m) is always minimizing the energy. There are solutions $x \neq 0$ as long as the magnetic flux and β_L satisfy $-4\beta_L \cos(x_0) \cos(\varphi_{\text{ext}}/4) > 1$, where $x_0 \approx 4.495$ and $-\cos(x_0) \approx +0.22$ are given by the tangent equation $x_0 \stackrel{!}{=} \tan(x_0)$. However, these solutions represent *local* minima, while $x = 0$ remains the *global* energy minimum solution. The other case, where $0 < -4\beta_L \cos(x_0) \cos(\varphi_{\text{ext}}/4) < 1$, has $x = 0$ as only solution. Thus in this magnetic flux region, the JRM is always described by the state labeled (m, m, m, m) above, and Eq. 2.65 holds. The red and pink trace in Fig. 2.13 show the JRM energy as a function of x for $-4\beta_L \cos(x_0) \cos(\varphi_{\text{ext}}/4) = 1$ and $-4\beta_L \cos(x_0) \cos(\varphi_{\text{ext}}/4) > 1$, respectively.

$\varphi_{\text{ext}} \in [2\pi, 6\pi]$: amplification sometimes possible

In this region, $\cos(\frac{\varphi_{\text{ext}}}{4}) < 0$ and the state (m, m, m, m) minimizes the energy only for particular flux values. Solutions $x = \pm x_1 \neq 0$ exist for $-4\beta_L \cos(\varphi_{\text{ext}}/4) > 1$ and these solutions correspond to global minima, leading to the state $(m, -m, m, -m)$. The black and blue traces in Fig. 2.13 show the energy for $-4\beta_L \cos(\varphi_{\text{ext}}/4) = 1$ and $-4\beta_L \cos(\varphi_{\text{ext}}/4) > 1$, respectively. For a given shunted JRM described by $\beta_L \equiv L/L_{J_0}$, the magnetic flux $\varphi_{\text{ext}}^{\text{crossover}} \in]2\pi, 4\pi[$ at which the crossover between the state (m, m, m, m) and the state $(m, -m, m, -m)$ occurs, is given by

$$\boxed{-4\beta_L \cos(\varphi_{\text{ext}}^{\text{crossover}}/4) = 1}. \quad (2.85)$$

This equation does not necessarily have solutions. In the case that the shunt inductors are sufficiently small so that $4L < L_J$ ($4\beta_L < 1$), the mode (m, m, m, m) is stable, and parametric amplification still possible. This happens at the expense of frequency tunability, as $L_{X,Y}$ remains small for any magnetic field Φ_{ext} (see Eq. 2.68). Additionally, by lowering L , E_L becomes large and starts to significantly alter the JPC resonance frequency.

Equation 2.68 suggests that the inductance $L_{X,Y}$ can become negative and thus ill-defined for fluxes such that $-2\beta_L \cos(\varphi_{\text{ext}}/4) > 1$, that is, only if $2\beta_L > 1$. This would however occur somewhere in the interval $\varphi_{\text{ext}} \in]\varphi_{\text{ext}}^{\text{crossover}}, 4\pi[$, in which Eq. 2.68 is not valid anymore, as $L_{X,Y}$ is described by Eq. 2.83.

Figure 2.14 shows the calculated resulting JPC (signal) frequency for the JRM in the relevant state (m, m, m, m) , and for different values of β_L . The ratio L_{J_0}/L_g is kept constant at 0.1, where L_g is linear inductance of the signal resonator. The dashed lines represent the locations of crossover between states (m, m, m, m) and $(m, -m, m, -m)$, given by Eq. 2.85. The location of the magnetic flux $\varphi_{\text{ext}}^{\text{zero}}$ for which the frequency (of the state (m, m, m, m)) goes to zero, is given by $-2\beta_L \cos(\varphi_{\text{ext}}^{\text{zero}}/4) = 1$. Figure 2.14 b) is a magnification of the region $\varphi_{\text{ext}} \in [\pi, 4\pi]$. Note that for $\beta_L \rightarrow \infty$ (blue trace), one recovers the result of the unshunted JRM, but *without degeneracy*.

2.2.6 Experiment

The JPC devices fabricated and measured in this thesis work were designed to have $2\beta_L$ values in the range $[0.5, 1]$, which means that they qualitatively lie somewhere between the orange and the black traces in Fig. 2.14. The advantage of such low values of the shunt inductances is that

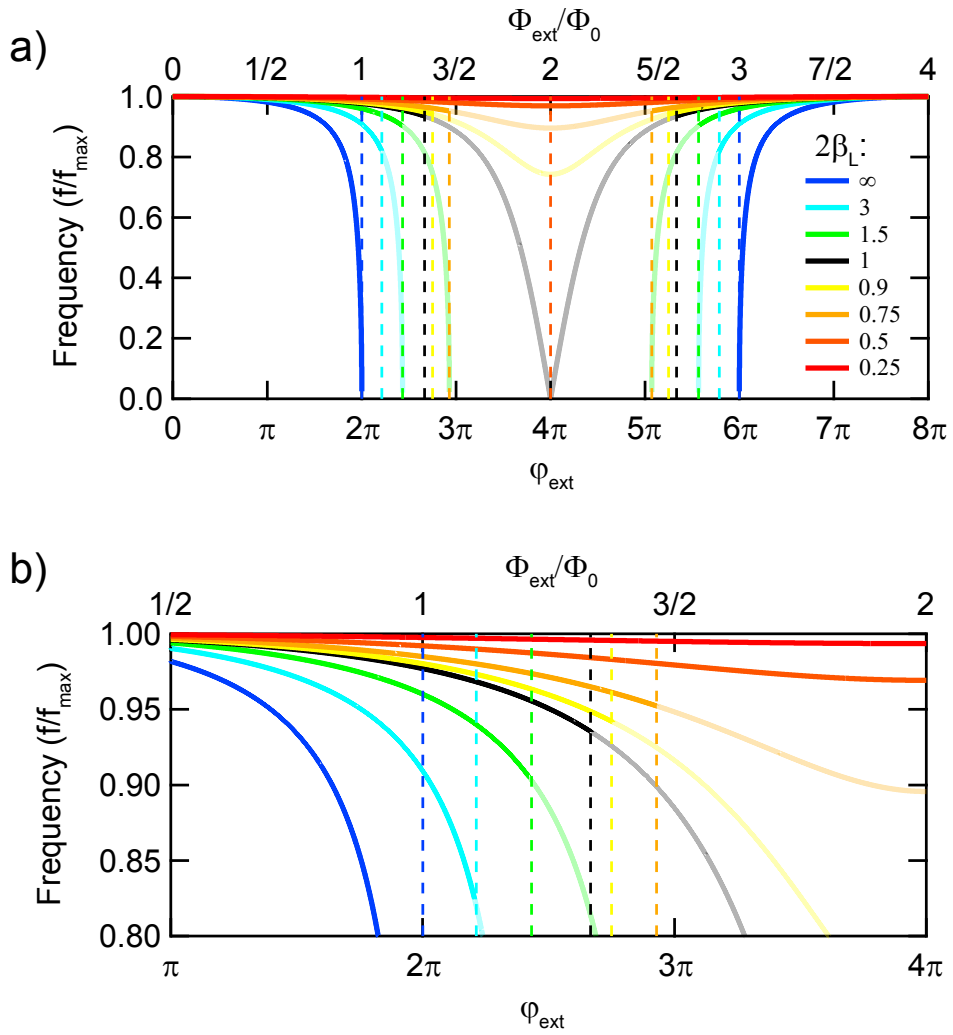


Figure 2.14: Calculated JPC frequency (e.g. of the signal mode) as a function of the applied magnetic flux, for different values of β_L and $L_{J_0}/L_g = 0.1$, where L_g is the inductance of the bare resonator without JRM. Dashed lines indicate flux locations where the lowest JRM energy state changes (from (m, m, m, m) to $(m, -m, m, -m)$).

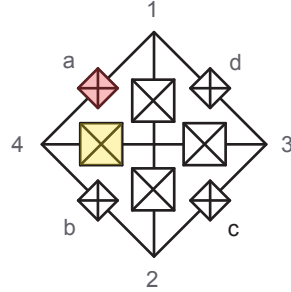


Figure 2.15: JRM with eight Josephson junctions. The outer four junctions are the JRM junctions (red), while the inner four junctions are the shunt junctions (yellow).

the state (m, m, m, m) , which is of interest for amplification, is relatively stable over the external magnetic flux range: the switching to state $(m, -m, m, -m)$ occurs rather late. On the other hand, L is large enough to show significant frequency tuning with shallower slope compared to the case of very large inductances. The disadvantage compared to higher shunt inductors however is that the flux dependent mode coupling term in the JRM energy goes as $\sin(\varphi_{\text{ext}}/4)$ (Eq. 2.65) and thus decreases away from $\varphi_{\text{ext}} = 2\pi$, where these devices have to be tuned to attain the lower frequencies. A compromise between shallow frequency slope, tunability and coupling strength would be to choose a value of β_L similar to the turquoise trace in Fig. 2.14: the tunable range is close to $\varphi_{\text{ext}} = 2\pi$ and thus around the maximal coupling strength.⁴

2.2.6.1 Shunting the JRM with Large Junctions

There are several possibilities to make shunt inductors that are of the order of the Josephson inductance $L_{J_0} \sim 100\text{pH}$ of the JRM Josephson junctions. The most straightforward option is to make wires that are comparable in width with the rest of the JRM wires, i.e. of the order of one μm . In this case, the geometric inductance of the wire is given by $\sim \mu_0 l$, where l is the length of the wire, so that the wires need to be between $50 - 100\mu\text{m}$ long. The wires then need to be meandered, in order not to make the loop size too large, which would lead to an increased sensitivity to magnetic field noise. A JPC using this approach has been successfully measured by the ENS group [28].

Another path is to fabricate short but narrow wires, making use of the kinetic inductance of the superconductor. This type of device has been shown to work in our group at Yale, however it is difficult to consistently fabricate identical narrow wires and thus to achieve the desired shunt inductances.

⁴Note that the situation is a bit more complicated: when the coupling strength is maximal, the junction phases are less likely to be driven too far up the energy well, but the devices is also less stiff.

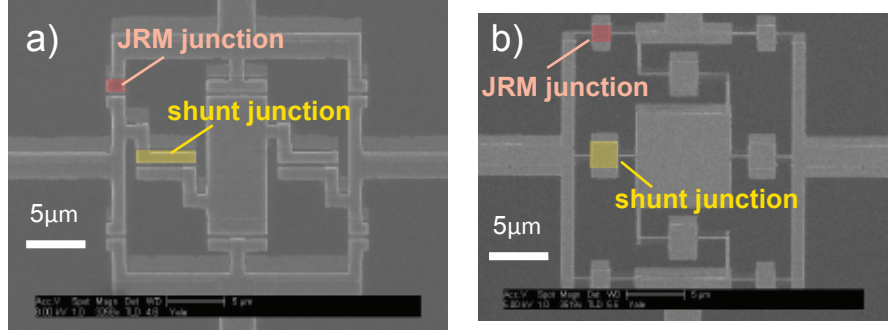


Figure 2.16: SEM image of two implementations of the JRM with eight junctions: a) Device fabricated using the Dolan bridge technique. b) Device fabricated using the bridge-free technique.

The strategy taken in this work is to fabricate additional larger Josephson junctions which shunt the JRM junctions, as shown schematically in Fig. 2.15. This method has the advantage of reliability and predictability in the fabrication of Josephson junctions with $L_{J_0} \sim 100$ pH. Two type of devices were developed and fabricated, one which made use of the Dolan bridge technique [62] and a second without suspended resist bridge, called the bridge-free technique [63]. These two type of JRMs are shown in Figs. 2.16 a) and b), respectively. The ratio of the junction areas in a) is 1:0.3 ($5\mu\text{m}^2$ to $1.5\mu\text{m}^2$), so that $2\beta_L = 0.6$, assuming the ideal case where the junction critical current scales exactly with the area⁵ and where the inductances of the connecting wires of the ring do not significantly contribute to the overall inductance. In this case the crossover as defined in Eq. 2.85 is expected at $\varphi_{\text{ext}}^{\text{crossover}} = 3.25\pi$. For the junctions in Fig. 2.16 b) the ratio of the junction areas is 1:0.43 ($5.3\mu\text{m}^2$ to $2.3\mu\text{m}^2$), so that $2\beta_L = 0.87$ and the expected crossover is at $\varphi_{\text{ext}}^{\text{crossover}} = 2.8\pi$.

Figure 2.17 shows the magnetic flux dependence of the resonance frequencies of a JPC (sample JPXs01) with shunted JRM (nominally identical to device shown in Fig. 2.16 a)). The three large lobes centered around $\Phi_{\text{ext}} = 0, \pm 4$ correspond to the state (m, m, m, m) , while the two small lobes correspond to the state $(m, -m, m, -m)$. It is apparent in this figure that 1. the degeneracy was successfully lifted by shunting the JRM junctions, as there is no hysteresis (data in sub-figure a) swept upward, in b) swept downward) and 2. that this devices is tunable in frequency over almost 1GHz on the signal port (sub figure a)). Further, the crossover appears to occur close to $\varphi_{\text{ext}} = 3\pi$, so that the expected value of $2\beta_L = 0.6$ cannot be far from the actual value.

Figure 2.18 shows the flux dependence of another JPC with shunted junctions, fabricated this

⁵This is approximately true for junctions of the sizes considered here.

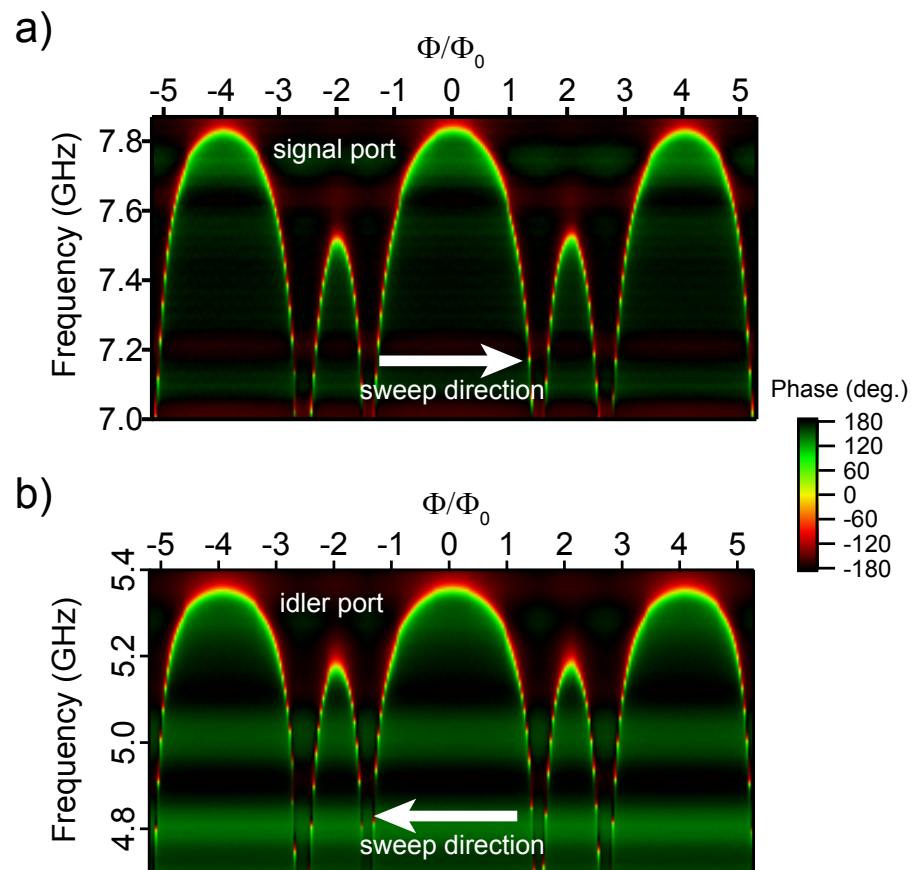


Figure 2.17: Phase response of JPC with shunted JRM for modulated magnetic flux (sample JPXs01; fabricated with Dolan bridges). No pump power is applied. a) Signal port. The yellow color indicates the location of the resonator center frequency. The flux is swept upward. b) Idler port. The flux is swept downward.

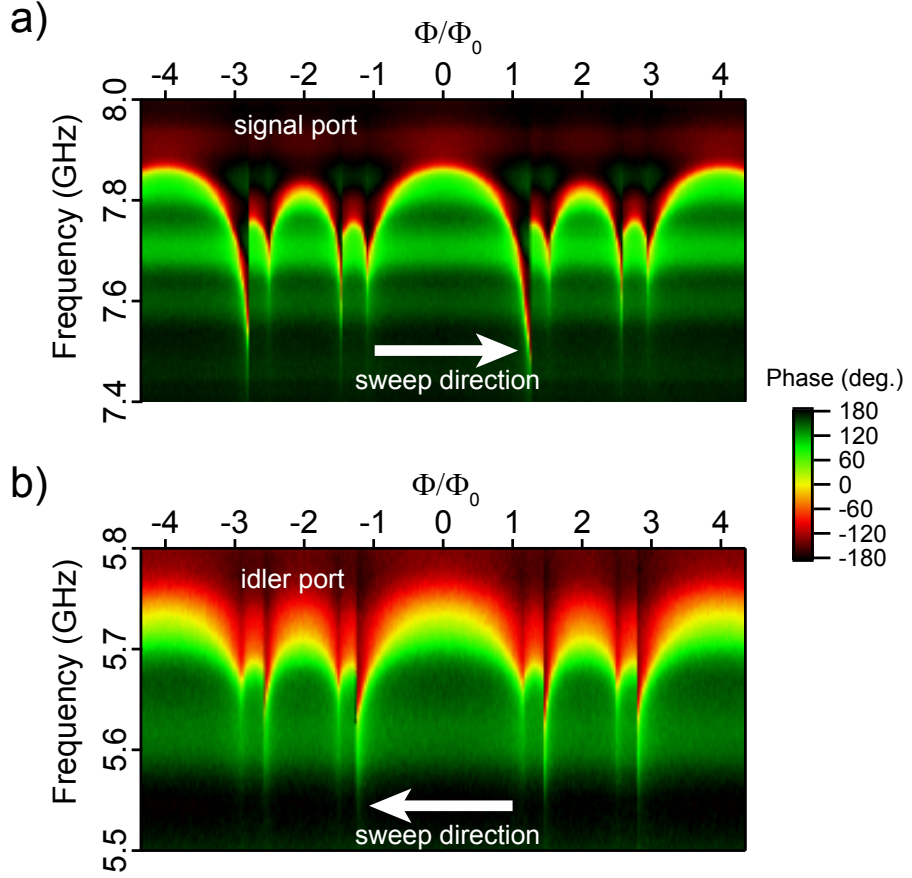


Figure 2.18: Phase response of JPC with shunted JRM for modulated magnetic flux (sample JPXs01; fabricated with bridge-free technique). No pump power is applied. a) Signal port. The yellow color indicates the location of the resonator center frequency. The flux is swept upward. b) Idler port. The flux is swept downward. An additional hysteretic state appears.

time with the bridge-free technique (sample JPXs04; nominally identical to device in Fig. 2.16 b)). This device again shows three large lobes, and the device is operated in that regime when used as an amplifier. On the signal port, the frequency tunability is around 300MHz. There are two reasons for this reduced (yet sufficient) tunability: first, the junctions have a higher critical current density than the junctions in the device of Fig. 2.17⁶, and thus the junctions overall participate more in the resonance frequency. And second, an additional state seems to appear, which is hysteretic. It is possible that this state is due to the fact that the wires connecting the junctions have non-negligible inductance, as they are only 200nm wide and 20-30nm thick. In future devices fabricated with the bridge-free technique, care should be taken to increase the wire width and especially the wire thickness.

⁶Sample JPXs04 underwent Ar-Ox cleaning before the evaporation step, JPXs01 did not.

Chapter 3

Scattering Matrix Description of Gain and Noise of Parametric Amplifiers

In this chapter, the scattering matrix description of parametric amplifiers (paramps) is presented, which allows one to explicitly calculate the gain and noise properties of these devices. The scattering matrix for the Josephson Parametric Converter (JPC), linking input and output field operators, is first derived from the Hamiltonian of three harmonic oscillators coupled through only a tri-linear term XYZ , and under the stiff pump approximation. By introducing flying oscillators and the two-mode squeezing operator, the same scattering matrix is re-derived and the noise properties of the JPC are explicitly calculated. The close link between phase-preserving and phase-sensitive paramps is established, and it is shown how phase-preserving amplifiers can be constructed from phase-sensitive amplifiers and vice versa. Lastly, the evolution of coherent states is calculated, showing that those states are a natural basis in which to describe the JPC operation.

3.1 JPC Scattering Matrix

An ideal non-degenerate parametric amplifier is composed of three LC oscillators coupled by a three-wave mixing term and described by a Hamiltonian of the form (neglecting damping and drive terms)

$$\begin{aligned}
H_0 = & \frac{\Phi_X^2}{2L_a} + \frac{\Phi_Y^2}{2L_b} + \frac{\Phi_Z^2}{2L_c} \\
& + \frac{Q_X^2}{2C_a} + \frac{Q_Y^2}{2C_b} + \frac{Q_Z^2}{2C_c} \\
& + K\Phi_X\Phi_Y\Phi_Z,
\end{aligned} \tag{3.1}$$

where $\Phi_{X,Y,Z}$ are the generalized flux variables and $Q_{X,Y,Z}$ the charge variables [69, 27]. This Hamiltonian represents three independent harmonic oscillators with frequencies $\omega_{a,b,c} = 1/\sqrt{L_{a,b,c}C_{a,b,c}}$ and characteristic impedances $Z_0^{a,b,c} = \sqrt{L_{a,b,c}/C_{a,b,c}}$, coupled to each other through the three-wave mixing coefficient K . In general, the modes are described by their (non-degenerate) resonant frequencies $\omega_{a,b,c}$ and (non-overlapping) bandwidths $\gamma_{a,b,c}$, which for the case $\omega_a < \omega_b < \omega_c$ means that $\omega_a + \gamma_a \ll \omega_b - \gamma_b$ and $\omega_b + \gamma_b \ll \omega_c - \gamma_c$. In terms of annihilation operators a , b , and c associated with each oscillator, the Hamiltonian can be written as

$$\begin{aligned}
H_0 = & \hbar\omega_a a^\dagger a + \hbar\omega_b b^\dagger b + \hbar\omega_c c^\dagger c \\
& + \hbar g_3(a + a^\dagger)(b + b^\dagger)(c + c^\dagger),
\end{aligned} \tag{3.2}$$

where the three-wave mixing interaction is now described by the coupling energy $\hbar g_3 = K\Phi_X^0\Phi_Y^0\Phi_Z^0$ and $\Phi_{X,Y,Z}^0 := \sqrt{\langle 0 | \Phi_{X,Y,Z}^2 | 0 \rangle}$ is the zero-point fluctuation of the flux.

As explained in Ch. 2, in the case of the JPC this tri-linear mixing term is realized by the Josephson Ring Modulator (JRM). As the generalized fluxes across the JRM represent only a fraction of the total generalized fluxes $\Phi_{X,Y,Z}$ described in Eq. 3.1, the participation ratios $p_{a,b,c} \approx L_{J_o}/L_{a,b,c}$ come into play. These participation ratios represent the fraction of the respective mode energy contained in the JRM. Consequently, the coupling term in the case of the JRM can be expressed as [27]

$$g_3^2 = \frac{p_a p_b p_c \omega_a \omega_b \omega_c}{E_J^{\text{eff}}/\hbar}, \tag{3.3}$$

where E_J^{eff} is the effectively available Josephson energy, proportional to E_J of the junctions.

With $\boxed{\omega_c = \omega_a + \omega_b}$ and under the rotating wave approximation (RWA) one finally arrives at

$$\boxed{H_0^{\text{RWA}} = \hbar\omega_a a^\dagger a + \hbar\omega_b b^\dagger b + \hbar\omega_c c^\dagger c + \hbar g_3 (a^\dagger b^\dagger c + abc^\dagger)}. \tag{3.4}$$

This Hamiltonian allows for a photon picture interpretation of the amplification process: the term $a^\dagger b^\dagger c$ describes the annihilation of one pump photon at ω_c that leads to the creation of a pair of signal and idler photons at ω_a and ω_b , respectively. The coherent amplification process (with non-zero signal or idler inputs) occurs for pump photon fluxes close to but below the threshold photon flux $\dot{n}_c^{\text{PO}} = \gamma_a \gamma_b \gamma_c / 4g_3^2$, which is the regime of interest in this work. Under the stiff pump approximation (see below) [27], only the term $a^\dagger b^\dagger c$ enters in the derivation of the JPC scattering matrix. The hermitian conjugate term abc^\dagger , which describes the reverse process of a pair of signal and idler photons being annihilated to create a pump photon and leads to Coherent Attenuation (CA), is the subject of Chapter 5.

By adding drive and dissipation to the Hamiltonian of Eq. 3.4, the coupled equations of motion (quantum Langevin equations) of operators a, b, c can be derived:

$$\begin{aligned}\frac{d}{dt}a(t) &= -i\omega_a a(t) - \frac{\gamma_a}{2}a(t) - ig_3 b^\dagger(t)c(t) + \sqrt{\gamma_a} \tilde{a}^{\text{in}}(t) \\ \frac{d}{dt}b(t) &= -i\omega_b b(t) - \frac{\gamma_b}{2}b(t) - ig_3 a^\dagger(t)c(t) + \sqrt{\gamma_b} \tilde{b}^{\text{in}}(t) \\ \frac{d}{dt}c(t) &= -i\omega_c c(t) - \frac{\gamma_c}{2}c(t) - ig_3 a(t)b(t) + \sqrt{\gamma_c} \tilde{c}^{\text{in}}(t),\end{aligned}\quad (3.5)$$

where $\gamma_{a,b,c}$ are the mode bandwidths and the $\tilde{a}^{\text{in}}, \tilde{b}^{\text{in}}, \tilde{c}^{\text{in}}$ are related to the input fields $a^{\text{in}}, b^{\text{in}}, c^{\text{in}}$ through $\tilde{a}^{\text{in}}(t) := (2\pi)^{-1/2} \int_0^\infty a^{\text{in}}[\omega] e^{-i\omega t} d\omega$ and similarly for $\tilde{b}^{\text{in}}, \tilde{c}^{\text{in}}$ (see Sec. 3.2.1.1 for field operator properties). When operating the JPC as an amplifier, the regime of interest is where the pump dynamics do not play a role. The incoming pump photon flux should be orders of magnitude above the incoming signal and idler photon flux while $\gamma_c \gg \gamma_{a,b}$, i.e. here of the order of ω_c , so that still only few pump photons occupy the pump resonator at any one time. This is the stiff pump approximation, in which the operator $c(t)$ can be replaced by the average value $\langle c(t) \rangle = \sqrt{\bar{n}_c} e^{-i\omega_c t - \varphi_p}$, where \bar{n}_c is the average photon number of the coherent state produced in the pump resonator. This number is assumed to be constant over time, so that the coupled equations of motion 3.5 reduce to two equations for signal and idler only. Finally, using Eq. 3.5 together with resonator input output relations $\sqrt{\gamma_a} a(t) = \tilde{a}^{\text{in}}(t) + \tilde{a}^{\text{out}}(t)$ and similarly for $b(t)$, which link the mode amplitudes $a(t), b(t)$ to the outside field operators $a^{\text{in/out}}[\omega], b^{\text{in/out}}[\omega]$, one arrives at probably the most important equation describing the JPC, the (reduced) two-port scattering matrix [25, 27]:

$$\begin{pmatrix} a^{\text{out}}[\omega_1] \\ b^{\text{out}\dagger}[\omega_2] \end{pmatrix} = \begin{pmatrix} r_{aa}[\omega_1, \omega_2] & s_{ab}[\omega_1, \omega_2] \\ s_{ba}[\omega_1, \omega_2] & r_{bb}[\omega_1, \omega_2] \end{pmatrix} \begin{pmatrix} a^{\text{in}}[\omega_1] \\ b^{\text{in}\dagger}[\omega_2] \end{pmatrix}, \quad (3.6)$$

where $\omega_{1,2}$ are linked to each other through $\boxed{\omega_1 + \omega_2 = \omega_c}$ and

$$r_{aa}[\omega_1, \omega_2] = \frac{A^*[\omega_1]B^*[\omega_2] + |\rho_0|^2}{A[\omega_1]B^*[\omega_2] - |\rho_0|^2} \quad (3.7)$$

$$r_{bb}[\omega_1, \omega_2] = \frac{A[\omega_1]B[\omega_2] + |\rho_0|^2}{A[\omega_1]B^*[\omega_2] - |\rho_0|^2} \quad (3.8)$$

$$s_{ab}[\omega_1, \omega_2] = \frac{-2i\rho_0}{A[\omega_1]B^*[\omega_2] - |\rho_0|^2} \quad (3.9)$$

$$s_{ba}[\omega_1, \omega_2] = \frac{2i\rho^*}{A[\omega_1]B^*[\omega_2] - |\rho_0|^2}, \quad (3.10)$$

with

$$A[\omega_1] = 1 - i\frac{\omega_1 - \omega_a}{\gamma_a/2} \quad (3.11)$$

$$B[\omega_1] = 1 - i\frac{\omega_2 - \omega_b}{\gamma_b/2} \quad (3.12)$$

and ρ_0 the dimensionless pump amplitude given by

$$\boxed{\rho_0 = \frac{2g_3\sqrt{\bar{n}_c}e^{-i\varphi_p}}{\sqrt{\gamma_a\gamma_b}}}. \quad (3.13)$$

For incoming and outgoing signal and idler tones at zero detuning, i.e. at $\omega_1 = \omega_a$ and $\omega_2 = \omega_b$ and $A = B = 1$, Eq. 3.6 becomes

$$\begin{pmatrix} a^{\text{out}}[\omega_1] \\ b^{\text{out}\dagger}[\omega_2] \end{pmatrix}_{\omega_1=\omega_a; \omega_2=\omega_b} = \begin{pmatrix} \sqrt{G_0} & -ie^{-i\varphi_p}\sqrt{G_0-1} \\ ie^{i\varphi_p}\sqrt{G_0-1} & \sqrt{G_0} \end{pmatrix} \begin{pmatrix} a^{\text{in}}[\omega_1] \\ b^{\text{in}\dagger}[\omega_2] \end{pmatrix}, \quad (3.14)$$

where G_0 is the power gain given by

$$\boxed{\sqrt{G_0} = \frac{1 + |\rho_0|^2}{1 - |\rho_0|^2}}. \quad (3.15)$$

Thus the gain diverges as the pump amplitude $|\rho_0| \rightarrow 1^-$, i.e. when $\bar{n}_c \rightarrow \bar{n}_c^{\text{po}} = \frac{\gamma_a\gamma_b}{4|g_3|^2}$. For

large gains $\sqrt{G_0 - 1} \approx \sqrt{G_0}$ and Eq. 3.14 predicts that the JPC essentially adds signal and idler amplitudes with power gain G_0 . When operated as a one-port amplifier, the JPC amplifies the input with power gain G_0 while adding half a photon of noise entering through the idler port and stemming from the zero point fluctuations of the incoming field $b^{\text{in}}[\omega]$.

While the frequency dependent scattering matrix of Eq. 3.6 looks rather complicated compared to the one obtained for zero detuning in Eq. 3.14, for large gains it simply predicts a Lorentzian shaped (power) gain function at frequencies close to the mode centers $\omega_{a,b}$ for both the signal and the idler port:

$$G_0(\Delta\omega) = G_0 \frac{B^2(G_0)/4}{B^2(G_0)/4 + \Delta\omega^2}, \quad (3.16)$$

where $\Delta\omega = \omega_1 - \omega_a = \omega_b - \omega_2$ and

$$B(G_0) = B_0 G_0^{-1/2} \quad (3.17)$$

is the full width at half maximum (i.e. the bandwidth) of the Lorentzian at gain G_0 , and which is determined by the pump strength through Eq. 3.15. The constant bandwidth B_0 is given by a sort of average of the signal and idler resonators γ_a, γ_b through

$$B_0 = \frac{2\gamma_a\gamma_b}{\gamma_a + \gamma_b}, \quad (3.18)$$

and it is clear from these expressions that the JPC bandwidth B is dominated by the smaller of the signal and idler resonator bandwidths, and it is thus desirable to make them equal.

Figure 3.1 summarizes how the reduced scattering matrix of Eq. 3.6 couples frequency components ω_1 and ω_2 of the signal and idler fields, respectively, which are linked by $\omega_1 + \omega_2 = \omega_c$. Figure 3.1 (a) shows the Lorentzian power gain response functions of signal and idler ports together with all relevant frequency relations and bandwidths. Figure 3.1 (b) shows graphically the frequency mixing process described by the JPC scattering matrix of Equation 3.6.

3.2 Phase-Sensitive and Phase-Preserving Amplification

Many of properties of the JPC (operated in its amplification mode) can be calculated using its reduced scattering matrix. It describes how the JPC processes classical signals and allows one to

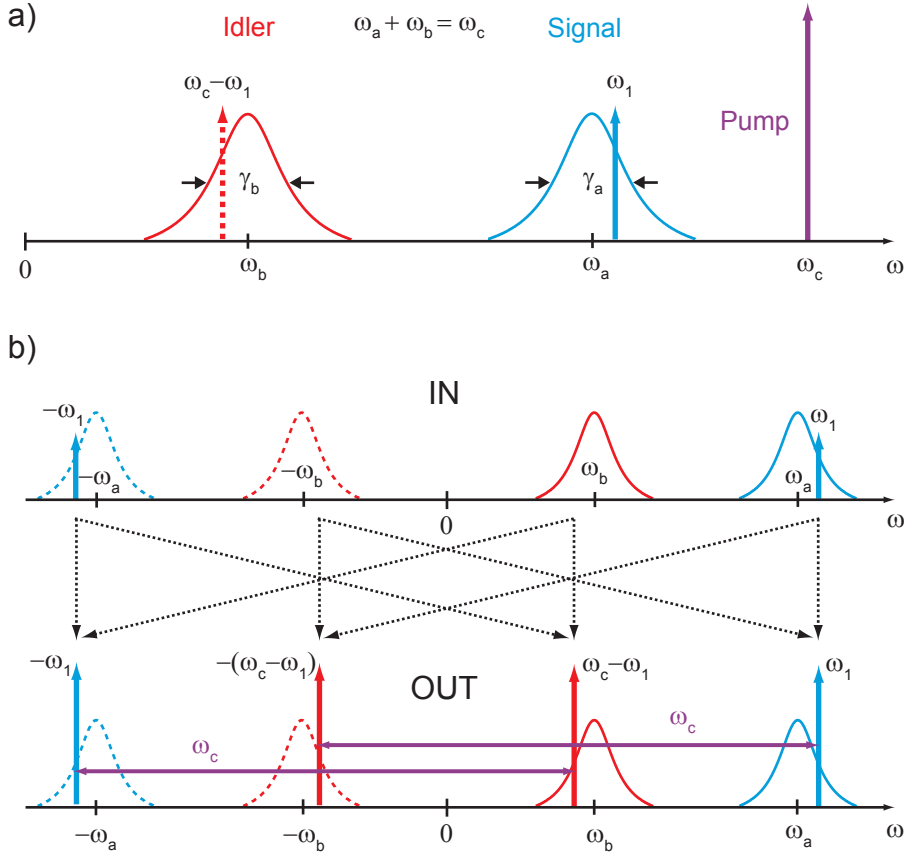


Figure 3.1: a) Schematic of JPC operation in frequency space, as could be observed with a commercial spectrum or network analyzer. The red and blue Lorentzian shapes represent the power gain response functions of the JPC, centered around the signal and idler center frequencies ω_a and ω_b respectively. The respective dynamical amplifier bandwidths are given by γ_a and γ_b . Colored arrows represent CW tone *powers*. The pump tone is applied at $\omega_c = \omega_a + \omega_b$. An applied signal tone at ω_1 within the signal bandwidth will be amplified and a further amplified copy will also appear at the idler port at $\omega_c - \omega_1$. b) Frequency mixing properties of the JPC, as calculated by scattering matrix 3.49. Vertical colored arrows represent CW tone *amplitudes* a^\dagger and a etc., corresponding to positive and negative frequency components. An applied CW tone with frequency ω_1 (top half of figure) is represented by its positive and negative frequency components at $\pm\omega_1$, and leads to amplified CW tones at frequencies ω_1 and $\omega_c - \omega_1$ (bottom half of figure), again represented by positive and negative frequency components. The dashed arrows show how the JPC mixes the different frequency components. The purple arrows show the frequency relation between signal, idler, and tones. Vertical dashed arrows correspond to amplitude gains $\sqrt{G_0}$ and diagonal to amplitude gains $\sqrt{G_0 - 1}$. Noise in the idler port (no applied tone) is mixed in to appear at the output of both the signal and idler port.

calculate statistical properties of e.g. coherent states. In particular, it makes it clear that the zero-point fluctuation on the idler port is at the origin of the JPC amplifier noise. It also makes it possible to predict the statistical properties of two-mode squeezed noise produced by the JPC [70, 71]. The scattering matrix approach further allows one to identify the relationship between a non-degenerate, phase-preserving paramp such as the JPC and a conceptually closely related device, the degenerate, phase-sensitive parametric amplifier, of which several different experimental implementations with superconducting Josephson circuits exist [20, 29, 22, 23]. Before (re-)deriving the scattering matrix using the two-mode squeezing operator $S_{ab}(\Lambda)$, it is useful to review some commutator properties of the signal and idler input annihilation operators a_{in} , b_{in} , derived from the input field operators $a^{\text{in}}[\omega]$ and $b^{\text{in}}[\omega]$, and their corresponding quadrature operators.

3.2.1 Commutation Relations

3.2.1.1 Field Operators

The equations of motion (quantum Langevin equations) of Eq. 3.5 describe the time evolution of operators $a(t)$, $b(t)$, and $c(t)$, associated with the three LC oscillators of the JPC. At $t = 0$, $a(0) = a$, $b(0) = b$, and $c(0) = c$ and these operators obey the usual harmonic oscillator commutation relations:

$$[a, a^\dagger] = 1 \quad (3.19)$$

etc. These standing wave amplitudes link incoming and outgoing field operators $a^{\text{in}}[\omega]$ ($b^{\text{in}}[\omega]$) and $a^{\text{out}}[\omega]$ ($b^{\text{in}}[\omega]$) to each other through the oscillator input-output relations

$$\sqrt{\gamma_a}a(t) = \tilde{a}^{\text{in}}(t) + \tilde{a}^{\text{out}}(t) \quad (3.20)$$

$$\sqrt{\gamma_b}b(t) = \tilde{b}^{\text{in}}(t) + \tilde{b}^{\text{out}}(t), \quad (3.21)$$

where

$$\tilde{a}^{\text{in}}(t) := \frac{1}{\sqrt{2\pi}} \int_0^\infty a^{\text{in}}[\omega] e^{-i\omega t} d\omega \quad (3.22)$$

$$\tilde{b}^{\text{in}}(t) := \frac{1}{\sqrt{2\pi}} \int_0^\infty b^{\text{in}}[\omega] e^{-i\omega t} d\omega \quad (3.23)$$

(e.g. see appendix of [27]). Further, these field operators satisfy

$$\begin{aligned} \left[a^{\text{in(out)}}[\omega], a^{\text{in(out)}}[\omega'] \right] &= \left[b^{\text{in(out)}}[\omega], b^{\text{in(out)}}[\omega'] \right] \\ &= \text{sgn}(\omega - \omega') \delta(\omega + \omega'), \end{aligned} \quad (3.24)$$

and

$$\langle \{a^{\text{in}}[\omega], a^{\text{in}}[\omega']\} \rangle = 2\mathcal{N}_a^{\text{in}}\left(\frac{\omega - \omega'}{2}\right) \delta(\omega + \omega') \quad (3.25)$$

$$\langle \{b^{\text{in}}[\omega], b^{\text{in}}[\omega']\} \rangle = 2\mathcal{N}_b^{\text{in}}\left(\frac{\omega - \omega'}{2}\right) \delta(\omega + \omega'), \quad (3.26)$$

where

$$\mathcal{N}_{a,b}^{\text{in}}(\omega) = \frac{\text{sgn}(\omega)}{2} \coth\left(\frac{\hbar\omega}{2k_B T}\right) + 2\pi\dot{n}_{a,b} [\delta(\omega - \omega_{1,2}) + \delta(\omega + \omega_{1,2})] \quad (3.27)$$

is the photon spectral density of the incoming fields, T is the temperature, and $\dot{n}_{a,b}$ is the photon flux of an applied tone at frequency $\omega_{1,2}$. Note that $a^{\text{in(out)}}[\omega]^\dagger = a^{\text{in(out)}}[-\omega]$, $b^{\text{in(out)}}[\omega]^\dagger = b^{\text{in(out)}}[-\omega]$.

3.2.1.2 Flying Oscillators

From the field operators, flying oscillator amplitudes can be defined using Shannon wavelets [72, 73]:

$$a_{\text{in(out)},n} := \frac{1}{\sqrt{\kappa}} \int_{\omega_a - \kappa/2}^{\omega_a + \kappa/2} a^{\text{in(out)}}[\omega] e^{+i\omega \frac{n}{\kappa}} d\omega \quad (3.28)$$

$$b_{\text{in(out)},n} := \frac{1}{\sqrt{\kappa}} \int_{\omega_b - \kappa/2}^{\omega_b + \kappa/2} b^{\text{in(out)}}[\omega] e^{+i\omega \frac{n}{\kappa}} d\omega, \quad (3.29)$$

(3.30)

with $\boxed{\kappa \ll \gamma_a, \gamma_b}$. Using 3.24 it is easy to show that

$$\begin{aligned} \left[a_{\text{in(out)},n}, a_{\text{in(out)},n}^\dagger \right] &= \left[b_{\text{in(out)},n}, b_{\text{in(out)},n}^\dagger \right] \\ &= \frac{1}{\kappa} \int_{-\infty}^{\infty} \int_{-\infty}^{\infty} \text{sgn}(\omega + \omega') \delta(\omega - \omega') e^{+i(\omega - \omega') \frac{n}{\kappa}} d\omega d\omega' \\ &= 1. \end{aligned} \quad (3.31)$$

In the following, the index n will be dropped to simplify the discussion. Note also that this discussion

is limited to flying oscillators defined at resonance, i.e. around ω_a and ω_b . This could be further generalized to off-resonance frequencies $\omega_a - \delta\omega$ and $\omega_b + \delta\omega$, as schematically done in Fig. 3.1.

The commutation relations of a_{in} and b_{in} are

$$[a_{\text{in}}, a_{\text{in}}^\dagger] = [b_{\text{in}}, b_{\text{in}}^\dagger] = 1 \quad (3.32)$$

$$[a_{\text{in}}^{(\dagger)}, b_{\text{in}}^{(\dagger)}] = 0. \quad (3.33)$$

The quadrature operators I and Q are defined as

$$I_{a_{\text{in}}} := \frac{a_{\text{in}} + a_{\text{in}}^\dagger}{2} \quad (3.34)$$

$$Q_{a_{\text{in}}} := \frac{a_{\text{in}} - a_{\text{in}}^\dagger}{2i} \quad (3.35)$$

$$I_{b_{\text{in}}} := \frac{b_{\text{in}} + b_{\text{in}}^\dagger}{2} \quad (3.36)$$

$$Q_{b_{\text{in}}} := \frac{b_{\text{in}} - b_{\text{in}}^\dagger}{2i}, \quad (3.37)$$

and from this follows that they obey the following commutation relations:

$$[I_{a_{\text{in}}}, Q_{a_{\text{in}}}] = [I_{b_{\text{in}}}, Q_{b_{\text{in}}}] = \frac{i}{2} \quad (3.38)$$

and

$$[I_{a_{\text{in}}}, I_{b_{\text{in}}}] = [Q_{a_{\text{in}}}, Q_{b_{\text{in}}}] = [I_{a(b)_{\text{in}}}, Q_{b(a)_{\text{in}}}] = 0. \quad (3.39)$$

Note that operators I and Q are hermitian, i.e. $I^\dagger = I$ and $Q^\dagger = Q$ and the corresponding eigenvalues are thus real. The annihilation operators a_{in} and b_{in} can be expressed in terms of I and Q as

$$a_{\text{in}} = I_{a_{\text{in}}} + iQ_{a_{\text{in}}} \quad (3.40)$$

$$b_{\text{in}} = I_{b_{\text{in}}} + iQ_{b_{\text{in}}}. \quad (3.41)$$

3.2.2 Two-Mode Squeezing Operator and JPC Scattering Matrix

The mode coupling term $g_3(a^\dagger b^\dagger c + abc^\dagger)$ in the JPC Hamiltonian (Eq. 1.7) leads to an evolution operator of the form $U_{\text{JPC}} = \exp[za^\dagger b^\dagger - h.c.]$, where $z \in \mathbb{C}$. The evolution of incoming signal and idler fields $|\Psi\rangle_{\text{in}}$ is described by $S_{a_{\text{in}} b_{\text{in}}}^\dagger(\Lambda) |\Psi\rangle_{\text{in}}$, where $S_{ab}(\Lambda)$ is the two-mode squeezing operator, defined as

$$S_{ab}(\Lambda) := \exp[\Lambda a^\dagger b^\dagger - \Lambda^* ab], \quad (3.42)$$

with $\Lambda \equiv \lambda e^{i\varphi}$, and $\lambda, \varphi \in \mathbb{R}$. Note that the phase φ is directly related to the pump phase φ_p through $\varphi = -\varphi_p + \pi/2$, whereas $\lambda = \ln(\sqrt{G_0} + \sqrt{G_0 - 1})$ is a measure of the JPC power gain G_0 . The two-mode squeezing operator is unitary:

$$S_{ab}^{-1}(\Lambda) = S_{ab}^\dagger(\Lambda) = S_{ab}(-\Lambda). \quad (3.43)$$

The Baker-Hausdorff formula

$$e^A B e^{-A} = B + [A, B] + \frac{1}{2!} [A, [A, B]] + \dots \quad (3.44)$$

together with the commutation relations of Equation 3.32 can then be used to calculate the output fields as a function of the input fields:

$$a_{\text{out}} = S_{a_{\text{in}} b_{\text{in}}}(\Lambda) a_{\text{in}} S_{a_{\text{in}} b_{\text{in}}}^\dagger(\Lambda) \quad (3.45)$$

$$= a_{\text{in}} + \frac{(-\Lambda)}{1!} b_{\text{in}}^\dagger + \frac{(-\Lambda)(-\Lambda^*)}{2!} a_{\text{in}} + \frac{(-\Lambda)(-\Lambda^*)(-\Lambda)}{3!} b_{\text{in}}^\dagger + \dots \quad (3.46)$$

$$= \left(\sum_{n=0}^{\infty} \frac{|\Lambda|^{2n}}{(2n)!} \right) a_{\text{in}} + \frac{(-\Lambda)}{|\Lambda|} \left(\sum_{n=0}^{\infty} \frac{|\Lambda|^{2n+1}}{(2n+1)!} \right) b_{\text{in}}^\dagger \quad (3.47)$$

$$= \cosh(|\Lambda|) a_{\text{in}} + \frac{(-\Lambda)}{|\Lambda|} \sinh(|\Lambda|) b_{\text{in}}^\dagger, \quad (3.48)$$

and similarly for b_{out}^\dagger , so that one finally arrives at the reduced JPC scattering matrix

$$\begin{pmatrix} a_{\text{out}} \\ b_{\text{out}}^\dagger \end{pmatrix} = \begin{pmatrix} \cosh(\lambda) & -e^{i\varphi} \sinh(\lambda) \\ -e^{-i\varphi} \sinh(\lambda) & \cosh(\lambda) \end{pmatrix} \begin{pmatrix} a_{\text{in}} \\ b_{\text{in}}^\dagger \end{pmatrix}, \quad (3.49)$$

where $\cosh(\lambda) \equiv \sqrt{G_0}$, $\sinh(\lambda) \equiv \sqrt{G_0 - 1}$ and $\lambda \equiv |\Lambda|$. Note that since $S_{a_{\text{in}} b_{\text{in}}}(\Lambda)$ is unitary, a_{out}

and b_{out} obey the same commutation relations as a_{in} and b_{in} :

$$[a_{\text{out}}, a_{\text{out}}^\dagger] = [b_{\text{out}}, b_{\text{out}}^\dagger] = 1. \quad (3.50)$$

Equation 3.49 also implies that $S_{a_{\text{in}}b_{\text{in}}}(\Lambda) \equiv S_{a_{\text{out}}b_{\text{out}}}(\Lambda)$.

Alternatively, the operation of the JPC can be described through the transformation of the quadrature operators I and Q , which can be easily calculated using the scattering matrix in Equation 3.49 together with definitions of Equations 3.34, 3.35, 3.36, 3.37:

$$I_{a_{\text{out}}} \equiv \frac{a_{\text{out}} + a_{\text{out}}^\dagger}{2} = \cosh(\lambda) I_{a_{\text{in}}} + \sinh(\lambda) I_{b'_{\text{in}}} \quad (3.51)$$

$$Q_{a_{\text{out}}} \equiv \frac{a_{\text{out}} - a_{\text{out}}^\dagger}{2i} = \cosh(\lambda) Q_{a_{\text{in}}} - \sinh(\lambda) Q_{b'_{\text{in}}} \quad (3.52)$$

$$I_{b'_{\text{out}}} \equiv \frac{b'_{\text{out}} + b'^{\dagger}_{\text{out}}}{2} = \cosh(\lambda) I_{b'_{\text{in}}} + \sinh(\lambda) I_{a_{\text{in}}} \quad (3.53)$$

$$Q_{b'_{\text{out}}} \equiv \frac{b'_{\text{out}} - b'^{\dagger}_{\text{out}}}{2i} = \cosh(\lambda) Q_{b'_{\text{in}}} - \sinh(\lambda) Q_{a_{\text{in}}}, \quad (3.54)$$

where $b'_{\text{in}} = e^{-i(\varphi+\pi)} b_{\text{in}}$, and $b'_{\text{out}} = e^{-i(\varphi+\pi)} b_{\text{out}}$ are simply the phase shifted incoming and outgoing idler wave annihilation operators. This phase shift corresponds in $I - Q$ space to a rotation by an angle $\varphi + \pi$:

$$\begin{pmatrix} I_{b'_{\text{in}(\text{out})}} \\ Q_{b'_{\text{in}(\text{out})}} \end{pmatrix} := \begin{pmatrix} \cos(\varphi + \pi) & \sin(\varphi + \pi) \\ -\sin(\varphi + \pi) & \cos(\varphi + \pi) \end{pmatrix} \begin{pmatrix} I_{b_{\text{in}(\text{out})}} \\ Q_{b_{\text{in}(\text{out})}} \end{pmatrix}. \quad (3.55)$$

This means that the effect of the pump phase on the idler field is equivalent to phase-delaying sections of loss-less transmission lines on the idler input and output ports (i.e. redefining the idler reference planes) with delay $\varphi + \pi$ and $-(\varphi + \pi)$ respectively. This justifies setting $-e^{i\varphi} \stackrel{!}{=} 1$, as done later in this chapter to simplify the discussion. Of course this makes sense only in situations when the pump phase is kept constant. Note again that the JPC preserves the commutation relations of I and Q (Equation 3.38), i.e. $[I_{a_{\text{out}}}, Q_{a_{\text{out}}}] = \frac{i}{2}$ etc.

Both the scattering matrix of Equation 3.49 and the transformation rules for the field quadratures of Equations 3.51 and 3.52 reveal how the JPC amplifies signal field amplitudes and quadratures with amplitude gain $\cosh(\lambda) \equiv \sqrt{G_0}$ in the absence of incoming idler fields. Further it becomes clear that the origin of amplifier noise is the incoming noise on the idler port which is amplified by

a factor $\sinh(\lambda) \equiv \sqrt{G_0 - 1} \approx \sqrt{G_0} \equiv \cosh(\lambda)$ for large gains.

3.2.3 One-Mode Squeezing Operator and JBA-paramp Scattering Matrix

There is a strong connection between a non-degenerate, phase-preserving paramp performing three-wave mixing operations, such as the JPC and a degenerate, phase-sensitive paramp performing four-wave mixing operations, such as the Josephson Bifurcation Amplifier (JBA) (in its paramp mode of operation). In fact, as will be shown below, a JPC can be constructed with two JBAs, and a JBA can be constructed with one JPC. It is useful to review the JBA scattering matrix, which can be calculated similarly to the JPC scattering matrix using the one-mode squeezing operator

$$S_a(\xi) := \exp\left[\frac{\xi}{2}a^\dagger a^\dagger - \frac{\xi^*}{2}aa\right], \quad (3.56)$$

with $\xi \equiv |\xi|e^{i\varphi_\xi}$,¹ where φ_ξ again is related to the pump phase φ_p , since $\varphi_\xi = -2\varphi_p + \pi/2$. The one-mode squeezing operator is also unitary:

$$S_a^{-1}(\xi) = S_a^\dagger(\xi) = S_a(-\xi). \quad (3.57)$$

Using the commutation relations $[a_{\text{in}}^\dagger a_{\text{in}}^\dagger, a_{\text{in}}] = [a_{\text{in}}^\dagger, a_{\text{in}}a_{\text{in}}]^\dagger = -2a_{\text{in}}^\dagger$ together with Equation 3.44 yields

$$a_{\text{out}} = S_{a_{\text{in}}}(\xi)a_{\text{in}}S_{a_{\text{in}}}^\dagger(\xi) \quad (3.58)$$

$$= \cosh(|\xi|)a_{\text{in}} - \frac{\xi}{|\xi|} \sinh(|\xi|)a_{\text{in}}^\dagger, \quad (3.59)$$

so that the phase-sensitive degenerate paramp (e.g.JBA) is described by

$$a_{\text{out}} = \cosh(|\xi|)a_{\text{in}} - e^{i\varphi_\xi} \sinh(|\xi|)a_{\text{in}}^\dagger, \quad (3.60)$$

and $\cosh(|\xi|) \equiv \sqrt{G_0}$ is the amplitude gain, and $\sinh(|\xi|) \equiv \sqrt{G_0 - 1}$. At first glance, Equations 3.49 and 3.60 look very similar, a closer look however reveals that the signal output field in the

¹Note that ξ is used as a parameter in the general one-mode squeezing operator, while λ is the parameter used in the two-mode squeezing operator. As will be shown below, the two-mode squeezing operation can be rewritten as two one-mode squeezing operations, with $|\xi| = |\lambda|$.

phase-sensitive amplifier depends only on the signal input field and its conjugate, and no mixing with an idler field occurs. The consequences of this relationship becomes much clearer when looking at the transformation rules for the field quadratures I and Q :

$$I_{\text{out}} \equiv \frac{a_{\text{out}} + a_{\text{out}}^\dagger}{2} = (\cosh(|\xi|) - \cos(\varphi_\xi) \sinh(|\xi|)) I_{\text{in}} - (\sin(\varphi_\xi) \sinh(|\xi|)) Q_{\text{in}} \quad (3.61)$$

$$Q_{\text{out}} \equiv \frac{a_{\text{out}} - a_{\text{out}}^\dagger}{2i} = -(\sin(\varphi_\xi) \sinh(|\xi|)) I_{\text{in}} + (\cosh(|\xi|) + \cos(\varphi_\xi) \sinh(|\xi|)) Q_{\text{in}}, \quad (3.62)$$

where $I_{\text{in}} \equiv \frac{a_{\text{in}} + a_{\text{in}}^\dagger}{2}$ and $Q_{\text{in}} \equiv \frac{a_{\text{in}} - a_{\text{in}}^\dagger}{2i}$. Again, a change in reference plane greatly simplifies the above expression, this time rotating both the input and output fields by the same phase $+\frac{\varphi_\xi}{2}$:

$$\begin{pmatrix} I'_{\text{in(out)}} \\ Q'_{\text{in(out)}} \end{pmatrix} := \begin{pmatrix} \cos(\frac{\varphi_\xi}{2}) & \sin(\frac{\varphi_\xi}{2}) \\ -\sin(\frac{\varphi_\xi}{2}) & \cos(\frac{\varphi_\xi}{2}) \end{pmatrix} \begin{pmatrix} I_{\text{in(out)}} \\ Q_{\text{in(out)}} \end{pmatrix}, \quad (3.63)$$

or equivalently

$$a'_{\text{in(out)}} := e^{-i\frac{\varphi_\xi}{2}} a_{\text{in(out)}}. \quad (3.64)$$

This finally leads to the following transformation rules for the quadrature operators:

$$I'_{\text{out}} = e^{-|\xi|} I'_{\text{in}} \quad \text{and} \quad Q'_{\text{out}} = e^{+|\xi|} Q'_{\text{in}}. \quad (3.65)$$

This means that a phase-sensitive degenerate paramp amplifies one quadrature (here Q) by a factor $e^{+|\xi|} \equiv \sqrt{G_0} + \sqrt{G_0 - 1}$, while deamplifying the conjugate quadrature (here I) by $e^{-|\xi|} \equiv \sqrt{G_0} - \sqrt{G_0 - 1}$. Thus signals with phase $+\varphi_\xi/2 + \pi/2 + n\pi$ ($n \in \mathbb{Z}$) are amplified, while signals with phase $+\varphi_\xi/2 + n\pi$ are deamplified. Of course one can formally interchange the amplified and deamplified quadratures ($I \leftrightarrow Q$) in Equations 3.65 by an appropriate redefinition of the reference plane (i.e. rotation of the incoming and outgoing fields) or by setting the pump phase to $\varphi_\xi = \pi$ in Equations 3.61,3.62.

3.2.3.1 Implementations of phase-sensitive amplifiers

Phase-sensitive parametric amplification is typically achieved with frequency degenerate amplifiers, but can also be done with non-degenerate amplifiers such as the JPC, as shown in Ch. 5. Several different implementations with Josephson devices exist, mainly differing in the frequency of the applied continuous wave (CW) pump tone. They all have in common that only one relevant resonant

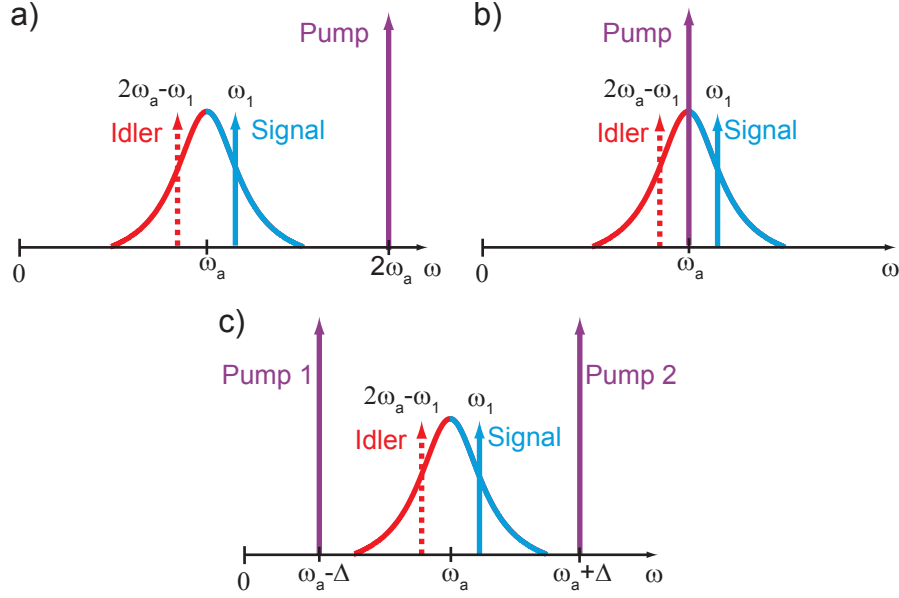


Figure 3.2: Different implementations of degenerate parametric amplifiers. a) Pump frequency at twice the amplification center frequency ω_a . This type of device corresponds to a non-linearity of the form X^2Z ($\chi^{(2)}$ -medium in optics) and has been implemented with Josephson junctions [22]. b) Pump frequency at the amplification center frequency ω_a . Several implementations of this X^4 type non-linearity ($\chi^{(3)}$ -medium in optics) have been achieved with superconducting circuits, e.g. JBA-paramp [23], Josephson junction array paramp [20], and non-linear CPW resonators [29]. c) Two pumps at equal distance and on opposite sides of center frequency ω_a . This operation can be achieved by e.g. applying two pumps in a JBA device [74].

mode exists. Figure 3.2 summarizes the operation of some degenerate paramps in frequency space.

3.2.3.2 Phase-preserving operation of a degenerate amplifier

One point of confusion that regularly arises in the discussion of frequency degenerate amplifiers is their operation as phase-preserving amplifiers, similar to the operation of the JPC. The natural mode of operation of degenerate amplifiers is as phase-sensitive amplifiers, as described by the scattering matrix of equation 3.60. In this case, the signal is centered around the band center of the amplifier, typically defined by the frequency of the CW pump tone (or half the frequency, see Figure 3.2). Should however the signal be injected asymmetrically on only one side of the amplifier band, then the device operates as a phase-preserving amplifier obeying Equation 3.49, and an idler field appears on the opposite side of the signal band. This case is schematically described in Figure 3.3.

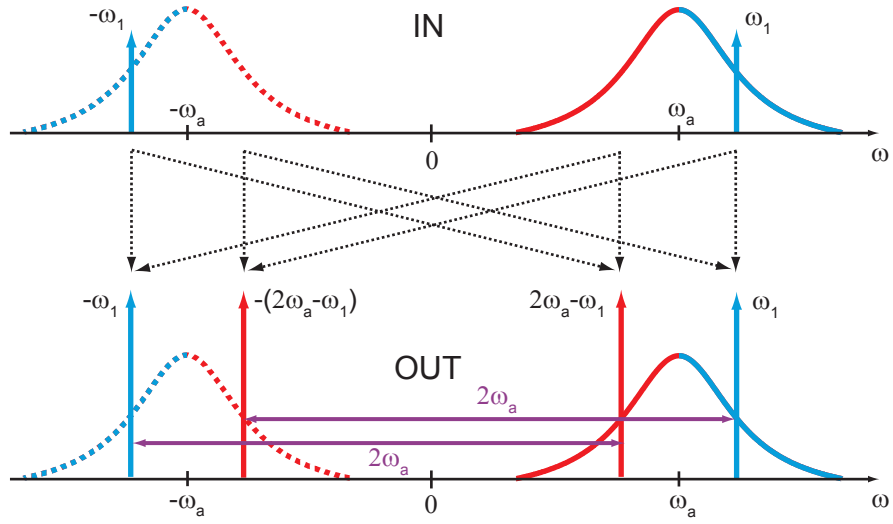


Figure 3.3: Operation of a degenerate paramp such as the JBA operated in the phase-preserving mode, represented in frequency space. Colored arrows represent wavelet *amplitudes* a^\dagger and a , when generalizing the flying oscillator definition to include frequencies off-resonance, and corresponding to positive and negative frequency components. For orientation, Lorentzian shapes representing amplifier *power* gain response functions are also shown. Blue represents the signal, red the idler. Top: CW tone with frequency ω_1 (represented by its positive and negative frequency components) injected on the signal side of the amplifier center frequency ω_a . Bottom: Output amplitudes present at both signal and idler sides. Dashed arrows show direction of frequency mixing. Purple arrow shows frequency relation between pump, signal, and idler tones.

3.2.4 Common and Differential Mode Representation: Link Between JPC and JBA-Paramp

As will be shown now, there is a close relationship between the two-mode JPC and the one-mode JBA. To simplify the discussion it will be assumed that $-e^{i\varphi}=1$ in the JPC scattering matrix, which, as mentioned above can be achieved by choosing the correct pump phase or by redefining the idler field reference planes through rotations, so that Equation 3.49 becomes

$$\begin{pmatrix} a_{\text{out}} \\ b_{\text{out}}^\dagger \end{pmatrix} = \begin{pmatrix} \cosh(\lambda) & \sinh(\lambda) \\ \sinh(\lambda) & \cosh(\lambda) \end{pmatrix} \begin{pmatrix} a_{\text{in}} \\ b_{\text{in}}^\dagger \end{pmatrix}. \quad (3.66)$$

Describing a phase-preserving parametric amplifier in terms of its signal and idler modes is naturally useful when operating it as a signal amplifier while disregarding the idler port output. This representation does not however make it easy to identify the correlations between signal and idler outputs. To reveal those correlations, common and differential modes will now be introduced:

$$a_{\Sigma_{\text{in(out)}}} := \frac{a_{\text{in(out)}} + b_{\text{in(out)}}}{\sqrt{2}} \quad (3.67)$$

$$a_{\Delta_{\text{in(out)}}} := \frac{a_{\text{in(out)}} - b_{\text{in(out)}}}{\sqrt{2}}, \quad (3.68)$$

and in terms of the quadrature operators

$$I_{\Sigma_{\text{in(out)}}} := \frac{I_{a_{\text{in(out)}}} + I_{b_{\text{in(out)}}}}{\sqrt{2}} \quad (3.69)$$

$$Q_{\Sigma_{\text{in(out)}}} := \frac{Q_{a_{\text{in(out)}}} + Q_{b_{\text{in(out)}}}}{\sqrt{2}} \quad (3.70)$$

$$I_{\Delta_{\text{in(out)}}} := \frac{I_{a_{\text{in(out)}}} - I_{b_{\text{in(out)}}}}{\sqrt{2}} \quad (3.71)$$

$$Q_{\Delta_{\text{in(out)}}} := \frac{Q_{a_{\text{in(out)}}} - Q_{b_{\text{in(out)}}}}{\sqrt{2}}. \quad (3.72)$$

These definitions assure that the usual commutation relations still hold, namely $[a_{\Sigma(\Delta)\text{in}}, a_{\Sigma(\Delta)\text{in}}^\dagger] = 1$, $[a_{\Sigma\text{in}}^{(\dagger)}, a_{\Delta\text{in}}^{(\dagger)}] = 0$, $[I_{\Sigma(\Delta)\text{in}}, Q_{\Sigma(\Delta)\text{in}}] = i/2$, $[I_{\Sigma\text{in}}, I_{\Delta\text{in}}] = 0$ etc. and similarly for Σ_{out} and Δ_{out} . This leads to the following

alternative formulation of the JPC scattering matrix :

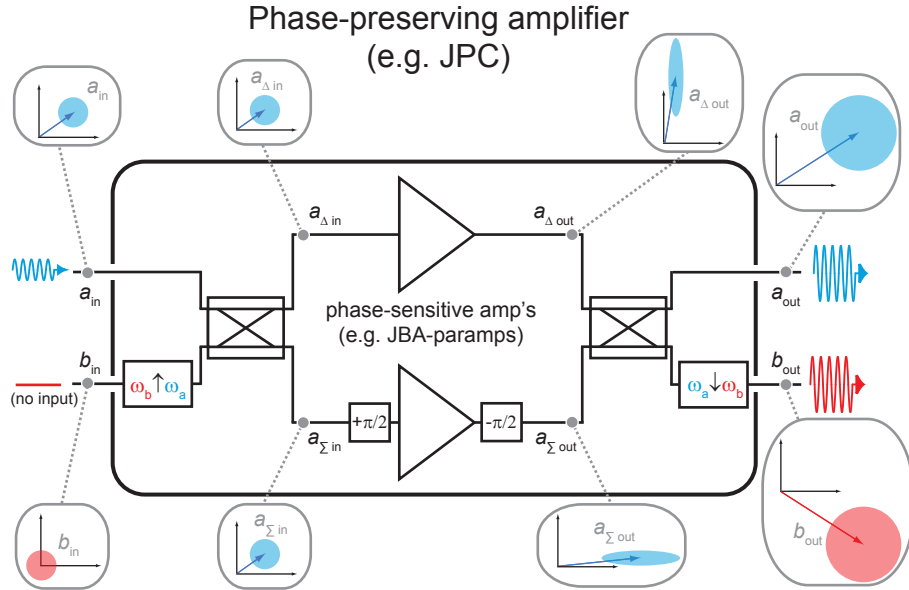


Figure 3.4: Equivalent circuit of a phase-preserving amplifier, consisting of two phase-sensitive amplifiers. To illustrate its operation, the amplification process of a wave injected on the signal port, noise on the idler port is shown. Grey boxes show the Fresnel representation of the wave as it progresses through the different stages of the circuit.

$$\begin{pmatrix} a_{\Sigma_{out}} \\ a_{\Sigma_{out}}^\dagger \\ a_{\Delta_{out}} \\ a_{\Delta_{out}}^\dagger \end{pmatrix} = \begin{pmatrix} \cosh(\lambda) & \sinh(\lambda) & 0 & 0 \\ \sinh(\lambda) & \cosh(\lambda) & 0 & 0 \\ 0 & 0 & \cosh(\lambda) & -\sinh(\lambda) \\ 0 & 0 & -\sinh(\lambda) & \cosh(\lambda) \end{pmatrix} \begin{pmatrix} a_{\Sigma_{in}} \\ a_{\Sigma_{in}}^\dagger \\ a_{\Delta_{in}} \\ a_{\Delta_{in}}^\dagger \end{pmatrix}. \quad (3.73)$$

The scattering matrix is not just block-diagonal (Equation 3.49 can easily be rearranged to have that property), but modes Σ and Δ are completely decoupled from each other. Further it becomes apparent (compare with Equation 3.60) that the JPC transforms each of these modes just like a phase-sensitive JBA:

$$I_{\Sigma_{out}} = e^{\lambda} I_{\Sigma_{in}} \quad \text{and} \quad Q_{\Sigma_{out}} = e^{-\lambda} Q_{\Sigma_{in}} \quad (3.74)$$

and

$$I_{\Delta_{out}} = e^{-\lambda} I_{\Delta_{in}} \quad \text{and} \quad Q_{\Delta_{out}} = e^{\lambda} Q_{\Delta_{in}}. \quad (3.75)$$

In principle, the Σ and Δ modes can be converted from and to modes a and b by using a 180-degree hybrid, whose scattering matrix is described by Equations 3.67, 3.68. Of course an

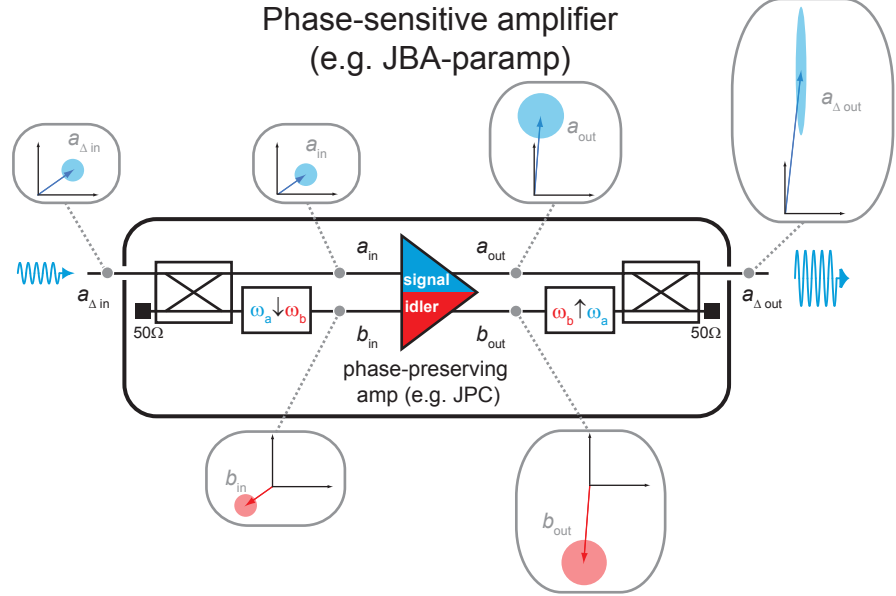


Figure 3.5: Equivalent circuit of a phase-sensitive amplifier, consisting of one phase-preserving amplifier. The phase-preserving amplifier is shown with two ports, one for the idler and one for the signal wave, generally at different frequencies $\omega_a > \omega_b$. Grey boxes show the Fresnel representation of a wave as it progresses through the different stages of the circuit.

additional step would be necessary to convert modes a and b to the same frequency. This can be achieved by employing additional JPCs in the noise-less frequency-conversion mode [75]. Figure 3.4 shows how to experimentally implement a phase-preserving JPC described by the scattering matrix of Equations 3.49 and 3.73 with two phase-sensitive JBA paramps operating at the same frequency, and both described by Equation 3.60, i.e. both fed with the same pump phase. The two phase-shifting elements before and after the bottom JBA rotate the axis of amplification from the I quadrature to the Q quadrature. Note that all elements of the circuit can be implemented with dispersive elements, so that no additional noise enters the system. In particular the frequency conversion $\omega_a \leftrightarrow \omega_b$ can be achieved noise-free with the JPC in its gain-less conversion mode of operation. The Fresnel representations of the wave as it progresses through the different stages of the circuit will be explained in more detail below. It is noteworthy that the noise ellipses in the top and bottom branches are tightly correlated.

The scattering matrix of Equation 3.73 reveals further how the JPC can be operated in phase-sensitive mode. To achieve this, a signal wave has to be split into signal and idler waves through a 180-degree hybrid, which are then injected into the JPC and then recombined using another 180-degree hybrid. Again two noise-less frequency conversion steps are necessary, and can be

implemented with JPCs in conversion mode. This operation is shown in Figure 3.5. Note that the matched termination at the input of the first hybrid will emit only quantum noise, provided the device is operated at low temperature ($k_B T \ll \hbar\omega_{a,b}$). This noise has no effect on the noise-less amplification along the amplification axis (here the Q quadrature), since it appears at both the signal and idler outputs and is ultimately canceled out through interference at the last hybrid. The axis of amplification is determined by the pump phase of the JPC.

It is also possible to cascade two JPCs, connecting the two signal ports and the two idler ports together and injecting and monitoring the fields on the signal port for instance. The first JPC then creates a copy of the signal on the idler port and the state of the fields is similar to the state right before the JPC in Fig. 3.5. There is however one important distinction to the case depicted in Fig. 3.5, as seen later in Eq. 5.9: the created idler tone is going to be phase-conjugated to the signal tone, so that all signal phase information will be lost in the two JPC process. The amplification process is still going to be phase-sensitive, but with respect to the difference of the two pump phases of the two amplification stages. It is thus important that the frequency conversion stage described in Fig. 3.5 does not phase-conjugate the signal.

In degenerate parametric amplifiers, the phase-sensitivity is sometimes measured by amplitude modulating a signal, creating two sidebands around the center frequency of the amplifier (e.g.[22]). The two created sideband tones are then phase-conjugated and the amplifier is sensitive to the relative phase between the carrier and the pump, but insensitive to the original signal phase.

3.2.5 Signal and Noise Properties: Averages and Standard Deviations

Now that quadrature transformation rules for both the JPC and the JBA have been established in Equations 3.51, 3.52, 3.65 it is time to investigate how input signals are transformed in general, by looking at their expectation values \mathbb{E} and variances \mathbb{D}^2 while assuming that no idler inputs are present (in the JPC case). To simplify the discussion, the \prime symbols will be dropped in the following and it will be assumed that the pump phases have been chosen appropriately².

Before looking at the signal output, it is useful to review some expectation values given the quadrature operator properties. The length of the Fresnel vector of a signal (input or output, since they obey the same commutation relations) can be expressed through the quadratures by

²Since only noise is presented to the idler port, the above result will hold true for any pump phase.

$$\sqrt{\langle I \rangle^2 + \langle Q \rangle^2} = \sqrt{\left\langle \frac{a + a^\dagger}{2} \right\rangle^2 + \left\langle \frac{a - a^\dagger}{2i} \right\rangle^2} \quad (3.76)$$

$$= \sqrt{\langle a \rangle \langle a^\dagger \rangle} \quad (3.77)$$

$$= |\langle a \rangle|, \quad (3.78)$$

where $\langle X \rangle \equiv \mathbb{E}(X)$ is the expectation value. As expected, the length of the Fresnel vector is given by the modulus of the average amplitude. The standard deviation of each quadrature can be expressed as³

$$\mathbb{D}^2(I) = \langle I^2 \rangle - \langle I \rangle^2 \quad (3.79)$$

$$= \left\langle \left(\frac{a + a^\dagger}{2} \right)^2 \right\rangle - \left\langle \frac{a + a^\dagger}{2} \right\rangle^2 \quad (3.80)$$

$$= \frac{1}{4} \left[\langle a^2 + a^{\dagger 2} + aa^\dagger + a^\dagger a \rangle - \langle a \rangle^2 - \langle a^\dagger \rangle^2 - 2 \langle a \rangle \langle a^\dagger \rangle \right] \quad (3.81)$$

$$= \frac{1}{4} [1 + \mathbb{D}^2(a) + \mathbb{D}^2(a^\dagger) + 2\text{Cov}(a^\dagger, a)], \quad (3.82)$$

and similarly

$$\mathbb{D}^2(Q) = \langle Q^2 \rangle - \langle Q \rangle^2 \quad (3.83)$$

$$= \frac{1}{4} [1 - \mathbb{D}^2(a) - \mathbb{D}^2(a^\dagger) + 2\text{Cov}(a^\dagger, a)], \quad (3.84)$$

where $\text{Cov}(X, Y) := \mathbb{E}((\mathbb{E}(X) - X)(\mathbb{E}(Y) - Y))$ is the covariance.

The mean-square fluctuation of a can be defined by

$$|\mathbb{D}|^2(a) := \frac{1}{2} \langle aa^\dagger + a^\dagger a \rangle - \langle a \rangle \langle a^\dagger \rangle \quad (3.85)$$

$$\equiv \mathbb{D}^2(I) + \mathbb{D}^2(Q). \quad (3.86)$$

An important case is that of coherent states, where $\mathbb{D}_{|\alpha\rangle}^2(a) = \mathbb{D}_{|\alpha\rangle}^2(a^\dagger) = \text{Cov}_{|\alpha\rangle}(a^\dagger, a) = 0$:

³ $\mathbb{D}^2(O)$ is used to designate the variance of observable O , while σ^2 is used to represent a particular value of the variance.

$$\boxed{\mathbb{D}_{|\alpha\rangle}^2(I) = \mathbb{D}_{|\alpha\rangle}^2(Q) = \frac{1}{4}, \quad \text{and} \quad |\mathbb{D}|_{|\alpha\rangle}^2(a) = \frac{1}{2}} \quad (3.87)$$

which means that the mean-square fluctuation of a corresponds to half a photon in energy.

3.2.5.1 JPC

When operating the JPC as an amplifier, typically only signal waves are injected into the device while noise is present on the idler port. An input signal represented by a Fresnel vector with quadratures $\langle I_{a_{\text{in}}} \rangle$ and $\langle Q_{a_{\text{in}}} \rangle$ and variances $\mathbb{D}^2(I_{a_{\text{in}}}) = \mathbb{D}^2(Q_{a_{\text{in}}})$ and no input on the idler port ($\langle Q_{b_{\text{in}}} \rangle = \langle Q_{b_{\text{id}}} \rangle = 0$ and $\mathbb{D}^2(I_{b_{\text{id}}}) = \mathbb{D}^2(Q_{b_{\text{id}}})$) is transformed according to the JPC scattering matrix given in Equations 3.66, 3.51, 3.52. The output quadratures then become

$$\langle I_{a_{\text{out}}} \rangle = \sqrt{G_0} \langle I_{a_{\text{in}}} \rangle + \sqrt{G_0 - 1} \langle I_{b_{\text{in}}} \rangle \quad (3.88)$$

$$\langle I_{b_{\text{in}}} \rangle = 0 \quad \sqrt{G_0} \langle I_{a_{\text{in}}} \rangle \quad (3.89)$$

$$\langle Q_{a_{\text{out}}} \rangle = \sqrt{G_0} \langle Q_{a_{\text{in}}} \rangle - \sqrt{G_0 - 1} \langle Q_{b_{\text{in}}} \rangle \quad (3.90)$$

$$\langle Q_{b_{\text{in}}} \rangle = 0 \quad \sqrt{G_0} \langle Q_{a_{\text{in}}} \rangle \quad (3.91)$$

so that for the output amplitude one finds

$$\begin{aligned} \sqrt{\langle I_{a_{\text{out}}} \rangle^2 + \langle Q_{a_{\text{out}}} \rangle^2} &= \sqrt{G_0 \langle I_{a_{\text{in}}} \rangle^2 + (G_0 - 1) \langle I_{b_{\text{in}}} \rangle^2 + G_0 \langle Q_{a_{\text{in}}} \rangle^2 + (G_0 - 1) \langle Q_{b_{\text{in}}} \rangle^2} \\ &= \sqrt{G_0 |\langle a_{\text{in}} \rangle|^2 + (G_0 - 1) |\langle b_{\text{in}} \rangle|^2} \end{aligned} \quad (3.92)$$

$$\langle I_{b_{\text{in}}} \rangle = \langle Q_{b_{\text{in}}} \rangle = 0 \quad \sqrt{G_0} \sqrt{\langle I_{a_{\text{in}}} \rangle^2 + \langle Q_{a_{\text{in}}} \rangle^2} \quad (3.93)$$

$$\Leftrightarrow |\langle a_{\text{out}} \rangle| = \sqrt{G_0} |\langle a_{\text{in}} \rangle|. \quad (3.94)$$

Equations 3.89, 3.91, 3.94 justify the appellation “phase-preserving” amplifier: both quadratures are amplified by the same factor so that the phase is preserved in the amplification process, and signals are amplified by an amplitude gain $\sqrt{G_0}$. The noise properties of the JPC can be calculated using the scattering matrix:

$$\mathbb{D}^2(I_{a_{\text{out}}}) = G_0 \mathbb{D}^2(I_{a_{\text{in}}}) + (G_0 - 1) \mathbb{D}(I_{b_{\text{in}}}) + 2\sqrt{G_0} \sqrt{G_0 - 1} \langle I_{a_{\text{in}}} I_{b_{\text{in}}} \rangle \quad (3.95)$$

$$\langle I_{a_{\text{in}}} I_{b_{\text{in}}} \rangle = 0 \quad G_0 \mathbb{D}^2(I_{a_{\text{in}}}) + (G_0 - 1) \mathbb{D}^2(I_{b_{\text{in}}}), \quad (3.96)$$

and

$$\mathbb{D}^2(Q_{a_{\text{out}}}) = G_0 \mathbb{D}^2(Q_{a_{\text{in}}}) + (G_0 - 1) \mathbb{D}^2(Q_{b_{\text{in}}}) - 2\sqrt{G_0} \sqrt{G_0 - 1} \langle Q_{a_{\text{in}}} Q_{b_{\text{in}}} \rangle \quad (3.97)$$

$$\langle Q_{a_{\text{in}}} Q_{b_{\text{in}}} \rangle = 0 \quad G_0 \mathbb{D}^2(Q_{a_{\text{in}}}) + (G_0 - 1) \mathbb{D}^2(Q_{b_{\text{in}}}), \quad (3.98)$$

where the fact that $I_{a_{\text{in}}}$, $I_{b_{\text{in}}}$ ($Q_{a_{\text{in}}}$, $Q_{b_{\text{in}}}$) commute and are independent has been used. For large gains ($G_0 \gg 1$) and only quantum noise on the idler port (see Equation 3.87) one arrives at the important result:

$$\mathbb{D}^2(I_{a_{\text{out}}}) = \mathbb{D}^2(Q_{a_{\text{out}}}) = G_0 \left(\sigma_{I,Q}^2 + \frac{1}{4} \right) \quad \text{and} \quad |\mathbb{D}|^2(a_{\text{out}}) = G_0 \left(\sigma_a^2 + \frac{1}{2} \right), \quad (3.99)$$

where the signal input noise is assumed to be isotropic $\mathbb{D}^2(I_{a_{\text{in}}}) = \mathbb{D}^2(Q_{a_{\text{in}}}) =: \sigma_{I,Q}^2$ and $\sigma_a^2 := |\mathbb{D}|^2(a_{\text{in}}) = 2\sigma_{I,Q}^2$ ⁴. The added noise of the JPC thus corresponds to only half a photon, which is the minimum of added amplifier noise for a linear phase-preserving amplifier [5]. The JPC minimally degrades the intensity signal-to-noise ratio (SNR) of input signals from $|\langle a_{\text{in}} \rangle|^2 / \sigma_a^2$ to $|\langle a_{\text{in}} \rangle|^2 / (\sigma_a^2 + \frac{1}{2})$. Figure 3.6 (top) shows this behavior graphically.

3.2.5.2 JBA-Paramp

The calculation of signal and noise properties of the output of a phase-sensitive paramp is particularly simple, using Equations 3.65. Again, it will be assumed (for legibility and without loss of generality) that the input and output fields are defined such that the ℓ -symbols in Equations 3.65 can be dropped (equivalently, φ_ξ can be set to zero in Equations 3.61, 3.62). Then an input field defined by $\langle I_{\text{in}} \rangle$ and $\langle Q_{\text{in}} \rangle$ and variances $\mathbb{D}^2(I_{\text{in}}) = \mathbb{D}^2(Q_{\text{in}}) =: \sigma_{I,Q}^2$ leads to output field quadratures

⁴More precisely, the error ellipse is circular, i.e. $\mathbb{D}^2(a_{\text{in}}) = 0$ [5].

$$\langle I_{\text{out}} \rangle = e^{-|\xi|} \langle I_{\text{in}} \rangle \quad (3.100)$$

$$\langle Q_{\text{out}} \rangle = e^{+|\xi|} \langle Q_{\text{in}} \rangle. \quad (3.101)$$

Thus the field is simply amplified by a factor $e^{+|\xi|}$ in the Q quadrature while deamplified by a factor $e^{-|\xi|}$ in the I quadrature. It is clear that this amplifier is strongly phase-dependent, and for large gains ($e^{+|\xi|} \gg 1$) all phase information is nearly erased. The noise properties of these devices are also easily calculated:

$$\mathbb{D}^2(I_{\text{out}}) = e^{-2|\xi|} \mathbb{D}^2(I_{\text{in}}) \quad (3.102)$$

$$= e^{-2|\xi|} \sigma_{I,Q}^2 \quad (3.103)$$

$$\mathbb{D}^2(Q_{\text{out}}) = e^{+2|\xi|} \mathbb{D}^2(Q_{\text{in}}) \quad (3.104)$$

$$= e^{+2|\xi|} \sigma_{I,Q}^2. \quad (3.105)$$

Noise (variance) in the I quadrature is squeezed by the same factor $e^{+2|\xi|}$ as it is amplified in the Q quadrature. The SNR of the quadratures remains unchanged, since the output intensity SNR of the quadratures stays the same as the input SNR: $\langle I_{\text{out}} \rangle^2 / \mathbb{D}^2(I_{\text{out}}) = \langle I_{\text{in}} \rangle^2 / \sigma_{I,Q}^2$ and $\langle Q_{\text{out}} \rangle^2 / \mathbb{D}^2(Q_{\text{out}}) = \langle Q_{\text{in}} \rangle^2 / \sigma_{I,Q}^2$. Figure 3.6 (bottom) graphically shows this phase-sensitive amplification process.

3.2.6 Evolution of Coherent States

In the following, the evolution of coherent states $U_{\text{JPC}} |\alpha, \beta\rangle_{\text{in}}$ will be studied explicitly, where $|\alpha, \beta\rangle_{\text{in}}$ describes coherent states α and β in the incoming signal and idler flying oscillator modes described above. The resulting state is described here in the same Hilbert space as the initial state, namely in that of the incoming flying oscillators.

Using the displacement operator

$$D_{a_{\text{in}}}(\alpha) \equiv e^{\alpha a_{\text{in}}^\dagger - \alpha^* a_{\text{in}}} \stackrel{\text{Eq. 3.44}}{=} e^{\alpha a_{\text{in}}^\dagger} e^{-\alpha^* a_{\text{in}}} e^{-\frac{|\alpha|^2}{2}}, \quad (3.106)$$

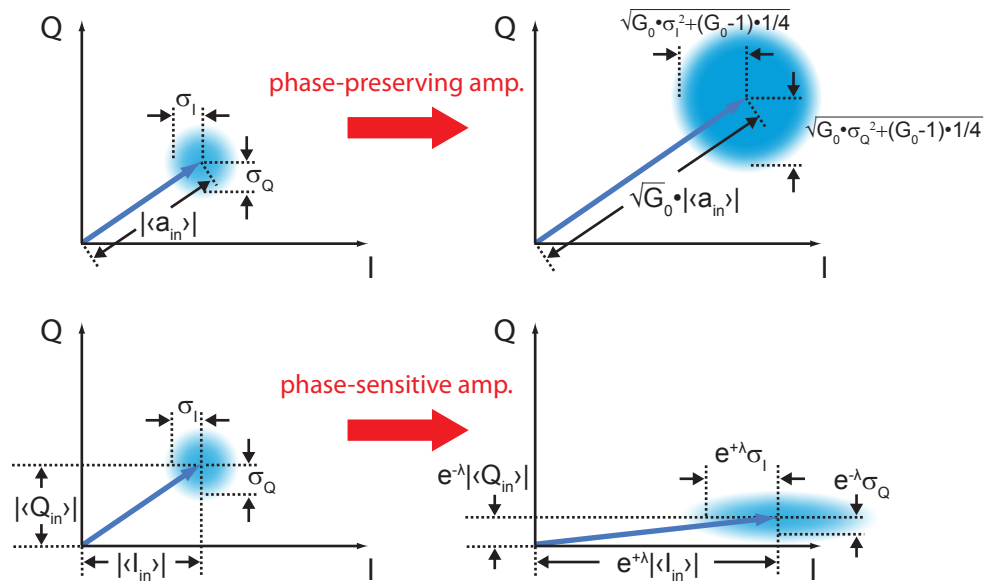


Figure 3.6: Fresnel vector representation of quasi-coherent signals and their transformation through quantum-limited paramps. Top: The phase-preserving operation of a quantum-limited paramp such as the JPC will amplify both field quadratures I and Q equally, so that the output phase is the same as the input phase. The added noise corresponds to half a photon at high gains when referred back to the input. Bottom: The phase-sensitive operation of a quantum-limited paramp amplifies one quadrature (here I) while deamplified the other quadrature (here Q). The SNR of either quadrature remains unaffected by the amplification process.

and similarly for b_{out} , the state of the outgoing signal and idler modes can be written as ⁵

$$U_{\text{JPC}} |\alpha, \beta\rangle_{\text{in}} = S_{ab}^\dagger(\Lambda) |\alpha, \beta\rangle_{\text{in}} \quad (3.107)$$

$$= S_{ab}^\dagger(\Lambda) D_{a_{\text{in}}}(\alpha) D_{b_{\text{in}}}(\beta) |0, 0\rangle_{\text{in}} \quad (3.108)$$

$$= \underbrace{S_{ab}^\dagger(\Lambda) D_{a_{\text{in}}}(\alpha)}_{S_{ab}^\dagger(\Lambda) D_{b_{\text{in}}}(\beta) S_{ab}(\Lambda)} \underbrace{S_{ab}^\dagger(\Lambda) D_{b_{\text{in}}}(\beta) S_{ab}(\Lambda)}_{S_{ab}^\dagger(\Lambda) |0, 0\rangle_{\text{in}}} \quad (3.109)$$

and the first two terms are just transformations of the displacement operators, using the inverse scattering matrix of Eq. 3.49:

$$S_{ab}^\dagger(\Lambda) D_{a_{\text{in}}}(\alpha) S_{ab}(\Lambda) = e^{\alpha S_{ab}^\dagger(\Lambda) a_{\text{in}}^\dagger S_{ab}(\Lambda) - \alpha^* S_{ab}^\dagger(\Lambda) a_{\text{in}} S_{ab}(\Lambda)} \quad (3.110)$$

$$\stackrel{\text{Eq. 3.49}}{=} e^{\alpha \cosh(\lambda) a_{\text{in}}^\dagger - \alpha^* \cosh(\lambda) a_{\text{in}}} \quad (3.111)$$

$$e^{-\alpha^* e^{i\varphi} \sinh(\lambda) b_{\text{in}}^\dagger + \alpha e^{-i\varphi} \sinh(\lambda) b_{\text{in}}}$$

$$= D_{a_{\text{in}}}(\alpha \cosh(\lambda)) D_{b_{\text{in}}}(-\alpha^* e^{i\varphi} \sinh(\lambda)) \quad (3.112)$$

where $\Lambda \equiv \lambda e^{i\varphi}$. This is exactly the result one would find using the scattering matrix for a classical field α in the signal port. Making use of the fact that two consecutive displacements can be written as

$$D_{a_{\text{in}}}(\alpha) D_{a_{\text{in}}}(\alpha') = e^{i\text{Im}[\alpha \alpha'^*]} D_{a_{\text{in}}}(\alpha + \alpha'), \quad (3.113)$$

the first two terms in Eq. 3.109 become

$$\begin{aligned} S_{ab}^\dagger(\Lambda) D_{a_{\text{in}}}(\alpha) D_{b_{\text{in}}}(\beta) S_{ab}(\Lambda) &= S_{ab}^\dagger(\Lambda) D_{a_{\Sigma_{\text{in}}}}\left(\frac{\alpha + \beta}{\sqrt{2}}\right) D_{a_{\Delta_{\text{in}}}}\left(\frac{\alpha - \beta}{\sqrt{2}}\right) S_{ab}(\Lambda) \quad (3.114) \\ &= D_{a_{\text{in}}}(\alpha \cosh(\lambda) - \beta^* e^{i\varphi} \sinh(\lambda)) \\ &\quad \otimes D_{b_{\text{in}}}(\beta \cosh(\lambda) - \alpha^* e^{i\varphi} \sinh(\lambda)). \end{aligned}$$

Again, the JPC scattering matrix reappears. Note that the phase factors of Eq. 3.113 exactly cancel. So finally, the evolution of coherent states can be written as

⁵The \dagger in the two-mode squeezing operator follows from the choice of definition 3.45.

$$\begin{aligned}
U_{\text{JPC}} |\alpha, \beta\rangle_{\text{in}} &= D_{a_{\text{in}}} (\alpha \cosh(\lambda) - \beta^* e^{i\varphi} \sinh(\lambda)) \\
&\otimes D_{b_{\text{in}}} (\beta \cosh(\lambda) - \alpha^* e^{i\varphi} \sinh(\lambda)) \\
&\otimes S_{ab}^\dagger (\Lambda) |0, 0\rangle_{\text{in}}.
\end{aligned} \tag{3.115}$$

This result is quite remarkable and shows that coherent states are the natural basis in which to describe the JPC operation. Coherent states *almost* transform as predicted by the (semi-)classical scattering matrix of Eq. 3.49: the displacement operators transform according to the scattering matrix, while additionally the vacuum state undergoes two-mode squeezing. Note that the case where the signal and idler input states are the vacuum state is sometimes also called spontaneous parametric down-conversion [76] or parametric fluorescence. Two-mode squeezing of the vacuum state with the JPC was experimentally observed in [70, 71].

Before looking at a more specific case, consider the change of basis from a, b to Σ, Δ as in Eqs. 3.67, 3.68:

$$D_{a_{\text{in}}} (\alpha) D_{b_{\text{in}}} (\beta) = D_{a_{\Sigma_{\text{in}}}} \left(\frac{\alpha + \beta}{\sqrt{2}} \right) D_{a_{\Delta_{\text{in}}}} \left(\frac{\alpha - \beta}{\sqrt{2}} \right). \tag{3.116}$$

Further, the two-mode squeezing operator can be decomposed into two one-mode squeezing operators:

$$S_{ab} (\Lambda) = e^{\Lambda a_{\text{in}}^\dagger b_{\text{in}}^\dagger - \Lambda^* a_{\text{in}} b_{\text{in}}} \tag{3.117}$$

$$= e^{\frac{\Lambda}{2} a_{\Sigma_{\text{in}}}^\dagger a_{\Sigma_{\text{in}}} - \frac{\Lambda^*}{2} a_{\Sigma_{\text{in}}} a_{\Sigma_{\text{in}}}} \tag{3.118}$$

$$\otimes e^{\frac{-\Lambda}{2} a_{\Delta_{\text{in}}}^\dagger a_{\Delta_{\text{in}}} - \frac{-\Lambda^*}{2} a_{\Delta_{\text{in}}} a_{\Delta_{\text{in}}}} \tag{3.119}$$

$$= S_\Sigma (\Lambda) S_\Delta (-\Lambda), \tag{3.120}$$

where $S_{\Sigma(\Delta)} (\xi) := e^{\frac{\xi}{2} a_{\Sigma(\Delta)}^\dagger a_{\Sigma(\Delta)} - \frac{\xi^*}{2} a_{\Sigma(\Delta)} a_{\Sigma(\Delta)}}_{\text{in}}$ is the one-mode squeezing operator. Then

$$S_{ab}^\dagger (\Lambda) D_{a_{\text{in}}} (\alpha) S_{ab} (\Lambda) = D_{a_{\Sigma_{\text{in}}}} \left(\frac{\alpha \cosh(\lambda) - \alpha^* e^{i\varphi} \sinh(\lambda)}{\sqrt{2}} \right) \tag{3.121}$$

$$\otimes D_{a_{\Delta_{\text{in}}}} \left(\frac{\alpha \cosh(\lambda) + \alpha^* e^{i\varphi} \sinh(\lambda)}{\sqrt{2}} \right), \tag{3.122}$$

and

$$S_{ab}^\dagger(\Lambda) D_{a_{\text{in}}}(\alpha) D_{b_{\text{in}}}(\beta) S_{ab}(\Lambda) = D_{\Sigma_{\text{in}}} \left(\frac{\alpha + \beta}{\sqrt{2}} \cosh(\lambda) - \frac{\alpha^* + \beta^*}{\sqrt{2}} e^{i\varphi} \sinh(\lambda) \right) \quad (3.123)$$

$$\otimes D_{\Delta_{\text{in}}} \left(\frac{\alpha - \beta}{\sqrt{2}} \cosh(\lambda) - \frac{\alpha^* - \beta^*}{\sqrt{2}} e^{i\varphi} \sinh(\lambda) \right). \quad (3.124)$$

Finally the result of Eq. 3.115 can be expressed as

$$U_{\text{JPC}} |\alpha, \beta\rangle_{\text{in}} = D_{\Sigma_{\text{in}}} \left(\frac{\alpha + \beta}{\sqrt{2}} \cosh(\lambda) - \frac{\alpha^* + \beta^*}{\sqrt{2}} e^{i\varphi} \sinh(\lambda) \right) \quad (3.125)$$

$$\otimes D_{\Delta_{\text{in}}} \left(\frac{\alpha - \beta}{\sqrt{2}} \cosh(\lambda) - \frac{\alpha^* - \beta^*}{\sqrt{2}} e^{i\varphi} \sinh(\lambda) \right)$$

$$\otimes S_\Sigma^\dagger(\Lambda) S_\Delta^\dagger(-\Lambda) |0, 0\rangle_{\text{in}}.$$

Again, this is the result expected from the (semi-)classical scattering matrix in Eq. 3.73, with the addition of the one-mode squeezing of both signal and idler vacuum states.

3.2.6.1 Coherent Attenuation

The case of balanced input coherent states ($\alpha = |\alpha|e^{-i\varphi_s}$, $\beta = |\alpha|e^{-i\varphi_i}$) can easily be analyzed using Eq. 3.115:

$$U_{\text{JPC}} \left| |\alpha|e^{-i\varphi_s}, |\alpha|e^{-i\varphi_i} \right\rangle_{\text{in}} = D_{a_{\text{in}}} \left(|\alpha|e^{-i\varphi_s} \left(\cosh(\lambda) - e^{i(\varphi_s + \varphi_i + \varphi)} \sinh(\lambda) \right) \right) \quad (3.126)$$

$$\otimes D_{b_{\text{in}}} \left(|\alpha|e^{-i\varphi_i} \left(\cosh(\lambda) - e^{i(\varphi_s + \varphi_i + \varphi)} \sinh(\lambda) \right) \right)$$

$$\otimes S_{ab}^\dagger(\Lambda) |0, 0\rangle_{\text{in}},$$

which, in terms of the displacement operators, is the same result found in Eq. 5.9:

$$\begin{aligned}
U_{\text{JPC}} \left| |\alpha| e^{-i\varphi_S}, |\alpha| e^{-i\varphi_I} \right\rangle_{\text{in}} &= \\
D_{a_{\text{in}}} \left(|\alpha| e^{-i(\varphi_S + \gamma)} \sqrt{e^{2\lambda} \sin^2 \left(\frac{\varphi_S + \varphi_I + \varphi}{2} \right) + e^{-2\lambda} \cos^2 \left(\frac{\varphi_S + \varphi_I + \varphi}{2} \right)} \right) \\
\otimes D_{b_{\text{in}}} \left(|\alpha| e^{-i(\varphi_I + \gamma)} \sqrt{e^{2\lambda} \sin^2 \left(\frac{\varphi_S + \varphi_I + \varphi}{2} \right) + e^{-2\lambda} \cos^2 \left(\frac{\varphi_S + \varphi_I + \varphi}{2} \right)} \right) \\
\otimes S_{ab}^\dagger (\Lambda) |0, 0\rangle_{\text{in}},
\end{aligned} \tag{3.127}$$

with $\varphi \equiv -\varphi_p + \pi/2$, and γ being the phase of the complex number $\cosh(\lambda) - e^{i(\varphi_S + \varphi_I + \varphi)} \sinh(\lambda)$ ($\lambda \in \mathbb{R}^+$). Thus for nonlinear phases $\varphi_S + \varphi_I + \varphi = 2\pi n$, $n \in \mathbb{Z}$, the output state for CA is

$$U_{\text{JPC}} \left| |\alpha| e^{-i\varphi_S}, |\alpha| e^{-i\varphi_I} \right\rangle_{\text{in}} \xrightarrow{\text{coh. atten.}} D_{a_{\text{in}}} (\alpha e^{-\lambda}) D_{b_{\text{in}}} (\beta e^{-\lambda}) S_{ab}^\dagger (\Lambda) |0, 0\rangle_{\text{in}}, \tag{3.128}$$

while for nonlinear phases $\varphi_S + \varphi_I + \varphi = (2n + 1)\pi$ the output state for coherent *amplification* is

$$U_{\text{JPC}} \left| |\alpha| e^{-i\varphi_S}, |\alpha| e^{-i\varphi_I} \right\rangle_{\text{in}} \xrightarrow{\text{coh. ampl.}} D_{a_{\text{in}}} (\alpha e^{+\lambda}) D_{b_{\text{in}}} (\beta e^{+\lambda}) S_{ab}^\dagger (\Lambda) |0, 0\rangle_{\text{in}}. \tag{3.129}$$

Equation 3.128 shows in particular that at the CA point and for large gains ($G_0, \lambda \rightarrow \infty$) (and still in the stiff pump approximation) the JPC puts out only two-mode squeezed vacuum noise, just as in the case when no tones are presented at the input ports [70, 71]. In terms of e.g. the signal port only, this state looks just like amplified vacuum noise, where an additional half photon in noise energy is added by the idler port (see Eq. 3.99).

Chapter 4

Operation of Amplifier, Experimental Results

In this chapter, further experimental results of Josephson Parametric Converter (JPC) samples not covered in Ch. 1 are presented. An overview of notable measured JPC samples with their most relevant parameters is given first, and the measurement of important circuit properties is explained, which were used throughout this work to characterize both the JPC microwave circuit properties and amplifier performance. The following sections describe how the amplifier performance depends on the pump parameters - frequency and power - which are used to set the gain and the exact center frequency. Lastly, the measured saturation power dependence of the working point in a shunted Josephson Ring Modulator (JRM) device is presented, showing that the exact working point significantly changes the amount of photons the JPC can handle.

4.1 Measured Devices

Many samples were fabricated and measured over the course of this thesis work. Table 4.1 summarizes some important amplifier properties of notable samples. For fabrication and design details see Table 6.1. As explained in Ch. 6, several changes to the microstrip design were made throughout this work. All devices have in common that the microstrip lines are of $300\text{ }\mu\text{m}$ width, and made of aluminum on silicon. Devices JPX01 through JPX21 were fabricated on a silicon wafer of $300\text{ }\mu\text{m}$ thickness, and with holes in the microstrip lines (see Sec. 6.1.1.1). Samples were glued to

device	JPX09	JPX14	JPX16	JPX22	JPX26	JPX30	JPXs01	JPXs04
$f_0^{\text{S/I}}(\text{GHz})$	8.32/6.63	8.12/6.45	8.18/6.22	7.63/5.4	7.90/5.37	7.26/5.3	7.4-7.8/5.2-5.3	7.7-7.8/5.7
$Q^{\text{S/I}}$	67/63	73/66	140/100	290/280	350/256	200/150	240/220	140/100
$\frac{\gamma_{\text{S/I}}}{2\pi}(\text{MHz})$	124/105	111/98	58/62	26/19	22/21	36/35	$\sim 38/\sim 24$	$\sim 55/\sim 57$
$p_L^{\text{S/I}}(\Phi_0/2)$	5%/4%	4%/3%	2%/3%	4%/3%	6%/4%	7%/6%	$\beta_L^{\text{S/I}} = 0.54/0.64$ $\frac{L_J}{L_q^{\text{S/I}}} = 0.12/0.07$ $\frac{L_J}{L_q^{\text{S/I}}} = 0.05/0.04$ $p_L^{\text{S/I}} = 7 - 15\% / 5 - 12\%$	$\beta_L^{\text{S/I}} = 0.71/0.46$ $p_L^{\text{S/I}} = 4 - 5\% / 3\%$
$p_L^{\text{S}} p_L^{\text{I}} Q^{\text{S}} Q^{\text{I}}$	8	6	8	97	215	126	185-950	17-21
gap ^{S/I} (μm)	13/13	12/14	12/13	12/13	12/13	6/6	12/13	12/3
meas. $C_{\text{in}}^{\text{S/I}}$ (fF)	-	-	-	34/34	30/36	43/48	37/40	34/55
sim. $C_{\text{in}}^{\text{S/I}}$ (fF)	-	-	-	39/37	39/37	46/46	39/37	39/55
meas. G_0^{max} (dB)	19	21	25	> 40	> 40	> 30	~ 30	> 30

Table 4.1: List of notable JPC samples with relevant measured parameters. Meaning of symbols is given in Sec. 4.2.

the sample box using poly methyl methacrylate (PMMA) or GE varnish (Lake Shore VGE-7031 varnish). The characteristic impedance of the resulting transmission lines is then expected to be close to 45Ω [61]. Devices JPX22 through JPX30 and JPXs01 through JPXs04 were fabricated on $250 \mu\text{m}$ thick silicon, and without holes in the resonators. silver was deposited on the wafer back side and samples were attached to the sample box using silver paste. The expected transmission line characteristic impedance is then around 41Ω [61].

Samples had typical signal frequencies of $7 - 8 \text{ GHz}$ and idler frequencies of $5 - 6 \text{ GHz}$. Linear bandwidths were typically between 20 and 100 MHz , while participation ratios were in the few % range. The newest device generation (JPX22 and up) routinely achieved gains of 30 dB and above.

4.2 Circuit Characterization

4.2.1 Quality Factor

The signal and idler mode resonance frequencies and quality factors are determined through simple reflection measurements using a vector network analyzer (VNA), as shown in Fig. 4.1. Since there is no amplitude response (the resonators are in the overcoupled regime), all information is contained in the phase response, and the phase undergoes a 360° phase shift when crossing the resonance. The resonance frequency is given by the zero crossing, while the bandwidth is approximately given by the $\pm 90^\circ$. These values can also be obtained by fitting the data to the phase of the reflection coefficient of an LC resonator measured with a 50Ω transmission line, as shown in the figure.

One of the reasons to evaporate silver on the substrate back was to ensure a constant distance

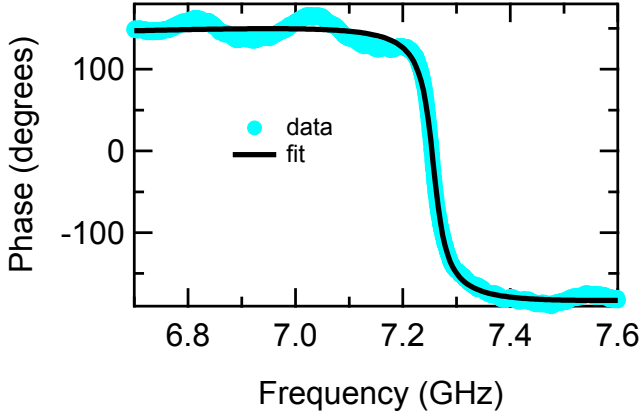


Figure 4.1: Measurement of JPC signal mode center frequency and quality factor (sample JPX30).

to the ground plane, which in earlier device generations (JPX01 through JPX21) was defined by the sample box. Microstrip resonator properties depend on the effective substrate dielectric and the distance to the ground plane, so this point proved crucial in the reproducibility of resonator frequencies and quality factors. Measurement of devices without junctions showed a variability in the measured resonance frequency between nominally identical devices of less than 5 MHz and a measured variability between cooldowns of less than 1 MHz. Typically the quality factor can be determined with a precision of about 10 %, due to the fact that the resonances are broad and the line impedance not being exactly constant over a broad frequency range (see wiggles in figure). The quality factor of nominally identical resonator devices was measured to be the same within about 30 %.

4.2.1.1 Coupling Capacitor

As explained in Appendix A, the quality factor of the overcoupled transmission line resonators used in this work is entirely determined by the coupling capacitors and depends inversely on the coupling capacitance squared. For a transmission line with characteristic impedance of Z_0 and symmetrically coupled to loads of impedance R_L with identical coupling capacitors C_{in} on both ports, the coupling Q for typical parameters of this work is given by

$$Q_{\text{ext}} = \frac{\pi}{4} \frac{1}{Z_0} \cdot \frac{R_L}{\omega_0^2 C_{\text{in}}^2 R_L^2}, \quad (4.1)$$

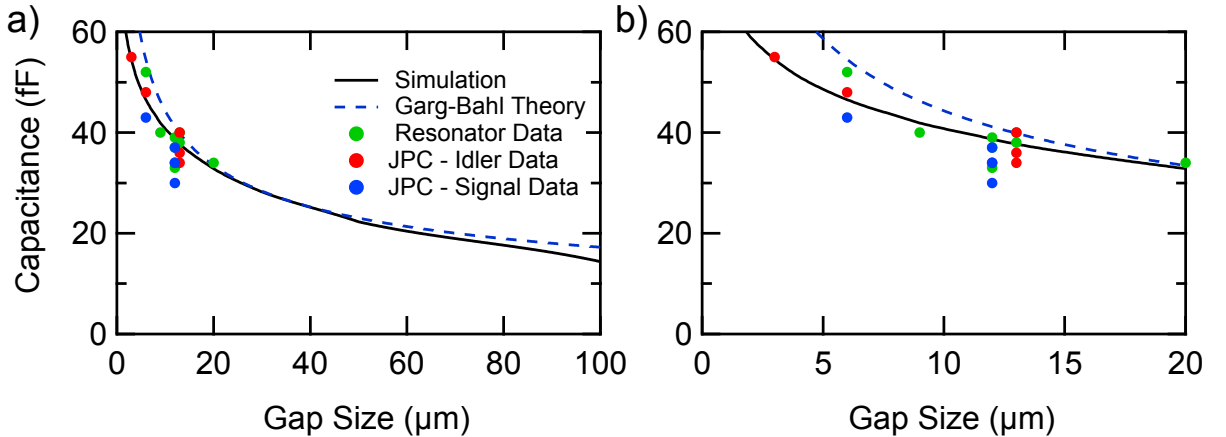


Figure 4.2: Coupling capacitance as function of microstrip gap size. a) Colored dots are measurements, black solid line is simulated in Maxwell, and the blue dashed line is a theoretical expression. b) Magnification of a) around small gap sizes.

where ω_0 is the resonance frequency. In the case of one feedline being shorted to ground, the Q is given by twice this expression.

It is therefore important to know how the capacitance scales with the designed geometric parameters, namely the microstrip gap between transmission line and feedline.

Figure 4.2 compares coupling capacitances inferred from quality factor measurements to those calculated with analytical expressions found in the literature [77, 78] and with values obtained through electrostatic calculations using Maxwell. The green dots correspond to data obtained from resonators fabricated without JRM, while red and blue dots correspond to idler and signal data. Since idler resonators have lower frequencies and higher geometric inductances, the modes are less perturbed by the junctions (the participation ratio is lower) than in the signal case and the inferred capacitance values are more accurate. As seen in the graphs, inferred coupling capacitances agree with the simulation within about 20 %. There are several reasons for this uncertainty: first, as explained above, there is an uncertainty in the measurement of quality factors due to their low values. Further, there is an uncertainty of up to $0.5 \mu m$ in the actual gap size compared to the mask gap size (which could of course be significantly improved by systematically measuring and confirming gap sizes with the scanning electron microscope (SEM)). Lastly, there is still the possibility that the simulation does not exactly represent the devices measured. The dashed blue line represents an analytical expression found in the literature, and which is claimed to be valid up to a gap size of 10 % of substrate thickness (here $25 \mu m$). Table 4.2 lists fabrication parameters of

device	JPX23	JPX25	$\mu\text{SR}01$	$\mu\text{SR}02$	$\mu\text{SR}03$	$\mu\text{SR}04$
fab name	110302_shortJPC_b	110302_shortJPC_c	110426_μSR_a	110426_μSR_b	110412_μSR	110415_μSR
substrate t (μm)	250 μm					
TL type	solid	solid	solid	solid	solid	solid
Ag backed	✓	✓	✓	✓	✓	✓
litho. system	NPGS	NPGS	NPGS	NPGS	NPGS	NPGS
length ^{S/I} (mm)	6.12/9	6.12/9	6.3/(n/a)	6.3/(n/a)	6.3/(n/a)	6.3/(n/a)
gap ^{S/I} (μm)	12/13	12/13	6/(n/a)	9/(n/a)	12/(n/a)	20/(n/a)
msmt. $C_{\text{in}}^{\text{S/I}}$ (fF)	37/40	33/38	52	40	39	34
sim. $C_{\text{in}}^{\text{S/I}}$ (fF)	39/37	39/37	47	42	39	33

Table 4.2: List of notable resonator samples with relevant fabrication parameters.

notable resonator samples used to calibrate the gap capacitors.

One is mainly interested in the JPC bandwidth, which is proportional to the linear signal and idler resonator bandwidths γ (see Eq. 1.11 ff.) for identical signal and idler bandwidths. According to Eq. 4.1 this bandwidth goes as

$$\gamma \propto \omega_0^3 C_{\text{in}}^2, \quad (4.2)$$

so that it is very sensitive on the mode frequency. Figure 4.2 shows simulation results for larger gap sizes in anticipation of future devices designed for higher quantum bit (qubit) readout frequencies.

4.2.2 Participation Ratio

An important concept in the description of the JPC is the inductance participation ratio of the JRM inductance to the total mode inductance. In all that follows, the participation ratio will be defined as

$$p_L(\varphi_{\text{ext}}) := \frac{L_{\text{JRM}}(\varphi_{\text{ext}})}{L_{\text{JRM}}(\varphi_{\text{ext}}) + L_g}, \quad (4.3)$$

where $L_{\text{JRM}}(\varphi_{\text{ext}})$ is the linear part of the inductance of the JRM of the signal (X) or idler (Y) mode (see Ch. 2) and L_g is the inductance of the resonant mode without junctions.

4.2.2.1 Four Junction JRM

In the case of a JPC with a four junction JRM, only the participation ratio evaluated at $\Phi_0/2$ is of relevance, as this is where the device is typically operated. The participation ratio depends on only the ratio of the Josephson inductance L_{J_0} to the geometric inductance L_g , just as does the variation of the mode frequency with flux:

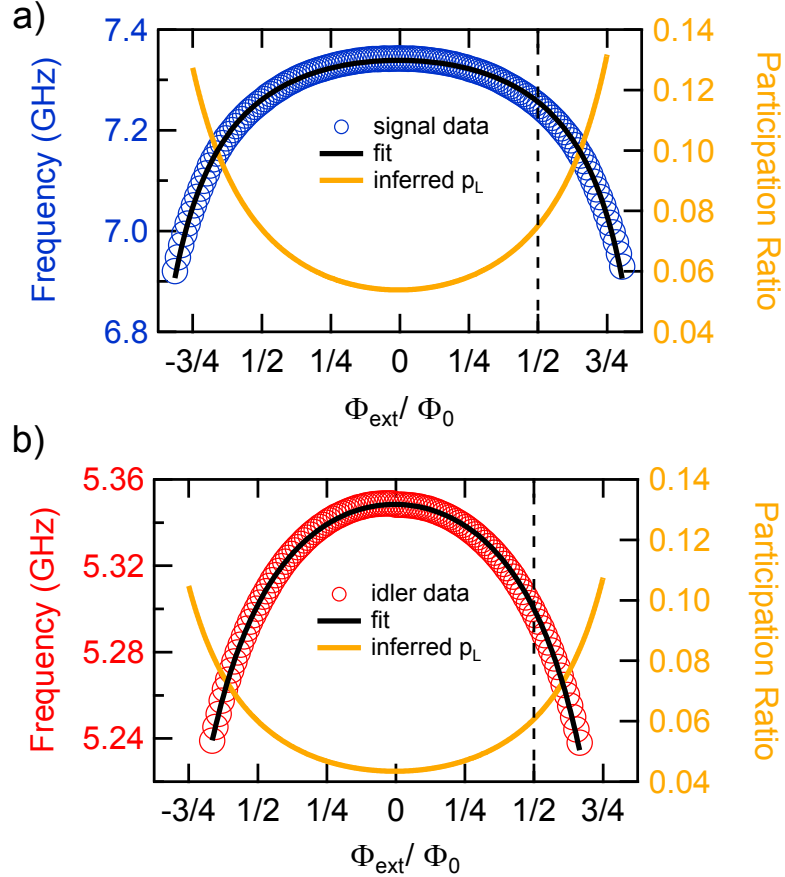


Figure 4.3: Participation ratio inferred from frequency tunability of a JPC with a four junction JRM (sample JPX30). a) Measured signal frequency as function of magnetic flux (blue circles). Black line is a fit. Yellow line is the participation ratio as a function of flux inferred from the fit parameter $p_L(\Phi_0/2)$. The dashed line shows the usual operating point $\Phi_{\text{ext}} = \Phi_0/2$. b) Same as in a) but for idler data.

$$\omega_0 \propto \frac{1}{\sqrt{L_g + L_{\text{JRM}}(\Phi_{\text{ext}})}}. \quad (4.4)$$

As shown in Eq. 2.32, for the signal and idler modes one finds $L_{\text{JRM}}(\Phi_{\text{ext}}) = L_{J_0}/\cos(\pi\Phi_{\text{ext}}/(2\Phi_0))$, where $\Phi_0 = h/2e$ is the magnetic flux quantum.

Figure 4.3 shows the measured signal and idler mode frequencies for varying magnetic flux. Note that the data is obtained by merging forward and backward flux sweeps, as the jumps when sweeping the flux in only one direction. The black line corresponds to a fit to 4.4 and yields the fit parameter $p_L^S(\Phi_0/2) = 7\%$ for the signal mode and $p_L^I(\Phi_0/2) = 6\%$ for the idler mode. This uniquely determines the shape of the participation ratio function of Eq. 4.3, which is plotted in

yellow and can be expressed as

$$p_L(\Phi_{\text{ext}}) \stackrel{4\text{JJ JRM}}{=} \frac{L_{J_0}}{L_{J_0} + L_g \cos\left(2\pi \frac{\Phi_{\text{ext}}}{4\Phi_0}\right)}, \quad (4.5)$$

or, in terms of $p_L(\Phi_0/2)$, as

$$\boxed{p_L(\Phi_{\text{ext}}) \stackrel{4\text{JJ JRM}}{=} \frac{p_L(\Phi_0/2)}{p_L(\Phi_0/2) + \sqrt{2}(1 - p_L(\Phi_0/2)) \cos\left(2\pi \frac{\Phi_{\text{ext}}}{4\Phi_0}\right)}}. \quad (4.6)$$

As expected, the higher frequency signal mode participation ratio is larger than the lower frequency idler participation ratio, due to the lower geometric inductance of the signal mode. It is important to note that the model presented above neglects stray inductances present in the JRM.

4.2.2.2 Eight Junction JRM

In the case of JPCs with shunted JRM, the concept of flux dependence of the participation ratio becomes important, as devices are operated over a range of different fluxes. In this case, the ring modulator inductance is given by Eq. 2.68 $L_{\text{JRM}}(\Phi_{\text{ext}}) = 2L / (2\beta_L \cos(\pi\Phi_{\text{ext}}/(2\Phi_0)) + 1)$, where $\beta_L = L/L_{J_0}$ and L is the shunt inductance. The participation ratio is this time given by two parameters, any two ratios of the three inductances involved: L_{J_0} , L , L_g . Here the two parameters β_L and $p_g := L_{J_0}/L_g$ will be chosen.

The flux dependence of the frequency is again of the form of Eq. 4.4, but this time two parameters determine its change with magnetic flux: β_L and p_g . Thus again the participation ratio can be obtained from the flux dependence of the mode frequencies.

Figure 4.4 shows the measured signal and idler resonance frequency as a function of applied magnetic flux. The black curves are fits, yielding $\beta_L^S = 0.54$, $p_g^S = 0.12$ for the signal mode and $\beta_L^I = 0.64$ and $p_g^I = 0.07$ for the idler mode. The resulting participation ratio is plotted in yellow and can be expressed as

$$\boxed{p_L(\Phi_{\text{ext}}) \stackrel{8\text{JJ JRM}}{=} \frac{2\beta_L p_g}{2\beta_L p_g + 1 + 2\beta_L \cos\left(2\pi \frac{\Phi_{\text{ext}}}{4\Phi_0}\right)}}. \quad (4.7)$$

Note that Eq. 4.7 converges toward Eq. 4.6 for $\beta_L \rightarrow \infty$, as it should.

For this particular device (JPXs01) and in the range of frequencies it is typically operated, the

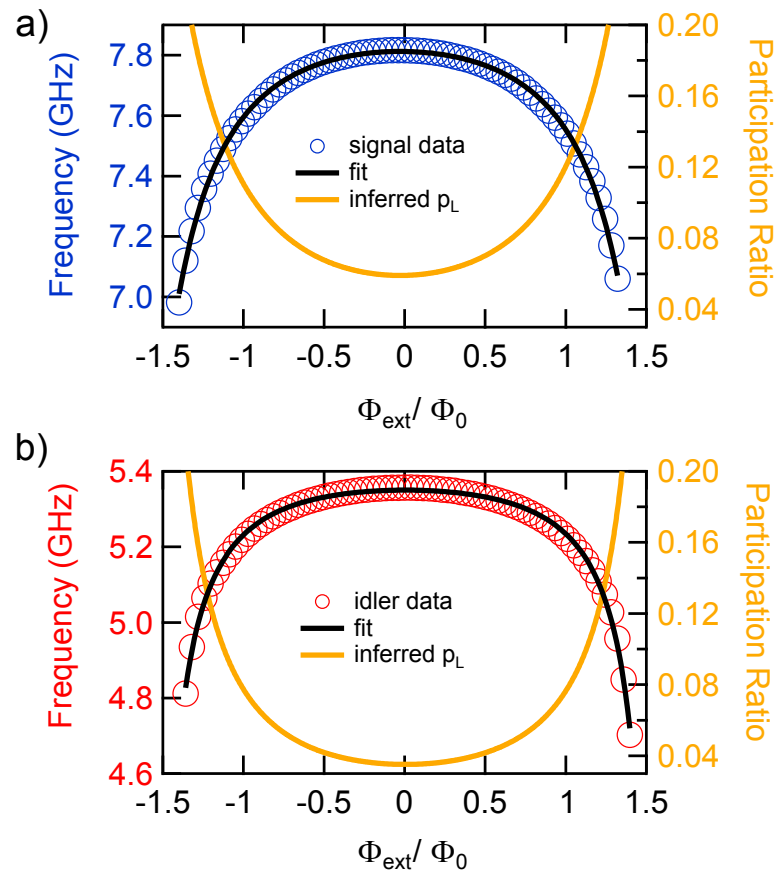


Figure 4.4: Participation ratio inferred from frequency tunability of a JPC with shunted JRM (sample JPXs01). a) Measured signal frequency as function of magnetic flux (blue circles). Black line is a fit. Yellow line is the participation ratio as a function of flux inferred from the fit parameters β_L and L_{J_0}/L_g . b) Same as in a) but for idler data.

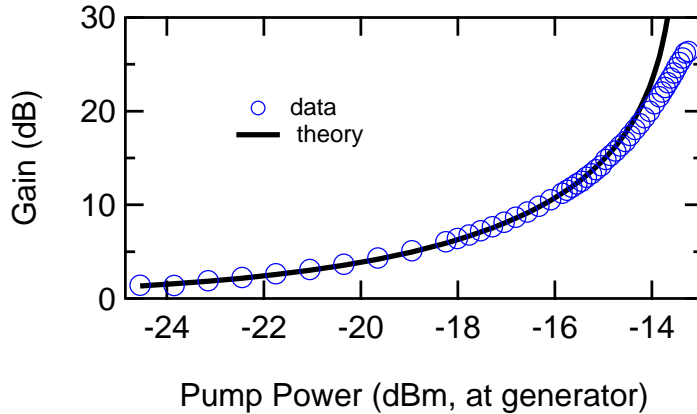


Figure 4.5: Measured gain vs. applied pump power (blue circles, sample JPXs01) and theoretical prediction (black).

participation ratio of the signal mode thus varies by a factor of two, between around 7% and 15% while the idler mode varies between around 5% and 12%.

4.3 Gain Scaling with Pump Power

As explained in Ch. 3 (Eq. 3.15), the JPC scales with the injected pump power P_p as

$$\sqrt{G_0} = \frac{1 + \alpha P_p}{1 - \alpha P_p}, \quad (4.8)$$

where α is a proportionality constant representing the losses between generator and the sample. At the critical pump power $P_p = P_{po}$, determined by $|\rho_0|^2 = 1$, where $|\rho_0|^2 = \alpha P_p$ is the normalized pump power, the gain is expected to diverge. In reality however, the gain remains finite and levels off more smoothly than expected by Eq. 4.8, as seen in Fig. 4.5. The data was taken in a resolution bandwidth (RBW) of 5 Hz at a center frequency of 7.64 GHz, and care was taken to reduce the probe tone power used to measure the gain as the gain increased, to assure the device was not saturating at any point. Two possible explanations for the flattening of the gain compared to the theoretical black curve (calculated from the experimental gain point at 11 dB), are that the pump impedance starts changing at higher gains, leading to a deviation from the simple proportionality $|\rho_0|^2 = \alpha P_p$, and/or that the device reaches gains which are sufficiently large to excite higher order nonlinearities in the signal mode with zero-point fluctuations alone. In the case where higher order non-linearities are excited, the equations of motion Eqs. 3.5 are not valid anymore and no analytical expression

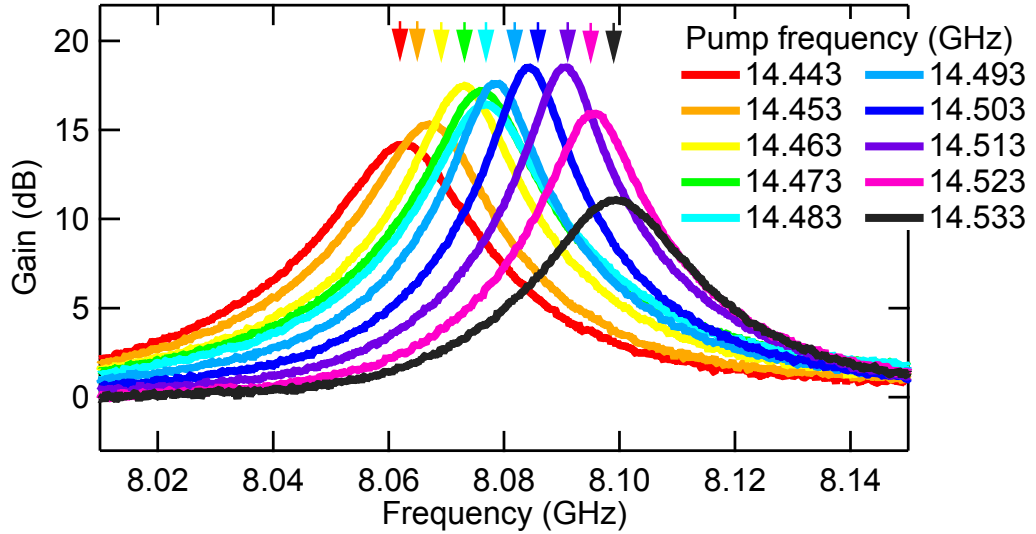


Figure 4.6: Measured gain curves for varying pump frequencies (sample JPX14).

of the gain dependence as a function of the pump power can be derived. One would need to use numerical methods to fit the curve of Fig. 4.5, which was beyond the scope of this work.

4.4 Tunability with Pump Frequency

The pump frequency ω_p is the second available parameter of the pump. As shown in Ch. 3 (Eq. 3.6), the center frequency of amplification depends on the exact value of the pump frequency:

$$G[\omega] = \left| \frac{A^*[\omega]B^*[\omega_p - \omega] + |\rho_0|^2}{A[\omega]B^*[\omega_p - \omega] - |\rho_0|^2} \right|^2, \quad (4.9)$$

where

$$A[\omega] = 1 - i\frac{\omega - \omega_a}{\gamma_a/2} \quad (4.10)$$

$$B[\omega] = 1 - i\frac{\omega - \omega_b}{\gamma_b/2}, \quad (4.11)$$

and $\omega_{a,b}$ and $\gamma_{a,b}$ are the signal/idler mode resonant frequencies and linear bandwidths.

Figure 4.6 shows this tunability with pump frequency, which in practice is of the order of $\gamma_{a,b}$ for the signal/idler mode. The arrows on top indicate the locations of the theoretically expected

center frequencies of the gain curves as described by Eq. 4.9. The linear bandwidth for this device is about 100 MHz and it is frequency tunable with the pump frequency over about 50 MHz. Note however that the curves represent approximately the maximum gains achieved at the shown tuning points, and that those maximum gains significantly decrease at the extrema of the tuning. The narrow range of tunability together with the decrease in gain away from the ideal tuning point $\omega_p = \omega_c = \omega_a + \omega_b$ make tunable JPC based on shunted JRMs necessary for practical operation.

4.5 Saturation Powers for Tunable JPC

For JPCs with JRMs without shunt only one working point is in practice considered ($\Phi = \Phi_0/2$), so that only one set of parameters determine its saturation behavior. In the tunable JPCs however, it was found that saturation powers can significantly change depending on the flux point and pump parameters chosen. Figure 4.7 shows the measured $P_{-1 \text{ dB}}$ saturation powers as a function of the gain, for amplifier frequencies tuned from 7.38 GHz to 7.8 GHz. The $P_{-1 \text{ dB}}$ are defined as the signal input powers at which the amplifier gain drops by 1 dB, and are extracted from data similar to the one presented in Fig. 1.9. As becomes apparent, the saturation powers decrease with increasing gain, with a slope of about -1.2 dB/dB . More importantly, the saturation powers differ starkly between tuning points, by up to 20 dB. Thus, when tuned to a gain of 20 dB at the center frequency of 7.8 GHz the device could handle about 10 photons from a qubit readout cavity with 5 MHz (black dotted line represents one photon at 5 MHz). But when tuned to the same gain at a center frequency of 7.4 GHz it could handle only a fraction of a photon. While this feature is partly due to the changing participation ratio and coupling strength g_3 at different bias points (see Ch. 2 and Sec. 4.2.2), differences of up to 10 dB were observed at close-by tuning points and frequencies, making it necessary to carefully set frequency bias points using both the flux and pump frequency tuning. This is likely due to the fact that there is a range of pump frequencies for each flux bias point at which amplification is possible, but which are not necessarily optimal, in the sense that the pump frequency is detuned away from the sum of the linear signal and idler frequencies (at the given flux bias). This question of saturation powers and mechanisms as a function of flux and pump settings needs to be studied in more detail in the future.

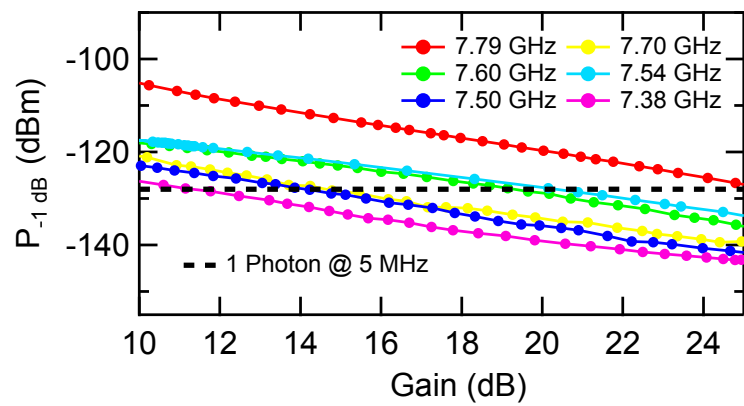


Figure 4.7: Measured $P_{-1 \text{ dB}}$ input signal saturation powers, at which the gain drops by 1 dB, as function of the gain and at different frequency points of a tunable JPC (sample JPXs01).

Chapter 5

Coherent Attenuation and Reverse Operation of the JPC

Three-wave mixing has been known since the early days of nonlinear optics to be a phase sensitive *three* wave process, depending on the phase $\varphi_n = \varphi_s + \varphi_i - \varphi_p$ relevant to this nonlinear system, where $\varphi_{s,i,p}$ are the signal, idler, and pump phases respectively [79], and provides a basic building block for measurements at the single photon level [80, 81]. Usually the Josephson Parametric Converter (JPC) is operated as a phase preserving amplifier, and only tones on the signal port are applied. As explained in Ch. 3, the JPC can also be operated in phase sensitive mode, when applying tones with equal photon fluxes on both the signal and idler ports. Depending on the phase φ_n , this can either lead to coherent amplification or its time-reversed equivalent, Coherent Attenuation (CA), analogous to time-reversal in lasers [82, 83] and optical parametric oscillators (OPO) [84]. Moreover, power conservation predicts that CA leads to an increase of the circulating pump amplitude, effectively leading to an increase of the gain of the JPC.

Both effects, the attenuation of signal and idler tones at the CA condition and the increase of pump photons as manifested through an increase of the gain, will be explored below [67], confirming that the JPC Hamiltonian must not only have a mixing term of the form $a^\dagger b^\dagger c$ but also the hermitian conjugate term abc^\dagger .

5.1 Theory

5.1.1 Coherent Attenuation

The absorption of balanced signal and idler input tones for small tone amplitudes (stiff pump approximation still applies) can be fully described by the JPC scattering matrix of Eq. 3.49. For classical signal and idler wave amplitudes $\alpha_{\text{in}} = |\alpha_{\text{in}}| e^{-i\varphi_S}$ and $\beta_{\text{in}} = |\beta_{\text{in}}| e^{-i\varphi_I}$ the scattering matrix becomes:

$$\begin{pmatrix} \alpha_{\text{out}} \\ \beta_{\text{out}}^* \end{pmatrix} = \begin{pmatrix} \cosh(\lambda) & -ie^{-i\varphi_P} \sinh(\lambda) \\ ie^{i\varphi_P} \sinh(\lambda) & \cosh(\lambda) \end{pmatrix} \begin{pmatrix} \alpha_{\text{in}} \\ \beta_{\text{in}}^* \end{pmatrix}, \quad (5.1)$$

where φ_P is the pump phase and $\sqrt{G_0} \equiv \cosh(\lambda)$. Balancing the input photon fluxes $|\alpha_{\text{in}}|^2 \equiv \dot{n}_S \stackrel{!}{=} \dot{n}_I \equiv |\beta_{\text{in}}|^2$ one obtains

$$\alpha_{\text{out}} = \cosh(\lambda) |\alpha_{\text{in}}| e^{-i\varphi_S} - ie^{-i\varphi_P} \sinh(\lambda) |\beta_{\text{in}}| e^{+i\varphi_I} \quad (5.2)$$

$$= |\alpha_{\text{in}}| (\cosh(\lambda) e^{-i\varphi_S} - ie^{-i\varphi_P} \sinh(\lambda) e^{+i\varphi_I}). \quad (5.3)$$

The CA $|\alpha_{\text{out}}|^2 / |\alpha_{\text{in}}|^2$ (or 'return loss' in microwave terminology) on the signal port then is

$$\frac{|\alpha_{\text{out}}|^2}{|\alpha_{\text{in}}|^2} = |\cosh(\lambda) e^{-i\varphi_S} - ie^{-i\varphi_P} \sinh(\lambda) e^{+i\varphi_I}|^2 \quad (5.4)$$

$$= \cosh^2(\lambda) + \sinh^2(\lambda) + i \cosh(\lambda) \sinh(\lambda) \left(e^{-i(\varphi_S + \varphi_I - \varphi_P)} - e^{+i(\varphi_S + \varphi_I - \varphi_P)} \right) \quad (5.5)$$

$$= \cosh(2\lambda) + \sinh(2\lambda) \cos(\varphi_S + \varphi_I - \varphi_P - \pi/2) \quad (5.6)$$

$$= \cosh(2\lambda) \left(\cos^2\left(\frac{\varphi_S + \varphi_I - \varphi_P - \pi/2}{2}\right) + \sin^2\left(\frac{\varphi_S + \varphi_I - \varphi_P - \pi/2}{2}\right) \right) \quad (5.7)$$

$$+ \sinh(2\lambda) \left(\cos^2\left(\frac{\varphi_S + \varphi_I - \varphi_P - \pi/2}{2}\right) - \sin^2\left(\frac{\varphi_S + \varphi_I - \varphi_P - \pi/2}{2}\right) \right) \quad (5.8)$$

so that finally one arrives at the [CA equation]:

$$\boxed{\frac{|\alpha_{\text{out}}|^2}{|\alpha_{\text{in}}|^2} = \frac{|\beta_{\text{out}}|^2}{|\beta_{\text{in}}|^2} = e^{2\lambda} \cos^2\left(\frac{\varphi_n - \pi/2}{2}\right) + e^{-2\lambda} \sin^2\left(\frac{\varphi_n - \pi/2}{2}\right)}, \quad (5.9)$$

where $\varphi_n := \varphi_S + \varphi_I - \varphi_P$ is the relevant phase of the three waves¹. Thus at large G_0 , one will observe a power gain of $e^{2\lambda} \approx 4G_0$ at $\varphi_n = +\pi/2$ or CA of $e^{-2\lambda} \approx 1/(4G_0)$ at $\varphi_n = -\pi/2$, with a periodicity of 2π .

The same result is of course obtained when considering the (amplitude) eigenvalues $e^{\pm\lambda} \approx (2\sqrt{G_0})^{\pm 1}$, and corresponding eigenvectors $\vec{e}_\pm = (\alpha, \alpha e^{i(\varphi_P \pm \pi/2)})^T$ of the scattering matrix of Eq. 5.9. These eigenvalues correspond to $\varphi_n = \pm\pi/2$, as expected from Eq. 5.9 and represent injecting tones α in the signal port and $\alpha^* e^{-i(\varphi_P \pm \pi/2)}$ in the idler port.

5.1.2 Gain Modulation

When increasing the signal and idler tone amplitudes (keeping them balanced) eventually the stiff pump approximation will break down and one has to consider the full nonlinear dynamics of all three modes (signal, idler, and pump) as predicted by Eq. 3.5. In this case the gain G_0 loses its meaning as power reflection coefficient, but can be interpreted as system state parameter in case the pump parameters stay untouched throughout the experiment, as is the case here. The return loss on the signal (and idler) port will then depend on the system state parameter G_0 (which still is the power gain at small injected tones) as well as on the signal and idler photon fluxes relative to the pump photon flux, captured by the parameter $x := \dot{n}_S/\dot{n}_P = (\omega_c/\omega_a) \cdot (P_S/P_p)$, where $P_S(P_p)$ is the injected signal (pump) tone power. The resulting signal port power reflection coefficient [G in the fully nonlinear regime] is calculated² by the coupled equations (see supplemental material of [67])

$$\boxed{\rho = \rho_0 \left| 1 + x \cdot \frac{\rho_0}{4} \frac{1}{\sqrt{G}} \left[\left(1 + \sqrt{G}\right)^2 e^{-i(\varphi_n + \pi/2)} - 2 \left(1 + \sqrt{G}\right) \sqrt{G-1} + (G-1) e^{i(\varphi_n + \pi/2)} \right] \right|}, \quad (5.10)$$

and

$$\boxed{\sqrt{G} = \frac{1 + \rho^2}{1 - \rho^2}}, \quad (5.11)$$

where

$$\boxed{\rho_0^2 \equiv \frac{\sqrt{G_0} - 1}{\sqrt{G_0} + 1}}. \quad (5.12)$$

Equations 5.10, 5.11 can be solved numerically but to gain some qualitative insight, one can

¹This nonlinear phase can of course be redefined by adding a constant offset.

²The theory was worked out by A. Roy.

expand Eq. 5.10 in terms of $1/\sqrt{G}$:

$$\rho = \rho_0 \left| 1 - x \cdot \frac{\rho_0}{2} \left[2(\sqrt{G} + 1) \cos^2 \left(\frac{\varphi_n - \pi/2}{2} \right) - \frac{1}{2\sqrt{G}} \right. \right. \quad (5.13)$$

$$\left. \left. + i \left(1 + \frac{1}{\sqrt{G}} \right) (\cos^2 \left(\frac{\varphi_n}{2} \right) - \sin^2 \left(\frac{\varphi_n}{2} \right)) \right] + O \left(\frac{1}{G} \right) \right| \quad (5.14)$$

$$= \rho_0 \begin{cases} \left| 1 - x \cdot \rho_0 \left(\sqrt{G} + 1 \right) + O \left(\frac{1}{\sqrt{G}} \right) \right| & , \text{ for } \varphi_n = +\pi/2 \\ \left| 1 + x \cdot \frac{\rho_0}{4\sqrt{G}} + O \left(\frac{1}{G} \right) \right| & , \text{ for } \varphi_n = -\pi/2 \end{cases} . \quad (5.15)$$

Equations 5.11, 5.12 show that G is a monotonous function of ρ , so that the minus sign in Eq. 5.15 means that the gain is reduced for $\varphi_n = +\pi/2$, while it is enhanced for $\varphi_n = -\pi/2$ (plus sign), since for large JPC gains, $G_0, G \gg 1$, $\rho_0, \rho \approx 1$, and further it can be assumed that $x \ll 1$. When φ_n is $+\pi/2$, Eq. 5.9 predicts that the JPC (i.e. the pump) has to provide a maximum amount of power for the amplification process, which for large signal and idler tones becomes unsustainable and leads to a reduction of the gain G as predicted by Eq. 5.15. At the phase $\varphi_n = -\pi/2$ on the other hand, signal and idler tones are coherently absorbed (they are suppressed by the factor $e^{-2\lambda}$, Eq. 5.9) and for large signal and idler amplitudes the power reappears as extra pump power, leading to an enhancement of the JPC gain, as shown by Eq. 5.15.

5.2 Some Experimental Details and JPC Characteristics

The JPC used in this experiment³ is tuned to have a signal center frequency $f_S = 7.6393$ GHz, an idler center frequency $f_I = 5.2277$ GHz with an applied pump tone $f_p = f_S + f_I = 12.867$ GHz. To observe the CA at low applied signal and idler powers of Eq. 5.9 as well as the modulation of the gain at large signal and idler powers as described by Eqs. 5.10, 5.11 the phase $\varphi_n = \varphi_S + \varphi_I - \varphi_p$ needs to be varied. To achieve this, the signal and pump phases (φ_S, φ_P) are being kept constant while the idler phase φ_I is varied in time at a rate of one cycle per 10 seconds, thus very slow compared to any other time scale in the experiment. This is equivalent to offsetting the idler tone by $\delta f = 0.1$ Hz ($\varphi_I(t) = \varphi_I(0) + \phi(t)$, $\phi(t) := 2\pi\delta f \cdot t$) which is what has been done experimentally. Further, since φ_n is defined only up to a constant, one can choose to set $\varphi_{n_0} := \varphi_S + \varphi_I(0) - \varphi_p \stackrel{!}{=} -\pi/2$, so that $\varphi_n = \varphi_{n_0} + \phi(t) = -\pi/2 + \phi(t)$ and Eq. 5.9 yields

³Sample JPXs01, with an inductively shunted Josephson Ring Modulator (JRM).

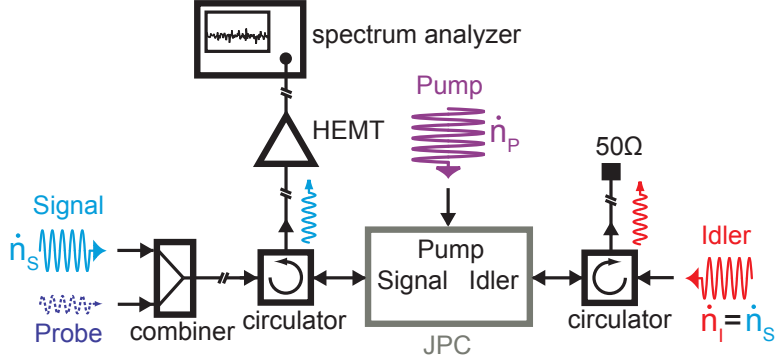


Figure 5.1: Schematic of the measurement setup. Signal, idler, and pump CW tones are applied, with photon fluxes $n_s = n_I$, n_p . Signal and idler tones are both injected to the signal port through a combiner. The signal port output power is monitored with a spectrum analyzer (set to different center frequencies and resolution bandwidths, see text).

$$\frac{P_{\text{out}}}{G_0 P_{\text{in}}} = \frac{|\alpha_{\text{out}}|^2}{G_0 |\alpha_{\text{in}}|^2} = G_0^{-1} \left(e^{2\lambda} \sin^2 \left(\frac{\phi(t)}{2} \right) + e^{-2\lambda} \cos^2 \left(\frac{\phi(t)}{2} \right) \right) \quad (5.16)$$

$$= 2 - G_0^{-1} - 2\sqrt{1 - G_0^{-1}} \cos(\phi(t)). \quad (5.17)$$

The observed output power on the signal port P_{out} thus varies between $\approx 4G_0 P_{\text{in}}$ (P_{in} is the signal input power) and $\approx (4G_0)^{-1} P_{\text{in}}$. When comparing this output power to the case without any applied idler tone it becomes apparent that it is increased by 6dB (a factor 4) or reduced by $(4G_0^2)^{-1}$ and varying sinusoidally with $\phi(t)$. According to Eq. 5.17 the maximum CA of the input signal power occurs at $\phi = 0$ and has the following G_0 dependence:

$$CA := \left(\frac{P_{\text{out}, \text{min}}}{P_{\text{in}}} \right)^{-1} = \left(2G_0 - 1 - 2\sqrt{G_0} \sqrt{G_0 - 1} \right)^{-1}, \quad (5.18)$$

where CA is defined so that it is positive when expressed in dB.

In both parts of the experiment (CA at small signal and idler photon fluxes and gain modulation at large signal and idler photon fluxes) the signal port is monitored with a spectrum analyzer (SA), set to different center frequencies and resolution bandwidths, as explained below. This is shown schematically in Fig. 5.1.

The small probe tone used in the gain modulation experiment is injected into the signal port together with the signal tone by using a power combiner. A 50Ω termination on the idler port

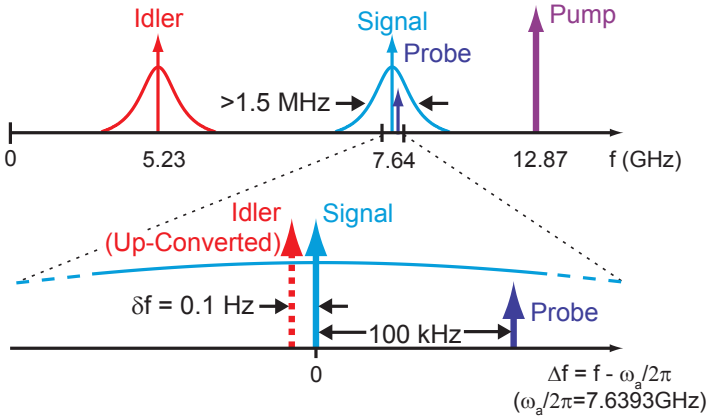


Figure 5.2: Schematic of frequencies involved in the experiment. Top: Signal (blue) and idler (red) amplification bandwidths are shown as Lorentzian shapes. Applied signal and idler tones (red and blue arrows) as well as the probe tone (dark blue arrow) are applied well within amplification bandwidth. The pump (purple arrow) is at the sum frequency of signal and idler resonators. Bottom: While the signal tone (blue arrow) is applied exactly at the center of amplification, the idler tone (dashed red arrow) is offset by $\delta f = 0.1$ Hz, and appearing in the signal resonator through up-conversion. The offset δf achieves a rolling of the phase φ_n . When applied, the small probe tone is offset by 100 kHz from the amplification center.

assures that no amplified outgoing idler port power gets reflected back into the JPC. As mentioned above, signal and idler input photon fluxes are balanced $\dot{n}_S = \dot{n}_I$ for all experiments described in this chapter. This is achieved by setting the JPC to very high gains of about 25 dB where the ratio between G and $G - 1$ is about 0.01 dB. A small idler tone is then injected in the idler port and detected at the signal port (after frequency conversion through the JPC and with gain $G - 1$) and compared to a small signal tone injected and detected at the signal port. When both tones are balanced, the resulting amplified tones on the signal port are within 0.01 dB of each other. After balancing signal and idler inputs this way at the beginning of each experiment, the balance is frequently checked in the course of the experiment, and typically found to be better than ~ 0.05 dB (i.e. $\sim 1\%$).

Figure 5.2 shows the location of signal, probe, idler, and pump tones in frequency space. The signal tone (blue arrow) is applied at the center of the amplification band (represented by the blue Lorentzian gain response function), while the idler tone (red arrow) is offset by the idler port center of amplification (red Lorentzian) by $\delta f = 0.1$ Hz to achieve the slow variation of the phase φ_n .

The probe tone is offset from the signal tone by 100 kHz, to assure that the signal tone output power or the probe tone output power can independently be measured. Figure 5.2 b) further shows that the idler tone is up-converted in frequency and appears as output power on the signal port

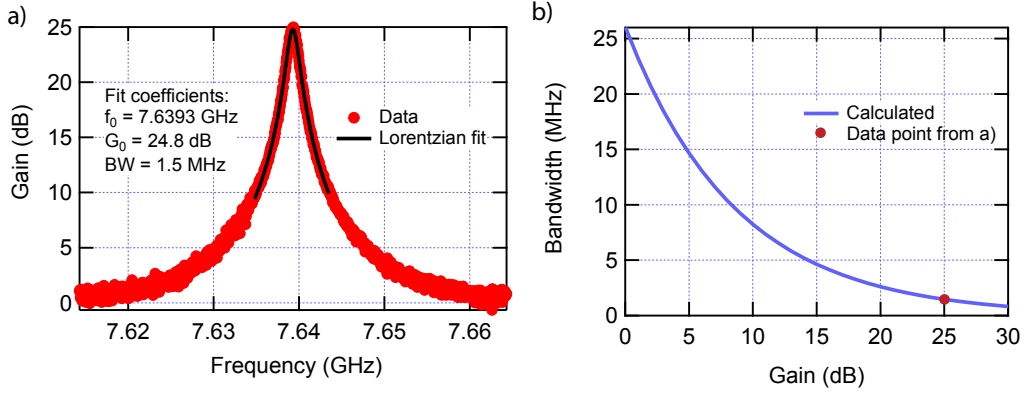


Figure 5.3: JPC amplification bandwidths in the experiment. a) Measured gain curve (red circles) at $G_0 \approx 25$ dB. The bandwidth at this gain point is 1.5MHz, as shown by the Lorentzian fit (black line). b) Predicted bandwidths of the JPC at different gains G_0 using the data point in a).

(dashed red arrow), as could be observed with a SA when setting the resolution bandwidth (RBW) appropriately.

To assure that all tones are well within the JPC amplification bandwidth, gain versus frequency curves were taken. Figure 5.3 a) shows such a gain curve for $G_0 \approx 25$ dB and 3 dB-bandwidth of 1.5 MHz, together with a Lorentzian fit. None of the gain settings G_0 in these experiments exceed 25 dB, so that the 1.5 MHz represents a lower bound on the JPC bandwidth, since the bandwidth as a function of gain varies as described by Eq. 3.17.

The calculated 3 dB-bandwidth vs. gain behavior based on this equation and the gain curve in a) can be seen in Fig. 5.3 b). This observation is important, as it means that all relevant bandwidths and frequency offsets in the experiments are far smaller than the JPC bandwidth. All tones can be assumed to be applied at the center of the amplification band and the exact shape of the gain response function can be neglected.

5.3 Coherent Attenuation

To observe the phase dependence of the JPC as predicted by Eq. 5.17, care must be taken to assure the JPC operates in the stiff pump approximation. The signal and idler photon fluxes $\dot{n}_S = \dot{n}_I$ (or in powers $P_S = \frac{\omega_S}{\omega_I} P_I$) need to be sufficiently small for every setting of G_0 to avoid saturation of the device. To confirm this, saturation curves were taken, where the signal input power P_S was varied and the signal port gain was measured for pump settings corresponding to different unsaturated

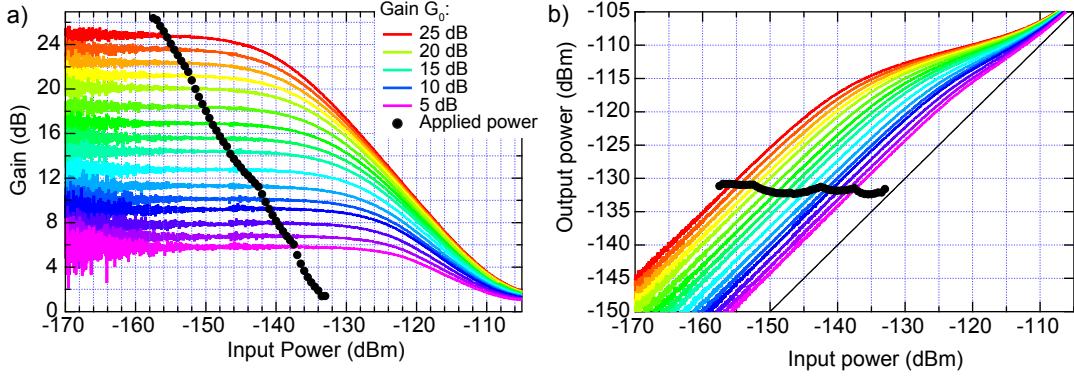


Figure 5.4: Applied power in small amplitude Coherent Attenuation experiment. a) The applied signal power (black discs) plotted together with gain vs. input power curves (colored traces). The applied powers are well within the linear JPC regime, the stiff pump approximation remains valid and the gain is insensitive to the input power. b) Same data as in a), plotted as output power vs. input power. The signal input power is chosen so that the total output power is approximately constant and stays above the system noise floor.

gains G_0 .

The colored traces in Fig. 5.4 a) clearly show that the JPC saturates at certain signal input powers, when the gain drops below the unsaturated value G_0 . The black dots in the figure represent the applied signal input powers in the CA experiment for a given G_0 setting. It clearly shows that the signal powers are in the linear gain region, so that the stiff pump approximation is valid in describing this section. Of course the signal and idler powers could have been kept small and constant for all gain settings G_0 . This however would have led to a degradation of the signal-to-noise ratio (SNR) of the experiment for decreasing G_0 , as the total output power goes as $G_0 P_S$. The signal and idler powers were chosen so that $G_0 P_S \approx \text{const.}$ for all G_0 , as seen in Fig. 5.4 b).

No probe tone is applied in this part of the experiment, as the fluxes $\dot{n}_S = \dot{n}_I$ are too small to change the device gain from G_0 . The frequency window (RBW) around f_S measured by the SA is chosen to be 36Hz, large enough to capture the signal output power dynamics due the rolling of the idler phase at $\delta f = 0.1$ Hz.

This gives a phase resolution of $\sim 1^\circ$. At the same time it is set small enough to be negligible compared to the JPC bandwidth and more importantly so that the power detected is dominated by the signal port output power and not by the system noise. This is summarized in Fig. 5.5.

The measured normalized output power $P = P_{\text{out}}/(G_0 P_{\text{in}})$ is shown in Fig. 5.6 (blue trace) for the gain setting $G_0 = 11$ dB and the white trace drawn on top is a fit to Eq. 5.17 (yielding the fit parameter $G_0 = 11$ dB, as expected). Further, several calibration traces are recorded, which are

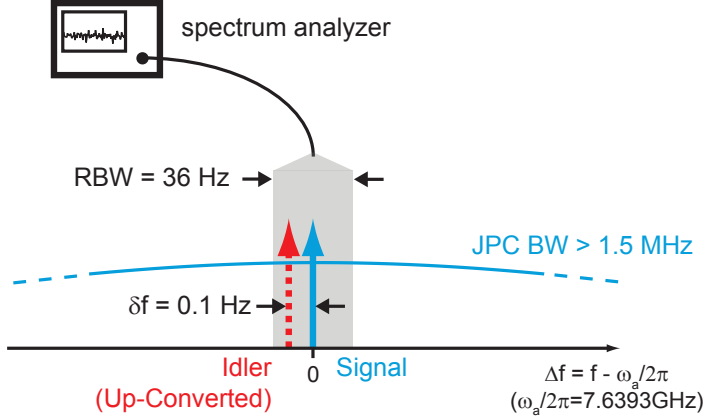


Figure 5.5: Schematic of frequency window measured by the spectrum analyzer in the small amplitude Coherent Attenuation experiment. The window is centered at the signal tone frequency and its width is set to 36 Hz, leading to a $\sim 1^\circ$ phase resolution (since $\delta f = 0.1$ Hz) in the change of the measured power. The signal tone power as a function of phase ϕ is measured for different values of JPC gain G_0 .

used to determine the gain G_0 and the maximum attenuation CA at $\phi = 2\pi n$, $n \in \mathbb{Z}$.

The pink trace is measured when the idler tone is turned off entirely, so that $P_{\text{out}} = G_0 P_{\text{in}}$ (where P_{in} is the injected signal power). The purple trace is measured with pump and idler tones turned off, so that $P_{\text{out}} = P_{\text{in}}$. The black trace shows the system noise floor (pump on; signal and idler tones off), which for large gains is dominated by the amplified JPC noise. CA is the fraction of input power that the JPC 'absorbs' at its maximum CA point $\phi = 2\pi n$, and thus a measure of how efficient the device is in converting signal and idler photons into pump photons.

Figure 5.7 shows the normalized output power $P = P_{\text{out}}/(G_0 P_{\text{in}})$ for varying gain G_0 . Clearly visible is how the maxima approach 6 dB for increasing G_0 , while the minima tend to $-\infty$.

Plotting the CA (as defined graphically in Fig. 5.6) vs. G_0 (blue dots) in Fig. 5.8 shows that there is good agreement between the experimental result and theory given by Eq. 5.18 (red trace) up to a gain of about 14 dB.

At larger gains the distance of the received power at $\phi = 2\pi n$ to the noise floor decreases, and eventually the minimum CA is not measurable anymore, as the power detected by the SA is dominated entirely by noise. There are two reasons for this effect: first the noise floor moves up at larger gains as G_0 , since the JPC gain at some point dominates the system noise; second the received power at $\phi = 2\pi n$ decreases as $(4G_0)^{-1}$. The black triangles in Fig. 5.8 are the measured distance to the noise floor, decreasing with larger gain until eventually crossing the red CA trace, at which point CA cannot be measured anymore. Note that the error bars on the measured (blue)

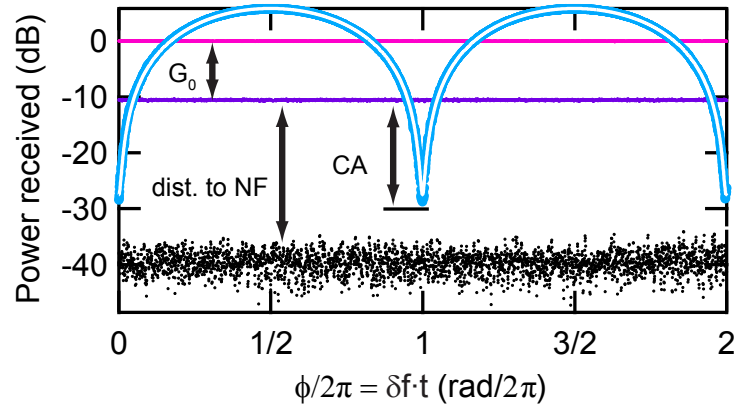


Figure 5.6: Normalized signal port output power as a function of the phase $\phi(t)$ at the gain point $G_0 \approx 11$ dB for balanced signal and idler tones (blue trace). The white trace (on top of the blue trace) is a fit to Eq. 5.17. The pink, purple, and black traces are calibration traces: idler turned off (pink); idler and pump turned off (purple); signal and idler turned off (black), the system noise floor. The arrows indicate how to determine the G_0 , the maximum absorption labeled 'CA', and the magnitude of the signal input power relative to the system noise floor, labeled 'dist. to NF'.

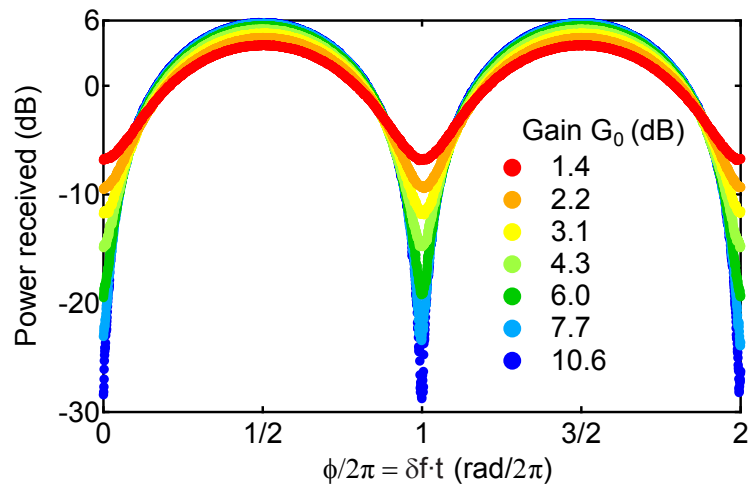


Figure 5.7: Normalized signal port output power for varying gain parameters G_0 . For increasing G_0 the maximum power approaches 6 dB while the minimum power tends to 0 ($-\infty$ in dB) as $(4G_0^2)^{-1}$.

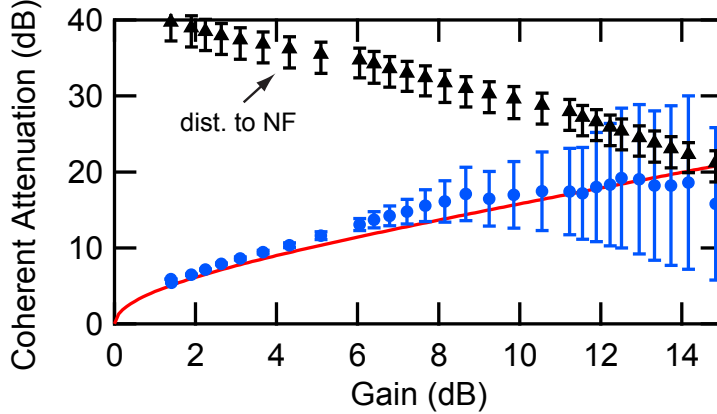


Figure 5.8: Coherent Attenuation at maximum interference point vs. gain setting G_0 (blue dots). The red curve shows the predicted behavior as described by Eq. 5.18. The black triangles represent the resolution limitation due to the finite distance of the input signal power to the noise floor.

CA points as well as on the 'dist. to noise floor' data (black) are calculated from the noise floor data using the Dicke radiometer formula [85], which states that the 'noise on the noise' power scales as the noise power itself (with coefficient $1/\sqrt{B\tau}$, where B is the bandwidth and τ the integration time). The error bars on the *CA* data increase with increasing JPC gain, which is somewhat counter intuitive. The reason for this is that the output power is kept constant for all G_0 , as shown in Fig. 5.4 b), while the system noise increases with G_0 (the amplified JPC noise increases).

5.4 Gain Enhancement

To prove that at $\phi = 2\pi n$ signal and idler powers are not simply absorbed (i.e. converted to uncontrolled modes) but converted into pump photons, the gain of the small probe tone injected into the signal port is monitored. Signal and idler powers are increased to levels that individually would saturate the JPC and would cause a significant drop in the device gain, as shown in Fig. 5.9.

At the CA point $\phi = 2\pi n$ however, the large signal and idler powers actually lead to an increase in gain, as signal and idler photons are pairwise annihilated and converted into pump photons. This increase in circulating pump current leads to an increase in ρ and thus an increase in JPC gain G .

Figure 5.10 shows the frequencies and offsets involved: the SA center frequency is set to the probe tone frequency with the RBW set to 51 Hz. The probe tone is offset by 100 kHz from the signal tone, which assures that no signal tone power is detected by the SA. The idler tone is still offset by $\delta f = 0.1$ Hz from the idler center frequency, causing the phase ϕ to roll at $2\pi/10\text{sec}$ and

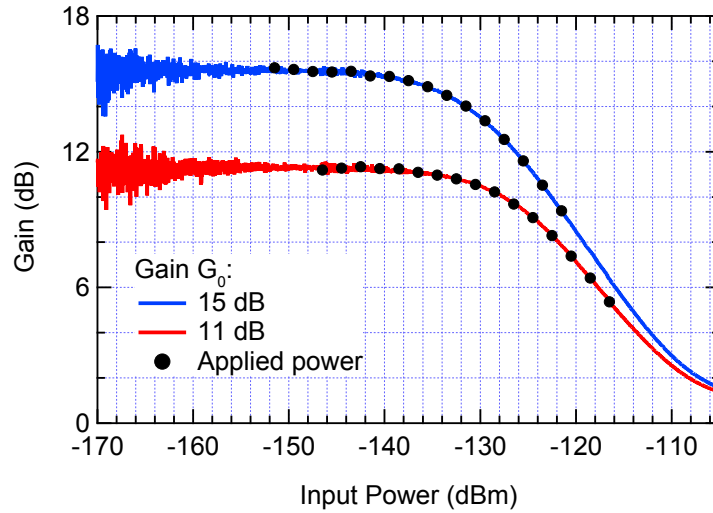


Figure 5.9: Signal input powers applied (black dots) in the Gain Enhancement experiment, increased in 2dB steps. The signal powers become large enough to saturate the JPC and cause a significant drop in gain.

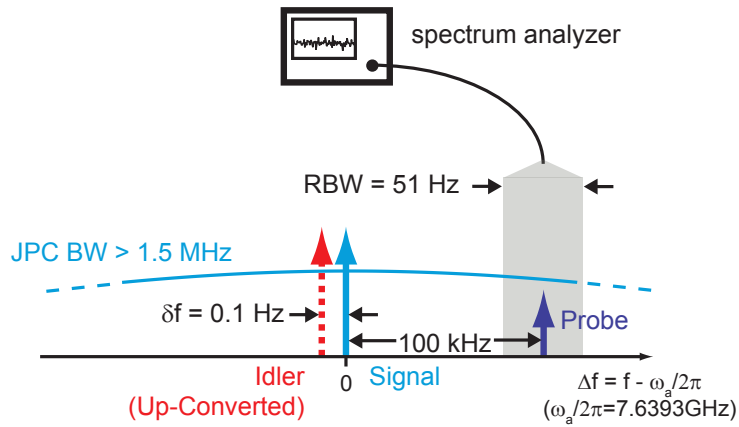


Figure 5.10: Schematic of frequency window measured by the spectrum analyzer in the Gain Enhancement measurement. The resolution bandwidth of 51 Hz captures only the small probe tone power, which is far detuned from the very large signal and idler tones. The probe tone power as a function of the phase ϕ for different signal and idler powers and gains G_0 .

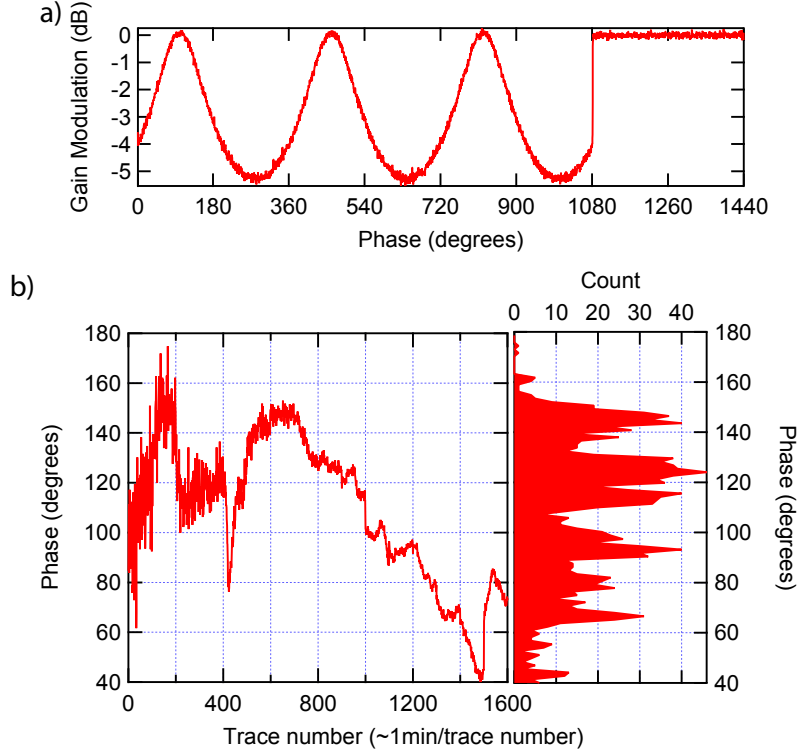


Figure 5.11: G_0 set to 11 dB. a) Single trace showing the change of the probe tone gain as a function of (uncalibrated) phase ϕ for a particular set of signal and idler powers (trace number 1000). Signal and idler tones are turned on and balanced ($\dot{n}_S = \dot{n}_I$) for three cycles and turned off for one cycle for calibration (determining the 0 dB level). b) Left: Tracking of the (uncalibrated) phase ϕ over the course of the experiment (24 h). For every signal (and idler) power setting, 100 traces similar to the one shown in a) are recorded and subsequently averaged. Right: Histogram of the phase.

leading to a change in JPC gain at a rate of 0.1 Hz.

At fixed G_0 , the probe power as a function of $\phi(t) = 2\pi\delta f \cdot t$ is measured for 16 different signal and idler power settings (again, $\dot{n}_S = \dot{n}_I$). Signal and idler powers are increased in steps of 2 dB. For each signal and idler power setting 100 traces of 4 cycles (40 sec) are collected (for later averaging), where signal and idler tones are turned on for 3 cycles and turned off for one cycle, as shown in Fig. 5.11 a). In this way slow drifts in the JPC gain can be calibrated out. Together with data transfer, trigger delays and further calibration traces to assure that signal and idler powers are balanced and the gain G_0 does not drift significantly, each trace acquisition takes about 1min, so that the entire experiment for one gain setting G_0 takes about 24 h.

The generator phases drift relative to each other over the course of the experiment, as seen in Fig. 5.11 b), where the location of the maxima of the individual traces is tracked. The decrease in noise is simply due to the fact that at small signal and idler power settings very little gain

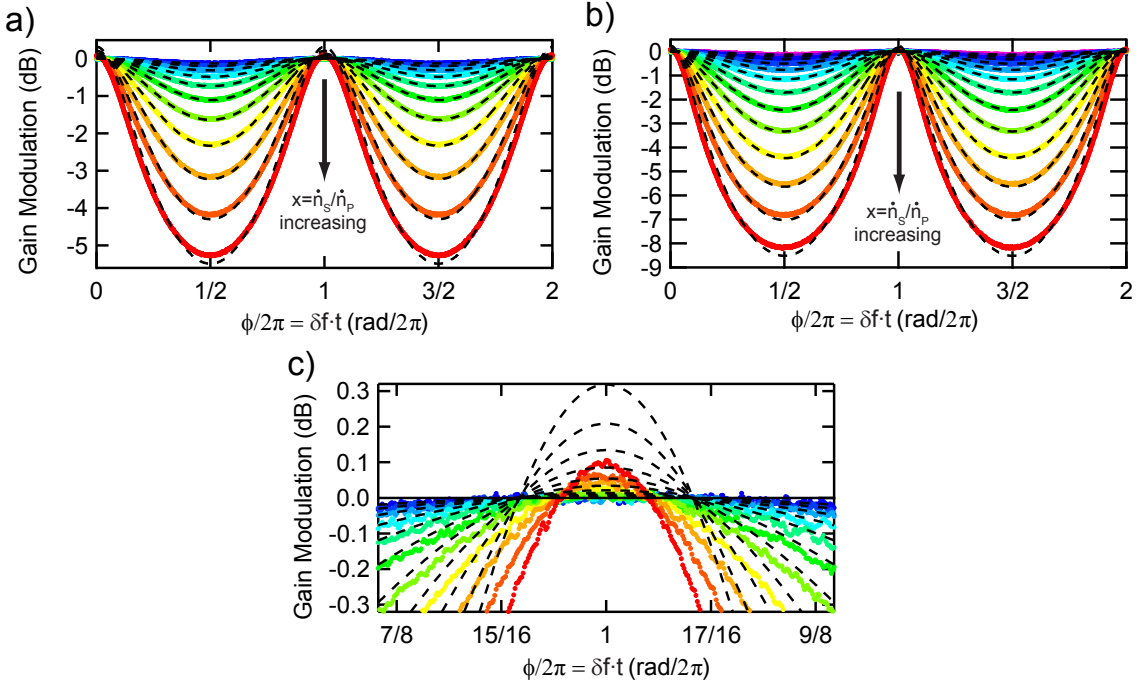


Figure 5.12: Measured (colored traces) probe gain vs. ϕ for different values of signal and idler powers. Signal and idler powers are increased (from blue to red traces) in 2 dB steps. Dashed traces are numerical least square fits to Eq. 5.10. a) Unsaturated gain set to $G_0 = 11$ dB. b) $G_0 = 15$ dB. c) Enlargement of region around $\phi = 2\pi$, for $G_0 = 11$ dB. Clearly visible is the increase of the gain above G_0 (0 dB line).

modulation occurs (the individual traces as in a) are flat) and it is more difficult to extract the location of the maxima. This phase drift is taken into account when averaging the 100 individual traces together at each signal and idler power setting.

Figure 5.12 shows the resulting (averaged) observed modulation of the gain as a function of the phase $\phi(t)$ for $G_0 = 11$ dB (Fig. 5.12 a) and c)) and $G_0 = 15$ dB (Fig. 5.12 b)). For increasing signal and idler powers (from blue to red traces) the gain drops significantly at $\phi = (2n+1)\pi$, since at these locations the maximum output power is extracted from the JPC (as seen in Fig. 5.6 in the stiff pump case, where $P_{\text{out}} \approx 4G_0P_{\text{in}}$). This leads to a significant depletion of the pump photons and a drop of ρ (and thus G), as predicted by Eq. 5.10. The dashed lines are fits to Eqs. 5.10 and 5.11, that correctly reproduce the 2 dB steps in x (or signal and idler powers). The fits start to deviate around $\phi = (2n+1)\pi$ from the experimental curves at large x , which is probably partly due the larger relative contribution of the system noise floor, as the detected probe power becomes very small. Further, imbalances in the signal and idler tones will have a more significant effect at high signal and idler powers. More spectacular however is the observed increase in gain around

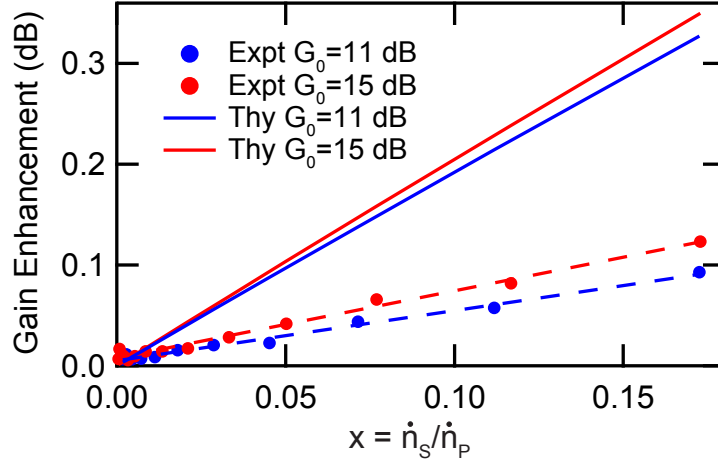


Figure 5.13: Gain Enhancement at $\phi = 2\pi$ for $G_0 = 11\text{ dB}$ (blue) and $G_0 = 15\text{ dB}$ (red) for increasing signal-to-pump photon flux ratio x . The circles show the measured values, while the lines are calculated with Eq. 5.10. Experimentally gain enhancement is clearly observed, even though only about 1/3 of what is theoretically predicted. Nonetheless the observation of gain enhancement is experimental proof of the reverse parametric operation and ultimately the trilinear nature of the JPC Hamiltonian. See text for possible explanations of the discrepancy between theory and experiment.

$\phi = 2\pi n$, as shown in Fig. 5.12 c). While the drop in gain can easily be achieved with one input tone (as in Fig. 5.9) and reflects the JPC saturation, the gain enhancement is a distinctly coherent effect, depending on the presence of both signal and idler tones that need to be balanced and need to be set to have a particular phase relation with the pump (expressed by the phase φ_n).

Figure 5.13 shows the maximum gain enhancement for $G_0 = 11\text{ dB}$ and $G_0 = 15\text{ dB}$ as a function of x . The solid lines are the calculated values using Eqs. 5.10 and 5.11, the dots are the data points extracted from the data shown in Figs. 5.12 a) and b). Several experimental factors can lead to the discrepancy between observed and predicted values, that all lead to diminishing the observed gain enhancement: since the phase modulation at 0.1 Hz is rather slow, the experiment is sensitive to 1/f-noise, as well as to the generator phases (Fig. 5.11 b)). Any mismatch between \dot{n}_S and \dot{n}_I will also significantly lower the gain enhancement. Beyond that, spurious dissipation into uncontrolled modes in this reverse amplification process will also contribute, so that the results of Fig. 5.13 can be understood as benchmarks (or lower bounds) on how much control one has over the signal, idler, and pump modes in JPCs.

Chapter 6

Experimental Methods

6.1 Sample Fabrication

The Josephson Parametric Converter (JPC) samples in this work were all fabricated on silicon using electron beam (e-beam) lithography. Initially (samples JPX01 through JPX20), 2 inch wafers with high resistivity of at least $9 \text{ k}\Omega\text{-cm}$ and $300 \mu\text{m}$ thickness were used. To increase the reproducibility of the resonator characteristics, these were substituted by double-sided polished 3 inch silicon wafers with resistivities of at least $1 \text{ k}\Omega\text{-cm}$ and $250 \mu\text{m}$ thickness (samples JPX22 through JPX30 and JPXs01 through JPXs04). The second polished side is necessary to deposit a $1.2 \mu\text{m}$ layer of silver on the back side of the sample, thus ensuring that the distance of the ground plane to the transmission line is given solely by the wafer thickness. The silver-backed samples were then glued to the sample box with silver paste (SPI Supplies Silver Paste Plus) and left to dry at room temperature, while the first generation of devices on the $300\mu\text{m}$ thick silicon were usually glued with poly methyl methacrylate (PMMA) or GE varnish (Lake Shore VGE-7031 varnish) . GE varnish is known to have good thermal conductivity at low temperatures and is often used to adhere sample chips to the sample boxes, but has the disadvantage for the microstrip design used here that in practice it is difficult to reproducibly have only a negligibly thin layer of it. It is easier to achieve thin layers with PMMA, but it also dries very quickly, so that sometimes only part of the sample area would be attached to the holder. This can lead to the sample detaching from the holder after thermal cycling.

All samples measured were fabricated in a single lithography and evaporation step, so that a

device	JPX09	JPX14	JPX16	JPX22	JPX26	JPX30	JPXs01	JPXs04
fab date	100210	100910	101110	110301	110511	110928	110928	120118
Resonator Properties:								
length ^{S/I} (mm)	6.5/8.5	6.3/8.5	6.3/9	6.12/9	5.8/9	5.8/9	5.8/9	5.9/8.35
gap ^{S/I} (μm)	13/13	12/14	12/13	12/13	12/13	6/6	12/13	12/3
substrate t (μm)	300 μm	300 μm	300 μm	250 μm				
TL type	w/ holes	w/ holes	w/ holes	solid	solid	solid	solid	solid
litho. system	NPGS	NPGS	NPGS	NPGS	NPGS	EBPG	EBPG	EBPG
Ag backed	no	no	no	✓	✓	✓	✓	✓
JRM	✓	✓	✓	✓	✓	✓		
shunted JRM							✓ (Dolan)	✓ (BFT)
Junction Properties:								
JRM JJ (μm^2)	5 × 1	5 × 1	5 × 1	5 × 1	5 × 1	5 × 1	1.5 × 1	1.5 × 1.5
shunt JJ (μm^2)	n/a	n/a	n/a	n/a	n/a	n/a	5 × 1	2.3 × 2.3
P (Torr) × t (min)	10 × 5	10 × 5	10 × 5	10 × 5	10 × 5	10 × 5	10 × 5	10 × 5
Ox cleaning	✓	✓	✓	✓	✓	no	no	✓
R_n after lift-off (Ω)	80	80	55	60	65	60	-	-
J_0^{inferred} (μA)	3.5	3.5	5.1	4.7	4.3	4.7	-	-
$L_{J_0}^{\text{inferred}}$ (pH)	93	93	64	70	76	70	-	-

Table 6.1: List of notable JPC samples with relevant fabrication parameters.

maximum of flexibility was achieved in the choice of sample parameters from one sample to the next. Aluminum was deposited for all samples in a Plassys MEB550S e-beam evaporator. The wafers were spun with dual layers of e-beam resist (~ 90 nm of PMMA on top of ~ 700 nm of PMMA), so that a resist undercut could be created and double angle evaporation techniques for the junction fabrication could be used.

All samples had microstrip resonators of 300 μm width, leading to characteristic impedances of the transmission lines of 45 Ω (300 μm thick silicon) or 41 Ω (250 μm thick silicon). Typically, resonators were around 6 mm (signal) and 9 mm (idler) long. Table 6.1 summarizes fabrication parameters of notable JPC samples measured throughout this thesis work. See Table 4.1 for measured amplifier parameters of these samples.

6.1.1 E-beam Lithography with Converted SEM

The e-beam lithography for samples JPX01 through JPX29 was done using a converted scanning electron microscope (SEM) (FEI type 6634/17 30kV) using the NPGS (Nanometer Pattern Generation System) software. All these devices had (unshunted) Josephson Ring Modulators (JRMs) with four junctions, all fabricated using the Dolan bridge technique [62]. Two layers of aluminum of thickness 35 nm and 120 nm were deposited at angles $\pm 40^\circ$, with an oxidation step in between.

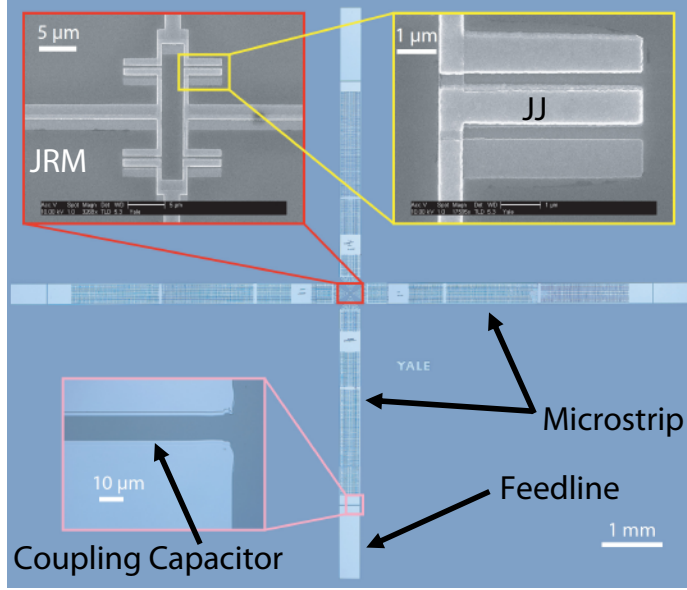


Figure 6.1: Typical JPC sample with designed holes in transmission line resonators (sample shown is JPX14). Top left: JRM with four junctions. Top right: Single Josephson junction. Bottom left: Gap capacitor for coupling to the $50\ \Omega$ environment.

6.1.1.1 Transmission Line Resonator with Holes

The first generation of samples (JPX01 through JPX21) were designed to have microstrip transmission line resonators with irregular holes, to avoid magnetic flux creep during operation. It was later realized that this precaution was unnecessary (though not harmful) and solid microstrip lines were fabricated (JPX22 through JPX30 and JPXs01 through JPXs04).

Figure 6.1 shows an optical image of a full JPC device, with two insets showing SEM images of the JRM (top left) and a single junction (top right). The bottom left inset shows a magnification of the coupling capacitor. The junctions of all (unshunted) JRM fabricated with the Dolan bridge technique were of $5 \times 1\ \mu\text{m}^2$.

6.1.1.2 Resist Mask

Figure 6.2 shows SEM images of resist masks created after the e-beam lithography step. Two features that need to be pointed out are the thin (260 nm wide) bridge that is completely suspended (no methyl methacrylate (MMA) underneath) and the undercuts above and below the junction trenches. Note also that the resist edges are not completely straight in the sample shown. This is not very important for junctions but can be adjusted by increasing the trench doses. The difficulty then is to make sure that the resistance bridge does not collapse either after the development step

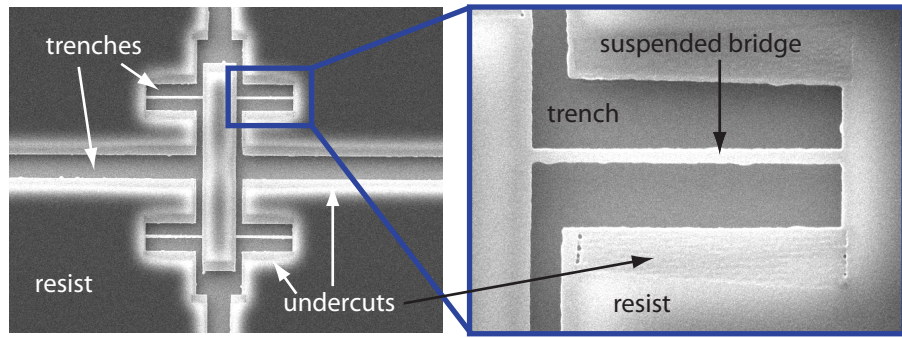


Figure 6.2: SEM images of typical resist masks created after e-beam lithography and used to fabricate Josephson junctions. A thin (13 nm) layer of aluminum was evaporated onto the resist to make imaging possible. Left: Resist mask of entire JRM. Right: Top right junction of same JRM. (Sample 110207_testJPC.)

or the oxygen cleaning step in the evaporator. With the converted SEM it was found that it was crucial not to apply an undercut dose to the bridge, *no matter how small*, as this caused bridges to regularly collapse. Just as an example, using a trench dose for the junctions of $260 \mu\text{C}/\text{cm}^2$ and a bridge dose of $10 \mu\text{C}/\text{cm}^2$ would sometimes lead to collapsed bridges, even though the resist edges looked rather rugged. Although it is not exactly clear why, removing this bridge dose made it possible for the junction trench dose to be increased to $400 \mu\text{C}/\text{cm}^2$ without seeing bridges collapse.

6.1.1.3 Transmission Line Resonators without Holes

The transmission line resonator design was simplified by removing the holes from sample JPX22 onward. At the same time, a new substrate type was used, with silver evaporated on the back side. While the new wafers were $250 \mu\text{m}$ instead of $300 \mu\text{m}$ thick, the width of the microstrip resonators was left unchanged, so that the characteristic impedance of the transmission lines changed slightly from 45Ω to 41Ω . Figure 6.3 shows a JPC device with solid microstrip lines.

6.1.2 E-beam Lithography with EBPG

The most recent generations of JPCs were fabricated using the 100 kV Vistec 5000+ electron beam pattern generator (EBPG). Sample fabrication is considerably simpler in such a designated e-beam lithography machine, as e.g. one needs not to worry much about alignment for the long resonators. Also, the proximity effect correction software allows one to more easily fabricate the $300 \mu\text{m}$ wide gap capacitors, without having to specify local doses. Figure 6.4 shows SEM images of a gap capacitor

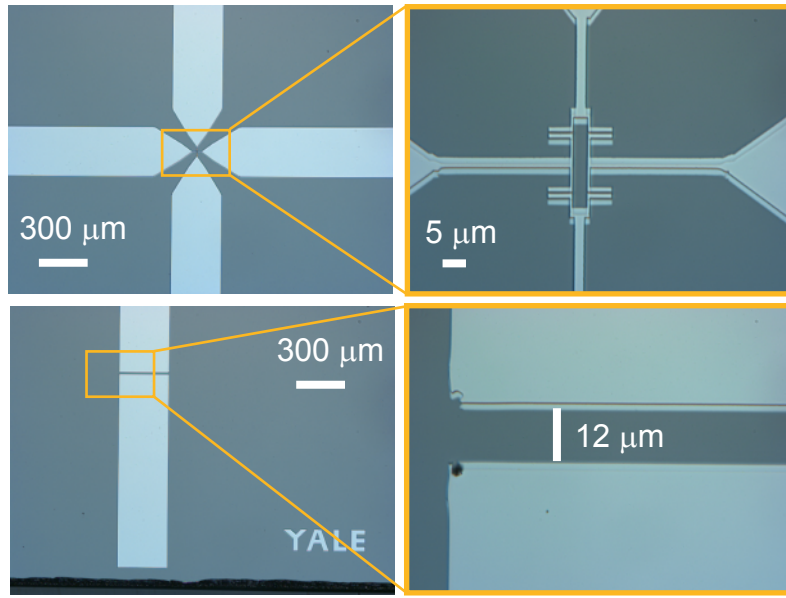


Figure 6.3: Optical images of a JPC with solid microstrip lines. The top pictures show the device center, with a magnification of the JRM on the right. The bottom pictures show the bottom gap capacitor, connecting the feed line to the transmission line resonator. (Sample JPX22.)

resist mask and a gap capacitor of a JPC test device. The mask was imaged after sputtering a thin layer (~ 10 nm) of gold. The gap capacitors are $5\text{ }\mu\text{m}$ and $3\text{ }\mu\text{m}$ wide over a length of $300\text{ }\mu\text{m}$ and were chosen here to demonstrate that the EBPG proximity correction software is quite good for these devices (gap sizes at or below $5\text{ }\mu\text{m}$ become difficult to fabricate with the converted SEM).

Three versions of JRMs were fabricated using the EBPG: Four junction rings very similar to the ones shown above; Shunted JRMs with junctions using the Dolan bridge technique; And shunted JRMs using the bridge-free technique.

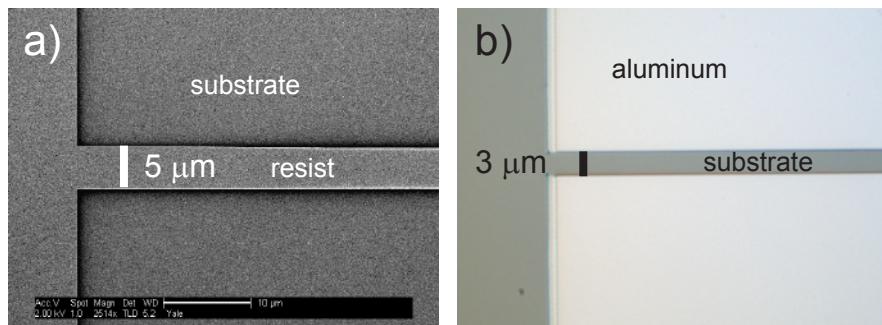


Figure 6.4: SEM and optical images of two samples: a) test chip with gap capacitor resist mask and b) JPC gap capacitor using the EBPG. (Samples 110816_captest and 111107_shuntedJPC.)

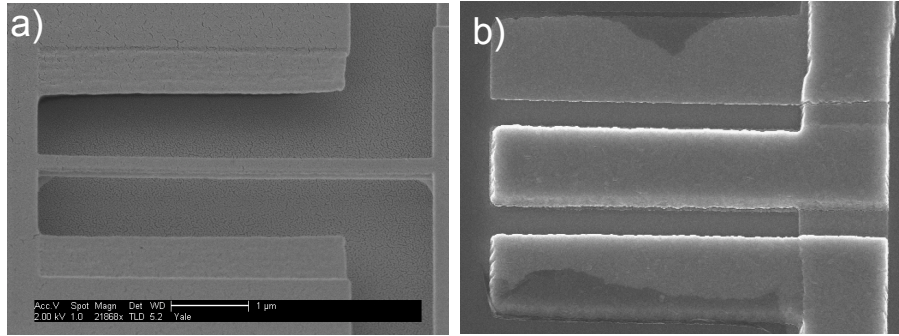


Figure 6.5: SEM images of junction resist mask (a), tilted by 40° and junction (b) fabricated with the EBPG. (Samples 110812_RMD and 110824_testJPC.)

6.1.2.1 JRM with Four Dolan Junctions

Figure 6.5 a) shows a SEM image of a junction resist mask, fabricated using the EBPG. The mask is shown at an angle of 40° , making it apparent that the bridge is suspended and that no resist remains underneath the undercuts. Figure 6.5 b) shows a Josephson junction fabricated with the EBPG. The dark areas are believed to be (insulating) aluminum oxide folding back onto the leads from the resist walls during lift-off.

6.1.2.2 Shunted JRM with Eight Dolan Junctions

Figure 6.6 shows a test device with eight Josephson junctions fabricated using the Dolan bridge technique. The large shunt junctions have a size of $5 \times 1 \mu\text{m}^2$ and the small junctions have an area of $1.5 \times 1 \mu\text{m}^2$. The one device successfully measured in the course of this work, which was fabricated with eight Dolan type Josephson junctions is JPXs01.

6.1.2.3 Shunted JRM with Eight BFT Junctions

A simpler way to make large Josephson junctions without having to worry about potentially collapsing bridges is to use the bridge-free technique (BFT) [63]. Instead of using a suspended bridge to separate the two junction electrodes, only one side of the leads connecting to the junction electrodes has undercuts. This way, arbitrary junction sizes and shapes can in principle be achieved, but constraints are set on the lead widths and lengths. Figure 6.7 shows a) a schematic of the mask design and b) an SEM image of the resulting Josephson junction. As can be seen, only one side of each junction lead receives an undercut dose (blue). When evaporating aluminum at two angles

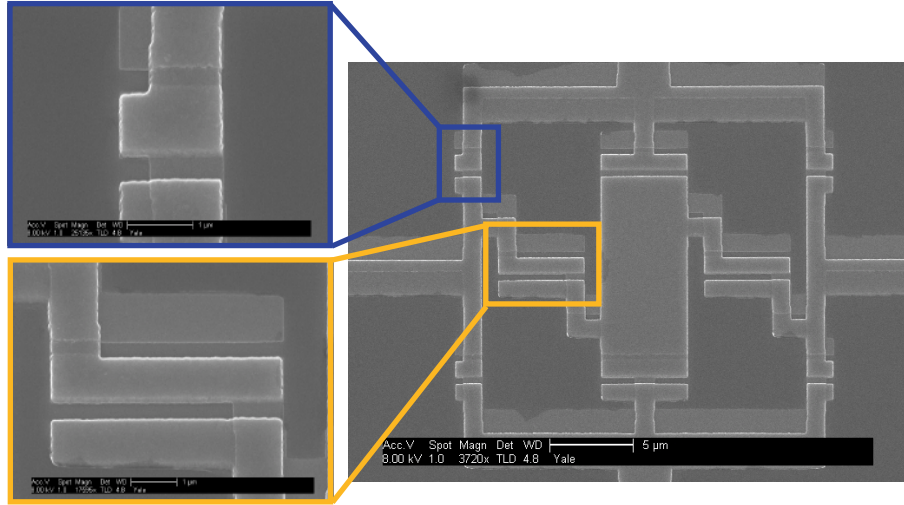


Figure 6.6: SEM image of a shunted JRM with eight Dolan type Josephson junctions. (Sample 2011-09-12_shuntedRMD.)

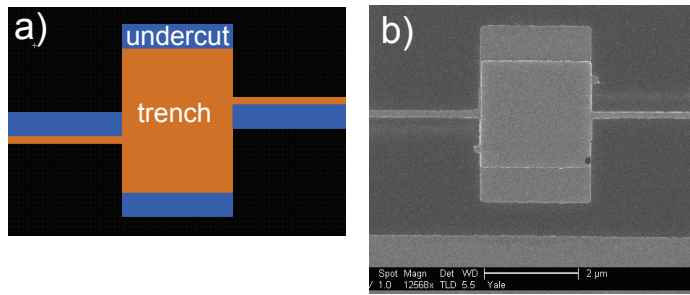


Figure 6.7: Josephson junction fabricated using the bridge-free technique. a) Mask design. b) SEM image of a resulting junction.

(here $\pm 25^\circ$), only one of the two layers will adhere to the substrate, the other will adhere to the resist walls and is removed during lift-off. Thus each junction electrode is connected only to one aluminum layer.

Figure 6.8 shows a) the CAD design and b) an SEM image of a shunted JRM. Junction sizes were chosen to be $1.5 \times 1.5 \mu\text{m}^2$ for the smaller JRM junctions and $2.3 \times 2.3 \mu\text{m}^2$ for the larger shunt junctions. In this thesis work, the aluminum layer thickness was 20 nm and 30 nm and as can be seen in the SEM images, the leads are of the order of 1-2 μm long and 200 nm wide. These dimensions are very likely to lead to non-negligible kinetic inductances of the wires (several tenths of pH) and subsequent generations of BFT JRMs were fabricated using thicker aluminum layers. One device with a shunted JRM fabricated with the BFT was extensively measured: JPXs04.

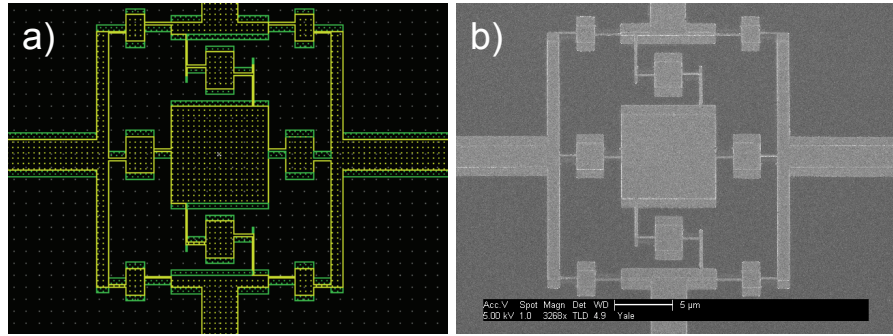


Figure 6.8: Shunted JRM fabricated using the bridge-free technique. a) CAD mask design. b) SEM image of a shunted JRM. (Sample 120114_BridgeFreeJRM)

6.1.3 Junction Aging

JPC samples were typically cooled down within a few days of sample fabrication. In this time, the large $5 \times 1 \mu\text{m}^2$ junctions fabricated with the Dolan bridge technique aged on average by $\sim 2 \Omega$ per day when cleaned with an argon-oxygen plasma before the deposition of the first aluminum layer. Typical resistance values (depending on the oxidation parameters) were from 50-100 Ω . Aging would vary significantly from wafer to wafer when removing the plasma cleaning step (e.g. to avoid collapsing bridges), and this although all wafers were cleaned with the same procedure before spinning resist. A “dirty” wafer could let the junctions age by as much as 300% within 24 hours of lift-off. Figure 6.9 shows the change of junction resistance vs. time for the junctions of a typical test JRM fabricated with the converted SEM. An optical microscope image of the measured device is shown on the right, which underwent plasma cleaning before the evaporation. The reference value of the junction resistance measured right after lift-off was 73Ω and the change refers to this initial value. In the first week after lift-off, the rate of change is approximately constant ($\sim 2 \Omega$ per day), and levels off afterward.

6.2 Sample Holder

JPC samples were mounted onto a copper sample holder base, initially using PMMA or GE varnish (Lake Shore VGE-7031 varnish), and most recently silver paste (SPI Supplies Silver Paste Plus). The advantage of silver paste is that it provides good thermal conductivity to samples with thin layers ($1 - 2 \mu\text{m}$) of silver evaporated on the substrate back side, while at the same time tying

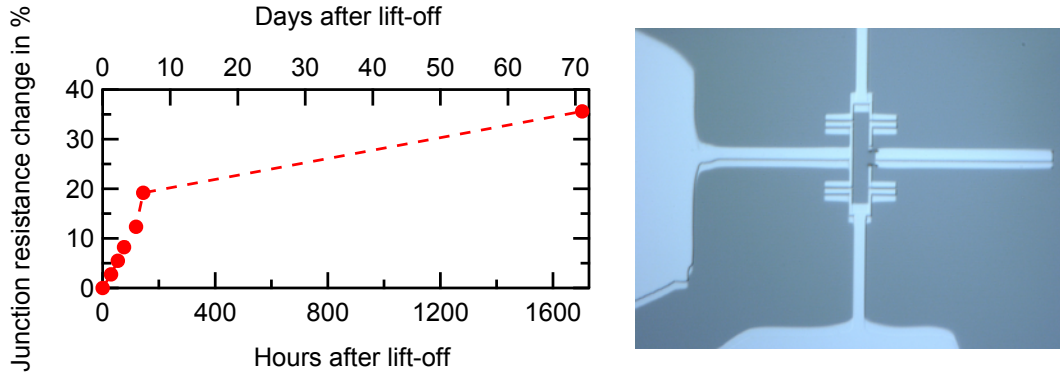


Figure 6.9: Change in measured Josephson junction resistance measured after lift-off. The test device is shown on the right. (Sample 100728_RMD.)

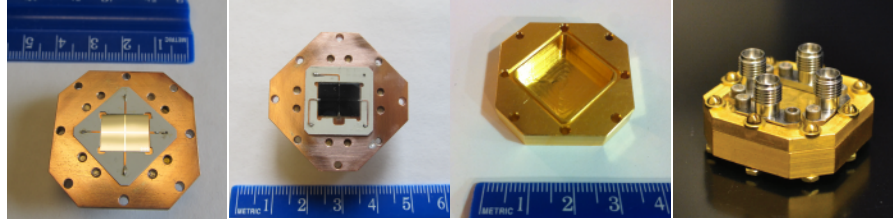


Figure 6.10: Photos of sample holder. From left to right: Sample holder base with mounted JPC sample, to be connected to two hybrids. Base with mounted JPC sample, to be connected to one hybrid (signal resonator shorted to ground on one side). Sample holder lid. Closed sample holder with Anritsu connectors (photo courtesy of Anirudh Narla).

together sample and sample holder ground planes. The sample holder lid together with the base form a cavity with approximate dimensions $1.85 \times 1.85 \times 0.5$ cm 3 . Anritsu K103F-R microwave connectors are attached to the holder base, designed with spacings compatible with Krytar hybrid couplers, so that they can be connected without additional transmission lines. Figure 6.10 shows JPC samples mounted onto sample holder bases (left two images), the sample holder lid, and the entire closed sample holder. A magnetic coil is placed in a small recess on the lid back side. Two types of printed circuit board (Rogers TMM 10I) 50 Ω transmission lines were used: One in a cross shape (left most image), when connecting both signal and idler resonators to hybrids, and the other with only one transmission line trace for the signal port (second image). In that case, the second resonator feed line was wire-bonded to ground.

A groove in the lid allows the box to be sealed with indium wire, ensuring good electrical contact

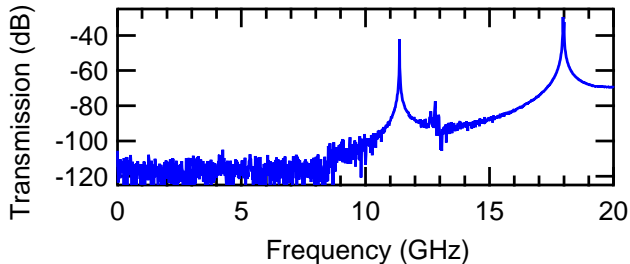


Figure 6.11: Insertion loss of sample box when connecting two of its ports to the network analyzer. The lowest box mode is above 11 GHz.

between lid and base. This is crucial to make sure no spurious resonant modes appear near the signal and idler frequencies. The lowest box mode for this geometry is at around 11 GHz, as can be seen in Fig. 6.11. Note that the presence of the sample and PC board pulls this frequency down by only a few 100 MHz, and thus it is still far away from typical signal and idler resonance frequencies of around 8 GHz and 6 GHz respectively.

6.3 Setup

6.3.1 Heliox Refrigerator

Experiments up to sample JPX09 were performed at around 250 mK in a Oxford Heliox ^3He refrigerator. One JPC sample was measured per cooldown, with a typical line diagram shown in Fig. 6.12. Signal and Idler input and output were separated by cryogenic circulators. Stainless steel cables were used between temperature stages inside the inner vacuum can (IVC), ensuring little thermal conductivity between them. high electron mobility transistor (HEMT) amplifiers on the output lines, separated by two isolators from the sample, amplified signals reflected off the device. The JPC samples were placed in high magnetic permeability Permalloy shields (Cryoperm by Amuneal) to minimize magnetic field noise in the JRM.

6.3.2 Triton Refrigerator

The majority of samples (JPX09-JPX30 and JPXs01-JPXs04) were measured in a cryogen free dilution refrigerator (Oxford Triton 200) at temperatures of around 25 mK. A typical wiring diagram of the microwave lines is shown in Fig. 6.13. A six-way switch (Radiall) at base allowed

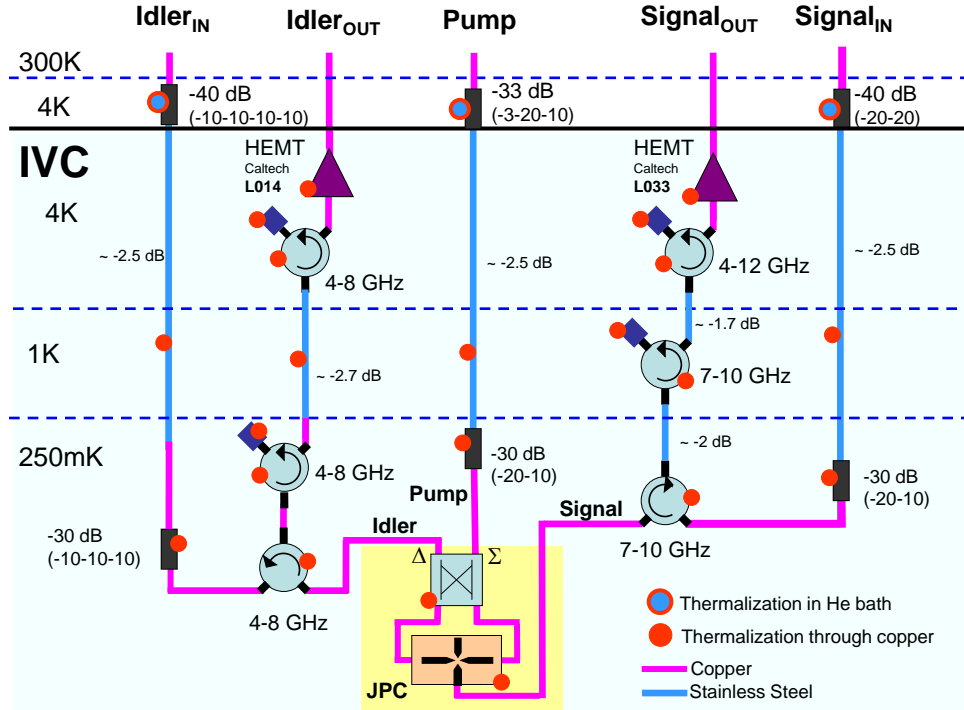


Figure 6.12: Wiring diagram of microwave lines in the Heliox refrigerator. One JPC sample can be measured at a time.

one to switch between several JPCs at low temperatures, so that several devices could be measured in a single cooldown. Also shown is a qubit which could be switched in or out with an additional transfer switch. Superconducting niobium-titanium cables were used to connect to the HEMT amplifiers and reduce losses without creating a thermal link between the temperature stages. Input lines were heavily attenuated to reduce room temperature noise to below quantum fluctuations.

Figure 6.14 shows a JPC sample at the refrigerator base temperature stage, symmetrically coupled to two hybrids, using short hand-formable copper cables. Also visible is a closed cryoperm shielding can on the left.

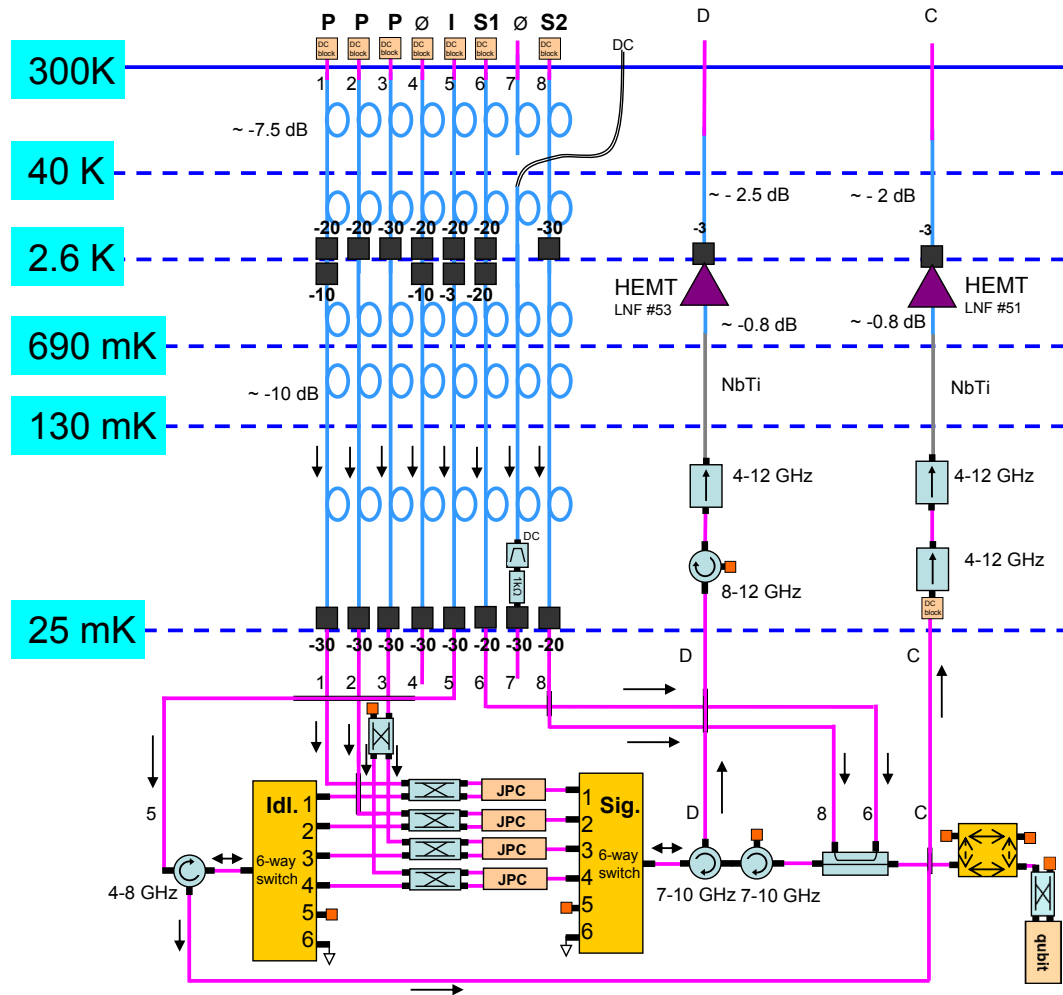


Figure 6.13: Wiring diagram of microwave lines in the Triton refrigerator. Six-way switches at the base stage allow for several samples to be measured during the same cooldown

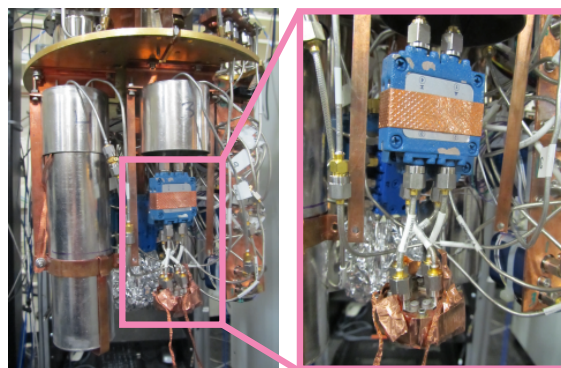


Figure 6.14: JPC sample mounted on dilution refrigerator base stage. Two cryoperm shields are visible, one open to access the sample. The right copper plate is a mount for the three microwave switches.

Chapter 7

Conclusion & Outlook

This thesis summarizes my work on building and operating a practical, quantum-limited, phase-preserving superconducting microwave parametric amplifier (paramp), the Josephson Parametric Converter (JPC), with the goal of making it useful for the readout of superconducting quantum bits (qubits). First, a new design of the JPC was developed, making the device parameters predictable and reproducible. The simple device fabrication, with only one lithography and evaporation step, considerably simplified device development, allowing to easily change all relevant parameters from one device to the next. The addition of a silver layer on the substrate back plane assured the reproducibility of resonator frequencies within a few MHz between nominally identical devices and thermal cycling.

Second, devices with parameters matching those of qubit readout cavities were developed. These JPCs had frequencies of between 5 and 8 GHz, amplifier bandwidths of 3 to 10 MHz at gains of 20 dB, while capable of processing a few photons and adding no more than 5/2 photons of noise, close to the quantum limit of 1/2. This allowed to improve the measurement efficiency in the measurement of a transmon qubit to 0.2 – 0.4, which is sufficiently close to the ideal value of 1 to perform variable strength measurements while observing the backaction, and to monitor the qubit state in real-time.

Third, the addition of shunt inductors in the Josephson Ring Modulator (JRM) made the new generation of JPCs frequency tunable, lifting the last major hurdle in using the JPC for qubit readout. Precise frequency matching of better than 5 MHz is required, the typical qubit readout cavity and JPC amplification bandwidths, and the tunable JPCs now easily achieve a tunability of

over 100 MHz.

Lastly, the experimental observation of Coherent Attenuation (CA) and gain enhancement in the reverse operation of the JPC fully demonstrates that the device is indeed described by a three-wave mixing term in the Hamiltonian of the form $a^\dagger b^\dagger c + abc^\dagger$, confirming that the JPC is close to the ideal quantum-limited, non-degenerate, phase-preserving paramp.

At this point, many new devices based on the work presented here have been fabricated and used in the readout of qubits, currently achieving measurement efficiencies of about 0.4. In future it might be desirable to have more amplification bandwidth available and to be able to measure with more than just a few photons. This could be achieved by moving towards a lumped (or more generally: low impedance) resonator design of the JPC and by increasing the junction critical currents. The fact that in a lumped circuit there should be no mode nearby the higher frequency pump, unlike in the microstrip case, would make the pump naturally stiff, so that these devices would be limited in gain and saturation powers by the available Josephson energy and need to be optimized only by engineering the $Q \cdot p$ -product and the ratio of the Josephson energy to the participation ratio to be sufficiently large. Since the lumped design makes it easy to increase the junction participation ratio, the resonator bandwidths could be increased without being penalized by a lowered $Q \cdot p$ -product. In fact, the participation ratio should be increased only as much as necessary to compensate for the decrease in Q , as the saturation power and maximum available gain increase with Josephson energy but decrease with p .

Bibliography

- [1] H. J. Kimble. Squeezed states of light: An (incomplete) survey of experimental progress and prospects. *Physics Report*, 219(3-6):227–234, 1992. Cited By (since 1996): 48. 3
- [2] P. A. Franken, A. E. Hill, C. W. Peters, and G. Weinreich. Generation of optical harmonics. *Phys. Rev. Lett.*, 7:118–119, Aug 1961. 3
- [3] W.H. Louisell. *Coupled mode and parametric electronics*. Wiley, 1960. 3
- [4] H. A. Haus and J. A. Mullen. Quantum noise in linear amplifiers. *Phys. Rev.*, 128:2407–2413, Dec 1962. 3
- [5] Carlton M. Caves. Quantum limits on noise in linear amplifiers. *Phys. Rev. D*, 26:1817–1839, Oct 1982. 3, 10, 89
- [6] A. A. Clerk, M. H. Devoret, S. M. Girvin, Florian Marquardt, and R. J. Schoelkopf. Introduction to quantum noise, measurement, and amplification. *Rev. Mod. Phys.*, 82:1155–1208, Apr 2010. 3
- [7] Chonghoon Kim, Ruo-Ding Li, and Prem Kumar. Deamplification response of a traveling-wave phase-sensitive optical parametric amplifier. *Opt. Lett.*, 19(2):132–134, Jan 1994. 3
- [8] Sang-Kyung Choi, Ruo-Ding Li, Chonghoon Kim, and Prem Kumar. Traveling-wave optical parametric amplifier: investigation of its phase-sensitive and phase-insensitive gain response. *J. Opt. Soc. Am. B*, 14(7):1564–1575, Jul 1997. 3, 6
- [9] Joseph Kakande, Carl Lundström, Peter A. Andrekson, Zhi Tong, Magnus Karlsson, Periklis Petropoulos, Francesca Parmigiani, and David J. Richardson. Detailed characterization of a fiber-optic parametric amplifier in phase-sensitive and phase-insensitive operation. *Opt. Express*, 18(5):4130–4137, Mar 2010. 3, 7

- [10] Takeshi Umeki, Osamu Tadanaga, Atsushi Takada, and Masaki Asobe. Phase sensitive degenerate parametric amplification using directly-bonded PPLN ridge waveguides. *Opt. Express*, 19(7):6326–6332, Mar 2011. 3
- [11] Masaki Asobe, Takeshi Umeki, and Osamu Tadanaga. Phase sensitive amplification with noise figure below the 3 dB quantum limit using CW pumped PPLN waveguide. *Opt. Express*, 20(12):13164–13172, Jun 2012. 3, 7
- [12] R. E. Slusher, L. W. Hollberg, B. Yurke, J. C. Mertz, and J. F. Valley. Observation of squeezed states generated by four-wave mixing in an optical cavity. *Phys. Rev. Lett.*, 55:2409–2412, Nov 1985. 3, 4
- [13] B. Yurke, P. G. Kaminsky, R. E. Miller, E. A. Whittaker, A. D. Smith, A. H. Silver, and R. W. Simon. Observation of 4.2-K equilibrium-noise squeezing via a Josephson-parametric amplifier. *Phys. Rev. Lett.*, 60:764–767, Feb 1988. 4
- [14] B. Yurke, L. R. Corruccini, P. G. Kaminsky, L. W. Rupp, A. D. Smith, A. H. Silver, R. W. Simon, and E. A. Whittaker. Observation of parametric amplification and deamplification in a Josephson parametric amplifier. *Phys. Rev. A*, 39:2519–2533, Mar 1989. 4
- [15] R. Movshovich, B. Yurke, P. G. Kaminsky, A. D. Smith, A. H. Silver, R. W. Simon, and M. V. Schneider. Observation of zero-point noise squeezing via a Josephson-parametric amplifier. *Phys. Rev. Lett.*, 65:1419–1422, Sep 1990. 4
- [16] H. Zimmer. Parametric amplification of microwaves in superconducting josephson tunnel junctions. *Applied Physics Letters*, 10(7):193–195, 1967. 4
- [17] N. F. Pedersen, M. R. Samuelsen, and K. Saermark. Parametric excitation of plasma oscillations in josephson junctions. *Journal of Applied Physics*, 44(11):5120–5124, 1973. 4
- [18] J. Mygind, N. F. Pedersen, O. H. Soerensen, B. Dueholm, and M. T. Levinsen. Low-noise parametric amplification at 35 GHz in a single Josephson tunnel junction. *Applied Physics Letters*, 35(1):91–93, 1979. 4
- [19] M. H. Devoret and R. J. Schoelkopf. Superconducting circuits for quantum information: An outlook. *Science*, 339(6124):1169–1174, 2013. 4

- [20] M. A. Castellanos-Beltran and K. W. Lehnert. Widely tunable parametric amplifier based on a superconducting quantum interference device array resonator. *Applied Physics Letters*, 91(8):083509, 2007. 4, 9, 74, 81
- [21] M. A. Castellanos-Beltran, K. D. Irwin, G. C. Hilton, L. R. Vale, and K. W. Lehnert. Amplification and squeezing of quantum noise with a tunable Josephson metamaterial. *Nat. Phys.*, 4(12):928–931, 2008. 4
- [22] T. Yamamoto, K. Inomata, M. Watanabe, K. Matsuba, T. Miyazaki, W. D. Oliver, Y. Nakamura, and J. S. Tsai. Flux-driven Josephson parametric amplifier. *Applied Physics Letters*, 93(4):042510, 2008. 4, 10, 74, 81, 86
- [23] M. Hatridge, R. Vijay, D. H. Slichter, John Clarke, and I. Siddiqi. Dispersive magnetometry with a quantum limited SQUID parametric amplifier. *Phys. Rev. B*, 83:134501, Apr 2011. 4, 9, 74, 81
- [24] N. Bergeal, F. Schackert, M. Metcalfe, R. Vijay, V. E. Manucharyan, L. Frunzio, D. E. Prober, R. J. Schoelkopf, S. M. Girvin, and M. H. Devoret. Phase-preserving amplification near the quantum limit with a Josephson ring modulator. *Nature*, 465(7294):64–68, May 2010. 4, 20
- [25] N. Bergeal, R. Vijay, V. E. Manucharyan, I. Siddiqi, R. J. Schoelkopf, S. M. Girvin, and M. H. Devoret. Analog information processing at the quantum limit with a Josephson ring modulator. *Nat. Phys.*, 6(4):296–302, April 2010. 4, 27, 70
- [26] Baleegh Abdo, Flavius Schackert, Michael Hatridge, Chad Rigetti, and Michel Devoret. Josephson amplifier for qubit readout. *Applied Physics Letters*, 99(16):162506, 2011. 4, 28, 31
- [27] Baleegh Abdo, Archana Kamal, and Michel Devoret. Nondegenerate three-wave mixing with the Josephson ring modulator. *Phys. Rev. B*, 87:014508, Jan 2013. 4, 27, 28, 30, 69, 70, 75
- [28] N. Roch, E. Flurin, F. Nguyen, P. Morfin, P. Campagne-Ibarcq, M. H. Devoret, and B. Huard. Widely tunable, nondegenerate three-wave mixing microwave device operating near the quantum limit. *Phys. Rev. Lett.*, 108:147701, Apr 2012. 4, 25, 26, 31, 64
- [29] Erik A. Tholén, Adem Ergül, Evelyn M. Doherty, Frank M. Weber, Fabien Grégis, and David B. Haviland. Nonlinearities and parametric amplification in superconducting coplanar waveguide resonators. *Applied Physics Letters*, 90(25):253509, 2007. 4, 74, 81

- [30] B. Ho Eom, P. K. Day, H. G. Leduc, and J. Zmuidzinas. A wideband, low-noise superconducting amplifier with high dynamic range. *Nat. Phys.*, 8(8):623–627, 2012. Cited By (since 1996): 5. 4, 7
- [31] M. Mück and R. McDermott. Radio-frequency amplifiers based on dc SQUIDs. *Superconductor Science and Technology*, 23(9), 2010. Cited By (since 1996): 10. 4
- [32] Lafe Spietz, Kent Irwin, and José Aumentado. Input impedance and gain of a gigahertz amplifier using a dc superconducting quantum interference device in a quarter wave resonator. *Applied Physics Letters*, 93(8):082506, 2008. 4
- [33] Lafe Spietz, Kent Irwin, and José Aumentado. Superconducting quantum interference device amplifiers with over 27 Ghz of gain-bandwidth product operated in the 4–8 Ghz frequency range. *Applied Physics Letters*, 95(9):092505, 2009. 4
- [34] Lafe Spietz, Kent Irwin, Minhyea Lee, and José Aumentado. Noise performance of lumped element direct current superconducting quantum interference device amplifiers in the 4–8 Ghz range. *Applied Physics Letters*, 97(14):142502, 2010. 4
- [35] Archana Kamal, John Clarke, and Michel H. Devoret. Gain, directionality, and noise in microwave SQUID amplifiers: Input-output approach. *Phys. Rev. B*, 86:144510, Oct 2012. 4
- [36] J. D. Teufel, T. Donner, M. A. Castellanos-Beltran, J. W. Harlow, and K. W. Lehnert. Nanomechanical motion measured with an imprecision below that at the standard quantum limit. *Nature Nanotechnology*, 4(12):820–823, 2009. Cited By (since 1996):107. 4
- [37] R. Vijay, D. H. Slichter, and I. Siddiqi. Observation of quantum jumps in a superconducting artificial atom. *Phys. Rev. Lett.*, 106:110502, Mar 2011. 5, 12, 17, 33
- [38] D. Ristè, C. C. Bultink, K. W. Lehnert, and L. DiCarlo. Feedback control of a solid-state qubit using high-fidelity projective measurement. *Phys. Rev. Lett.*, 109:240502, Dec 2012. 5, 17
- [39] D. Ristè, J. G. van Leeuwen, H.-S. Ku, K. W. Lehnert, and L. DiCarlo. Initialization by measurement of a superconducting quantum bit circuit. *Phys. Rev. Lett.*, 109:050507, Aug 2012. 5

- [40] R. Vijay, C. MacKlin, D. H. Slichter, S. J. Weber, K. W. Murch, R. Naik, A. N. Korotkov, and I. Siddiqi. Stabilizing Rabi oscillations in a superconducting qubit using quantum feedback. *Nature*, 490(7418):77–80, 2012. Cited By (since 1996): 7. 5, 17
- [41] P. Campagne-Ibarcq, E. Flurin, N. Roch, D. Darson, P. Morfin, M. Mirrahimi, M. H. Devoret, F. Mallet, and B. Huard. Stabilizing the trajectory of a superconducting qubit by projective measurement feedback. *ArXiv e-prints*, January 2013. 5, 17
- [42] M. Hatridge, S. Shankar, M. Mirrahimi, F. Schackert, K. Geerlings, T. Brecht, K. M. Sliwa, B. Abdo, L. Frunzio, S. M. Girvin, R. J. Schoelkopf, and M. H. Devoret. Quantum back-action of an individual variable-strength measurement. *Science*, 339(6116):178–181, 2013. 5, 17, 33, 35
- [43] B. Yurke and E. Buks. Performance of cavity-parametric amplifiers, employing Kerr nonlinearities, in the presence of two-photon loss. *Journal of Lightwave Technology*, 24(12):5054–5066, 2006. Cited By (since 1996):40. 9
- [44] I. Siddiqi, R. Vijay, F. Pierre, C. M. Wilson, M. Metcalfe, C. Rigetti, L. Frunzio, and M. H. Devoret. RF-driven Josephson bifurcation amplifier for quantum measurement. *Phys. Rev. Lett.*, 93:207002, Nov 2004. 9
- [45] Rajamani Vijayaraghavan. *Josephson Bifurcation Amplifier: Amplifying quantum signals using a dynamical bifurcation*. PhD thesis, Yale University, 2008. 9
- [46] R. Vijay, M. H. Devoret, and I. Siddiqi. Invited review article: The Josephson bifurcation amplifier. *Review of Scientific Instruments*, 80(11), 2009. Cited By (since 1996): 43. 9
- [47] Archana Kamal, Adam Marblestone, and Michel Devoret. Signal-to-pump back action and self-oscillation in double-pump Josephson parametric amplifier. *Phys. Rev. B*, 79:184301, May 2009. 9
- [48] J. M. Manley and H.E. Rowe. Some general properties of nonlinear elements-part i. general energy relations. *Proceedings of the IRE*, 44(7):904–913, 1956. 14
- [49] M. Devoret, S. Girvin, and R. Schoelkopf. Circuit-QED: How strong can the coupling between a Josephson junction atom and a transmission line resonator be? *Annalen der Physik (Leipzig)*, 16(10-11):767–779, 2007. Cited By (since 1996):61. 16

- [50] A. Wallraff, D. I. Schuster, A. Blais, L. Frunzio, R. . Huang, J. Majer, S. Kumar, S. M. Girvin, and R. J. Schoelkopf. Strong coupling of a single photon to a superconducting qubit using circuit quantum electrodynamics. *Nature*, 431(7005):162–167, 2004. Cited By (since 1996):1129. 16, 33
- [51] D. I. Schuster, A. A. Houck, J. A. Schreier, A. Wallraff, J. M. Gambetta, A. Blais, L. Frunzio, J. Majer, B. Johnson, M. H. Devoret, S. M. Girvin, and R. J. Schoelkopf. Resolving photon number states in a superconducting circuit. *Nature*, 445(7127):515–518, 2007. Cited By (since 1996):257. 16
- [52] S. Haroche and J.-M. Raimond. *Exploring the Quantum: Atoms, Cavities, and Photons*. Oxford University Press, USA, 2006. 16
- [53] S. Gleyzes, S. Kuhr, C. Guerlin, J. Bernu, S. Deléglise, U. Busk Hoff, M. Brune, J. . Raimond, and S. Haroche. Quantum jumps of light recording the birth and death of a photon in a cavity. *Nature*, 446(7133):297–300, 2007. Cited By (since 1996):149. 16
- [54] N. Wadefalk, A. Mellberg, I. Angelov, M. E. Barsky, S. Bui, E. Choumas, R. W. Grundbacher, E. L. Kollberg, R. Lai, N. Rorsman, P. Starski, J. Stenarson, D. C. Streit, and H. Zirath. Cryogenic wide-band ultra-low-noise IF amplifiers operating at ultra-low DC power. *IEEE Transactions on Microwave Theory and Techniques*, 51(6):1705–1711, 2003. Cited By (since 1996):67. 17
- [55] Jens Koch, Terri M. Yu, Jay Gambetta, A. A. Houck, D. I. Schuster, J. Majer, Alexandre Blais, M. H. Devoret, S. M. Girvin, and R. J. Schoelkopf. Charge-insensitive qubit design derived from the Cooper pair box. *Phys. Rev. A*, 76:042319, Oct 2007. 17
- [56] J. A. Schreier, A. A. Houck, J. Koch, D. I. Schuster, B. R. Johnson, J. M. Chow, J. M. Gambetta, J. Majer, L. Frunzio, M. H. Devoret, S. M. Girvin, and R. J. Schoelkopf. Suppressing charge noise decoherence in superconducting charge qubits. *Physical Review B - Condensed Matter and Materials Physics*, 77(18), 2008. Cited By (since 1996):126. 17
- [57] A. A. Houck, J. Koch, M. H. Devoret, S. M. Girvin, and R. J. Schoelkopf. Life after charge noise: Recent results with transmon qubits. *Quantum Information Processing*, 8(2-3):105–115, 2009. Cited By (since 1996):22. 17, 33

- [58] V. E. Manucharyan, J. Koch, L. I. Glazman, and M. H. Devoret. Fluxonium: Single Cooper-pair circuit free of charge offsets. *Science*, 326(5949):113–116, 2009. Cited By (since 1996):57. 17, 33
- [59] Hanhee Paik, D. I. Schuster, Lev S. Bishop, G. Kirchmair, G. Catelani, A. P. Sears, B. R. Johnson, M. J. Reagor, L. Frunzio, L. I. Glazman, S. M. Girvin, M. H. Devoret, and R. J. Schoelkopf. Observation of high coherence in Josephson junction qubits measured in a three-dimensional circuit QED architecture. *Phys. Rev. Lett.*, 107:240501, Dec 2011. 17, 33
- [60] M. Hatridge et al. In preparation. 2013. 17
- [61] D.M. Pozar. *Microwave engineering*. Wiley, 1997. 18, 97
- [62] G. J. Dolan. Offset masks for lift-off photoprocessing. *Applied Physics Letters*, 31(5):337–339, 1977. 20, 46, 65, 124
- [63] F. Lecocq, I. M. Pop, Z. Peng, I. Matei, T. Crozes, T. Fournier, C. Naud, W. Guichard, and O. Buisson. Junction fabrication by shadow evaporation without a suspended bridge. *Nanotechnology*, 22(31), 2011. Cited By (since 1996):3. 20, 65, 128
- [64] M. Goppl, A. Fragner, M. Baur, R. Bianchetti, S. Filipp, J. M. Fink, P. J. Leek, G. Puebla, L. Steffen, and A. Wallraff. Coplanar waveguide resonators for circuit quantum electrodynamics. *Journal of Applied Physics*, 104(11):113904, 2008. 22
- [65] K. Sliwa and M. Hatridge. Private communication. 26
- [66] N. Bergeal, F. Schackert, L. Frunzio, D. E. Prober, and M. H. Devoret. Mesoscopic resistor as a self-calibrating quantum noise source. *Applied Physics Letters*, 100(20):203507, 2012. 31
- [67] Flavius Schackert, Ananda Roy, Michael Hatridge, Michel H. Devoret, and A. Douglas Stone. Three-wave mixing with three incoming waves: Signal-idler coherent attenuation and gain enhancement in a parametric amplifier. *Phys. Rev. Lett.*, 111:073903, Aug 2013. 36, 108, 110
- [68] E. Flurin. Amplificateur paramétrique Josephson près de la limite quantique. Master’s thesis, École Normale Supérieure, 2011. 45
- [69] B. Abdo, A. Kamal, and M. H. Devoret. *Fluctuating Nonlinear Oscillators: From Nanomechanics to Quantum Superconducting Circuits*. OUP Oxford, 2012. 69

- [70] N. Bergeal, F. Schackert, L. Frunzio, and M. H. Devoret. Two-mode correlation of microwave quantum noise generated by parametric down-conversion. *Phys. Rev. Lett.*, 108:123902, Mar 2012. 74, 93, 95
- [71] E. Flurin, N. Roch, F. Mallet, M. H. Devoret, and B. Huard. Generating entangled microwave radiation over two transmission lines. *Phys. Rev. Lett.*, 109:183901, Oct 2012. 74, 93, 95
- [72] C. E. Shannon. A mathematical theory of communication. *The Bell System Technical Journal*, 27:379–423, 623–656, 1948. 75
- [73] C. E. Shannon and W. Weaver. *The Mathematical Theory of Communication*. University of Illinois Press, 1971. 75
- [74] Archana Kamal, John Clarke, and M. H. Devoret. Noiseless non-reciprocity in a parametric active device. *Nat. Phys.*, 7(4):311–315, Apr 2011. 81
- [75] Baleegh Abdo, Katrina Sliwa, Flavius Schackert, Nicolas Bergeal, Michael Hatridge, Luigi Frunzio, A. Douglas Stone, and Michel Devoret. Full coherent frequency conversion between two propagating microwave modes. *Phys. Rev. Lett.*, 110:173902, Apr 2013. 85
- [76] S. Friberg, C. K. Hong, and L. Mandel. Measurement of time delays in the parametric production of photon pairs. *Phys. Rev. Lett.*, 54:2011–2013, May 1985. 93
- [77] I. J. Bahl and Ramesh Garg. Simple and accurate formulas for a microstrip with finite strip thickness. *Proceedings of the IEEE*, 65(11):1611–1612, 1977. Cited By (since 1996):38. 99
- [78] Ramesh Garg and I. J. Bahl. Microstrip discontinuities. *International Journal of Electronics*, 45(1):81–87, 1978. Cited By (since 1996):22. 99
- [79] J. A. Armstrong, N. Bloembergen, J. Ducuing, and P. S. Pershan. Interactions between light waves in a nonlinear dielectric. *Phys. Rev.*, 127:1918–1939, Sep 1962. 108
- [80] Alain Aspect, Philippe Grangier, and Gérard Roger. Experimental tests of realistic local theories via Bell’s theorem. *Phys. Rev. Lett.*, 47:460–463, Aug 1981. 108
- [81] Paul G. Kwiat, Klaus Mattle, Harald Weinfurter, Anton Zeilinger, Alexander V. Sergienko, and Yanhua Shih. New high-intensity source of polarization-entangled photon pairs. *Phys. Rev. Lett.*, 75:4337–4341, Dec 1995. 108

- [82] Y. D. Chong, Li Ge, Hui Cao, and A. D. Stone. Coherent perfect absorbers: Time-reversed lasers. *Phys. Rev. Lett.*, 105:053901, Jul 2010. 108
- [83] Wenjie Wan, Yidong Chong, Li Ge, Heeso Noh, A. Douglas Stone, and Hui Cao. Time-reversed lasing and interferometric control of absorption. *Science*, 331(6019):889–892, 2011. 108
- [84] Stefano Longhi. Time-reversed optical parametric oscillation. *Phys. Rev. Lett.*, 107:033901, Jul 2011. 108
- [85] R. H. Dicke. The measurement of thermal radiation at microwave frequencies. *Review of Scientific Instruments*, 17(7):268–275, 1946. 118

Appendix A

Transmission Line Resonators

The purpose of this appendix chapter is to calculate the quality factor of transmission line resonators capacitively coupled to a $50\ \Omega$ environment. As will be shown below, for a fixed resonator frequency and characteristic transmission line impedance, the quality factor is entirely determined by the coupling capacitors. This is important as it allows to engineer the Josephson Parametric Converter's (JPC) signal and idler linear resonator bandwidths, which in turn determine the amplification bandwidth of the device.

A.1 Parallel RLC Resonator

In this section, we review the parallel RLC circuit¹. It is the basis to all further analysis and will allow us to easily determine the resonance frequency as well as the quality factor Q of a transmission line resonator. There are three references we use for all of the following notes: Wallraff's notes on SC solid state qubits, Pozar, and chapter 3 of Dave Schuster's PhD thesis.

¹See Pozar, 3rd edition, pages 269-272

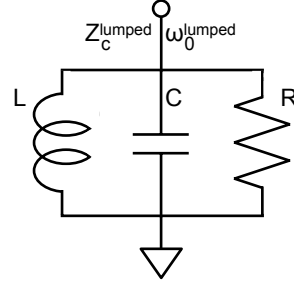


Figure A.1: RLC resonant circuit.

The input impedance of a parallel RLC resonant circuit is ² (see figure A.1):

$$\begin{aligned}
 Z_{in}(\omega) &= \left(\frac{1}{R} + \frac{1}{j\omega L} + j\omega C \right)^{-1} \\
 &= \left(\frac{1}{R} + \frac{1}{j\omega_0^{lumped} L} \left(\frac{1}{1 + \Delta\omega/\omega_0^{lumped}} \right) + j\omega_0^{lumped} C + j\Delta\omega C \right)^{-1} \\
 &\approx \left(\frac{1}{R} + \frac{1}{j\omega_0^{lumped} L} \left(1 - \Delta\omega/\omega_0^{lumped} \right) + j\omega_0^{lumped} C + j\Delta\omega C \right)^{-1} \\
 &= \left(\frac{1}{R} + \frac{j\Delta\omega}{(\omega_0^{lumped})^2 L} + j\Delta\omega C \right)^{-1} \\
 &= \left(\frac{1}{R} + 2j\Delta\omega C \right)^{-1} \\
 &= \frac{R}{1 + 2j\Delta\omega RC}
 \end{aligned} \tag{A.1}$$

for $\boxed{\omega = \omega_0^{lumped} + \Delta\omega \text{ and } \Delta\omega \ll \omega_0^{lumped}}$. We thus find:

$$\begin{aligned}
 Z_{in} \approx \frac{R}{1 + 2jQ\Delta\omega/\omega_0^{lumped}} \quad &\text{for } \omega = \omega_0^{lumped} + \Delta\omega \\
 &\text{and } \Delta\omega \ll \omega_0^{lumped}
 \end{aligned} \tag{A.2}$$

Where we have used the following identities:

²See Pozar, page 270, eqn. (6.19)

$$\omega_0^{lumped} \equiv \frac{1}{\sqrt{LC}} \quad (A.3)$$

$$Q \equiv \omega_0^{lumped} RC = \frac{R}{Z_c^{lumped}} \quad (A.4)$$

$$Z_c^{lumped} \equiv \sqrt{\frac{L}{C}} \quad (A.5)$$

A.2 Transmission Line Resonator

In this section we want to show that an open-circuited $\lambda/2$ transmission line (TL) has the same input impedance as a parallel RLC circuit when $\Delta\omega \ll \omega_0$. The input impedance of an open-circuited TL of length l is³ (see figure (A.2)):

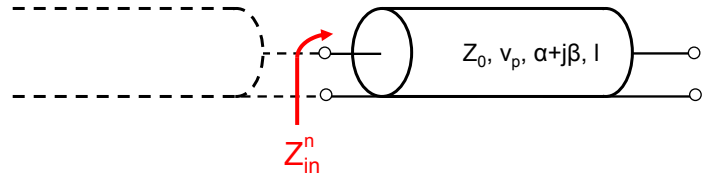


Figure A.2: Open-ended TL.

$$Z_{in} = Z_0 \coth(\alpha l + j\beta l) \quad (A.6)$$

$$= Z_0 \frac{1 + j \tan \beta l \tanh \alpha l}{\tanh \alpha l + j \tan \beta l}, \quad (A.7)$$

³see Pozar, page 276; Wallraff notes, section 2.2, page 8

where $\alpha(\omega)$, $\beta(\omega)$, $Z_0(\omega)$, $l(=\text{const.})$ completely define the transmission line, with

$$Z_0(\omega) = \sqrt{\frac{\mathcal{R} + j\omega\mathcal{L}}{\mathcal{G} + j\omega\mathcal{C}}} \quad (\text{A.8})$$

$$\gamma(\omega) = \alpha + j\beta = \sqrt{(\mathcal{R} + j\omega\mathcal{L})(\mathcal{G} + j\omega\mathcal{C})} \quad (\text{A.9})$$

$$v_p(\omega) = \frac{1}{\beta(\omega)}\omega = \frac{\lambda(\omega)}{2\pi}\omega = \lambda(f)f. \quad (\text{A.10})$$

Note at this point that in the most general case $v_p = v(\omega)$ which defines the dispersion relation of the TL. In most cases we encounter, $v_p = \text{const.}$, as for instance for TEM waves where $v_p = \frac{c}{\sqrt{\epsilon_r}} = \text{const.}$ (assuming ϵ_r is not a function of frequency). Also in the lossless case (or low-loss case, see below) we have $v_p = \frac{1}{\sqrt{\mathcal{L}\mathcal{C}}} = \text{const.}$ (unless \mathcal{C} or \mathcal{L} are frequency dependent through e.g. ϵ_r).

We now want to consider only frequencies ω around the harmonics ω_n of the TL. The condition for a TL line of fixed length l to be resonating is that a multiple of half a wavelength fits into l :

$$\boxed{n \frac{\lambda_n}{2} = l.} \quad (\text{A.11})$$

This equation defines the wavelengths of the n-th harmonic, which occur at the frequency ω_n . Equation (A.10) then allows us to explicitly calculate the frequencies at which the resonant condition is met:

$$\boxed{\omega_n = n \frac{\pi v_p}{l} = n\omega_1} \quad (\text{A.12})$$

and

$$\beta l = n\pi \frac{\omega}{\omega_n} = n\pi + \pi \frac{\Delta\omega_n}{\omega_1}, \quad (\text{A.13})$$

with $\Delta\omega_n := \omega - \omega_n$.

For frequencies close to resonance, i.e. for $\boxed{\omega = \omega_n + \Delta\omega_n \text{ and } \Delta\omega_n \ll \omega_1}$ ⁴, and using the identity $\tan(n\pi + x) = \tan x$ and $\tan \beta l \approx \pi \frac{\Delta\omega_n}{\omega_1}$ and assuming that the TL has small losses ($\tanh \alpha l \approx \alpha l$), we then find the input impedance of the TL around the n -th mode to be:

$$\boxed{Z_{in}^n \approx \frac{Z_0/n}{(\alpha/n)l + j\pi \frac{\Delta\omega_n}{\omega_n}} \quad \text{for } \omega = \omega_n + \Delta\omega_n \text{ and } \Delta\omega_n \ll \omega_1} \quad (\text{A.14})$$

⁴Note that this condition is the same as for the parallel RLC case only for the first mode. For higher modes this condition is stricter.

A.3 Mapping of an (unloaded) TL Resonator to a RLC Resonator

Comparing equation (A.2) to equation (A.14) shows that around the n -th harmonic ($\omega \approx \omega_n$), we can map an (unloaded) TL resonator to a RLC resonator, with the following equalities (see figure A.3):

$$Z_{c,n}^{\text{lumped}} = \sqrt{\frac{L_n}{C_n}} = \frac{2 Z_0}{\pi n} \quad (\text{A.15})$$

$$\omega_n^{\text{lumped}} = \omega_n = \frac{1}{\sqrt{L_n C_n}} = n\omega_1 \quad (\text{A.16})$$

$$R_n = \frac{Z_0}{\alpha l} = R_1 \quad (\text{A.17})$$

$$C_n = \frac{\pi}{2\omega_n Z_0 / n} = \frac{\pi}{2\omega_1 Z_0} = C_1 \quad (\text{A.18})$$

$$L_n = \frac{2Z_0/n}{\pi\omega_n} = \frac{L_1}{n^2}, \quad (\text{A.19})$$

where R_n , L_n , and C_n are the parameters for the equivalent RLC resonator around ω_n .

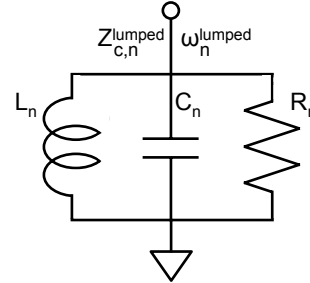


Figure A.3: Parallel RLC resonant circuit equivalent to an open-ended TL (see figure (A.2)) around resonance.

Finally the correspondence allows us to determine the quality factor of the unloaded TL resonator around the n -th harmonic as

$$Q_n = \frac{n\pi}{2\alpha l} = nQ_1 \quad (\text{A.20})$$

For the low-loss case⁵ where $Z_0 \approx \sqrt{\frac{C}{\mathcal{L}}}$ and $v_p \approx \frac{1}{\sqrt{\mathcal{L}C}}$ and $\alpha \approx \frac{1}{2}(\frac{\mathcal{R}}{Z_0} + \mathcal{G}Z_0)$ we further have:

$$C_n = \frac{l}{2}\mathcal{C} \quad (\text{low-loss}) \quad (\text{A.21})$$

$$L_n = \frac{2l}{n^2\pi^2}\mathcal{L}. \quad (\text{low-loss}) \quad (\text{A.22})$$

A.4 Loaded TL Resonator

A.4.1 Admittance of Load

Now that we have established the equivalence between an unloaded TL resonator and a parallel RLC resonator, we will look at the case where a TL resonator is coupled to the environment through an input capacitance (figure (A.4)). This is equivalent to a RLC resonator coupled to the same environment.

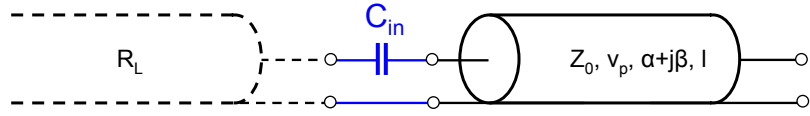


Figure A.4: Open-ended TL resonator with input capacitor.

First, let's calculate the admittance of the load:

$$Y_{load} = \left(\frac{1}{j\omega C_{in}} + R_L \right)^{-1} \quad (\text{A.23})$$

$$= \left(\frac{1 + j\omega R_L C_{in}}{j\omega C_{in}} \right)^{-1} \quad (\text{A.24})$$

$$= \frac{j\omega C_{in}}{1 + j\omega R_L C_{in}} \quad (\text{A.25})$$

$$= \frac{\omega^2 R_L C_{in}^2 + j\omega C_{in}}{1 + \omega^2 R_L^2 C_{in}^2}, \quad (\text{A.26})$$

⁵Pozar chapter 2.7, p.79-80

where C_{in} and R_L are the input capacitor and the load resistor (or impedance of the measurement line) respectively. This is equivalent to an effective capacitor C^* and effective resistor R^* in parallel, which has the admittance

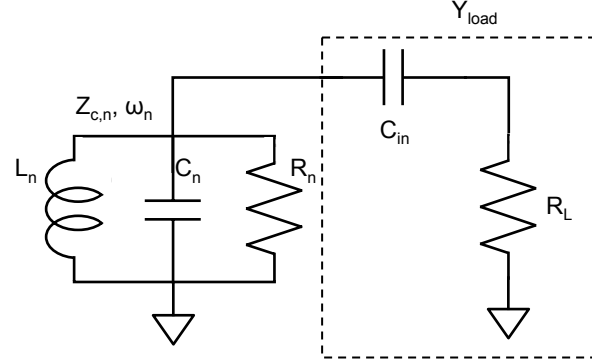


Figure A.5: A transmission line with impedance R_L capacitively coupled to a TL-resonator is equivalent to a loaded RLC resonant circuit. Parallel RLC resonator loaded with an input capacitor and a load resistor.

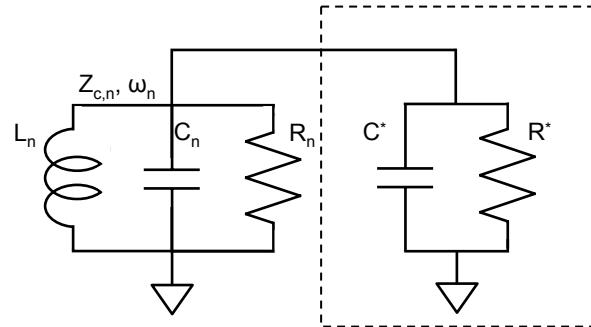


Figure A.6: A transmission line with impedance R_L capacitively coupled to a TL-resonator is equivalent to a loaded RLC resonant circuit. Equivalent circuit to figure A.5.

$$Y_{load} = j\omega C^* + \frac{1}{R^*}. \quad (\text{A.27})$$

Comparing equation (A.27) to equation (A.26) allows us to identify:

$$C^* = C^{in} \frac{1}{1 + q_{in}^2} \quad (\text{A.28})$$

$$R^* = R_L \frac{1 + q_{in}^2}{q_{in}^2} \quad (\text{A.29})$$

$$q_{in} := \omega R_L C_{in}. \quad (\text{A.30})$$

A.4.2 External Q: Input Coupling Only

As a last step we will now determine the Q of the *loaded* resonator. For this we can just use the results from section A.1 a second time with

$$C = C_n + C^* \equiv C_1 + C^* \quad (\text{A.31})$$

$$R = \left((R_n)^{-1} + (R^*)^{-1} \right)^{-1} \equiv \left((R_1)^{-1} + (R^*)^{-1} \right)^{-1} \quad (\text{A.32})$$

$$L = L_n \equiv \frac{L_1}{n^2} \quad (\text{A.33})$$

$$\omega_{0,n} = \frac{1}{\sqrt{LC}} = n \frac{1}{\sqrt{L_1(C_1 + C^*)}} \quad (\text{A.34})$$

According to equation (A.4) we then have

$$Q = \frac{1}{Z_c} \cdot \frac{1}{\text{Re}\{Y_{total}\}} \quad (\text{A.35})$$

$$= \sqrt{\frac{C}{L}} \cdot R \quad (\text{A.36})$$

$$= \sqrt{\frac{C_n}{L_n}} \sqrt{\frac{C_n + C^*}{C_n}} \cdot \left(\frac{1}{R_n} + \frac{1}{R^*} \right)^{-1} \quad (\text{A.37})$$

$$= \underbrace{\sqrt{\frac{C_n}{L_n}} \frac{\omega_n}{\omega_{0,n}}}_{\text{correction factor}} \cdot \left(\frac{1}{R_n} + \frac{1}{R^*} \right)^{-1} \quad (\text{A.38})$$

$$\stackrel{\text{eqn. (A.15)}}{=} \frac{n\pi}{2} \frac{1}{Z_0} \frac{\omega_n}{\omega_{0,n}} \cdot \left(\frac{1}{R_n} + \frac{1}{R^*} \right)^{-1} \quad (\text{A.39})$$

$$= \frac{n\pi}{2} \frac{1}{Z_0} \frac{\omega_1}{\omega_{0,1}} \cdot \left(\frac{1}{R_1} + \frac{1}{R^*} \right)^{-1} \quad (\text{A.40})$$

$$\stackrel{\text{eqn. (A.28)}}{=} \frac{n\pi}{2} \frac{1}{Z_0} \frac{\omega_1}{\omega_{0,1}} \cdot \left(\frac{1}{R_1} + \frac{1}{\frac{1}{\omega_n^2 C_{in}^2 R_L} + R_L} \right)^{-1} \quad (\text{A.41})$$

$$= \left(\frac{1}{Q_{int}} + \frac{1}{Q_{ext}} \right)^{-1}. \quad (\text{A.42})$$

With this definition of Q_{int} we have already taken care of the loading⁶. For the external quality factor we thus find:

$$Q_{ext} = \frac{1}{Z_c \operatorname{Re}\{Y_{load}\}} = \frac{\omega_1}{\omega_{0,1}} \frac{1}{Z_{c,n} \operatorname{Re}\{Y_{load}\}} \quad (\text{A.43})$$

$$Q_{ext} = \frac{n\pi}{2} \frac{1}{Z_0} \frac{\omega_1}{\omega_{0,1}} \cdot \left(\frac{1}{n^2 \omega_1^2 C_{in}^2 R_L} + R_L \right) \quad (\text{A.44})$$

with

Z_0 : Impedance of the resonant TL section (typically 50Ω)

R_L : Impedance of the measurement TL (typically 50Ω)

C_{in} : Input capacitor (what you actually DESIGN)

$\omega_{0,1}$: Fundamental of LOADED resonator (what you MEASURE)

ω_1 : Fundamental of unloaded resonator

n : number of harmonic

A.4.3 External Q: Input and Output Coupling

According to Wallraff's notes⁷, having an [input and output capacitor] C_{in} and C_{out} on each side of the TL resonator (figure (A.7)) corresponds just to having two load circuits, which are effectively in parallel.

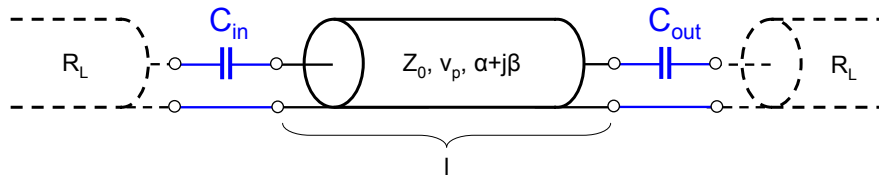


Figure A.7: TL resonator with input and output capacitor.

⁶Alternatively we could define Q_{int} as the quality factor of the bare (unloaded) resonator. Then $Q^{-1} = \frac{\omega_{0,1}}{\omega_1} Q_{int}^{-1} + Q_{ext}^{-1}$ and $Q_{int} \equiv Q_n$.

⁷Section 2.4.1, equation (2.25), page 10. See also Goeppel's and Wallraff's 2008 CPW paper.

For $C_{in} = C_{out}$ we then have to replace $C^* \rightarrow 2 \cdot C^*$ and $R^* \rightarrow \frac{1}{2} \cdot R^*$:

$$\boxed{Q_{ext} = \frac{n\pi}{4} \frac{1}{Z_0} \frac{\omega_1}{\omega_{0,1}} \cdot \left(\frac{1}{n^2 \omega_1^2 C_{in}^2 R_L} + R_L \right)}, \quad (\text{A.45})$$

where now $\frac{\omega_1}{\omega_{0,1}} = \sqrt{\frac{C_1 + \boxed{2} C^*}{C_1}}$.

Appendix B

Recipes Used for JPC Fabrication

B.1 Spinning Resist

B.1.1 Wafer Cleaning

- 2 minutes ultrasound in NMP
- 2 minutes ultrasound in acetone
- 2 minutes ultrasound in methanol
- blow dry

B.1.2 Spinning

Co-polymer MMA-MAA EL13 (see Fig. B.1):

- 3000 rpm for 90 seconds
- bake at 175° C for 60 seconds

PMMA 950K A4 (see Fig. B.2):

- 4000 rpm for 90 seconds
- bake at 175° C for 30 minutes

MMA(8.5)MAA Copolymer in Ethyl Lactate

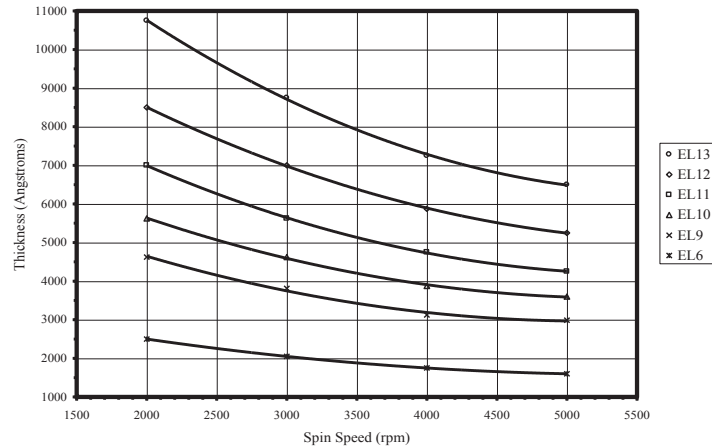


Figure B.1: Co-polymer spinning curves, provided by manufacturer.

950 A4 Spin Speed vs Film Thickness

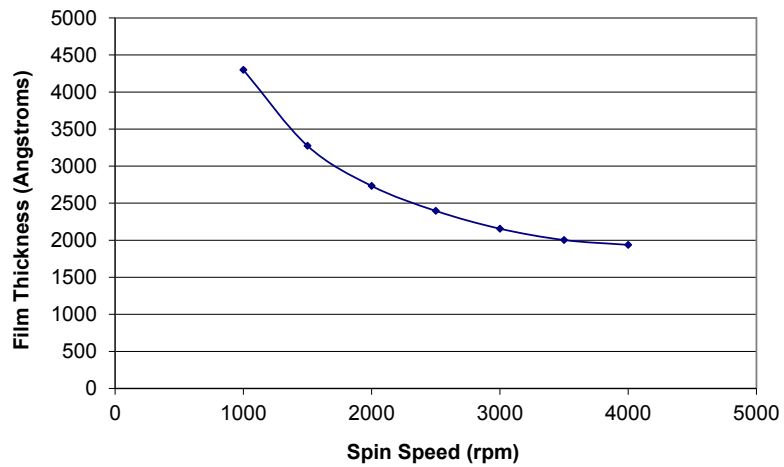


Figure B.2: PMMA spinning curve, provided by manufacturer.

B.2 Development

B.2.1 Dolan Bridge Technique

- with tweezers, slowly wave sample in MIBK:IPA solution (3:1) for 50 seconds at 25° C
- remove and dip sample in IPA for 10 seconds, to stop resist development
- blow dry with dry nitrogen

B.2.2 Bridge Free Technique

- submerge sample (with tweezers or preferably with strainer) in IPA:water solution (1:3) for 2 minutes, ultra-sound turned on
- dry off with dry nitrogen

B.3 Aluminum Deposition

All samples were evaporated in the Plassys MEB550S electron beam (e-beam) evaporator.

B.3.1 Dolan Bridge Technique

- oxygen-argon (1sccm:3.5sccm) plasma cleaning: 250 V, 30 seconds
- titanium sweep
- evaporation of first Al layer: 35 nm at rate of 1 nm/s and +40°
- oxidation (15% oxygen, 85% argon): at 10 Torr for 5 minutes (typical values)
- evaporation of second Al layer: 120 nm at rate of 1 nm/s and -40°
- capping oxidation: at 10 Torr for 5 minutes
- lift-off: place in hot (65° C) acetone for ca. 20 min. Rinse with (cold) acetone and IPA, blow dry with dry nitrogen

B.3.2 Bridge-Free Technique

Same as above with following differences:

- angles are $\pm 25^\circ$
- Al layer thickness: 20 nm and 30 nm
- lift-off: place in hot (90° C) NMP for ca. 1h. Ultrasound for 20 seconds. Rinse with IPA, blow dry with dry nitrogen